The Synthesis, Crystal Structure, and Properties of Bichalcogenides

Dissertation for the degree of Philosophiae Doctor

Emil Herman Frøen

Department of Chemistry

Faculty of Mathematics and Natural Sciences

University of Oslo

December 2023

Acknowledgments

Summary

This thesis consists of two parts: The main project, which seeks to discover and characterize novel inorganic compounds incorporating multiple chalcogenide anion species in their crystal structures, and a secondary project focused on optimizing the synthesis of Zn_3N_2 nanoparticles. As the latter ended up thematically isolated due to the reduction of scope following complications, it is discussed independently at the end of the thesis.

The main project resulted in the discovery of 13 novel compounds incorporating an anionic superstructure, of which three exhibit novel crystal structures. Four systems were prepared as reasonably pure phases investigated in detail by X-ray diffraction, magnetic susceptibility, heat capacity, electric conductivity, Mössbauer spectroscopy, and DFT analysis.

$La_{18}Fe_5Cu_4S_{26}O_8$ was found to exhibit a novel orthorhombic crystal structure mostly described by the $Cmcm$ space group. However, the crystal structure exhibited an unusual guest-in-host structure, with significant apparent disorder in the ionic positions. A structural model of the origin of the disorder was determined. The compound was found to be a magnetic cluster glass without long-range magnetic order.

$La_{14}TME_6CuS_{24}O_4$ (TME = Fe, Cr) exhibits a novel monocline crystal structure described by the $C2/m$ space group. The compound was found to exhibit minor structural disorder, with two ionic positions exhibiting partial occupancies, as well as multi-valent chains of the transition-metal elements. The compounds were found to exhibit spin domain formation, but the acquired data is contradictory on the size of these domains.

$Ba_6Fe_2Te_3S_7$ exhibits a novel orthorhombic crystal structure, described by the $Cmcm$ space group. The Fe positions are arranged in isolated, linear $[Fe_2S_7]$ units, while the tellurides assume a rare $[Te_3]^{4-}$ polytelluride structure. The compound was found to exhibit spin singlets due to strong coupling within each $[Fe_2S_7]$ unit.

The series of compounds $BaMTeS$ (M = Fe, Mn, Zn Ge) was found to exhibit a known crystal structure described by their oxysulfide analogs. The Ge analog is isostructural with the other three analogs but exhibits a half-occupied structure $BaGe_{0.5}TeS$. The BaFeTeS analog was further investigated and found to exhibit a lack of long-range magnetic ordering, as well as a Mössbauer anomaly.

Additionally, the crystal structures of the novel compounds Ba_3VTeS_4, $Ba_9Fe_4Te_{3.5}S_{12.5+\delta}$, $Ba_2Mn_3Te_2S_3$, $La_{10}Te_{14+x}S_{1-x}$, and La_2TeS_2, all analogs of known phases, are reported.

The secondary project aimed to improve and optimize a Zn_3N_2 nanoparticle synthesis procedure described in the literature. The target of the project was to improve the product monodispersity by altering the original synthesis approach, which utilized multiple hot-injections of precursor to tune the particle size, with a single-injection methodology. Rather, the particle size was to be tuned by varying the synthesis temperature instead. This project did not reach completion in time due to several unexpected difficulties arising during the work. The obtained results indicate significant improvement in the monodispersity of the synthesized Zn_3N_2 nanoparticles, compared with the original approach from literature. Furthermore, the results show it is possible to control the size of the synthesized nanoparticles by controlling the temperature of the synthesis.

Sammendrag

Denne avhandlingen består av to deler: Et hovedprosjekt, med mål om å oppdage og karakterisere nye uorganiske forbindelser som inkluderer to eller flere kalkogenid anion spesier i sin krystallstruktur, og et sekundærprosjekt som fokuserer på optimering av en syntesemetode for Zn_3N_2 nanopartikler. Sekundærprosjektet endte opp tematisk isolert grunnet reduksjon i prosjektets omfang etter vanskeligheter oppsto. Sekundærprosjektet er derfor diskutert som et separat prosjekt ved slutten av denne avhandlingen.

Hovedprosjektet resulterte i oppdagelsen av 13 nye forbindelser som inkluderer en superstruktur av anioner, samt tre nye krystallstrukturer. Fire systemer ble framstilt som relativt rene faser; disse ble undersøkt i detalj med X-ray diffraksjon, magnetisk susceptibilitet, varmekapasitet, elektrisk ledningsevne, Mössbauer spektroskopi og DFT.

$La_{18}Fe_5Cu_4S_{26}O_8$ krystalliserer i en ny, ortorombisk krystallstruktur, for det meste beskrevet av *Cmcm* romgruppen. Krystallstrukturen inkluderer en uvanlig gjest-vert struktur, med betydelig tilsynelatende uorden i de ioniske posisjonene. En strukturell modell av uordenen ble bestemt. Forbindelsen ble funnet å være et magnetisk cluster glass uten magnetisk orden over større avstander.

$La_{14}TME_6CuS_{24}O_4$ (*TME* = Fe, Cr) krystalliserer i en ny, monoklin krystallstruktur beskrevet av *C*2/*m* romgruppen. Forbindelsen be funnet til å inkludere mindre ionisk uorden, hvor to ioniske posisjoner har delvis okkupasjon, samt multivalente kjeder av overgangselementer. Forbindelsene ble funnet til å danne spinn domener, men de tilgjengelige data er selvmotsigende angående størrelsen på disse.

$Ba_6Fe_2Te_3S_7$ krystalliserer i en ny, ortorombisk krystallstruktur, beskrevet av *Cmcm* romgruppen. Fe-posisjonene er arrangert i isolerte, lineære $[Fe_2S_7]$ enheter, mens telluridionene er arrangert i en veldig sjelden $[Te_3]^{4-}$ polytelluridstruktur. Forbindelsen ble funnet til å danne en singlet-tilstand, grunnet sterk magnetisk kobling innen hver $[Fe_2S_7]$ enhet.

Serien med forbindelser $BaMTeS$ (*M* = Fe, Mn, Zn, Ge) ble funnet til å krystalliserer i en kjent krystallstruktur, identisk med deres oksysulfid analoger. Ge analogen er isostrukturell med de andre tre, men med en halv-okkupert struktur $BaGe_{0.5}TeS$. BaFeTeS ble videre karakterisert, og ble funnet til å ikke magnetisk ordne seg, samt til å vise en Mössbauer anomali.

I tillegg, krystallstrukturene til de nye forbindelsene Ba_3VTeS_4, $Ba_9Fe_4Te_{3.5}S_{12.5+\delta}$, $Ba_2Mn_3Te_2S_3$, $La_{10}Te_{14+x}S_{1-x}$, og La_2TeS_2, alle analoger av kjente forbindelser, er rapportert.

Sekundærprosjektet siktet på å forbedre og optimere en Zn_3N_2 nanopartikkel synteseprosedyre beskrevet i litteraturen. Prosjektet hadde som mål å forbedre monodispersiteten til produktet ved å endre den originale synteseprosedyren, som benyttet flere runder med «hot-injections» av forløper for å styre partikkelstørrelsen, med en metode som kun benyttet én injeksjon. Partikkelstørrelsen ble heller styrt ved å variere syntesetemperaturen. Prosjektet ble ikke fullført i tide grunnet flere uforventede vanskeligheter med arbeidet. De oppnådde resultatene foreslår betydelig økning i monodispersitet av de syntetiserte Zn_3N_2 nanopartiklene, sammenlignet med hva som har blitt tidligere rapportert i litteraturen. Videre, resultatene viser at det er mulig å kontrollere størrelsen til de dannede nanopartiklene ved å styre temperaturen til syntesen.

Table of Contents

List of Papers

1. **Synthesis and Properties of $Ba_6Fe_2Te_3S_7$, with an Fe Dimer in a Magnetic Singlet State**

   Emil H. Frøen, Peter Adler, and Martin Valldor

   DOI: 10.1021/acs.inorgchem.3c01775

2. **Synthesis and Properties of $La_{18}Fe_5Cu_4S_{26}O_8$, Containing Large Magnetic Clusters**

   Emil H. Frøen, Peter Adler, and Martin Valldor

   To be submitted

3. **Synthesis and Properties $La_{14}TME_6CuS_{24}O_4$, a Multivalent Spin-Chain Compound (TME = Cr, Fe)**

   Emil H. Frøen and Martin Valldor

   To be submitted

4. **Synthesis and Properties of BaMTeS (M = Fe, Mn, Zn) and the Disordered Structural Analog $BaGe_{0.5}TeS$**

   Emil H. Frøen, Domenic Nowak, Peter Adler, and Martin Valldor

   To be submitted

List of Papers – Not First Author

1. **Untitled Oxysulfide Article**

   Valldor et al.

Other Public Presentations

1. Synthesis and Characterization of Zn_3N_2 Quantum Dots

   Poster at the 2021 Norwegian Chemical Society – Functional Inorganic Materials (NKS-FUM) meeting.

2. The Absence of Expected Paramagnetic Behavior in $Ba_6Fe_2Te_3S_7$

   Presentation at the 2023 European Conference on Solid-State Chemistry (ECSSC)

Glossary

AC	–	Alternating Current
AE	–	Alkaline Earth Element
BSE	–	Backscattered Electron
CFS	–	Crystal Field Spitting
DC	–	Direct Current
DFT	–	Density Functional Theory
DOS	–	Density of States
EDX	–	Energy Dispersive X-ray
FC	–	Field Cooling
FWHM	–	Full Width Half Maximum
GGA	–	Generalized Gradient Approximation
HSAB	–	Hard-Soft Acid-Base
LAN	–	Lanthanide group elements
LDA	–	Local Density Approximation
LED	–	Light Emitting Diode
LCCSO	–	$La_{14}Cr_6CuS_{24}O_4$
LFCSO	–	$La_{18}Fe_5Cu_4S_{26}O_8$
LICSO	–	$La_{14}Fe_6CuS_{24}O_4$
LTCSO	–	$La_{14}TME_6CuS_{24}O_4$ (*TME* = Cr, Fe)
M	–	Any element considered a metal (Includes *TME*, *RE*, *s*- and *p*-block metals)
PAW	–	Projected Augmented Wave
PBE	–	Perdew – Burk – Eisenhower
PPM	–	Parts per million
PPMS	–	Physical Property Measurement System
PXRD	–	Powder X-ray Diffraction
QLED	–	Quantum (Dot) Light Emitting Diode
RE	–	Rare-Earth elements
SCCM	–	Standardized Cubic Centimeters per Minute
SC-XRD	–	Single Crystal X-ray Diffraction
SE	–	Secondary Electron
STEM	–	Scanning Transmission Electron Microscope
TEM	–	Transmission Electron Microscope
TME	–	Any element of the transition metals
VASP	–	Vienna *ab initio* simulation package
XRD	–	X-Ray Diffraction
ZFC	–	Zero Field Cooling

1. Introduction and Motivation

The initial prospect of this project included two parts, pertaining to the synthesis of multianionic compounds in both bulk and nanoparticle form. The nanoparticle project was scaled back midway due to the unexpected difficulties of the work and focused on preparing a monoanionic forerunner to the original multianion synthesis. As such, the projects ended up somewhat thematically isolated. Regarding this thesis, the nanoparticle section of the project will be treated as a second project, with a smaller scope and emphasis detailed in chapter 6.

1.1. Solid-State Multianion Synthesis

Throughout most of modern history, inorganic material synthesis has primarily focused on the cations, utilizing only a single anion, typically oxygen. Comparatively little work has been done pertaining to solid-state chemistry involving multianion materials; that is, materials with a crystal lattice incorporating more than one anion. Historically, this discrepancy may be attributed to the scarcity of multianion compounds in nature, resulting in a lack of attention directed to the field. In modern times, as interest in multianion compounds have started to grow, the limiting factor is rather the thermodynamic challenges inherent in synthesis involving multiple anions.

With two distinct anions involved, reacting two binary precursors may be complicated by major differences in their respective properties. For example, tellurides generally have a much lower melting point than oxides, and may evaporate or sublimate away at reaction temperatures sufficient for the oxides. Additionally, the resulting compounds are often metastable and only exist within a limited temperature range, placing further constraints on the applicable synthesis conditions. As such, synthesis of multianionic compounds entails the determination of an appropriate synthesis approach, and optimization of this approach to favor the formation of the desired product.

Multianionic compounds have been found to show potential not just for novel structures but also catalysis,[1–3] iron-based superconductivity,[4] batteries,[5,6] phosphors,[7–10] non-linear optics,[11] tunable properties,[12] and more. As such, it is of interest to explore the phase diagrams of the multianionic space to identify the compounds that exist and characterize them for future work.

With the previous in mind, the first objective of this Ph.D. project was the discovery, synthesis, and characterization of novel multianionic compounds. The aim was to further explore the wide

range of possibilities offered by this relatively scarcely explored approach to materials synthesis, and lay the groundwork for further investigation. While the starting point focused on oxyfluorides and nitride-fluorides, this switched to a focus on bichalcogenides, as searching for novel phases proved more rewarding in this field.

The discovered compounds were to be investigated with a range of standard characterization methods, including magnetic susceptibility, X-ray diffraction (XRD), heat capacity, and, for iron-based compounds, Mössbauer spectroscopy. This was later expanded to include theoretical investigations with density functional theory (DFT).

2. Background and Previous Literature

2.1. Multianions

2.1.1. Multianions in General

Multianion compounds, by simple linguistic consideration, refer to any compound incorporating more than a single anion into its matrix. How a given compound that fulfills this definition is considered depends on the context, the relative anion content of the different species, whether the site occupation is ordered or mixed, and a certain degree of arbitrariness.

Suppose the content of a secondary anion is significantly less than the primary, generally non-stoichiometric, and a solid solution of anions. In this case, it is rarely thought of as a multianion compound. Such compounds are typically referred to as doped. Doping has been a common approach for tuning the properties of materials for a long time, but anion-doped compounds are not typically considered a multianion.

Compounds are generally considered multianionic if they contain a significant (ideally stoichiometric) amount of multiple anions in solid solution or exhibit anionic superstructure. In the latter case, the relative proportion of anionic species is typically irrelevant for the classification.

Multianion compounds exist for every available combination of anions: Single group multianions like multichalcogenides or multi-group variations like chalcogenide-halides. Still, there is a vast gulf in the extent to which each group has been investigated. The oxyhalides are historically the most extensively studied, with thousands of published crystal structures, while other categories have only a dozen or fewer.

Another distinction must be made between single-atom anions and complex anions. Complex anions comprise units of multiple ionic species that bond particularly strongly to act as a single anion. Typical examples are the carbonate, phosphate, and sulfate ions. Complex anions exhibit their range of multianionic compounds, for example, the solid solution $Pb_4(PO_4)_2(SO_4)$,[13] or the ordered $Na_3Mg(PO_4)(CO_3)$,[14] but in this work, the focus is on the single atom anions. Polyanions, such as the polychalcogenides,[15] may be considered as a third category of anionic species, but through this text, they are grouped with their respective monoanionic constituents unless specifically considered.

2.1.1.1. Historically Early Work

Multianion research, while overshadowed by monoanion topics in most fields, has been ongoing in the background for a long time. Multianionic compounds, such as oxyhalides, have been well-known since further back in time than the modern literature trails. Searching back through the literature, one will find articles on investigations of multianionic compounds from the beginning of the 1900s. Of these, some further refer to widespread information on certain oxyhalides during that period.[16] In brief, the possibility of combining multiple anions into a single structure has been well-known throughout the whole history of modern chemistry. The advent of structural determination of atoms in crystalline materials arrived with the development of X-ray diffraction techniques. After the first atomic crystal structure, that of table salt,[17] was solved in 1913, what was the first multianion compound to be determined is difficult to say for certain. Some of the earliest examples easily found are Fe_2SSe, resolved in 1925 to be a solid solution,[18] and the sulfide-pnictides $NiSbS$, $NiAsS$, and $CoAsS$ from the same year,[19] representing some of the earliest examples of anion superstructures, disregarding the significant bonding between anions in the latter three examples.

A point of note concerning the lack of scientific interest in the early 1900s is related to the fact that multianionic compounds are very rare in nature. The conditions necessary for the formation of single-atom-anion multianionic compounds in nature are strict; thus, such minerals are rare indeed. While examples do exist, such as ullmannite ($NiSbS$),[19] matlockite ($PbFCl$),[20] and the recently discovered hitachiite ($Pb_5Bi_2Te_2S_6$),[21] multianion compounds are primarily made in a lab, and most of earlier scientific works were focused on reproducing the chemistry seen in nature.

A pioneer of the modern material chemistry of multianionic compounds is physicist and crystallographer William Houlder Zachariasen. In his works, he provided some of the earliest structural determinations of multianion compounds in 1948 on the structures of the *5f*-element compounds. This started with Ce_2O_2S and UO_2F_2, describing the anionic superstructure these compounds assume.[22] This initial work was expanded in 1949, first investigating oxysulfides, which proved to be analogs of Ce_2O_2S.[23]

This work continues in his 1949 study on the structures of several sulfides and oxysulfides, the latter on thorium, uranium, and neptunium.[24] These were all found to assume the PbFCl structure, which had been previously characterized in 1932 by Nieuwenkamp and Bijvoet.[25] Zachariasen went on to characterize the structures of a range of oxysulfides and oxyhalides.[26,27]

While some early work was carried out on multianionic compounds, their presence in the scientific literature remained relatively marginal until 1968, when the potential of rare-earth oxysulfides as hosts for optically active rare-earth doping became a topic of interest.[28] From here, multianionic compounds saw a slim but constant stream of literature each year. This continued until about 1990, when interest again started to grow sharply. As this followed immediately after the discovery of the famous high-temperature superconductor YBCO in 1987,[29] these events were likely correlated.

2.1.1.2. Recent Work

Interest in multianion materials has only really taken off in the last three decades since 1990. Consequently, most known multianionic compounds are comparatively recent discoveries, although the reason is still somewhat tangential. The discovery of most multianionic compounds is typically not from people explicitly searching for them, but rather from accidental synthesis while attempting to achieve different products.[30]

2.1.1.2.1. Nitride-Halogenides and Oxynitrides

Nitride-halogenides are among the less studied multianions. Due to the difference in the ionic radii between nitride and halogenide anions, they typically form anion superstructures. Nitride-fluorides, in particular, have only a handful of known compounds beyond the single-element nitride-fluorides. Typically, these are difficult to prepare in a pure form and often require exotic synthesis procedures. The quaternary $Ce_2MnN_3F_{2-\delta}$ phases, for instance, were synthesized at very low temperatures (~100 °C) under a F_2/N_2 gas mixture.[31] The synthesis of the quinary $LiAE_4Si_4N_8F$ (AE = Ca, Sr) and quaternary $La_3[SiN_4]F$ involved the decomposition of alkaline earth hydrides to form reactive intermediates.[32,33] Even the simpler syntheses involve weld-shut crucibles, such as for $LiSr_2[TaN_3]F$, the AE_2BN_2F (AE = Ca, Sr) phases, and the $Ba_8(BN_2)_5F$ phase.[34–36] Notably, among the more complex nitride-fluorides, the structure typically involves a coordination between one of the more stable nitride-cation pairings: Si_3N_4, TaN, and BN are all among the most stable nitride species.

Known quaternary and higher nitride-chlorides are somewhat more abundant than the fluorides, partly due to a rush in interest in nitride-chloride intercalation structures, explained in the next paragraph. The heavier halogenides, Br and I, again have very few known multianion compounds with nitride.

An important compound among the nitride-halogenides is the β-Li$_x$ZrNCl structure. First reported by Yamanaka et al. in 1996, it represented the first discovery of a layered nitride superconductor.[37] The compound exhibits an intercalation structure, where lithium is introduced into the van der Waals gap of the precursor compound β-ZrNCl. The compound assumes a trigonal crystal structure described by the space group *R*-3*m* (No. 166) illustrated in Figure 1.
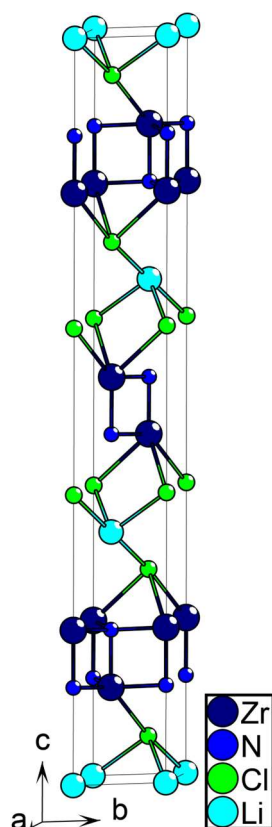
Figure 1: Layered structure of the Li$_x$ZrNCl superconductor. Occupancies are not shown. Crystal data obtained from the work of Shamoto et al.[38]

The structure may be considered in terms of two layers: the matrix layers, consisting of the β-ZrNCl precursor structure, and the intercalated Li layers.

The initial report of Li$_x$ZrNCl gave a critical temperature of about 12.5 K for a lithium content x=0.16. The critical transition temperature was found to be significantly dependent on the lithium content. In 1998, the isostructural hafnium analog achieved superconductivity at 25.5 K,[39] showing the structure type's potential for superconductivity at elevated temperatures. These discoveries resulted in a small rush of activity to investigate these systems, ultimately finding

the optimized critical temperatures by Li-intercalation to be about 15 K for β-ZrNCl and 26 K for β-HfNCl.[40]

Compared with the nitride-halides, the scope of known oxynitrides is much larger. This may be attributed to the greater stability of the oxynitrides and the fact that oxynitrides are one of the more likely impurities to form during the synthesis of complex nitrides if the synthesis environment is not kept sufficiently free of oxygen. Due to the similar ionic radii of the oxide and nitride ions, many oxynitrides form solid solutions in contrast to the superstructures of the nitride-halides, although N-O superstructures are also known.[41]

The most common structural motifs of the oxynitrides are simply the same as the oxides, courtesy of the similarities between the oxide and nitride ions. One example are the perovskite structures. With general compositions of $M_1TME_1ON_2$, $M_1TME_1O_2N$, or solid solution intermediates (M = Alkaline earth, Lanthanides) (TME = Groups 4, 5, 6), they exhibit a wide range of perovskite structures with either mixed, ordered or both forms of anion occupancy.[42–44] Results from investigations with neutron diffraction have reported clear anion ordering in some cases; an example is TaNO, which exhibits a N-O superlattice.[41] They are considered materials of interest as they exhibit mixed character between oxide and nitride structures and, as such, are considered for the same potential applications as oxide perovskites in general, including pigments, colossal magnetoresistors, and photocatalysts.[45]

2.1.1.2.2. Superconducting Iron Pnictides

The discovery of the iron-based layered superconductors likely caused the single greatest surge in interest for multianionic compounds.

The first report on the properties of the layered iron superconductors was with the discovery of LaOFeP, with a superconducting temperature of ~4 K, by Kamihara et al. in 2006.[46] The stoichiometric compound exhibits a tetragonal crystal structure described by the $P4/nmm$ (No. 129) space group, illustrated in Figure 2.[47] The structure exhibits two distinct layers: A positively charged lanthanum oxide layer, and an oppositely charged iron phosphide layer. It may be noted that the two layers are arranged as anti-structures of each other: Within their respective layers, the Fe position is equivalent to the O position situated directly adjacent along the c-axis and correspondingly for the La and P positions.
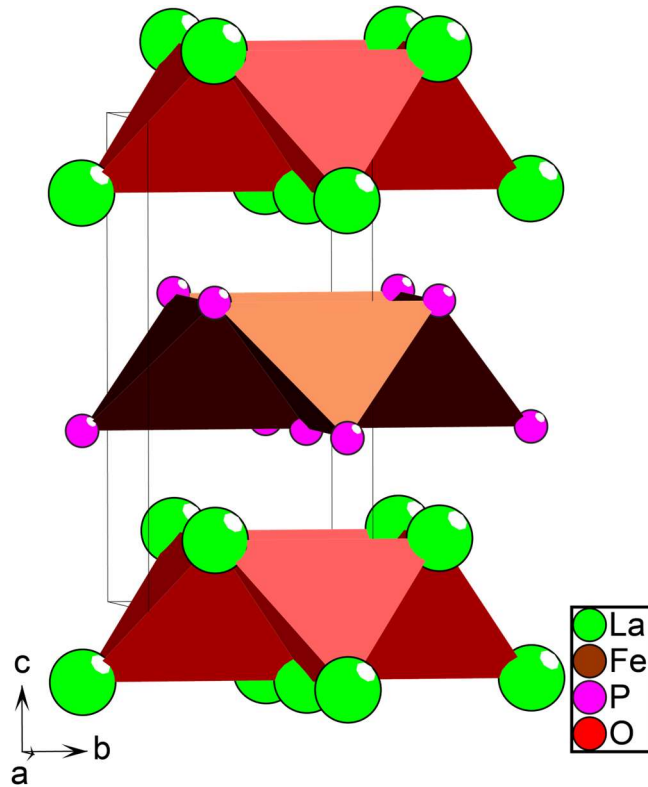
Figure 2: Crystal structure of LaOFeP. Crystal structure from the work of McQueen et al.[47]

Initially, the discovery was met with muted reception, likely due to the low critical temperature, garnering only eight citations through 2007 (According to Web of Science). Interest only exploded in 2008, with the report of La[$O_{1-x}F_x$]FeAs exhibiting a critical temperature of 26 K.[48] This discovery attracted significant attention to the layered iron superconductor, resulting in a rush of work in this field of study. Over the next couple of years, several superconducting iron compounds were discovered. Simple analogs with switched rare earth metals of the *RE*[$O_{1-x}F_x$]FeAs (*RE* = Ce, Sm, Nd, Pr, Gd, La:Y)[49–54] motif were reported in quick succession within the same year, elevating the known ceiling for critical temperatures of layered iron superconductors to 52 K. This was a remarkable milestone, as only cuprate high-temperature superconductors have achieved higher critical temperatures, and, in the words of the authors who reported the discovery: "*As the first non-cuprate compound that superconducts above 50 K, this discovery places these iron arsenide compounds to the second high temperature super-conducting family explicitly.*".[51]

In addition to the oxypnictides, a second family of multianionic superconductors emerged in the form of arsenide-fluorides. With the same structure, they were candidates for similar superconducting properties. Indeed, it was found that samarium-doped SrFeAsF could attain

similar critical temperatures to the oxypnictides, with a critical temperature of 56 K for $Sm_{0.5}Sr_{0.5}FeAsF$.[4]

While this initial rush for increasing critical temperatures quickly leveled out, with no further improvements under ambient pressure after $Sm_{0.5}Sr_{0.5}FeAsF$,[55,56] the discovery made a significant example of how properties of potentially paramount importance hide in systems where no one would expect or predict. Such unexpected discoveries also drive the theoretical background of the properties in question forward. The conventional origin of superconductivity is from electron-phonon coupling,[57] but this is not found to be the case in iron superconductors. Instead, it is believed to be a consequence of a pairing mechanism generated by the electron-electron Coulomb interaction.[56,58]

Due to the discovery of high-temperature iron superconductivity, similar systems also saw a surge in interest. An example of compounds that garnered renewed interest of particular note to this work are the iron chalcogenides, which may exhibit the same planar structures as the FeAs motifs in the iron superconductors.

2.1.2. Bichalcogenides

Bichalcogenides are, by definition, a subcategory of the broader field of multianion compounds. And these may again be subdivided into two groups; the bichalcogenides anion pairs which tend to form solid solutions, and those which tend to form anion superstructures. According to Hume-Rothery, the former category comprises the sulfide-selenides and the selenide-tellurides. The remaining pair combinations, namely the oxide-sulfides, oxide-selenides, oxide-tellurides, and sulfide-tellurides, will tend to form anionic superstructures. The latter category is of principal interest in this thesis.

2.1.2.1. Structure and Configurations

The basis of the structural considerations of the bi- or even multi-chalcogenides lies in the difference between the ionic radii of the chalcogen group. Starting from the top, the respective radii are 126 pm (O^{2-}), 170 pm (S^{2-}), 184 pm (Se^{2-}) and 207 pm (Te^{2-}).[59] Polonides could likely form bichalcogenide compounds with the same pairings as the tellurides, but no chalcogenide-polonides are known, for obvious reasons.

Bichalcogenide structures may be divided into two categories: The first is the comparatively simple partial substitution structural motifs, where specific sites of a monoanionic structure are

selectively substituted with a second anion. The second group consists of structures that exclusively form with multiple anions.

2.1.2.1.1. Ordered Monoanion Analogs

A simple example of the first category is the La_2O_3 structure,[60] which is also assumed by La_2O_2S.[61] A reason for the stability of structural analogs such as this, despite the significant difference in ionic radii, is the release of stressed configurations compared with monoanionic analogs. Taking a closer look at the coordination of La in La_2O_3, each cation position has seven coordinated oxygen (Figure 3). Three of these assume shorter interatomic distances of 2.37 Å, three assume longer distances of 2.73 Å, and the final one assumes an intermediate distance of 2.45 Å. The interactions are thus strained, resulting in a higher energy state than the seven-fold coordination of anions could achieve without structural limitations. In the ordered oxysulfide analog, this tension seems to be diminished. With three of the coordinated oxygen of each La position substituted by S, the longer La-S distance, along with the adjustment in the La-O distance from the presence of the sulfide ions, allow the structure to rearrange such that the four remaining La-O distances are equal at 2.42 Å.
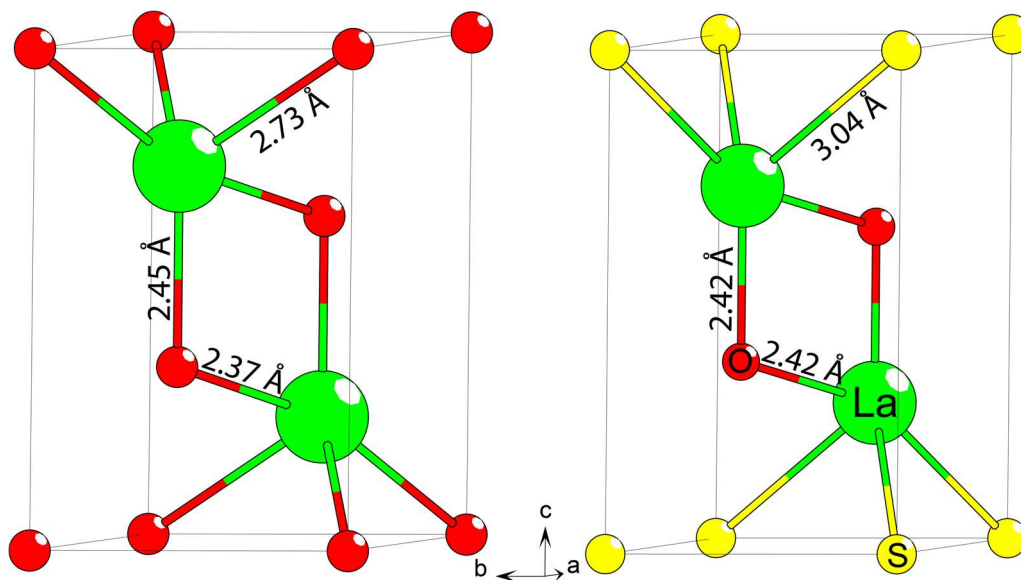
Figure 3: A comparison of the interatomic distances between the isostructural La_2O_3 and La_2O_2S. Crystal structure data from Koehler et al.[60] and Morosin et al.,[61] respectively.

The oxygen-rich La_2O_2S phase may be considered as a solubility limit for sulfur in the La_2O_3 crystal structure. There is also a sulfur-rich phase in the same system, $La_{10}S_{14+x}O_{x-1}$.[62] This

sulfur-rich phase is also known to form a solid solution, with the oxygen position being substitutable by more sulfur. Again, the $La_{10}S_{14}O$ structure is the solubility limit of oxygen in the corresponding crystal structure.

There is always a degree of solubility at the edges of the phase diagrams. In many instances, it may be practically insignificant, but in others the solubility may extend to complete substitution of selected ionic sites, forming ordered multianion compounds.

2.1.2.1.2. Bianion Dependent Structures

Regarding the second category of bichalcogenides, the structural considerations are much more complex. The additional degrees of freedom in how a structure may be arranged with another anion make the resulting ionic arrangements very difficult to predict.

An obvious consequence of introducing more than one anion into a compound is the effect on the symmetry of the resulting crystal structure: Multianion substitution will generally reduce the symmetry. Further, because of the additional anionic radius present, the resulting structures are not necessarily simple tight-packing motifs, either. Rather, preferential ion coordination (elaborated upon in a later paragraph) complicates descriptions of crystal structures and necessitates the introduction of new concepts and considerations to describe (or predict) multianionic coordinations effectively.

An applicable rule of thumb for bianions is that the dimensionality (D) of the anion superstructure is often shared with the full structure, and this factor is dependent on the ratio between the anionic species. At unity, the superstructure is likely to assume a 3D arrangement, while ratios of 1:2 and 1:6 (or less) will usually result in 2D and 0D structures, respectively. The 2D structures will often take the form of a planar layer stacking order, while 0D structures exhibit the lesser component in isolated individual species. It is also possible for intermediate arrangements with features of multiple dimensionalities to form. The La_2O_2S structure described previously (Figure 3) is an example of a 1:2 structure with a planar dimensionality of the anion superstructure. $Zn_4B_6O_{12}S$ is an example of a 0D structure with the lesser anionic component being arranged as individual species in the crystal structure (Figure 4a).[63]

1D structures are generally less common, but they do occur, such as in $Sm_3Ti_3Se_2O_8$,[64] an oxyselenide where the scarce selenides are arranged parallel with one axis. The selenides almost form a planar structure in this compound, but a narrow oxide matrix segregates the continuity.

Another example is the $Pr_2Ta_3Se_2O_8$ structure type (Figure 4b),[65] where edge-linked $[TaSe_4O_2]$ octahedra arrange all selenium positions parallel with the c-axis. Not all cases are equally clear-cut with regard to dimensionality; an intermediate case between 1- and 2D is seen in $Sr_2Mn_2O_4Se$. The compound exhibits 1D chains of both the Mn and the Se positions, but these are arranged further into 2D planes, interspaced by 2D Sr-O planes.[66] The selenides and tellurides may be a partial exception to the rule of scarcity for 1D structures, however, due to their tendency to form polychalcogenides. Polychalcogenide formation selectively stabilizes crystal structures where the chalcogenides are directly adjacent, which could promote 1D structures.[15]
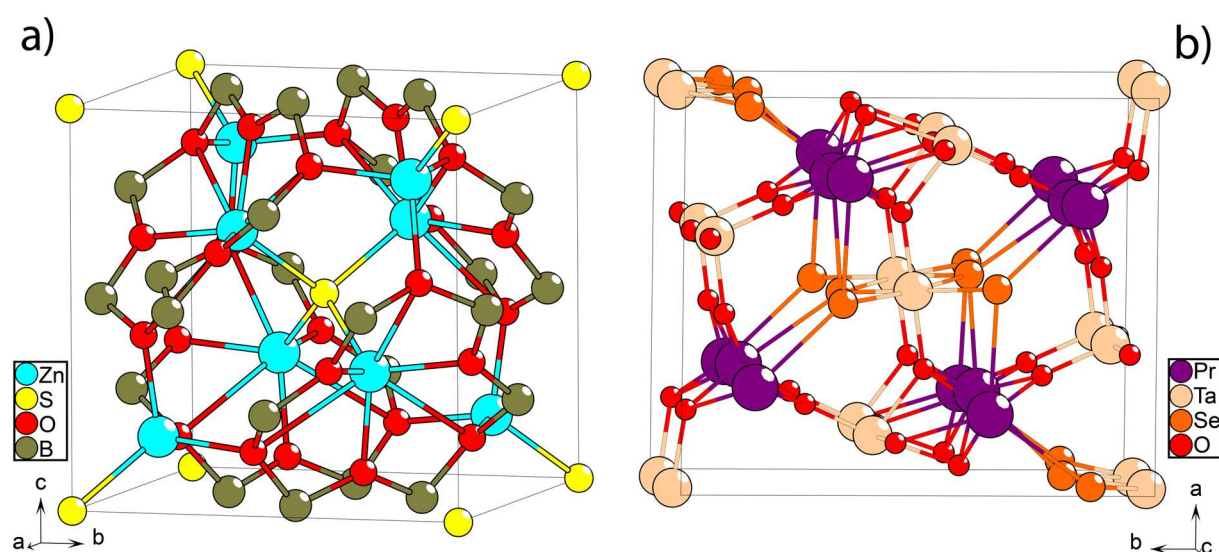
Figure 4: An illustration of anion dimensionality. a): $Zn_4B_6O_{12}O$, exhibiting a single sulfide in the center of the unit cell. b): $Pr_2Ta_3Se_2O_8$, exhibiting a chain of selenides along the c-axis, surrounded by an oxide matrix. The crystal structure data is from Zhou et al.[63] and Brennan et al.,[65] respectively.

In addition to a dependence on the ratio of anions, the relative radii of the anions may also affect how the crystal structure arranges itself. For instance, the ratio between the ionic radii of S^{2-} and O^{2-} is about 1.35, which happens to be close to the square root of two ($\sqrt{2} \approx 1.41$). A common motif in tetragonal (or rectangular lattices with two sufficiently similar lattice parameters in general) oxysulfides with a planar structure is thus a square lattice of sulfide positions, along with a second square lattice of oxygen, rotated 45° relative to the sulfide lattice, which fits both square planar arrangements within the same unit cell. This motif is seen in several compounds, including $CeBiOS_2$[67] (Figure 5) and $Ce_4Ga_2S_5O_4$.[68] Another possible motif is placing the two anions in parallel square lattices, with one anion situated in-plane, and the

other situated out-of-plane with a given cation lattice. Examples of this latter structure are seen in $Na_2Fe_2OS_2$ and CsV_2OS_2.[69,70] These are not mutually exclusive arrangements; both anion ordering motifs are observed, for instance, in the $ErU_2S_3O_2$ and $La_2Fe_2O_3Se_2$ structure types.[71,72]
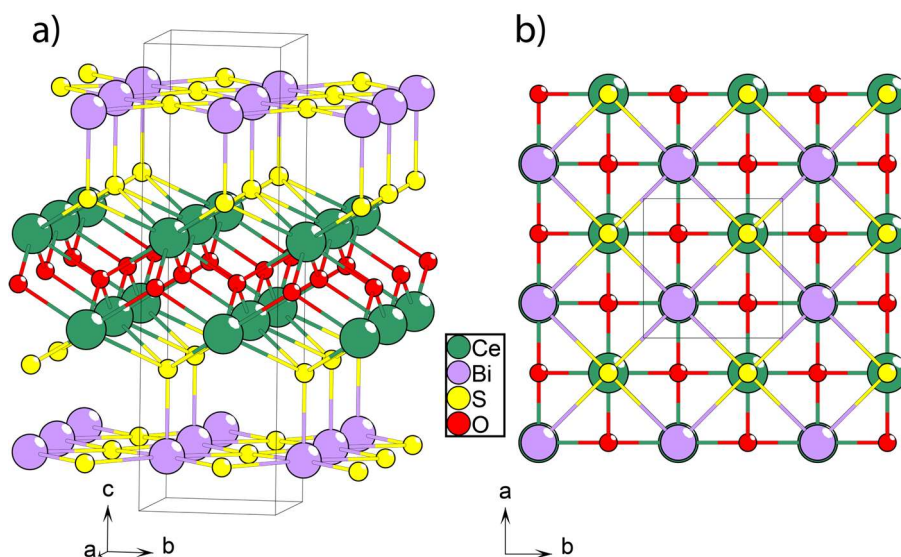
Figure 5: a) The crystal structure of $CeBiOS_2$. B) A *c*-axis view of the $CeBiOS_2$ crystal structure, illustrating the 45 ° tilt between the sulfide and oxide square lattices. The crystal structure data is from the work of Céolin et al.[67]

A structural feature observed in many multianion compounds in general, is that anionic species will preferentially coordinate with certain cations over others. This tendency may be considered in terms of the hard-soft acid-base (HSAB) concept.[73] In general, hard anions (for bichalcogenides, oxygen) are more likely to be found coordinated to hard cations (high positive charge and smaller size). The opposite also applies, where the softer anions (S, Se and Te) will preferentially coordinate with the softer cations (smaller charge and larger size). Depending on the components of a given compound, this effect can manifest in several ways: A repeatedly observed pattern is that preferential cation-anion coordination often coincides with the dimensionality rules to expand the structural dimensionality to incorporate both cat- and anions.

To give a couple of examples, for a sulfur-rich oxysulfide with hard spacer ions like the trivalent lanthanides, along with softer transition metals, the oxygen will often exclusively coordinate with the spacer ions. The spacer ions will tetrahedrally coordinate the oxygen, forming a larger spacer unit of the form $[LAN_4O]^{10+}$ (LAN = Lanthanides). An example of such coordination is found in La_4MnS_6O (Figure 6a).[74] As the oxygen content increases from the sulfur-rich

extreme, the spacer-oxygen coordinations will increase in size and complexity, according to the dimensionality rules laid down previously. Depending on the composition, they can form spacer-oxygen chains within a sulfide matrix, such as in $La_3CuO_2S_3$ (Figure 6b),[75] or planes like LaAgOS (same crystal structure as Figure 2).[76] On the oxygen-rich side of the phase diagram, the structures arrange themselves to preferential coordination of sulfur to the soft transition elements, but with similar features. The $La_3WTMES_3O_6$ (*TME* = transition metal element) series of analogs is an example of this category.[77]
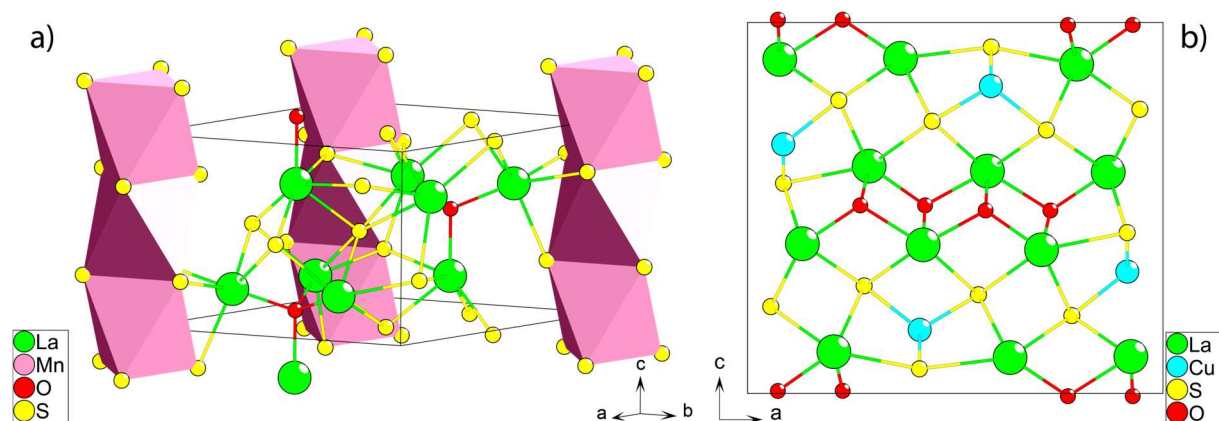
Figure 6: a) The crystal structure of La_4MnS_6O, illustrating the $[LaO_4]$ unit. b) The crystal structure of $La_3CuO_2S_3$, illustrating an example of a La-O chain. Crystal structures from the works of Ijjaali et al.[74,75]
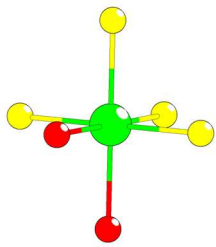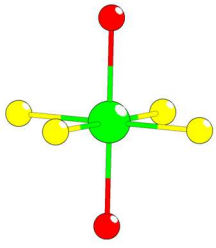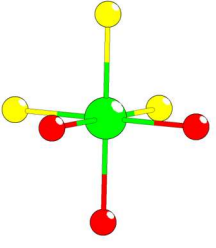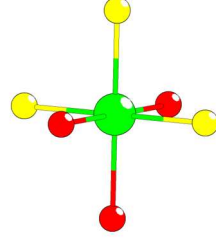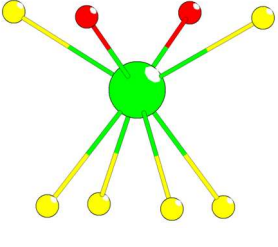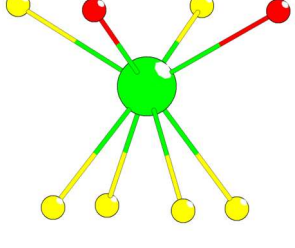
2.1.2.1.3. Naming Conventions of Complex Multianion Coordinations
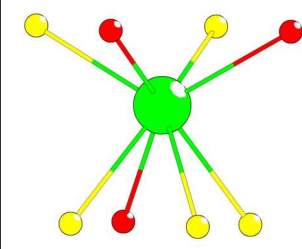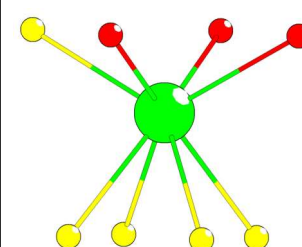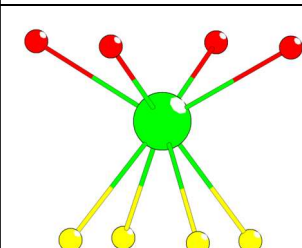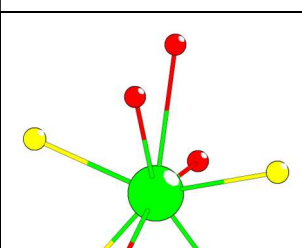
In general, a problem that crops up with more complex multianion compounds is that many of the potential coordinations possible with a heteroleptic anion configuration do not have an established naming convention. Describing the coordination can be difficult, especially for cations that tend to coordinate larger numbers of anions.

Lower coordinations are simple. For 2- and 3-coordinate arrangements, one only needs to specify what anions are present and in what number. From some 4-coordinate arrangements and higher, additional information is necessary. The nomenclature utilized in this thesis to describe heteroleptic anion coordination is given and illustrated in Table 1. Additionally, the 9-fold coordinated capped square (anti)prismatic configurations follow the same nomenclature as the 8-fold coordinations, clarified for whether the heteroleptic coordination is on the same or opposite side of the cap-position with a *c*- or *ac*- notation, respectively.

Table 1: Nomenclature for unambiguous description of heteroleptic anion coordination.

Coordination Number	Number of Substitutions	Coordination (Name)	Coordination (Image)
6	2	*cis-*	
		trans-	
	3	*fac-*	
		mer-	
8	2	*fac/trans-*	
		fac/cis-	

	3	belt-	
		fac-	
	4	fac-	
		mer-	

2.1.2.1.4. Coordination Disproportionation

While the range of potential ionic coordinations that may be achieved in a bianionic system is high, not all configurations are equally stable in all systems. Depending on the cations present in analogs of the same structure type, the anions may preferentially rearrange such that the crystal structure changes from exhibiting a single heteroleptic configuration to two different coordinations: one homoleptic, and one heteroleptic. This property has been coined *coordination disproportionation.*[30] One example of this effect is observed in *LAN*CrS$_2$O.[78,79] The lanthanum variation exhibits a single octahedral, heteroleptic, 1+5 coordination of Cr with a single oxygen coordination. If the lanthanum is substituted with the smaller cerium or neodymium ions, the structure rearranges to exhibit one 2+4 *trans*-coordination of chromium, along with one homoleptic sulfide coordination (Figure 7).

16
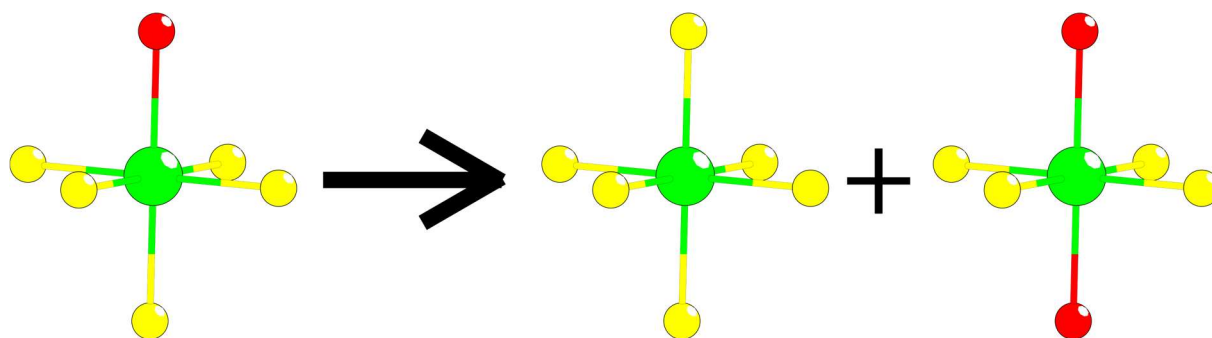
Figure 7: An illustration of coordination disproportionation; a single 1+5 heteroleptic coordination disproportionates into one homoleptic and one 2+4 heteroleptic coordination.

2.1.2.2. Heteroleptic Anion Interactions

The presence of multiple anionic species within a single compound substantially affects the interatomic distances in a given crystal structure. For the interatomic distances from a given cationic species to adjacent anions, there are substantial differences between homoleptic and heteroleptic coordination of a cation. Further, this effect is further modified with the number of each anionic species, although other structural factors may dominate depending on the local symmetry. The general trend for oxychalcogenides, as stated in previous literature, is simple: in a heteroleptic coordination of a cation, cation-oxygen distances will tend to be shorter, and cation-chalcogenide distances will tend to be longer.[30] This property arises from the difference in the electronegativity of the different anions. As such, it could also be expected to occur for sulfide-tellurides, if to a more limited degree, as the difference in electronegativity between sulfur and tellurium is about half the difference between oxygen and sulfur. The sample size of known sulfide-tellurides is relatively small, with a given cation typically having a select few known compounds at most with heteroleptic coordination. A table of comparisons between select known compounds are shown in Table 2.

Table 2: A comparison between the interatomic distances observed in homo- and heteroleptic coordinations. The value provided for the homoleptic interatomic distances are averaged over five arbitrarily chosen compounds with the same oxidation states and coordination.

Compound	Cation	Coordination Number		Average $M - S$ interatomic distance (Å)	Average $M - Te$ interatomic distance (Å)
		S	Te		
Ga_2S_2Te ([80])	Ga	3	1	2.339	2.559
Homoleptic	Ga	4	4	2.271[81–85]	2.608[86–90]
LaCuSTe ([91])	Cu	3	1	2.535	2.717
Homoleptic	Cu	4	4	2.351[92–96]	2.672[97–101]
$K_3Cu_8Te_2S_4$ ([102])	K	4	3	3.240	3.543
Homoleptic	K	7	7	3.331[103–107]	3.604[108–111]
$Ba_5In_4Te_4S_7$ ([112])	Ba1	4	4	3.110	3.726
	Ba2	6	2	3.269	3.801
Homoleptic	Ba	8	8	3.290[113–117]	3.603[88,118–121]
$CsTb_3Te_4S$ ([122])	Tb1	2	4	2.710	3.134
	Tb2	1	5	2.764	3.051
$CsS_2Tb_5Te_6$ ([122])	Tb1	2	4	2.745	3.066
	Tb2	2	4	2.729	3.100
	Tb3	1	5	2.725	3.075
Homoleptic	Tb	6	6	2.784[123–127]	3.087[105,128–131]

While Table 2 is a very limited selection and based on mostly a single example for each heteroleptic coordination, the chosen examples don't corroborate the expected trend. The examples range from following the expected rule to directly contradicting it.

Specifically, the tetrahedral 3+1 coordination of Ga exhibits the exact opposite trend, where the $M - S$ ($M - Te$) interatomic distances are notably longer (shorter) than the homoleptic equivalents. Similarly, the same heteroleptic coordination of Cu exhibits longer interatomic distances for both species compared with the homoleptic equivalents. The latter could be

explained as a consequence of steric repulsion due to the size of the anions in a small tetrahedral arrangement.

On the other hand, some larger cations, like Ba, do appear to follow the same rule as the oxysulfides, although there were examples among the reference homoleptic compounds that went against the trend even if the average is in accord. K appears to be another exception, where the average interatomic distances are all shorter. Finally, Tb appears to show marginal effect on the sulfide distances, while the telluride distances show no clear trend.

From the data presented here, it seems that while the effect that causes the oxychalcogenide trend would be present as a contribution, it is sufficiently weak that other effects appear to dominate the interatomic distances in more complex compounds.

A different avenue of comparison is between the monoanionic Nd_2Ch_3 (Ch = O, S, Te) phases, against Nd_2SO_2 and Nd_2TeS_2, both isostructural with Nd_2O_3. Nd_2TeO_2 is also included for completeness. The averaged interatomic distances are shown in Table 3.

Table 3: A comparison between neodymium-chalcogenide interatomic distances in homo- and heteroleptic coordinations. The shown homoleptic Nd – O distance is the one which corresponds with the corresponding Nd – O coordination in the heteroleptic equivalent.

Compound	Nd – O	Nd – S	Nd – Te
Nd_2O_3 ([132])	2.324		
Nd_2S_3 ([133])		2.888	
Nd_2Te_3 ([134])			3.172
Nd_2SO_2 ([133])	2.364	2.969	
Nd_2TeO_2 ([135])	2.328		3.503
Nd_2TeS_2 ([136])		2.787	3.358

For this series of comparisons, the sulfide and telluride interatomic distances fulfill the expected trend. The heteroleptic telluride distances are both longer than the homoleptic equivalent. The sulfide distances vary with the heteroleptic pairing: with O, the distance is greater, while with Te it is longer than the homoleptic, exactly according to what should be expected from the described trend. The outliers are the Nd – O distances, which are both longer than the corresponding homoleptic distance, likely due to some of the homoleptic oxygen positions being strained.

2.1.2.2.1. Crystal Field Splitting

The crystal field splitting (CFS) is strongly affected by heteroleptic coordination. The standard CFS diagrams are usually devised for homoleptic coordinations and are therefore distorted by the introduction of multiple anions. What the CFS for a given heteroleptic coordination looks like is difficult to predict, but in general terms, the degeneracy of the homoleptic CFS states would be broken, and the relative energy of the nondegenerate states would be rearranged. This effect may be considered akin to forcibly imposing a Jahn-Teller distortion on a given lattice site, causing a rearrangement of the orbitals by control of the composition rather than through intrinsic properties of spin and coordination. The CFS of a heteroleptic coordinated cation depends not only on the species involved but also on the number of each species and what sites of the coordination are substituted. Consequently, tuning the CFS and, by extension, the spin states of the first-row transition metal elements is potentially possible. Some work with theoretically predicting the CFS of heteroleptic complexes has been reported, for instance, investigating the CFS in trigonal bipyramidal Fe^{3+} complexes.[137]

In addition to the direct effects on the CFS, multianion arrangements typically result in a lower local symmetry (Schönflies). This has significant consequences for optical and magnetic properties, with strong effects on compounds such as lanthanide phosphors.

2.1.2.2.2. Local Ion Polarity

While in a homoleptically coordinated configuration, the identical character of the anions results in the cation typically assuming an average position near the center of the anions. Even so, there is often some degree of deviation in the interatomic distances, which results in polarization of the central cation. ZnO is a famous example of a polar oxide,[138] with the polarity originating from tetrahedrally coordinated Zn where the polar Zn-O interatomic distance differs by just about 0.02 Å from the other three.[139]

It is a well-known fact of inorganic chemistry that only compounds that crystallize in non-centrosymmetric space groups may exhibit a sum polarity. This effect may be substantially amplified by the greater local polarization induced by heteroleptic coordination of a cation (Figure 8).

A couple of notable examples of ion polarization are $CaZnSO$[140] and the compositionally similar $SrZn_2S_2O$.[141] The former compound assumes the hexagonal space group $P6_3/mc$, exhibiting tetrahedrally coordinated Zn ions, with a 3+1 coordination to S and O. This results

in the polarization of the individual zinc ions adding up to a global polarization of the structure, which results in a substantial second harmonic generation property. $SrZn_2S_2O$ crystallizes in a different space group (*Pmn2$_1$*) but exhibits the same 3+1 coordinated Zn and similarly exhibits second harmonic generation, *albeit* with differences in the precise optical properties.
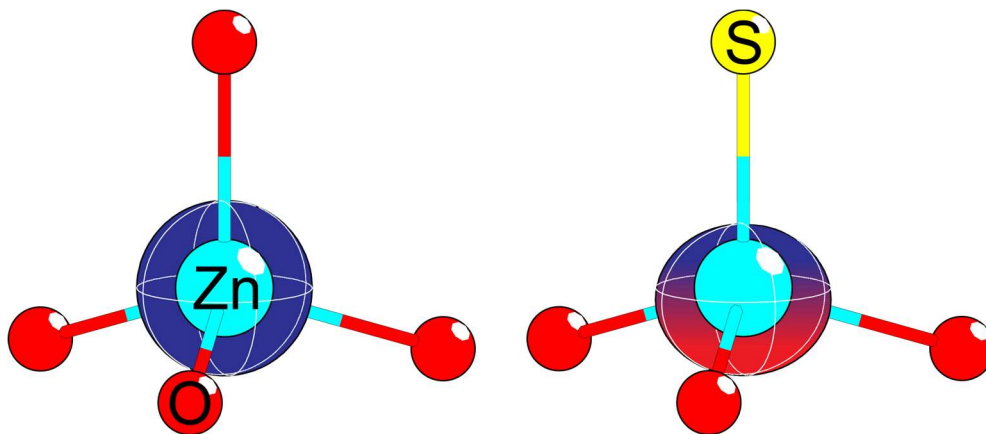
Figure 8: Schematic illustration of differences in local polarity between homo- and heteroleptic coordinations.

2.1.2.2.3. Band Gap Tuning

An effect of heteroleptic coordination that has received a deal of attention is the tuning of the band gap. While this effect of heteroleptic coordinations is well known, it is typically considered on the topic of solid solutions. A comparatively well-known example would be the CdS-CdSe solid solution system, which may exhibit band gaps in the full range of 2.4 to 1.7 eV, corresponding to the sulfide and selenide pure phases, respectively.[142–144] Similar effects may be achieved with ordered multianions. While ordered substitution would necessarily be done with stoichiometric degrees of substitution, it would not be subject to the same restrictions in how only similar anionic species could be substituted.

Estimating many properties of bichalcogenide solid solutions is relatively simple, and can, in many cases, be an extrapolation between the single anion systems. Further, for bichalcogenides, there is a predictable trend where, moving down the chalcogenide group, the corresponding compounds exhibit decreasing band gaps. Predicting the properties of an oxide-telluride, however, is comparatively challenging. The oxide of a given cation may be an insulator, while the telluride is metallic; there is no simple intermediary rule to give the answer. Depending on the crystal structure, the properties may even be anisotropic.

2.1.2.2.4. Anisotropic Magnetic Coupling

The fact that magnetic coupling between adjacent ions with unpaired electrons takes place via the shared anion coordinations as an intermediary, is a well-known fact, well expressed by the Kanamori-Goodenough rules.[145,146] The fact that the anions are involved in the magnetic interactions via these superexchange pathways creates interesting possibilities for multianionic materials. For a heteroleptically coordinated magnetic species, the superexchange pathways are dependent not only on the arrangement of anions, but also on their species. Thus, it is possible to form structures where the magnetic coupling is explicitly anisotropic, and couple exclusively across distinct anions along specific crystallographic directions.

A good example of this is the BaCoSO structure type, illustrated in Figure 9.[147] It is an oxysulfide with a crystal structure exhibiting the *Cmcm* (No. 63) space group. The cobalt ions are coordinated in a 2+2 tetrahedral coordination, where the Co – S – Co couplings and Co – O – Co couplings are arranged along separate directions, here even defined by crystallographic axes.
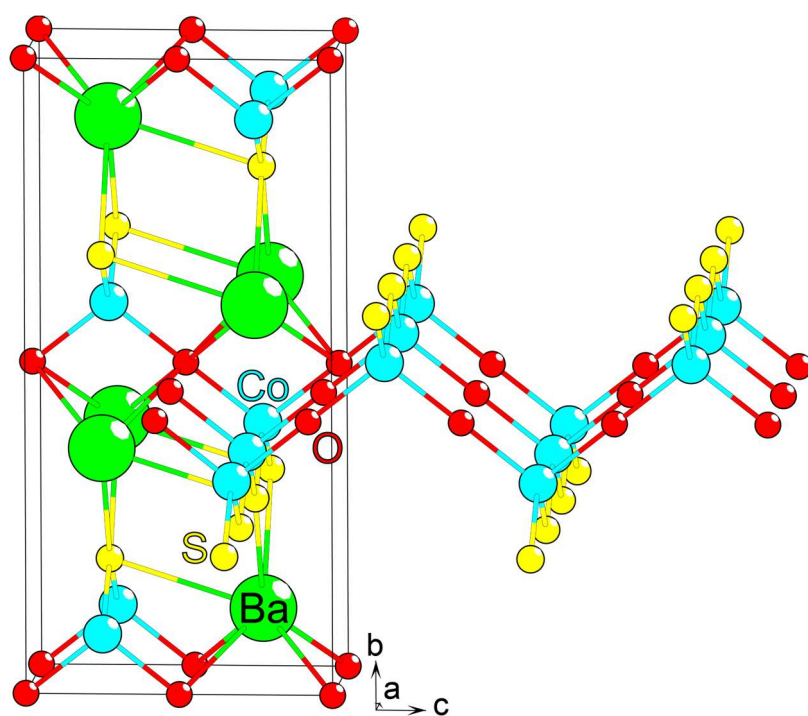
Figure 9: The BaCoSO crystal structure, illustrating an example of a 2+2 heteroleptic coordination of Co resulting in anisotropy in the magnetic coupling between the *a*- and *c*-axes. The crystal structure data is taken from the work of Valldor et al.[147]

2.1.3. Other Notable Bichalcogenides

2.1.3.1. Rare-Earth Oxysulfide Phosphors

As mentioned briefly in the historical section, the discovery of the rare-earth oxysulfides as hosts for optically active doping by, for instance, Er^{3+} or Eu^{3+} is what originally lit the spark for research of multianionic materials.

Rare-earth phosphors allow for emission of a wide range of wavelengths. Different doping of Y_2O_2S allows for emission ranging from red light with Eu-doping,[148] to green light for Tb-doping.[149] Several of the simpler rare-earth compounds of the RE_2O_2S motif have been investigated for such purposes, but the most prevalent in the literature are probably the yttrium, gadolinium, and possibly lanthanum compounds, which have significant work devoted to different synthesis approaches carried out.[8,9,150,151] While the simple oxysulfide compounds have been rather extensively characterized for phosphor applications, investigations of more complex oxysulfides for this purpose are much more limited. Eu^{2+}-activated CaZnSO has been investigated for such considerations, but other examples are lacking.[152]

2.1.3.2. $Sr_{n+1}TME_nO_{3n-1}Cu_{2m}S_{m+1}$ − A Homologous Series of Oxysulfides

A consequence of the predisposition of bichalcogenides for lower-symmetry crystal structures is that compositions which allow for the construction of homologous series are rare, but it is possible for such series to form. An example of a homologous oxysulfide series with a notable number of known phases is the $Sr_{n+1}TME_nO_{3n-1}Cu_{2m}S_{m+1}$ series, which is strongly reminiscent of layered oxide perovskites. The known compounds include the phases represented by $n = 1$, 2, 3 with $m = 1$, and $n = 1$ with $m = 2, 3$.[153]

The crystal structures exhibit a stacking order of two different structural elements; a Sr-TME-O layer consisting of vertex-sharing octahedral *TME* positions, interspaced with Sr, and a Cu − S antifluorite layer. Varying the composition, the thickness of these layers changes to accommodate.

These phases have been reported to exhibit a range of properties, depending on the stoichiometry and choice of transition metal, ranging from 3D antiferromagnetism for $Sr_2MnO_2Cu_2S_2$,[154] more complex electronic behavior with indications of strong correlation between the magnetic state and charge-transport properties for $Sr_2CoO_2Cu_2S_2$,[155] to metamagnetism for $Sr_2MnO_2Cu_6S_4$ and $Sr_2MnO_2Cu_4S_3$.[153]

3. Theory and Methodology

3.1. Solid-State Synthesis

In addition to air exposure during synthesis being problematic due to oxidation of the intended anions, the synthesis of multianion compounds often involves the use of air-sensitive elements and compounds. Depending on the composition, the products may be unstable as well. As such, it is necessary to carry out all work under inert conditions. Most bichalcogenides are, however, sufficiently stable against atmospheric conditions to not affect characterization.

Due to this, all work with the samples except characterization was carried out in an argon glove box where O_2 and H_2O levels were maintained below 1.0 and 0.1 parts per million (ppm), respectively.

The basic approach followed a cyclic workflow, illustrated in Figure 10. Upon deciding on a synthesis, a stoichiometric quantity of precursors was weighed out, which was then crushed and mixed into a homogeneous mass in an agate pestle and mortar. Once homogenized, if the sample was planned for characterization beyond XRD, the homogenous mixture was pressed into a 13 mm diameter pellet with about 30 kN of force. The resulting pellet was then broken into chunks that could fit in the corundum crucibles. If the sample was not expected to be subject to further characterization, the homogenized mixture was added straight to the crucible as powder. The crucible was placed in a silica ampoule, which was plugged with a rubber stopper (Figure 11, left). The sealed ampoule was then removed from the glove box and moved to be sealed. To seal the ampoule, a vacuum pump was connected to evacuate the argon atmosphere, which came over from the glove box. The ampoule was then sealed using an oxyhydrogen torch (Figure 11, right).
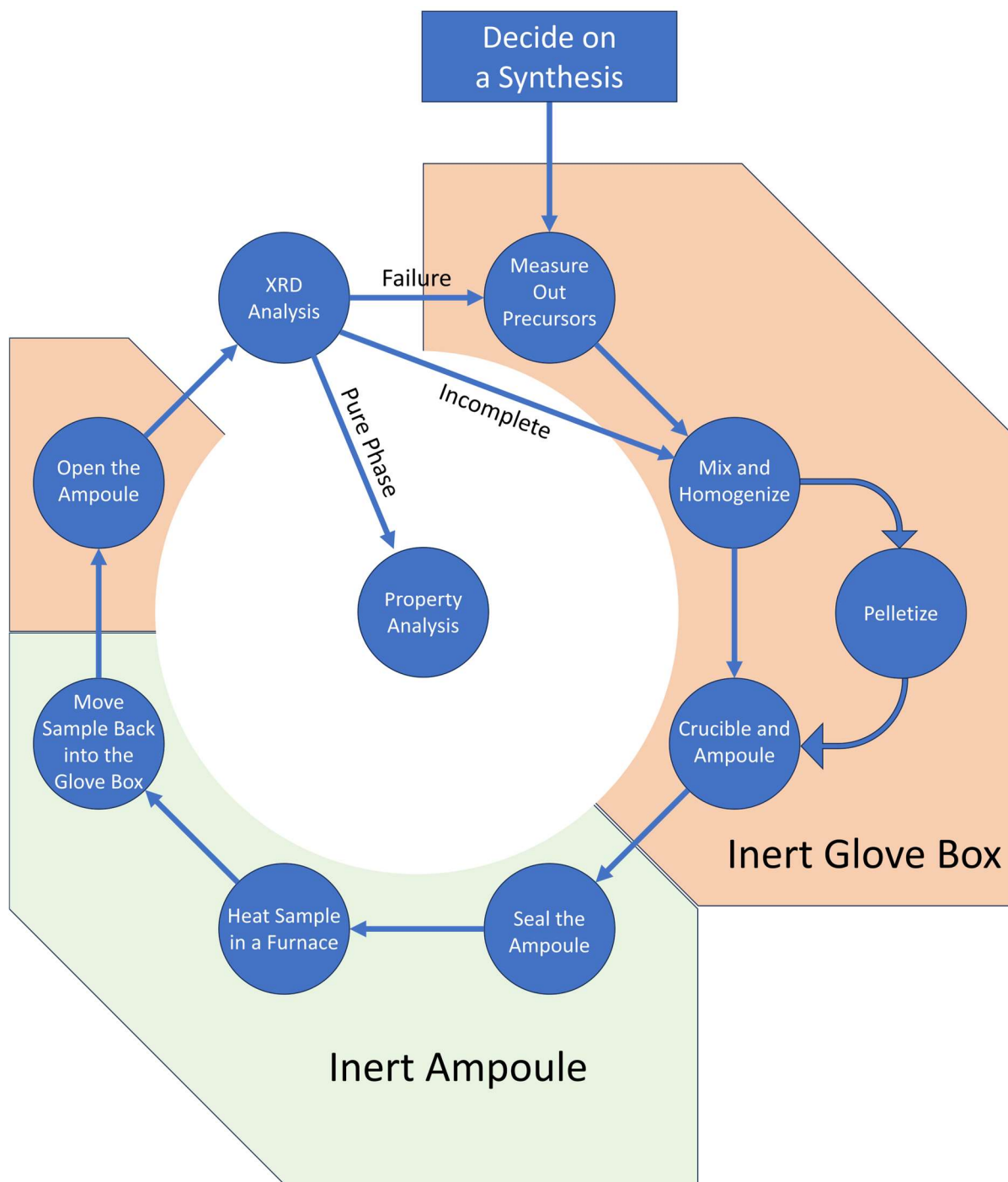
Figure 10: The cyclic workflow of the solid-state synthesis approach. The colored boxes represent how the sample is protected from the atmosphere.
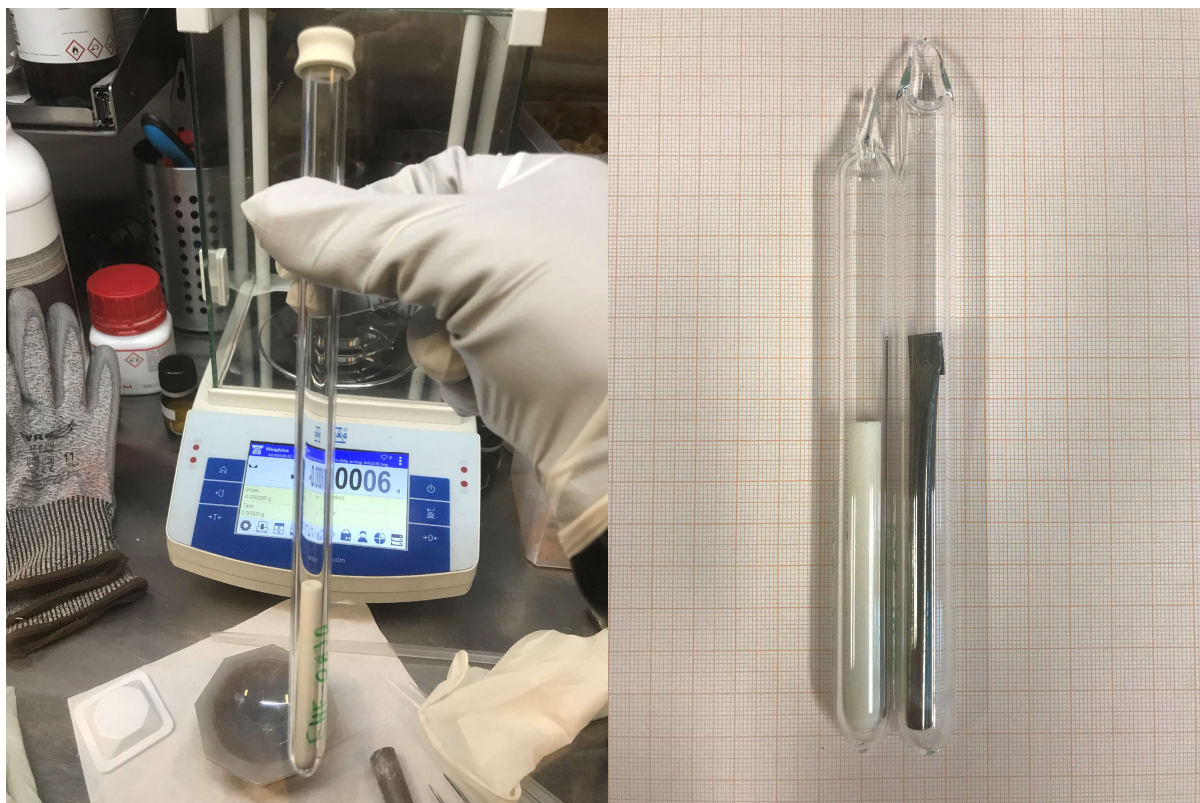
Figure 11: (Left) Corundum ampoule prepared for removal from the glove box. (Right) Sealed ampoules with corundum and Monel crucibles.

Once sealed, the ampoule was placed in a muffle furnace and heated to the appropriate temperature. The target temperature was predominantly decided by the composition of the synthesis, as well as any potential intermediates. Oxysulfides and their corresponding monoanion intermediates are typically very stable. Thus, a ramp of 5 °C min^{-1} to a temperature of 1000 °C was typically used as a standard. If elemental sulfur was present at the start of a synthesis, the reaction would be initiated by a slow (1 °C min^{-1}) ramp up to 400 °C and left to rest for five hours to avoid loss of reagent to rapid sulfur boiling out of the crucible. Then, the temperature would be raised to 1000 °C at 5 °C min^{-1} for the appropriate amount of time. For a pure oxysulfide phase, the rest time could vary from 72 hours, with one or two regrindings, to 200 hours, with four or five regrindings, depending on the target phase.

Synthesis of sulfide-tellurides was more involved. Both sulfide-tellurides and tellurides are comparatively volatile, and the specifics also depend on the cations. For a crude investigation into whether a phase exists or not, a 5 °C min^{-1} ramp to 700 °C and resting for 24 hours would typically be sufficient to determine if something would form, but there were several exceptions. Pure phases could take 2-4 weeks and several regrindings to form. One exceptional system,

BaZnTeS, forms a melt at 1000 °C instead of decomposing. On the opposite extreme, the low-temperature phase BaFeTeS required a synthesis temperature of 660 °C to avoid decomposition or irreversible secondary phase formation.

For regular synthesis, when the heating program was concluded, the furnace was turned off and allowed to cool at an ambient rate. Salt smelt syntheses were rather allowed to ramp down at an as-slow rate as schedule allowed, from about 100 °C above the salt's melting point to 100 °C below. (Salt smelt synthesis is mentioned mostly for completeness; few were carried out, as they were not found to be an effective approach for bichalcogenide synthesis.) Then, the furnace would be turned off and allowed to cool. The cooled ampoule was returned to the glove box and opened to retrieve the sample. (A part of) The sample was crushed down and characterized by powder XRD (PXRD).

If the PXRD showed the reaction not yet to have gone to completion, the sample was returned to the grinding step of the cycle. If the sample were a pure phase, it would be moved on to in-depth characterization. If the synthesis was, for any reason, found to be a failure, the whole synthesis process was started over. Failures, specifically, would entail fractured crucibles or ampoules, air exposure, loss of reagents to sublimation or spillage from boiling, as well as syntheses that reached completion but contained too large a proportion of secondary phases to be considered sufficiently pure. Finally, if the synthesis was found to have formed something unknown or unexpected, or if the synthesis was part of a search for unknown phases, the sample would be taken for single-crystal XRD (SC-XRD) to attempt to determine the structure of the unknown compound.

3.2. Characterization

3.2.1. X-ray Diffraction (XRD)

When identifying crystalline phases or determining their crystal structures, XRD is today the default approach due to the technique's ease of use as a non-destructive characterization method.

X-rays are a form of high-energy electromagnetic radiation, classified as photons with wavelengths ranging from about 0.1 to 10 nanometers. As it happens, this range of wavelengths happens to coincide with the periodicity of crystallographic planes in the stacking order of inorganic crystals. This allows crystalline materials to interact with X-rays, acting as a

diffraction grating. Depending on the specific wavelength of the X-rays and the structure of the crystalline lattice, the X-rays are diffracted at specific angles. The mathematical specificities of how and why are beyond the scope of this text; readers are invited to consult the reference for an extensive explanation of crystallographic principles.[156]

The qualitative method at the center of modern powder XRD is the Bragg equation, often called the diffraction condition:

$$2d * \sin(\theta) = n\lambda$$

In this equation, d is the spacing between parallel crystallographic planes, θ is the angle between any given crystallographic plane and the incident X-ray beam, λ is the wavelength of the X-rays, and n is the natural numbers.

An incident beam of X-rays will penetrate deeply into a crystal and interact with a large number of crystallographic planes at once. Reflection of the primary beam thus occurs from multiple crystallographic planes at once. Unless the condition of the Bragg equation is fulfilled, these reflections will interfere destructively and not return a signal in XRD. Note that the range of permitted values for n means each plane returns reflections at multiple angles, referred to as the n-th order of a reflection. By the Bragg equation, one may determine the spacing of the lattice planes that caused the diffraction by measuring the angle at which the primary X-ray beam was reflected.

In addition to the diffraction angle, another critical factor of XRD is the intensity of the reflections. The key factor controlling this is the fact that reflections are dominated by the electron density associated with each atom. The greater the electron density, the greater the reflected intensity. This allows for the determination of what species are associated with what crystallographic plane, which is of critical importance for structure determination. This is particularly useful for determining the anion superstructure in bichalcogenides, as the electron density associated with each species is clearly distinguishable in the XRD data. Difficulties arise when anion solid solutions occur or when attempting to differentiate between elements in the same row, especially for isoelectronic species like oxynitrides and oxyfluorides. In these cases, what anions occupy what positions must instead be determined from other factors, such as the composition and the interatomic distances within the structure.

There are multiple variations of XRD in common usage, of which two are relevant to this work: Powder XRD (PXRD) and single-crystal XRD (SC-XRD). The fundamental difference is given

by the names: SC-XRD entails employing the XRD technique on a single crystal, while PXRD measures on thousands of grains of a powder simultaneously. Each method has its respective benefits and downsides.

The greatest advantage of PXRD is that sample preparation for the technique is fast, requires little effort, works for any crystalline sample, and data collection is usually complete in minutes. The main downside is the loss of intensity precision in the data. PXRD measures reflection data averaged over thousands of crystals, each with different orientations. The orientation of the crystallites is necessarily assumed random, which is not always the case, a point that introduces complications as well. The averaging of reflections may also result in the signal from distinct crystallographic planes overlapping, further convoluting the data. As such, refinement of an unknown crystal structure may be difficult to impossible, especially for more complex and non-centrosymmetric lattices. A particular shortcoming of PXRD is the inability to determine whether a structure exhibits inversion symmetry or not, as this information is hidden by perfect intensity overlap. As such, a structure determined exclusively by PXRD is inherently more challenging.

The main advantage of SC-XRD is precisely that it suffers no loss of information to averaging as it measures the reflections of a single crystal with a known orientation. The intensity of any given reflection may thus be assigned to precise crystallographic planes, allowing for accurate determination of crystal structures. The downside to SC-XRD lies in the complexity of sample preparation. Firstly, the sample to be investigated must form crystals of sufficient size, which is not always possible. Second, the crystal must be individually isolated, picked out, and mounted on the instrument. Third, the crystal must be of sufficient quality, at best without twinning, distortion, or major defects. Finding and measuring an adequate sample is time-consuming, and requires experimental experience. Further, the morphology of a single crystal affects the intensity of the scattered X-rays. As such, it is necessary to correct for the absorption, which may be challenging, and constitutes a further source of systematic errors in the data. As such, SC-XRD is primarily used to determine the crystal structure of a compound.

Through this work, the PXRD data was gathered using a Bruker D8 Discover with Bragg-Brentano geometry, a Ge(111) Johanssen monochromator, Cu$K\alpha_1$ X-rays, and a Lynxeye detector. The PXRD samples were prepared by applying a thin layer of silicone grease to a zero-background-oriented silicon XRD sample plate and adding a small amount of sample. A detector energy filter was used to suppress the fluorescence from Fe-containing samples. SC-XRD data were collected at room temperature or at 100 K using a BRUKER D8 Venture single

crystal diffractometer equipped with a Mo$K\alpha$ InCoatec microfocus X-ray source and a Photon 100 detector. The atomic structures were determined using either JANA2006 or JANA2020 software.[157,158]

3.2.2. Scanning Electron Microscopy (SEM) and Energy Dispersive X-ray spectroscopy (EDX)

The operating principles of SEM are well encapsulated by the name of the technique. A beam of electrons is accelerated toward the sample and scanned over the target area. Electrons reemitted from the sample are picked up by detectors, depending on their angle and energy, which is used to determine topographic and compositional information.

There are two broad categorizations for the electrons that are emitted from the sample: The first category is the secondary electrons (SE), which are low-energy electrons (about 10 eV on average) emitted from within a few nanometers depth of the surface of the sample. This category of electrons primarily carries information about the surface topography of samples. The second category are the backscattered electrons (BSE). Unlike SE, BSE have high energy, comparable to the incident electrons. They are also emitted from deeper within the bulk of the target sample and thus carry compositional information. The BSE yield is directly correlated with the average atomic number in the specimen. Thus, phases with heavier elements, on average, appear brighter in BSE imaging, making it a useful tool for identifying impurity phases or inhomogeneities in an inorganic synthesis product.

While SEM is a very useful technique for imaging objects too small to resolve with optical techniques, it has a very particular shortcoming in that the samples must be electrically conducting. If they are too insulating, the electrons fired at the sample will remain on the sample, building up charge, which will start to deflect electrons, distorting the image. There are techniques for imaging isolating samples, such as coating the sample in a conducting layer, but it is fundamentally more challenging to image highly insulating targets.

When the electron beam from the SEM strikes a sample, it is typically with a substantial amount of energy, up to several 10s of keV. When these energetic electrons impact a sample, they transfer this energy into the electrons in orbitals around the nuclei, which results in core-level electrons of these atoms being excited from their ground state. This excited state is transient, and the atoms quickly return to the ground state, accompanied by the release of an X-ray photon. EDX is a technique for elemental analysis that takes advantage of the fact that the energy levels

of atomic core electron shells, and by extension, the energy of the emitted X-rays when these states relax, are characteristic of specific elements. By detecting these emitted X-rays and comparing the photon energy to a tabulated dataset of the emission energies of all elements, the elements present in a sample may be quickly identified. The relative quantities of any given elements are determined by the relative intensity of the signal.

EDX does have limitations. Firstly, while qualitative determination of what elements are present is usually accurate, excepting the cases where the signal from certain elements completely overlap, quantitative determination suffers from a lack of accuracy. One factor that may severely impact the quantitative result from an EDX analysis is simply the angle of the sample relative to the incident electron beam. If the sample is not level, the detected signal from lighter elements may be disproportionally altered compared with heavier elements. A second limitation is that EDX cannot detect elements lighter than boron, and quantitative analysis of elements of the second row is often inaccurate to the point of being useful only as a qualitative indicator.

SEM imaging and EDX analysis in this work were carried out with a Hitachi SU8230 field emission scanning electron microscope with an Xflash 6|10 EDX detector. EDX compositional analysis was carried out by taking a spectrum from ~20 or more different crystallites and averaging the results. The final composition is determined using the heaviest element (or the best alternative, should be heaviest element potentially be partially substituted) in the compound as a reference point, setting it equal to the expected value for the composition, and determining the percentage of other elements present by relative proportion.

3.2.3. Heat Capacity

The heat capacity of a material, by fundamental definition, is the thermal energy that must be added to increase the temperature of a material by a certain amount. Formally, it is defined as the limit

$$C = \lim_{\Delta T \to 0} \frac{\Delta Q}{\Delta T}$$

where C is the heat capacity, and ΔQ is the thermal energy that must be added to obtain a temperature change of ΔT. From a classical perspective, the heat capacity of a solid arises from the constituent atom's three degrees of freedom of oscillation within a lattice. Heat capacity is a property determined by quantum mechanics, and the classical image fails to describe heat

capacity at lower temperatures, but it is still a useful idea. The classical image gives that the molar heat capacity of materials should be $3NR$, where N is the total number of atoms, and R is the gas constant (8.3145 J mol^{-1} K^{-1}). This value turns out to be correct in the high-temperature limit and is known as the Dulong-Petit limit. It may be interpreted as the maximum heat capacity achievable by purely phononic contributions. While the phononic contribution dominates in solid crystalline materials, it is important to note there are other contributions present. For example, electronic and magnetic contributions can be present, but an extensive description of these are beyond the scope of this text. A full description of the heat capacity requires consideration of the quantum mechanical aspects of atomic scale properties. Specifically, the quantization of the possible atomic oscillations plays a critical role at lower temperatures. The total heat capacity is described by the Debye formula:[159]

$$C_{V,m}(T) = 3Rf_d(T) \quad f_d(T) = 3\left(\frac{T}{\theta_D}\right)^3 \int_0^{\frac{\theta_D}{T}} \frac{x^4 e^x}{(e^x - 1)^2}\, dx$$

where $C_{V,m}(T)$ is the molar heat capacity at constant volume, R is the gas constant and $\theta_D = \frac{h\nu_D}{k}$ is the Debye temperature. Of the last parameter, k is the Boltzmann constant, h is the Planck constant, and ν_D is the maximum frequency at which the atoms oscillate.

In an insulating sample, the heat capacity, as a function of the sample temperature, is a critical investigative tool for determining the presence, nature, and temperature of transitions within a novel material. Theoretically, a material with no phase transitions should follow the Debye formula, meaning that any deviations should be non-phononic in origin. First-order phase transitions appear as discontinuous divergences from the Debye formula and are easily observed. These appear in accompaniment with regular 3D magnetic transitions, as well as structural transitions. Information on second-order phase transitions may also be found in heat capacity measurements, but the value of these decreases with the temperature span of the transition increasing. Low-dimensional magnetic transitions are a typical example of second-order transitions. Magnetic ordering phenomena, often seen as second-order phase transitions, were investigated in this work by this technique.

A useful technique in analyzing heat capacity measurements is plotting $C_{V,m}(T)/T$ against T. The resulting plot makes it easier to spot any non-phononic contributions to the heat capacity. Further, the units of $C_{V,m}(T)$ is J K^{-1} mol^{-1}; thus $C_{V,m}(T)/T$ is J K^{-2} mol^{-1}. As such, subtracting

the Debye contribution from the integral $\int_{T_1}^{T_2} \frac{C_{V,m}}{T} dT$ directly returns the energy of the entropy contribution of the non-phononic features.

The approach used to measure the heat capacity of the samples in this work is called the non-adiabatic thermal relaxation method. A sample is mounted to a holder with a known thermal conductivity and a calibrated heat capacity under high-vacuum conditions. The sample is thus only able to dissipate heat through the known conditions of the holder, in addition to thermal radiation. When the system has been cooled to the desired temperature and allowed to equilibrate, the temperature of the sample is increased above the system equilibrium by a designated amount. When the external application of heat stops, the temperature of the sample, which is constantly measured, will fall back down towards the system equilibrium. As the thermal conductivity, and thus the energy transferred away from the sample per unit time, of the sample holder is known, the rate at which the temperature of the sample falls gives the heat capacity.

The heat capacity data in this project was determined using a Quantum Design PPMS, utilizing pellets, sintered if possible, or several smaller chunks.

3.2.4. Magnetic Susceptibility

The definition of a material's magnetic susceptibility is a measure of how magnetized a material becomes in response to the application of an external magnetic field. More formally, it is defined as the ratio (χ) of magnetization (*M*) to the applied magnetic field (*H*) by the formula

$$M = \chi H$$

The units of magnetic susceptibility are somewhat of a confusing subject, as there are two equivalent groups of units in use today: CGS and SI. This thesis will exclusively refer to the CGS units.

In CGS units, the magnetization of a material is expressed in terms of electromagnetic units (emu), and the magnetic field strength is expressed in terms of Oersted (Oe). The molar susceptibility is thus expressed in terms of emu Oe^{-1} mol^{-1}.

The magnetic susceptibility of a material is a consequence of the arrangement of electrons within a material. A fundamental interaction exhibited by all materials is diamagnetism. This is observed as a material being slightly repulsed by a magnetic field. This effect is typically

much weaker than other magnetic effects and, as such, will only dominate when it is the sole contribution. As a general rule, any material where all electrons are paired, will only exhibit diamagnetism. In terms of susceptibility, a diamagnet exhibits a negative value of χ. Generally, diamagnetic effects are considered temperature independent.

The second common effect is paramagnetism (positive value of χ), which appears as a weak attraction to a magnetic field. Paramagnetism occurs when there are unpaired electrons in a given material, but these are randomly arranged, without any ordering. It occurs as a consequence of electrons acting as tiny magnets, which, in the presence of an external magnetic field, will adjust to align with the field and create a small sum attractive force from the induced dipole. The temperature at which a material loses its magnetic ordering and assumes a paramagnetic state is known as the Curie temperature for ferromagnetic materials (or Néel temperature for antiferromagnets). The temperature dependence of paramagnetic materials is typically characterized by the Curie-Weiss law

$$\chi(T) = \chi_0 + \frac{C}{T - \theta}$$

where χ_0 is a diamagnetic constant contribution, T is the temperature, θ is the Weiss constant, and C is the Curie constant. The Weiss constant may be interpreted as a measure of the mean spin-to-spin interaction strength. The Curie constant is directly correlated with the effective magnetic moment by the equation

$$\mu_{eff} = \sqrt{\frac{3k_B C}{N_A \mu_B^2}} = 2.828\sqrt{C} \; \mu_B$$

where k_B is the Boltzmann constant, N_A is Avogadros number and μ_B is Bohr's magneton. This value is further correlated with the number of unpaired electrons by the equation

$$\mu_{cal} = g_j\sqrt{J(J + 1)}\mu_B$$

where J is the total angular momentum, and g_j is the Landé-factor, an electron spin g-tensor (approximately equal to 2 in solid materials). As such, the susceptibility may inform on not just the magnetics, but also on the oxidation states of the atoms present in the structure, as these directly correlate with the number of unpaired electrons.

Susceptibility may also inform on the magnetic structure of a material, below the Curie (or Néel) temperature. For illustrations of the following, see Figure 12. In a ferromagnet, unpaired

electrons align in parallel with the applied magnetic field, adding a comparatively large magnetic field on top of what is applied externally. In a susceptibility plot against temperature, this appears as a sharp increase in susceptibility below the transition temperature, which eventually saturates and levels off. Antiferromagnets, on the other hand, align the unpaired electrons in antiparallel, reducing the susceptibility below the transition temperature. Additionally, there are superconductors, where the susceptibility falls to an extreme diamagnetism at the superconducting transition temperature and remains constant. These four examples are the typical four examples of magnetic behavior, but there are many other possibilities for how the spin in a material may arrange itself. These may involve local magnetic ordering, competing interactions, and metastable states, preventing a fully ordered configuration of spin alignment.
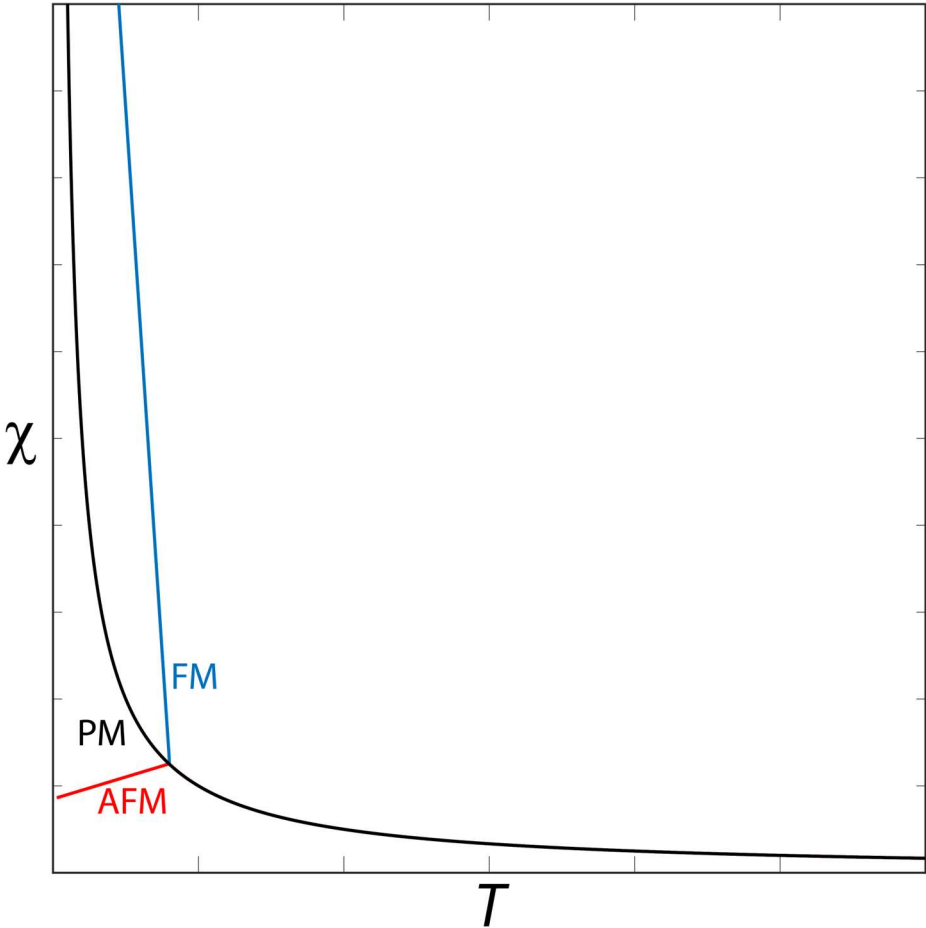
Figure 12: The three most common qualitative properties of magnetic DC susceptibility: ferromagnetism (FM), antiferromagnetism (AFM), and paramagnetism (PM).

A typical direct current (DC) magnetic measurement that is commonly carried out for magnetic compounds, are field-cooled (FC) and zero-field-cooled (ZFC). Like the names imply, a sample is initially cooled to the initial measurement temperature, either with (FC) or without (ZFC) an applied external magnetic field. The susceptibility of the sample is then measured against temperature as the sample is reheated. Observing a difference between these measurements indicates the formation of magnetic domains in the sample.

The features described so far relate to DC magnetic susceptibility analysis. It is, for certain magnetic behaviors of compounds, also of interest to measure the susceptibility response to an alternating current (AC) magnetic field. While DC susceptibility informs on magnetic structure by the number of unpaired electrons, AC susceptibility probes, in addition, the dynamic response of materials. It is employed to inform on mechanistic features of magnetic properties. It may provide information of particular importance when dealing with (partially) disordered magnetic structures, such as superparamagnets, the many variants of spin-glasses, mictomagnets and similar. Measuring the AC susceptibility with varying frequencies may inform, for instance, on the activation energy of the magnetic domains.

Measurements of magnetic susceptibility were carried out with the same Quantum design PPMS as the heat capacity. A sample of about 10-20 mg of powder, typically reground from a pellet, was placed in a polypropylene sample holder, which was then mounted in the instrument. For any form of susceptibility measurements, the instrument was cooled down to the initial start temperature first and allowed to equilibrate. The actual measurements were carried out while the temperature was being raised between measurements, as this is typically more stable.

3.2.5. Mössbauer Spectroscopy

Mössbauer spectroscopy is a spectroscopic technique based on the eponymous Mössbauer effect, based on recoil-free absorption and emission of gamma rays.

During absorption and emission of photons, conservation of momentum demands free nuclei undergo a change in momentum (recoil). If a free nucleus at rest is to absorb a photon, the photon energy must be slightly greater than the fundamental transition energy. Equivalently, if a nucleus at rest emits a photon, the energy of the photon will be slightly less than the transition resulting in the emission. As a consequence of this shift, the emission and absorption spectra of gamma rays have practically no overlap.

Mössbauer spectroscopy is based on the fact that nuclei fixed in position in a crystal lattice predominantly tend to undergo recoil-free absorption and emission. With no recoil, there is no shift in the energy that a nucleus will absorb and emit. Due to this, it is possible to attain measurable absorption and emission of gamma rays utilizing a gamma emitter of the same isotope as the target.

To obtain gamma ray emission of suitable wavelength, a source consists of a parent isotope which decays to an excited state of the desired isotope. The source utilized for the Fe^{57} isotope is Co^{57}.

Mössbauer spectroscopy yields three general features of note: The isomer shift, the quadrupole splitting, and the magnetic hyperfine splitting. These three together inform on the coordination and spin-state of the target isotope within a crystal structure.

All work with Mössbauer spectroscopy, both measurements and interpretation, was not carried out by the author of this thesis, but by an external collaborator, accredited in the acknowledgments section.

3.3. Density Functional Theory (DFT)

3.3.1. Motivation for Including DFT in this Thesis

The original prospect for this project was intended to be fully experimental. The decision to expand the scope of the investigation to include DFT was based on several facets, but the key reasoning was the prevalence of crystal structure uncertainties in many of the compounds discovered. Structural uncertainty, where the atomic positions and ordering were ambiguous, as well as uncertainty in oxidation states of cations or polytelluride species. It also provided a secondary perspective on the origin of the magnetic properties of several compounds.

3.3.2. Wavefunctions – Basic Principles of Quantum Mechanics

The theory discussed herein, pertaining to DFT and quantum mechanics, is sourced from the book referenced here.[160] For a more detailed introduction to quantum chemistry and DFT beyond the scope of this text, the reader is referred to the same.

The basis of quantum chemistry is the fact that the properties of any atomic system are fully described by its wavefunction, as laid down by the theory of quantum mechanics. The fundamental framework of the theory may be represented by the time-independent non-relativistic Schrödinger equation:

$$\hat{H}\psi = E\psi$$

Here, $\hat{H}$ represents the Hamiltonian operator, E is the total energy of the system, and ψ represents the wavefunction of a given system. The Hamiltonian operator is defined as an operator that gives the energy of a system. In the context of a many-electron atomic system, the energy may be decomposed into a sum of individual contributions originating from both the kinetic and potential energy of all electrically charged entities in the system.

The bottleneck for solving the Schrödinger equation, is deriving the wavefunction. The exact, analytical solution is only possible to obtain for simple systems; mostly cases where there is only a single particle in a static potential, and similar. For practical applications in quantum chemistry, systems typically consider large numbers of electrons, which are all mutually interacting with each other. Under these conditions, the only practical approach are numerical methods, which rapidly grow in demand for computational resources with time. This is the many-body problem of quantum mechanics.

In order to achieve a practical degree of efficiency in solving the Schrödinger equation, a number of approximations are utilized. The Born-Oppenheimer approximation is one of the most widely utilized, nearly ubiquitous. In simple terms, this approximation assumes the nuclei are fixed charges, on which the wavefunction which describes only the electrons depends only parametrically. For most applications of quantum chemistry, it is this electronic wavefunction that is the central concern; the properties of the nuclei beyond treating them as point charges, is only required for specific applications.

3.3.3. DFT – Theoretical Background

DFT is a technique that has gained popularity in recent years, for its favorable tradeoff between the accuracy of the calculations against its computational demands. It is now one of the most dominant approaches for electronic structure calculations.

The basic idea behind DFT is that the energy of an electronic system may be written in terms of the electron probability density. This is formalized by the Hohenberg-Kohn theorems, which forms the foundation of DFT, and allows for the unambiguous description of the ground state energy for a given electron density.

The practical implementation of DFT is based on the Kohn-Sham approach. Under the Kohn-Sham formalism, the total ground state energy may be written as the sum of several contributions from a simplified reference system of non-interacting electrons, plus a correctional term to compensate the difference between the energy of the true and reference systems. This correction term is the exchange-correlation functional.

The main challenge of DFT is thus to determine the exchange-correlation functional $E_{XC}[\rho]$. A wide range of approaches have been employed to approximate the exchange-correlation energy, with varying degrees of complexity and computational demand. They are, however, to varying degrees, ad hoc corrections to the energy. The main sources of error within the DFT formalism stem from the approximate nature of these exchange-correlation functionals.

3.3.3.1. DFT – Functionals

The many approximations of the exchange-correlation contribution are broadly categorized by complexity: The simplest category of approximations are the local density approximation (LDA) functionals, which only take into consideration the electron density at any given point. More elaborate functionals also consider the density gradient, an approach which is known as the generalized-gradient approximation (GGA) functionals. Further steps include the introduction of energy terms dependent on higher derivatives, as well as kinetic energy density terms, which is known as meta-GGA (mGGA) functionals. The higher the complexity of the approximation, the closer to the true exchange-correlation energy one may theoretically (elaborated shortly in section 3.3.4) approach, and the more computationally demanding the calculations. Apart from these, a popular approach to functionals that falls adjacent to others are the hybrid functionals, where the exact exchange energy is calculated from wave-function

calculations at the Hartree-Fock level and combined with a DFT functional as a linear combination.

3.3.3.2. DFT+U

A fundamental complication of DFT, is that as the exchange-correlation is approximated, and as such, highly correlated systems show substantial qualitative and quantitative errors. In general, this is a major concern for both partially filled *d*- and *f*-orbital electrons, but the former tends to be the most prevalent as it controls many properties of the transition metal elements. In particular, the inaccuracies result in substantial underestimates of properties such as the band gap, Mott-insulators in particular, to the point where many functionals predict metallic ground states for semiconductors. The magnitude of the energy contributions of magnetic interactions are also severely impacted, often resulting in overestimations of 100% or more compared with experimental values. LDA, GGA, and mGGA functionals all suffer from this problem. Hybrid functionals improve the accuracy, but these are so demanding the computational costs swiftly become prohibitive for systems with larger unit cells.

DFT+U is an *ad hoc* correction scheme that was introduced to improve the representation of strongly correlated orbitals, without resorting to more demanding functionals. This approach was originally proposed by Anisimov et al.[161] and further developed by Dudarev et al.[162] It employs a Hubbard-like model to add an extra repulsive term, referred to as the U_{eff} term, to the relevant orbitals, increasing their energy to compensate for the errors of the basic DFT approach.

There are many approaches to choosing the correct U_{eff} term for a given system. A more common approach is to set the value empirically, to match a given property from experimental data. This approach obviously fails if no such experimental data is available. Another approach is to look up values used previously in literature, especially if one wishes to compare values.

3.3.4. The Limitations of DFT

DFT is today a widely used approach for theoretical modelling of atomic systems, for its favorable tradeoff between low complexity of calculations against decently accurate results, sufficient to be useful in most cases. Ultimately, however, there is a tradeoff, and the approach

does have its limitations. The fundamental origin of these is the inherently approximate nature of the approach.

One of the most fundamental issues of DFT relates to the exchange-correlation functional: Being an inherent *ad-hoc* correction scheme, there is no systematic approach to improving the results. While there is generally the impression that accuracy of DFT calculations improves with the complexity of the functional, this is not strictly true. At most, a higher level functional improves the likelihood that a result is more accurate. Validation of the accuracy of a given functional is empirical, based on simply testing it with a range of different systems, and comparing the results with experimental values.

While the specifics may vary greatly from system to system, certain shortcomings are so pervasive of DFT they are practically expected to be the case. Spurious electron self-interactions and over-delocalization of electrons is a consistent difficulty. As mentioned previously, underestimation of the band gaps of insulators and semiconductors and the energy contributions of magnetic interactions being greatly overestimated are a constant concern.

There is also a human factor involved on several levels. Some parts of the approach are easily misinterpreted by a user considering DFT as a black-box methodology. One such aspect is the fact that the absolute energies by themselves are meaningless; only relative energies have any significance, in contrast to wavefunction-based approaches. Another factor a human user must consider, is the fact that the final state a DFT calculation converges to is dependent on the start conditions. If these are not suitably set, the system may converge to a local minimum. Even if the start conditions are sensible, local minima typically becomes an increasing concern with greater complexity of the system under consideration.

3.3.5. Practical Implementation of DFT

Throughout this project, DFT calculations were carried out with the Vienna *ab initio* simulation package (VASP).[163,164]

The common functional for the exchange-correlation energy utilized throughout this work was the generalized gradient approximation (GGA) as formulated by Perdew-Burk-Ernzerhof (PBE).[165] Other functionals were utilized less broadly, including the strongly constrained and appropriately normed (SCAN) mGGA functional,[166] and the hybrid functionals PBE0[167] and HSE06.[168] The calculations utilized projected augmented-wave (PAW) pseudopotentials,[169]

with plane-wave energy cutoffs chosen according to the system. A self-consistent-field cutoff energy convergence criterion of 10^{-6} eV was chosen for all final calculations. The ionic relaxation convergence criterion was all forces being less than 0.01 eV Å^{-1}. To account for the strongly correlated $3d$ orbitals with the PBE functional, the DFT+U approach under the rotationally invariant Dudarev approach was employed. The U_{eff} values were either chosen based on values from previous studies, or calculations were carried out with a range of U_{eff} values to observe how this affected the properties of the compounds in question.

The sampling of the Brillouin zone utilized gamma-centered grids, with the integration being carried out with either Gaussian smearing, or the tetrahedron method with Blöchl corrections, depending on the system and target of the calculation.

3.3.5.1. Considerations for Ionic Disorder in Crystal Structures

For many of the crystal structures considered in this work, there is major structural disorder in the ionic positions and occupancies. Treating such crystal structures with DFT requires special considerations, as simply carrying out the calculations on the disordered cell directly does not work, and the exact process depends on the nature of the disorder. There were two different types of disorder among the compounds considered in this work: Intrinsic disorder, where the occupancy is assumed random, and apparent disorder, where there is local order in the structure, but which cannot be fully represented by a simple unit cell.

For intrinsically disordered compounds, there is no method to achieve a perfect representation of the target compound for calculations, as this would necessitate an infinitely large calculation cell. As such, the calculations instead utilize the most favorable configuration with the correct composition achievable in a reasonable period of time with the computational resources available. In this work, the relevant phase (discussed in section 4.2) exhibited a 0.5 occupancy on two mutually exclusive positions. To avoid a higher occupancy parallel with any one axis, a supercell structure equivalent with 8 unit cells in a 2x2x2 lattice was utilized. Within this supercell, every reasonably distributed (i.e. assuming that for each half-occupied position, one of the two is always occupied), symmetrically inequivalent arrangement of the partial occupied positions were arranged to test the relative energetic favorability. However, rather than the computationally demanding 2x2x2 supercell, minimal representations (i.e. the smallest cell which represents the same full crystal structure) of these same structures were employed instead to speed up the calculations. The arrangement of partial occupancies that was found to be the

most favorable was used for the final calculations, but the other arrangements were also considered as an indicator on how the properties of the compound varies with the occupancy (do note that the use of minimal representation in this instance is not ideal; comparing total energy between different unit cells introduces error, the use of minimal representations was necessitated by the size of the full supercells being too large to use).

In the case of apparent disorder (the relevant phase is discussed in section 4.1), one of the major goals of the calculations was to determine the most favorable local structure. In this case, as opposed to the intrinsically disordered structure, there is a specific range of structural arrangements that must be achieved. From the experimental crystal structure, we had determined the likely structural elements of the disordered regions. With this as the initial starting point, supercells were chosen such that the disorder could be unfolded into a complete structure, corresponding with a full occupancy of sites, and the correct composition. The most favorable structure was determined by systematic comparison of the possible configurations. Similar to the intrinsically disordered structure, some configurations required supercells too large to reasonably use, but the corresponding crystal structure was already a minimal representation. In these instances, energetic comparison between a series of truncated structures were employed instead. Supercells which did not correspond to a full structure, but as close as achievable to fully represent one set of structural features under consideration at a time. Errors pertaining to the use of different unit cells were minimized by calculating the energy of identical structures with the different unit cells, and using the energy of these as qualitative reference points.

In addition to the above considerations, the supercells employed in the calculations were also required to allow the correct magnetic structure to be represented. Otherwise, an appropriate (magnetic) supercell of the structural supercells would be utilized.

4. Process, Results and Discussion

Due to the fundamental nature of this work in discovering and characterizing novel compounds with *a priori* unpredictable physical properties, the structuring of this chapter will be split into two sections. Each compound (or series of analogs, as relevant) will first be considered individually, to discuss the relevant points primarily pertaining to this compound or series, as well as directly relevant tangents into broader field. These compounds are then used as the basis for broader analysis of the fields of bichalcogenides and multianions at large, which is included towards the end of this chapter in section 4.6.

4.1. $La_{18}Fe_5Cu_4S_{26}O_8$ – Magnetic Cluster Glass

4.1.1. $La_{18}Fe_5Cu_4S_{26}O_8$ – Synthesis and Structural Determination

$La_{18}Fe_5Cu_4S_{26}O_8$, henceforth referred to as LFCSO, was discovered while attempting to incorporate a mixed cation composition into a previously known oxysulfide, although that compound has yet to be published.[170] Initial attempts at obtaining a single crystal for structural determination failed, but after a few syntheses, an adequate nominal composition for single crystal formation was reached. The major structural elements, namely the lattice parameters, crystal group and bulk of the atomic order were resolved quickly. It was, however, found that the compound exhibited a guest-in-host structure. To specify what is meant by a *guest-in-host structure*, such a crystal structure can exhibit two key components: First, a *host*-component, which comprises the bulk of the structure, and is fully described by the nominal space group of the structure as a whole. The second component is a distinct *guest* structure, with a different (In the case of LFCSO, lower) local symmetry than the *host*. The guest structure of LFCSO presented a substantial number of cationic positions which could potentially be either Fe or Cu, overlapping too closely to resolve accurately (Paper II, Figures 5 and 6). As a consequence, determining the full stoichiometry of the phase directly from the SC-XRD data was not viable. By identifying the La, S and O compositions, the SC-XRD data did serve to greatly narrow down the possible compositions for the compound. Together with the synthesis temperature thermodynamically constraining the Cu ions to the monovalent state, and the neutrality condition necessitating a divalent state of Fe, the possibility space for correct composition has further constraints when trying to find the correct ratio of Fe and Cu (henceforth referred to as the Fe:Cu ratio or composition). This Fe:Cu ratio had to be manually determined. Further, as

45

the guest structures exhibited a lower symmetry than the host, the correct space group was in question.

To resolve the Fe:Cu composition, an iterative process was employed: A synthesis was carried out with a trial composition. The resulting PXRD was investigated to determine what impurity phases were present, and thus what elements were in excess, and compared with previous syntheses. Finally, a SEM/EDX analysis was carried out, to determine again what impurities were present, but also to measure the elemental composition of LFCSO, and observe the crystals for hints on any process that could be complicating the acquisition of a pure phase. With all data points gathered and considered, a revised guess on the LFCSO composition was synthesized. The revised guess was typically based on what may be referred to as "subtraction chemistry"; if phases of a particular element were prominent in the secondary phases, then that is the component in excess of the stoichiometric composition. The revised synthesis decreased the amount of that element and balanced the other unknown element accordingly to satisfy the neutrality condition. This continued until a reasonably pure phase was attained.

A couple of oddities were noted during the SEM/EDX analyses. The SEM analysis showed that the LFCSO crystals appeared to lack habitus, appearing with rounded surfaces and corners (Paper II, Figure 9). Further, crystals with habitus of secondary phases (prismatic crystals) appeared to either grow inside the LFCSO crystals, or LFCSO formed around other crystals. This trait of crystal intergrowth was found to be decreasingly prominent as the composition approached the correct stoichiometry. The results of the EDX analyses were found to vary oddly, always suggesting that the correct Fe:Cu ratio was only slightly off from the nominal composition of the relevant synthesis. The possibility that the LFCSO composition might have a significant degree of variability was considered, but no real evidence to this end was found in the end. EDS also has a rather large margin of error, which is problematic when attempting to determine the ratio of two lesser components. After experiments had concluded, it was discovered that a second unknown phase, $La_{14}Fe_6CuS_{24}O_4$ (discussed in section 4.2), also existed in the same phase diagram, which could be part of the reason for why it was difficult to achieve a single-phase sample.

Changing other variables, such as altering the synthesis temperature, was also attempted, but increasing the synthesis temperature to 1100 °C resulted in severely decreased crystallinity of the product.

Eventually, the best composition for synthesizing LFCSO was found to be $La_{18}Fe_{4.8}Cu_{4.4}S_{26}O_8$. Increasing the Fe:Cu ratio beyond this resulted in Fe-based impurities, and Cu-based impurities were present at a lower ratio, so this was deemed optimal. The product was still not perfect, there remained traces of $La_{10}S_{14+x}O_{1-x}$,[62] which formed in every synthesis, and possibly La_2O_2S,[61] but these are the least problematic impurities for material characterization (Paper II, Figure 8). The nominal stoichiometric composition was chosen as it was deemed sufficiently close that it was quite likely the real composition, with the need for a non-stoichiometric synthesis composition being attributed to a quirk of the synthesis.

With the composition of LFCSO established, it was now possible to determine a crystal structure that agreed with the nominal composition. The resulting structure retained the *Cmcm* structure of the host material but left a large uncertainty in the details of how the true crystal structure was arranged. The partial occupation could be matched to a range of physical structures, but which possibility was correct could not be determined. The final structure was attained as a compromise between a sensible structural motif, decent refinement parameters and correct composition.

To make up for the lack of data in the SC-XRD and determine the crystal structure, the investigation of the compound was expanded to include a DFT investigation. The first step of the DFT investigation was an extensive search of the possibility space of the potential crystal structures. Comparing and cross-referencing the relative energy of these potential structures resulted in the establishment of three postulates on the structure of the disordered region, which unambiguously defined the guest structure (Paper II, Figure 7). Further, the most favorable relative arrangement of the adjacent guest regions was also determined.

A simple investigation on whether the Fe and Cu positions were correctly assigned was also carried out, calculating the structure with Fe and Cu positions swapped. This was found not only to be highly energetically unfavorable, but also resulted in unreasonable oxidation- and spin states for the swapped cations. Certain positions were also unstable, and the ions would shift to positions not observed to be occupied in the experimental crystal structure. As such, the DFT calculations indicate that the nominally assigned occupations of the elements are indeed the more likely to be correct.

4.1.2. La$_{18}$Fe$_5$Cu$_4$S$_{26}$O$_8$ – Property Determination

Initial magnetic DC susceptibility measurements established LFCSO to be either a magnetic cluster glass (or equivalently for conductors, a mictomagnet), a superparamagnet, or a spin-glass compound, based on the difference between the FC and ZFC measurements (Paper II, Figure 11). The latter option was ruled out, on the basis that the magnetic susceptibility of the compound did not appear to exhibit significant ageing effects with respect to magnetic relaxation upon the removal of the external magnetic field. Magnetic AC susceptibility measurements (Paper II, Figure 12) were used to determine that the size of the magnetic domains greatly exceeded the expected value of a superparamagnet, establishing LFCSO as a magnetic cluster glass by process of elimination.

In addition to determining the crystal structure, DFT was also employed to determine the magnetic interactions of LFCSO. This was approached in much the same way as the structural determination, due to the complexity of the system: through an exhaustive search of the possibility space, finding the lowest energy configuration, and cross referencing what features were favorable or not. Certain parts of the magnetic arrangement could be predicted according to the Kanamori-Goodenough rules, but the presence of distinct magnetic structures weakly and mutually interacting, made anything other than an exhaustive search at risk of errors.

The final question with LFCSO was the origin of the magnetic cluster glass properties. Structural defects and disorder are both viable explanations for the formation of magnetic domains in LFCSO; the DFT analysis suggests the band gap should be much wider than what is seen for the electrical conductivity. Magnetic cluster glasses are attributed to a combination of magnetic frustration and disorder, as well as competing FM and AFM interactions. There was a decent case to be made that the formation of the magnetic cluster glass is closely tied to the magnetic arrangement in the Fe-layer structure, based on the observation that the magnitude of the paramagnetic signal only corresponds to the Fe-layer iron content, along with the DFT results. For a plane of weakly interacting magnetic ions (which could be expected to act similar to a dilute magnetic system), however, one could expect a simple spin-glass (if it orders at all), which would relax to the lower energy state upon the removal of the external magnetic field. This is not the case with LFCSO. The partially ordered magnetic state was attributed to strongly coupled magnetic chains, which remain significantly coupled up to room temperature, but also exhibiting considerable spin dynamics, pinning the weakly interacting Fe-layer. Only the Fe-layer was expected to assume a fully paramagnetic state above ~10 K, while assuming a frozen spin-state below the transition.

To obtain further structural and magnetic information, the sample was sent for Mössbauer spectroscopy. With respect to the structure, the results were possible to model with three Fe-positions in a 1:2:2 ratio, but the respective signals were very broad, suggesting disorder between the positions (Paper II, Figure 10). The results suggested that there was no long-range ordering at any temperature, while the low-temperature effects could be attributed to a freezing of the spin dynamics.

4.1.3. La$_{18}$Fe$_5$Cu$_4$S$_{26}$O$_8$ – Discussion of the Crystal Structure

The crystal structure of LFCSO is novel, crystallizing in the *Cmcm* (No. 63) space group. The full structure is highly complex, and described in detail in the relevant article, so only particular features will be discussed here. The full crystal structure is illustrated in Figure 13.
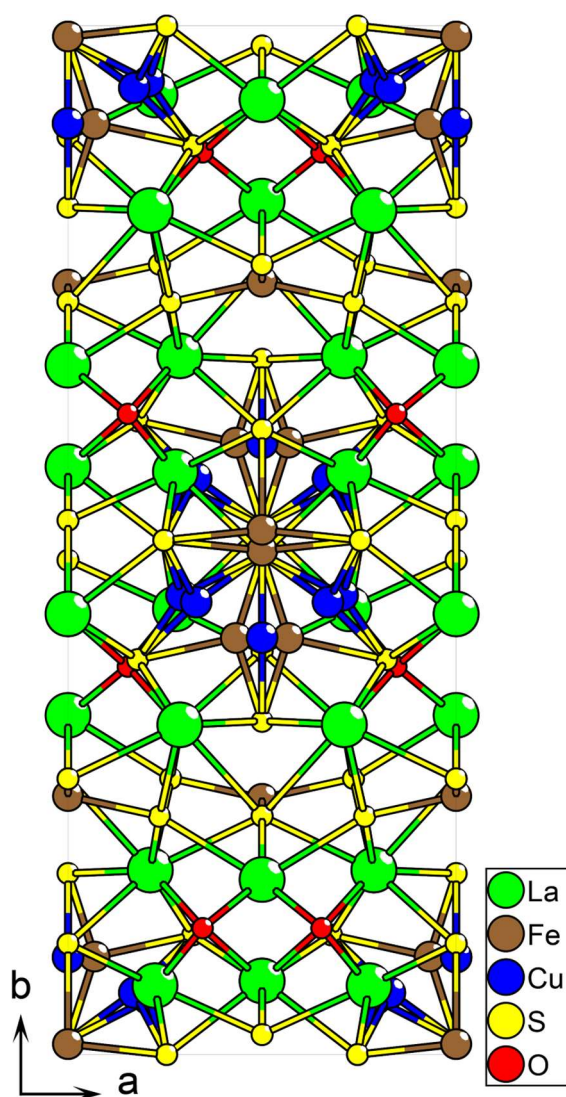
Figure 13: The complete crystal structure of LFCSO.

There are three defining elements of the LFCSO structure: larger spacer units of the form $[La_9O_4]$, a 2D planar layer of Fe positions henceforth referred to as the Fe-layer, and 1D chains exhibiting disordered occupation of Fe and Cu positions, henceforth referred to as the Fe/Cu chains Refer to Paper II, Figure 3 for a schematical representation of how these elements are arranged within the crystal structure.

The main spacer unit of LFCSO, $[La_9O_4]$ (Paper II, Figure 2), is a typical example of HSAB behavior in multianion compounds. All the oxide ions in the structure are caught up in these structures and coordinate solely with La^{3+}. The $[La_9O_4]$ units are technically an example of 0D arrangement of anions, as each unit is surrounded on all sides by sulfide coordinations. Unlike the general rule established in the previous section on dimensionality, LFCSO breaks with the general trend, exhibiting features of both 1D and 2D substructures, despite the 0D anion ordering.

The $[La_9O_4]$ units exhibit a rectangular prism structure with two nearly equal side lengths, along with one shorter edge, resulting in the units being stacked in 2D layers, allowing a pseudo-2D arrangement for the anion ordering.

The $[La_9O_4]$ unit observed in LFCSO is, to the extent of the authors' knowledge, unique among currently known rare-earth oxychalcogenides. The internal structure of the $[La_9O_4]$ unit itself is not unusual: It is a simple extension of the $[La_4O]$-unit observed in oxygen-scarce compounds such as La_4MnS_6O, and an intermediate before the infinite $[LaO]$ planes observed in many layered lanthanum bianion compounds, such as $La_2O_2S_2$,[171] LaAgOS and its family of structural analogs,[172,173] and $LaOInS_2$.[174] If a compound has a composition with a 1:1 La:O ratio, and no equally or harder cations than La^{3+}, the $[LaO]$ plane structure will typically form.

With the possibility of expanding from the 2x2 $[La_4O]$ unit to the 3x3 $[La_9O_4]$ unit established, the question becomes; can this structural element extend further? Continuing the square expansion, the next unit in the sequence becomes $[La_{16}O_9]$ (Figure 14), continuing with a general formula for the *n*-th unit of the sequence as $\left[La_{(n+1)^2}O_{n^2}\right]$. Further such square arrangements are not known, but non-square arrangements have been reported previously. A couple of examples are the arrangement observed in $La_5Cu_6O_4S_7$[175] and $La_3CuO_2S_3$,[75] with a 5-La wide arrangement along one axis, and an infinite chain along the other (∞x5), the ∞x4 arrangement observed in $La_4O_3(AsS_3)_2$,[176] and the ∞x3 structure in $La_5In_3O_3S_9$.[177] A distorted arrangement is observed in La_3GaOS_5,[178] where every lanthanum in the 1D chains exhibits a 3+5 coordination. These planar $[La_xO_y]$ units exhibit a similar layer stacking arrangement as

the [La$_9$O$_4$] units of LFCSO, and the same characteristic where the LaO-elements are connected either sulfide connections, or by transition metal – sulfide coordinations. As such, it is possible that the LaO-elements can adjust to a wide range of potential structures, depending on the composition.
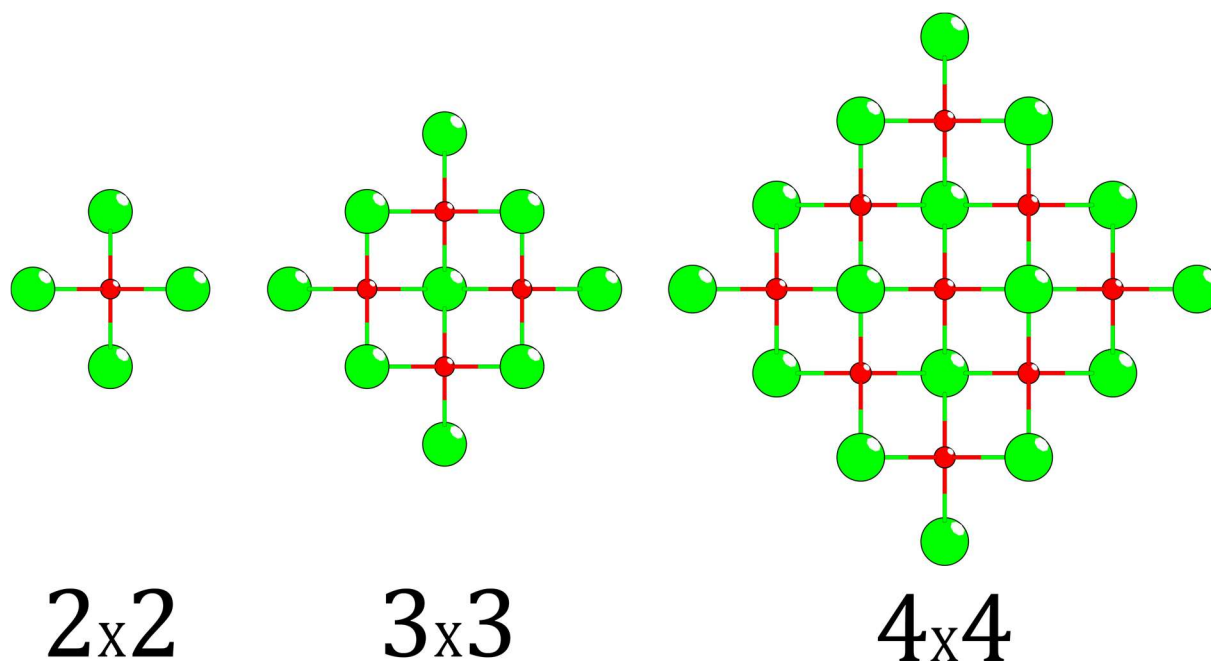
Figure 14: An illustration of the potential expansion of the $\left[La_{(n+1)^2}O_{n^2}\right]$ sequence as structural elements of lanthanum oxychalcogenides.

The [La$_9$O$_4$] unit happens to occupy an interesting middle ground with respect to coordination. The infinite [LaO] planes usually exhibit La in a 4+4 *fac*-square antiprismatic coordination (the 4+5 *fac*-capped square antiprismatic coordination is also possible), while on the opposite side, the unary [La$_4$O] unit exhibits exclusively the 1+7(8) coordination. [La$_9$O$_4$] exhibits three different coordinations (Paper II, Figure 4): The 4+4 *fac*-square antiprismatic coordination, an intermediate 2+6 *fac/cis*-square antiprismatic coordination, and the 1+7 coordination in a 1:4:4 ratio. While LFCSO does not make a good candidate for optical doping with other lanthanides due to the small band gap and low resistivity, the [La$_x$O$_y$] units may provide essentially a test bed for the effects of heteroleptic coordination on the properties of optically active species, if incorporated with cations that result in greater band gaps. While the currently known variations of the [La$_x$O$_y$] units are limited, they could potentially also serve as a system for tailoring particular lanthanide coordinations for specific properties. As an example, a straight 1D chain of edge sharing [La$_4$O] units (with a total composition [La$_2$O]) could potentially exhibit only a

single heteroleptic coordination (either 2+6 or 2+7) for all lanthanum positions, should this specific arrangement be useful.

The Fe-layer exhibits Fe^{2+}, coordinated in a homoleptic, distorted square planar coordination of S. This is a very unusual arrangement for Fe^{2+}, but it is also the only cation that could potentially be present in this position. The only alternative would be a copper position, which would imply a Cu^{2+} oxidation state. Considering the synthesis temperature, this state of copper would be thermodynamically unfavorable. Fe^{2+} is not known for assuming square planar arrangements, and even similar arrangements are scarce. One compound with slight similarities is the chemically similar $La_2Fe_2S_2O_3$,[179] which exhibits a 2+4 octahedrally coordinated Fe^{2+} with a sulfide belt and *trans*-oxygen coordination. It is technically also possible to consider the coordination a severely distorted tetrahedral coordination. Fe^{2+} tetrahedra are the more common coordination, but the 156.1° and 159.0° S-Fe-S angles observed in LFCSO are closer to the planar 180° than the tetrahedral 109.5°.

The cation positions situated within the Fe layer are rather far apart. As a consequence, the intralayer magnetic coupling is very weak resulting in a persistent paramagnetic-like behavior at low temperatures. This is not an unusual feature; it occurs in many compounds where the proportion of Fe (or any other magnetic ion) is comparatively low, relative to the spacer ions or other nonmagnetic species.

The guest-in-host motif is a defining structural element of LFCSO, but it is also a rare occurrence in inorganic compounds. Host-guest is usually a term pertaining to organic chemistry or composite materials. There are compounds that could be considered, at a stretch, to exhibit a similar character. One such example would be $Ba_{16}Fe_4S_{16.72}$.[180] The compound exhibits a localized section of disordered sulfide positions, along a 1D distribution through the structure, suggesting the local symmetry in this particular region is lower than the rest of the structure.

4.1.4. $La_{18}Fe_5Cu_4S_{26}O_8$ – Outlook and Potential Structural Analogs

There are further experimental measurements that could be performed to improve our understanding of the LFCSO phase; neutron diffraction in particular would be useful as a further confirmation of the cationic occupancies, and a second look at the magnetic arrangement.

In consideration of the possibility of analogs, the structure of LFCSO is highly complex, and likely requires pairs of transition metal cations with very specific preferences for coordination to form. Structural analogs with extensively or completely substituted elements are difficult to predict, if they are likely to exist at all. Partial substitution analogs may exist, however. The first candidates are the trivalent lanthanide substitutions, which are possible analogs of many other lanthanide compounds. Considering the complexity of the magnetic structure of the lanthanum variant, the effects of introducing f-magnetic lanthanides would be difficult to predict. A second approach is substituting S with Se, which is a common approach to analogs. The Cu^+ (91 pm) positions may be substituted with Li^+ (90 pm) as the ions have very similar ionic radii.[59] Replacing Cu^+ with the isoelectronic Zn^{2+} (88 pm) is also a possibility, but fulfilling the neutrality condition would necessitate partial substitution or valence states in another element.[59] A replacement for Fe^{2+} is probably the least likely, due to the unusual square-planar arrangement in this structure. One possibility is Cr^{2+}, as indicated by the chemically similar compound described in section 4.2 having Fe and Cr analogs. Mn^{2+} is also a common substitute for Fe^{2+}, but whether manganese will assume the unusual configurations of LFCSO is uncertain; Mn^{2+} substitution is more likely to succeed with spherically symmetric coordinations. This substitution was tested (along with all compositions of the form LaTMECuSO) with a negative result, but manganese bichalcogenides have a tendency of being difficult to synthesize, and often failing to form. From experience in this project, many manganese bichalcogenide phases only form either at higher temperatures than the decomposition point of either certain precursors or product, or in impure phases with other crystallite species. A cause is likely the stability of MnS inhibiting reaction at temperatures low enough to avoid decomposition and loss of products.

4.2. La$_{14}TME_6$CuS$_{24}$O$_4$ (TME = Cr, Fe) – Multivalent Spin-Chains

4.2.1. La$_{14}TME_6$CuS$_{24}$O$_4$ – Synthesis and Structure Determination

The La$_{14}TME_6$CuS$_{24}$O$_4$ (TME = Cr, Fe) (henceforth referred to as LTCSO, the chromium analog specifically is referred to as LCCSO, while the iron analog is referred to as LICSO to differentiate from the other phase with identical elements) structure type was discovered during a cursory search of the first-row transition metals for phases in the La$_x TME_y$Cu$_z$S$_w$O$_u$ space, following the discovery of LFCSO. The composition and structure of the chromium variant was determined first by SC-XRD, but its discovery revealed that a previously observed specimen which was believed to be a phase in the La-Fe-S-O system was in fact an analog of this phase.

The synthesis of LCCSO proceeded without significant complications. As one atomic position in the crustal structure exhibits disorder, there was some uncertainty in whether it was oxygen or sulfur, but this was resolved with a few synthesis tests of alternate starting compositions.

The synthesis of LICSO proved more challenging. While the phase forms from a direct solid-state synthesis, it was found to be metastable at the regular synthesis temperature of 900-1000 °C, decomposing by what is suspected to be sublimation of a copper sulfide, which was deposited on the crucible and ampoule away from the reaction mixture, preventing reformation of LICSO. The LICSO phase forms faster than the decomposition takes place, so attaining a reasonably pure phase is still possible.

Both phases were a crystalline, black solid. The chromium variant sintered notably badly, with the resulting product being a porous, crumbly pellet, which complicated measurements.

4.2.2. La$_{14}$*TME*$_6$CuS$_{24}$O$_4$ – Property Determination

Initial measurements of the DC magnetization properties of LCCSO showed that the compound exhibits elevated magnetization at low temperatures, with a transition temperature of 88.5-79 K, depending on the applied field (Paper III, Figure 8). The transition was marked in the DC susceptibility by a broad transition. Notably, the compound did not exhibit regular paramagnetic behavior up to room temperature, rather assuming a state with a nearly temperature independent susceptibility for most of the temperature range between the magnetic transition and room temperature.

To further analyze these properties, the AC susceptibility was measured with varying frequencies to probe for dynamic effects (Paper III, Figure 9). There were three features of particular note: A broad peak in the temperature range where the DC susceptibility transition took place, a discontinuous shift at the transition temperature, and a temperature independent region between the transition- and room temperatures.

Heat capacity measurements of LCCSO showed that the compound underwent no first-order transition in the 2-300 K temperature range (Paper III, Figure 11), which significantly limits the possibilities for the nature of the sharp transition observed in the AC measurements. Considered along with the nearly temperature-independent susceptibility in the high-temperature regime, a metal-insulator transition was suggested to explain the observed transition.

To investigate whether such a transition was present, a simple two-point conductivity measurement was set up, to investigate whether both metallic and semiconductor states could be observed, but the results showed that LCCSO exhibited resistive properties characteristic of a semiconductor with variable-range hopping throughout the 10-300 K temperature range (Paper III, Figure 12).

Initial measurements showed that LICSO exhibited different behavior from LCCSO. While the ZFC behavior was broadly in agreement, the FC measurements rather placed LICSO as exhibiting properties typical of spin-domain formation, although subsequent AC measurements indicated that the size of these domains would approach complete ordering.

The magnetic structure, as well as the atomic disorder of LTCSO, was investigated by DFT. A mismatch between theory and experimental results occurred when it was found that DFT consistently predicted the ground states of both LCCSO and LICSO to be a fully antiferromagnetic arrangement, for any tested ordered arrangement of Cu occupancy or sulfur disorder (Paper III, Figure 13). It was initially thought that an appropriate Cu ordering or magnetic arrangement simply had not been found yet. Further, there were difficulties with converging the systems to the correct minimum states, as the correlation between magnetic ordering and oxidation states made local minima trapping the convergence of the calculations an unusually prevalent issue. Ultimately, the magnetic ground states of the LTCSO phases could not be established with certainty. A hypothesis, assigning the observed properties to formation of spin domains due to intrinsic Cu disorder, was presented as a potential explanation, but further measurements of the magnetic ground state are necessary to ascertain the correct magnetic ground state.

4.2.3. La$_{14}$*TME*$_6$CuS$_{24}$O$_4$ – Discussion of the Crystal Structure

The crystal structure is novel, exhibiting the space group *C*2/*m*. The full crystal structure is shown in Figure 15. There are three features of note in the structure: lanthanum oxide chains, transition metal chains, and a disordered part with two sites of equal partial occupancy. The lanthanum oxide chains exhibit an example of a 1D anion superstructure, arranged with [La$_4$O] units altering between edge- and vertex-sharing of lanthanum positions. Referring back to the remarks on La-O structure in LFCSO, this is not an ideal [La$_2$O] 1D chain, which could exhibit only a single heteroleptic coordination for all lanthanum positions, but an adjacent [La$_5$O$_2$]. It

is constructed from dimers of La edge-sharing [La_6O_2] units, which are again interconnected by a vertex-sharing arrangements, illustrated in Figure 16.
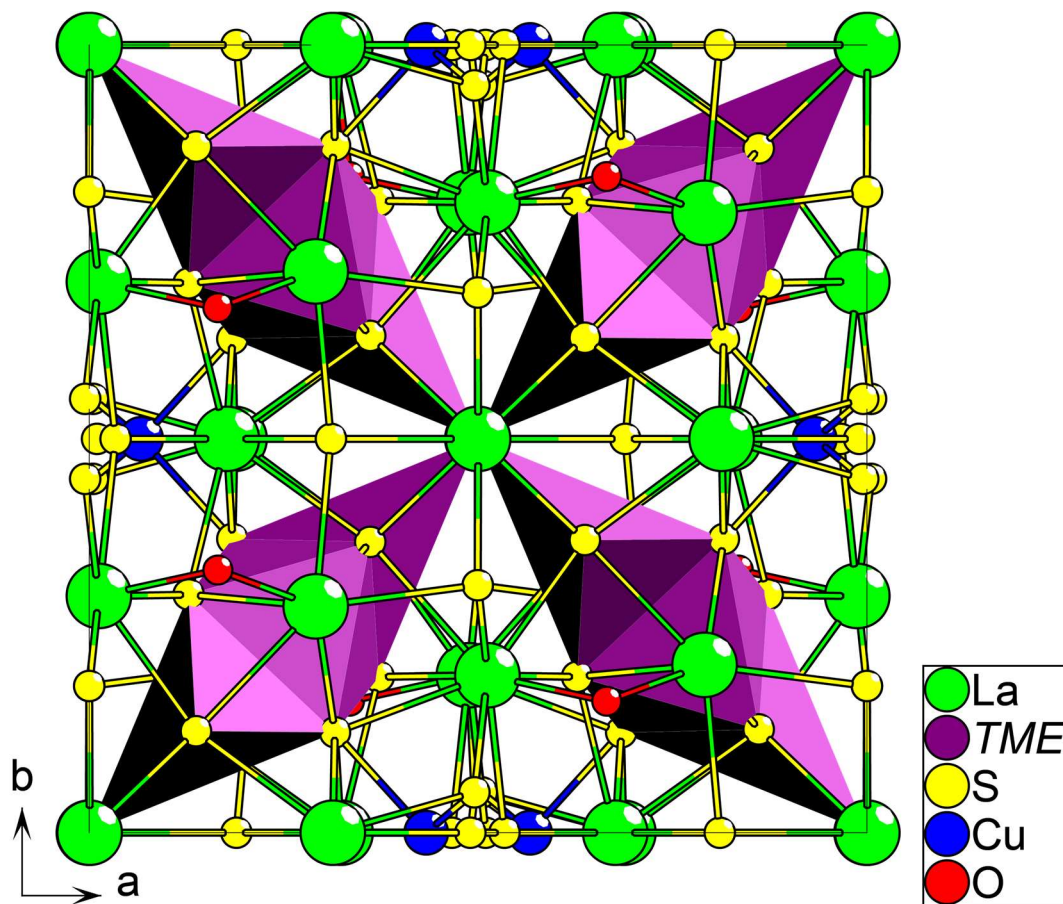
Figure 15: The full crystal structure of the LTCSO compounds.
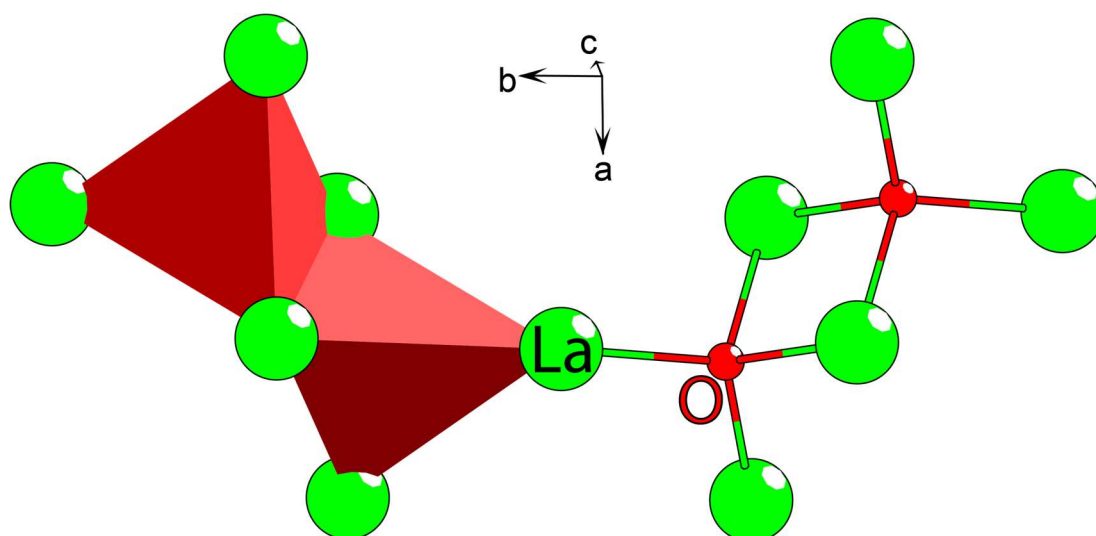
Figure 16: The lanthanum-oxygen coordination in the LTCSO crystal structure.

The chain exhibits doublets of the 2+7 *ac-fac/trans*-coordination from the [La$_2$O] arrangement, a *c-fac/trans* 2+7 coordination for the vertex-sharing lanthanum positions, and a 1+7 coordination on the outliers (See also Paper III, Figure 3). In addition to the oxide chain, there is one lanthanum position homoleptically coordinated by sulfide with a capped square antiprism coordination.

The *TME* lattice sites are arranged into triplets of face-sharing coordinations, which are further arranged into 1D chains (Figure 17). The chains are then further coupled to form a magnetic ladder. The triplets are arranged with symmetric coordination, in the sequence trigonal bipyramidal – octahedral – trigonal bipyramidal. These triplets are not a wholly unique arrangement, similar arrangements are observed in other compounds containing divalent Cr, although a full structural match has not been found. An example of a similar arrangement is observed in Li$_5$Cr$_3$(PO$_4$)$_4$,[181] where the trigonal bipyramidal arrangements are replaced with square pyramidal, and the three coordinations are interconnected by edge- rather than face-sharing arrangements. Cr$_3$Ti$_4$(PO$_4$)$_6$ exhibits the natural extension of this motif,[182] assuming the same coordinations of the three chromium positions as Li$_5$Cr$_3$(PO$_4$)$_4$, but with the polyhedra arranged in a vertex-sharing arrangements. Face-sharing arrangements consisting of octahedrally coordinated transition elements is not too unusual; for specifically trimers, the 9*R* hexagonal perovskites exhibit precisely such structure.
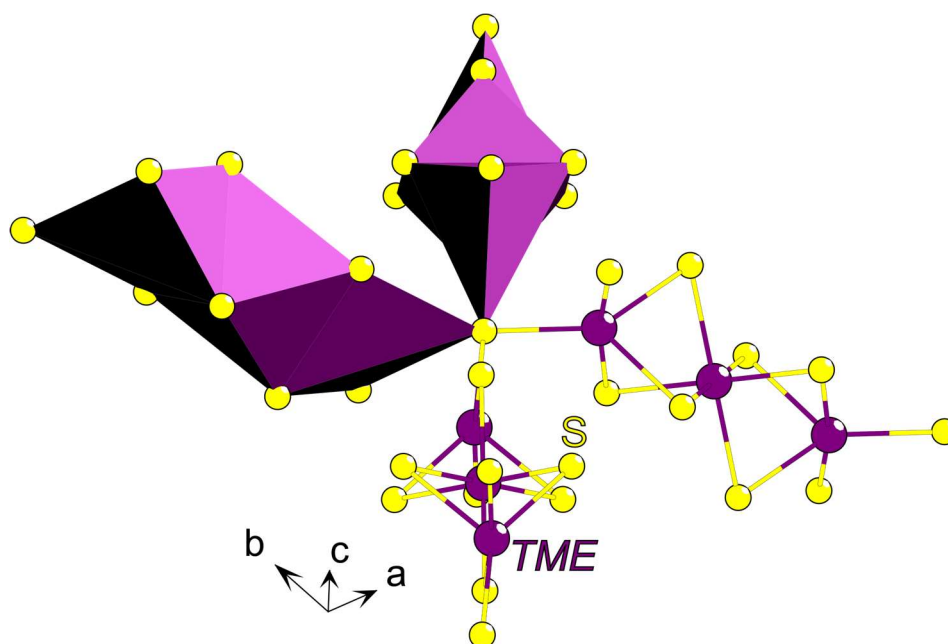
Figure 17: Illustration of the *TME* lattice with sulfide coordination within the LTCSO crystal structure.

Similar to LFCSO, LTCSO exhibits disorder in its crystal structure, although to a much lesser degree. Only two atomic sites are disordered: The copper position, with a 0.5 occupancy, and an adjacent sulfide position, which may assume several positions, depending on which adjacent Cu site is occupied.

As indicated by the stoichiometry, LTCSO has an unusual oxidation state that would nominally resolve as $TME^{2\frac{1}{6}+}$, however DFT analysis shows that the oxidation state is best described as $TME^{2+}{}_5TME^{3+}$, as the trivalent oxidation state is highly localized to the octahedral lattice sites.

4.2.4. La$_{14}$*TME*$_6$CuS$_{24}$O$_4$ – Outlook and Potential Structural Analogs

Beyond the characterization methods employed on these compounds, additional measurements which would be of value, would be neutron diffraction for both analogs, and Mössbauer for the Fe-analog specifically. Either method could provide valuable data on the magnetic structure of the compounds, and potentially resolve the ambiguity pertaining to the magnetic ground states of these compounds.

If one was to search for further analogs of the LTCSO structure types, the trivalent rare-earth elements, as well as the oxyselenide analogs are the most likely candidates. The Cu$^+$ position could potentially be substituted by equivalently charged Li$^+$, or the isoelectronic Zn^{2+}, both which have slightly smaller ionic radii than Cu$^+$. The latter substitution may require co-doping with another species to balance the charges, but it is possible that the trivalent oxidation states of the magnetic chain could be reduced to form monovalent 2+ chains, of the form $RE^{3+}{}_{14}TME^{2+}{}_6Zn^{2+}S_{24}O_4$ (*RE* = Rare Earth Elements) (*TME* = Cr, Fe).

There are several approaches to substituting the magnetic elements. The first is a full substitution, with a formula of the form $RE_{14}M_6MS_{24}O_4$. With copper as the non-magnetic element, there are limited candidates, as the other metal species would necessarily have to be stable in both the 2+ and 3+ oxidation states and assume both trigonal bipyramidal and octahedral coordinations. Cobalt fulfills these conditions, although the trigonal bipyramidal arrangement is rare, making it a potential candidate. Vanadium and manganese may assume the necessary oxidation states, however the trigonal bipyramidal coordination occurs primarily with the trivalent oxidation state, which is not conducive to forming this structure. Trigonal bipyramidal Mn^{2+} does exist in complex chemistry, but the author knows of no inorganic

examples.[183] If zinc is used as the non-magnetic metal, only the divalent oxidation state is necessary for chain positions, but this is not of much importance with a single magnetic cation, as the trigonal bipyramidal coordination remains the bottleneck.

The second possibility is incorporating multiple elements into the spin chain, depending on the desired coordination. The general formula would be of the form $RE_{14}M^{2+}_4M^{2/3+}_2Cu^+S_{24}O_4$, $RE_{14}M^{2+}_4M^{2+}M^{3+}Cu^+S_{24}O_4$ or $RE_{14}M^{2+}_4M^{2+}_2Zn^{2+}S_{24}O_4$ corresponding to the four trigonal bipyramidal sites, and the two octahedral sites. The trigonal bipyramidal sites could be occupied by Fe, Cr or possibly Co, based on species known to assume this coordination. For the octahedral sites, all divalent first row transition elements may assume this coordination. The most likely candidates to successfully incorporate, according to ionic radii, would be Mn^{2+} (97 pm) and V^{2+} (93 pm).[59] Mn is a typical substitute for Fe^{2+}, while vanadium exhibits an intermediate ionic radius between Fe^{2+} (92 pm) and Cr^{2+} (94 pm). For the trivalent octahedral position, the most likely candidates are V^{3+} (78 pm) and Ga^{3+} 76 (pm).[59] Finally, it was noted in the DFT calculations that depending on the ordering of the Cu^+ positions, the octahedral positions may be warped such that two oppositely situated sulfide coordinations are significantly distanced from the cation position, forming a nearly square planar coordination site instead. This could potentially incorporate Ni^{2+}, Pt^{2+} or Cu^{2+} if the synthesis could be carried out at sufficiently low temperature, but this is a significant stretch.

If the octahedral sites are specifically substituted, this would likely have major effects on the magnetic properties of the compound. As the octahedral positions are situated at the center of the presumed ferrimagnetic triplets, the trimer coupling could be interrupted if the substituent is nonmagnetic, which could result in a qualitative change in the magnetic behavior.

Finally, as there are two known compounds in the La-Fe-Cu-S-O system with widely different crystal structures, it is fully possible that the system could potentially form further stable phases. However, due to the lack of obvious shared structural elements between the two phases, deriving a general stoichiometric formula for predicting other possible phases from the known two examples would be difficult.

4.3. $Ba_6Fe_2Te_3S_7$ – Dimeric Magnets and Polytelluride Oligomers

4.3.1. $Ba_6Fe_2Te_3S_7$ – Synthesis and Structure Determination

The synthesis of $Ba_6Fe_2Te_3S_7$ was comparatively straightforward. The compound was initially discovered by SC-XDR of a sample from an attempt at synthesizing a pure phase of a different composition, detailed in section 4.5.1.

Being a low-temperature phase of the Ba-Fe-Te-S phase diagram, the synthesis had to be carried out at a lower temperature of 700 °C. As such, the synthesis was comparatively slow, requiring two weeks of heating and three regrindings to obtain a pure phase. The crystal structure was determined by SC-XRD, and the lattice parameters were further refined by PXRD. The product was a highly crystalline, specular black solid.

4.3.2. $Ba_6Fe_2Te_3S_7$ – Property Determination

The unusual magnetic properties of the compound were first noted when measuring the DC susceptibility of the compound with temperature; it showed what initially appeared to be nearly temperature independent susceptibility (Paper I, Figure 7). As the oxidation state of the iron was ambiguous due to the unknown state of the polytelluride, there were two potential causes for the observed properties: The compound could either be in a low-spin Fe^{2+} state, or a strongly coupled Fe^{3+} state. To determine which, the sample was sent for Mössbauer spectroscopy. Consideration of the Mössbauer measurement (Paper I, Figure 6) concluded that the latter Fe^{3+} configuration was the correct description.

During a literature search for a mechanism to explain the observed susceptibility curves, it was found that the magnetic susceptibility of Fe-dimers behaves very differently from conventional inorganic magnetic materials. Unlike in structures with 3D magnetic coupling, where magnetic transitions are typically considered to be abrupt transitions, magnetic dimers do not exhibit a paramagnetic transition at any temperature. Rather, their behavior is described by each dimer assuming a magnetic singlet state (at absolute zero), with thermal filling of successively higher spin states until a state of effectively complete paramagnetism is attained at an arbitrarily high temperature. This behavior is described by the van Vleck equation (Paper I, Equation 1),[184] which may be adapted for any dimeric coupling of magnetic elements. While an obscure property, this equation is in fact used in similar cases of dimeric magnetic arrangements in inorganic materials. It is more commonly used in metalorganic chemistry, where magnetic

dimers are a more common occurrence, which made it difficult to track down from an inorganic perspective.

An attempt was made to measure the electric resistance of the compound. The specular black appearance of the material suggested the compound could be a metallic conductor. Contrary to these expectations, the compound was found to be highly insulating, with electric resistance beyond available measuring limits (>2 MΩ) at room temperature, preventing measurements.

To theoretically calculate the strength of the magnetic coupling, as well as to determine whether the telluride triplets observed in the structure were a polytelluride species or not, the investigation was expanded with a DFT analysis.

4.3.3. $Ba_6Fe_2Te_3S_7$ – Discussion of the Crystal Structure

The compound crystallizes in a novel structure, described by the *Cmc*2_1 space group. The full crystal structure is shown in Figure 18. There are two features of particular note in the compound: Linear, vertex-linked iron dimers with a formula $[Fe_2S_7]^{8-}$ (Paper I, Figure 3), and an oligomeric telluride species best described as $[Te_3]^{4-}$. Only the Ba ions are heteroleptically coordinated, with each of the four symmetrically distinct positions in the structure exhibiting a different coordination, and all Ba positions are 8-fold coordinated by anions (Paper I, Figure 2). Of the four Ba positions in the structure, two are coordinated with an even number of Te-positions, two and four each. These positions exhibit a more symmetric arrangement compared with the other two Ba positions, which are both coordinated with three Te-positions each.

The higher-symmetry 2+6 and 4+4 coordinations assume *fac/trans* and *mer*idional arrangements respectively, while the two 3+5 coordinations assume *fac-* and *belt-* coordinations. Each of these coordinations exhibits significant structural distortion from a regular 8-fold coordinations. These distortions arise due to two factors: the large size of the telluride ions, as well as the polytelluride formation. The former effect results in the sulfide positions being arranged comparatively distant from any telluride positions, and the latter effect arranges adjacent telluride positions significantly closer together than a regular 8-fold coordination would assume.
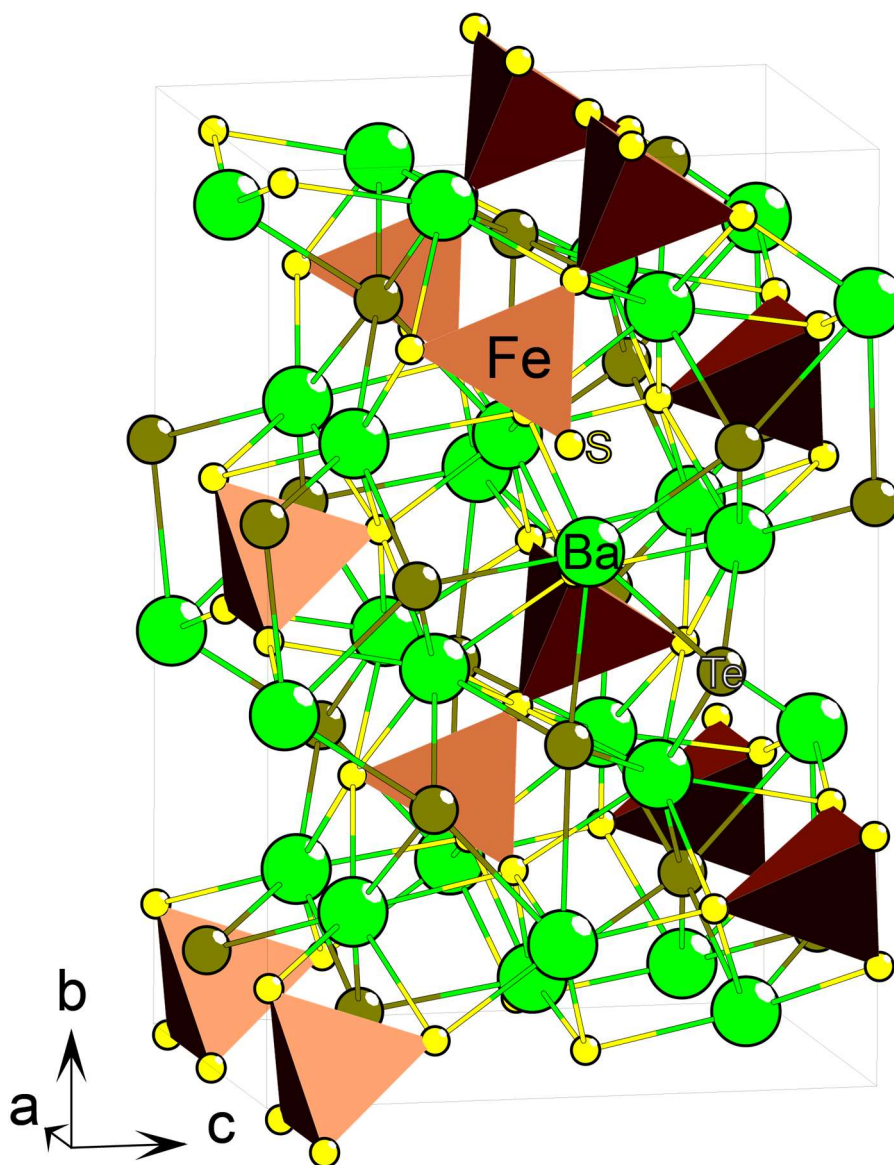
Figure 18: The unit cell content of $Ba_6Fe_2Te_3S_7$, with a few extra atoms to complete coordinations.

Fe coordinated into a dimeric arrangement is common, however the majority of examples of such an arrangement are edge-sharing. The only instance of which the author is aware of isolated, linear, vertex-sharing iron dimers in inorganic crystals are the oxide $AE_8Fe_2O_7$ ($AE =$ Rb, Cs) phases.[185,186]

The polytelluride species is actually very rare; in isolated form, it was unreported at the time of the compound's discovery. It was, however, theoretically expected to exist, due to the existence of several isoelectronic analogs, such as the $[I_3]^-$ and $[Sb_3]^{7-}$ species.[15] While the article was in peer review, a report on the centrosymmetric variation of the same polytelluride species was

published.[187] It was found that the centrosymmetric variation of the polytelluride spanned the same full length, lending additional credence upon the DFT-derived result.

4.3.4. Ba$_6$Fe$_2$Te$_3$S$_7$ – Outlook and Potential Structural Analogs

Searching for analogs of the structure, there are not many options that may work as substituents. The most likely option is selenide substitution of the sulfide, but in this case, whether the structure will form a complete anionic superstructure is uncertain. Complete substitution of the anions to form an oxyselenide may be viable. On the basis of ionic radii, the Fe^{3+} (78.5 pm) positions may be substituted by Ga^{3+} (76 pm) or V^{3+} (78 pm).[59] Mn has a similar radius, but it is not known to make a good substituent for trivalent iron generally. The barium may potentially be substituted with other alkaline earth elements, but a smaller species than strontium is not likely to work. For potential substituents for the telluride, there would be the requirement the anionic species may form the linear polyanion unit. One potential candidate is selenium, but this runs into the issue of potentially forming a solid solution with sulfur. Generally, the isoelectronic linear units adjacent to Te$_3^{4-}$ in the periodic table such as Sb$_3^{7-}$ and I$_3^-$ would be the more likely candidates for forming the same structure, although incorporating these elements would likely warrant a completely different set of elements. To fulfill the neutrality condition with I$_3^-$, either a mixed composition at either the Fe or Ba positions, or a partial valence state of +1.5 for the Fe substituent would be necessary. Sb$_3^{7-}$ would face the same issue, as well as the restriction that sulfides do not typically stabilize the high oxidation states (+4.5) necessary to balance the charges.

4.4. BaMTeS (M = Fe, Mn, Zn, Ge) – An Isostructural Series

4.4.1. BaMTeS – Synthesis and Structure Determination

The existence of the BaMTeS series was anticipated from the existence of the structural analogs BaMSO (M = Co, Zn).[188,189] After the confirmation of the existence of BaMnTeS by SC-XRD, a full search of the first-row transition elements, plus germanium, yielded three more isostructural compounds.

The synthesis of the BaMTeS phases were very different, depending on the cation. The Fe analog was the only one that could be synthesized in a sufficiently pure state for further analysis. As the low-temperature phase of the Ba-Fe-Te-S phase system, the synthesis had to proceed at

a low temperature of 600-660 °C over a long synthesis period of 26 days at temperature, with six regrinds for the reaction to go to completion. Going any higher in temperature risked the irreversible formation of $Ba_6Fe_2Te_3S_7$ or $Ba_9Fe_4Te_{3.5}S_{12.5+\delta}$ (Section 4.5.1) contaminating the sample.

The Mn analog, in accordance with the typical behavior observed in most syntheses, proved difficult to produce pure due to the low rate of formation, as well as the fact that its formation was exclusively observed at temperatures above the point where loss of reactants to sublimation occurred. It was also noted that the compound would form at lower temperatures in a non-stoichiometric mixture. The single crystals, along with the EDX elemental analysis, showed that the compound was about 10% telluride deficient (Paper IV, Tables 1 and 2). The latter analysis also indicated that the missing telluride was possibly substituted by sulfide ions.

The Zn analog reacted in a markedly different manner from the other three analogs. As far as was observed, the compound would not form by solid-state synthesis. Forming the compound required heating a stoichiometric composition to a complete melt at 1000 °C, and allowing this melt to recrystallize upon cooling. The product would form a single rounded lump in the crucible, consisting of large crystals. The difficulties were caused by the evaporation of ZnS from the melt, which resulted in BaTe contamination of the product. Interestingly, the majority of the BaTe ended up concentrated in a layer around the surface of the solidified BaZnTeS, although there was still enough within the crystal to render the product impure.

The Ge analog proved difficult to obtain pure as the product would decompose to form Ba_3GeTeS_4[190] by sublimation of GeTe from temperatures lower than the synthesis temperature. The best results were obtained by pre-reacting GeTe, mixing this with a stoichiometric 1:1 ratio of BaS, and heating at 700 °C for 24 hours, but this sample was still heavily contaminated with impurities. The compound was initially believed to exhibit the same (1111) composition as the other three phases, implying the presence of germanium in the unusual divalent state, but the SC-XRD data showed this to be false. The germanium analog does, as far as available experimental data informs, exhibit the same *Cmcm* crystal structure as the other three phases, but the Ge positions are only half occupied resulting in the effective stoichiometry $BaGe_{0.5}TeS$. The possibility of the half occupancy being ordered, and that the crystal structure was for instance a twin with a $P2_1/m$ symmetry, was considered, but insufficient evidence to support this perspective was found. The only indication was the observation of weaker SC-XRD peaks which could suggest a doubled unit cell along each axis, but this observation was assigned to

half-λ reflections, as attempting to refine the data according to this larger cell resulted in much worse statistics.

The structures of the compounds were all determined by SC-XRD. The Fe analog was a crystalline black solid, the Mn analog was orange, and the Zn analog was a bright yellow compound. The Ge analog was a deep red color.

4.4.2. Ba*M*TeS – Property Determination

Of the four phases, only the Fe analog was subject to full experimental analysis; a cursory DC susceptibility analysis was carried out on the Ge analog. All four phases were analyzed by EDX and DFT.

DC susceptibility analysis of the Fe analog (Paper IV, Figure 7) showed that the compound did not exhibit a paramagnetic state in the 2-300 K temperature range. Rather, the temperature dependence appeared similar to what was observed for the dimers in $Ba_6Fe_2Te_3S_7$ (refer back to chapter 4.3). At this point, it was hypothesized the phase was simply magnetically ordered up past 300 K, so a sample was sent for Mössbauer spectroscopy to confirm. The results, unexpectedly, showed that the compound exhibited no long-range ordering down to 6 K (Paper IV, Figures 5 and 6). Rather, there was an unusual result where the Mössbauer data showed a distinct asymmetry from about 200 K and down. Attempts to identify what this anomaly was, including heat capacity (Paper IV, Figure 4) and low temperature crystal structure determination, came up short. Electric resistance measurements found properties mirroring the Mössbauer data (Paper IV, Figure 8), providing an independent confirmation that there is a real effect, but provided limited assistance to determining the origin of these. Unfortunately, we lack the data to determine what exactly the observed properties represent and can only discuss the possibilities. The most likely possibilities, as we are aware, are a charge density wave and/or a Peierls distortion, but these fail to fully describe the observed behavior and properties. A more exotic option was also considered, namely a resonance valence bond arrangement, where each magnetic ion forms local magnetic couplings with the adjacent atoms in an oscillating manner, resulting in transient, dynamic Peierls distortions (Paper IV, Figure 10), but it should be noted that this is only presented as a hypothetical explanation.

The susceptibility measurements on the impure Ge analog were predominantly to check the phase for superconductivity, as the crystal structure had previously been theoretically predicted as a potential host for unconventional superconductivity.[191] At this point, the compound was

65

believed to contain Ge^{2+}, which could form a metallic compound. The susceptibility measurement did indeed show a superconducting transition at 4.5 K, but the signal was too small to originate from the $BaGe_{0.5}TeS$ phase, or any species visible to PXRD analysis. The origin of the superconducting effect has not been identified, but no known phase in the Ba-Ge-Te-S system should be superconducting near this temperature at ambient pressure. It is possible the signal originated from an impurity; trace presence of niobium in the germanium could result in superconducting properties.

The EDX analysis (Paper IV, Table 2) showed some nuances between the four different phases. The SC-XRD analysis had indicated that the BaMnTeS analog might be non-stoichiometric, with sulfur occupancy of the telluride positions, and this was affirmed by the elemental analysis. Similarly, the half-occupancy of germanium the BaGeTeS analog was confirmed like this. The BaFeTeS and BaZnTeS were found to be about stoichiometric to the 1:1:1:1 ratio. During the analysis of the BaZnTeS phase, multiple compositions other than the 1:1:1:1 ratio were also observed at least once, specifically 2:1:1:2, 2:3:2:3 and 4:1:1:4. It is plausible there are other stable phases in the Ba-Zn-Te-S system; the elemental ratios observed could suggest structural analogs of for instance Ba_2GaAsO_2[192] and $Sr_2Fe_3S_2O_3.$[193]

The DFT analysis showed that, largely as would be expected, the transition metal analogs were all predicted to be semiconductors of varying band gap and character.

While experimental determination of band gaps was not a part of the general characterization performed for each pure compound, the BaZnTeS phase is a direct analog to BaZnOS,[188] which makes for an interesting comparison. The oxysulfide is a wide, direct band gap semiconductor with a colorless appearance. Comparatively, the sulfide-telluride has a smaller band gap, exhibiting a vivid yellow color. While the exact band gap has not been measured, this places the expected band gap of BaZnTeS in the absorption range of blue and purple light, i.e. close to 2.5 eV, compared with the oxysulfide 3.9 eV. This difference is qualitatively as expected from the general trend of the chalcogenides, the band gap decreasing moving down the group.

4.4.3. Ba*M*TeS – Discussion of the Crystal Structure

Unlike the three other phases discussed in detail, the Ba*M*TeS phases do not form a novel crystal structure. Rather, they crystallize in a structure type is also assumed by a couple of oxysulfides: BaCoOS[147] and BaZnOS,[188] of which the Ba*M*TeS phases are exact structural analogs if the partial occupancies are not considered. The crystal structure was shown previously in Figure 9.

66

The key structural feature is a structure of 2D planes, consisting of 2+2 heteroleptically coordinated tetrahedral metal sites. These tetrahedra are interconnected by a vertex-sharing arrangement along two axes, with each anion species exclusively occurring along one axis. Straight-chain M – S – M couplings occur along the c-axis, while the a-axis exclusively exhibits M – Te – M couplings. This results in an anisotropic magnetic coupling arrangement, marking it as a significant departure from the three novel structure types discovered over the course of this work.

The Ba position is also heteroleptically coordinated, assuming a 4+4 fac-square antiprism arrangement.

While the coordination of the M-positions in BaMTeS is hetero-, rather than homoleptic, the structure still bears similarities to the previously discussed $Ba_6Fe_2Te_3S_7$ phase, in the vertex-sharing arrangement of the tetrahedra along the c-axis.

4.4.4. BaMTeS – Outlook and Potential Structural Analogs

Through the course of this project, only the BaFeTeS analog was investigated in depth. Future work on this system would include full characterization of the remaining three analogs. Additionally, there are some further measurements that may be beneficial for understanding the observations of BaFeTeS: If a single crystal sample of sufficient size may be obtained, Raman spectroscopy could elucidate on potential dynamic behavior in the compound. Neutron data of the Fe analog could potentially also be useful, although with the lack of magnetic ordering observed in the Mössbauer spectra, this is tenuous.

On the topic of discovering further substitutions and analogs, the full range of first-row transition metal elements were all tested for whether they could achieve this structure, but only the four species mentioned were found. Interestingly, while BaCoSO exists, the Co variant failed to form a sulfide-telluride analog during trials. Exhibiting an ionic radius between Zn and Fe, there is no structural reason why BaCoTeS should not form, so the failure of the phase to form should be rooted in thermodynamic origins. In fact, cobalt has no reported instances of a sulfide-telluride phase in the literature, which would corroborate this perspective.

It should be noted that the possibility of a partially occupied structure with a four-valent cation was not considered until it was observed in the Ge analog, so such half-occupied structure compositions have not been tested. The most likely elements that could potentially assume the

half-occupied structure are Ti and V. Vanadium could be considered a decent candidate, as the V^{4+} species has been observed to assume a structural analog of the chemically related Ba_3GeTeS_4, (section 4.5.2) but this compound exhibits homo- rather than heteroleptic coordination. Titanium, like cobalt, is among the elements with a low likelihood for forming sulfide-tellurides, and $BaTi_{0.5}TeS$ is thus unlikely to form under simple synthesis conditions.

For this structure type, reducing the size of the spacer cation is unlikely to work, as observed when the Ba in the Ba-*TME*-S-O is substituted with Sr, which assumes a hexagonal structure of the CaZnSO type. The SrFeTeS analog was attempted, but no evidence of any compound beyond simple binaries were observed in the product. Substituting the sulfide with selenide may work, but it is likely the composition will end up as a solid solution, rather than a superstructure. Iodide substitution of the telluride is possible, which could allow for monovalent substitution of the heteroleptic position, with either monovalent Li or Cu exhibiting a suitable ionic radius. Finally, in consideration of the half-occupied structure, there aren't any (high spin) divalent species which could match the ionic radii of Ge^{4+}, so there are no obvious candidates for this arrangement in a sulfide iodide.

4.5. Other Bichalcogenides

In addition to the previous four categories, several other phases were discovered throughout the course of this project. These were all found to be analogous to previously discovered sulfides or oxysulfides. A pure phase for further analysis could not be attained for these phases in time, thus only the structural refinement data are provided in the appendix.

4.5.1. $Ba_9Fe_4Te_{3.5}S_{12.5+\delta}$

This compound comprises the high-temperature phase of the Ba-Fe-Te-S system, being observed as a side product whenever the other two phases decomposed. It was initially discovered during a cursory investigation of the Ba-Fe-Te-S system. Upon heating past the decomposition temperature of this compound (some point below 1000 °C), only simple sulfides and tellurides have been observed. The compound is a specular black, same as the other phases of the Ba-Fe-Te-S system. The compound assumes the $P4_1$ (No. 76) space group, with lattice parameters a = 9.7818(3) Å and c = 34.851(2) Å.[194] The structure refinement parameters and ionic positions are given in appendix 9.1.1.

The difficulties with synthesizing this compound lie in the fact that the synthesis appears to require temperatures which exceed the decomposition or sublimation temperatures of the precursors and intermediates, which leads to a loss of reactants and thus loss of stoichiometry.

The $Ba_9Fe_4Te_{3.5}S_{12.5+\delta}$ crystal structure is a partial substitution analog of the $Ba_9Fe_4Se_{16}$ structure type,[195] as well as α-$Ba_9Fe_4S_{15}$ (the reported crystal structure gives a nominal stoichiometry $Ba_9Fe_4S_{16.63}$),[180] the latter of which was reported first. It should be noted that while it is certain that the crystal structure of the sulfide-telluride is related to the respective monoanion sulfide- and selenide compounds, the exact composition (and thus the site occupancies) is not known. Due to several partial occupancies and potentially mixed-occupancy sites, determining the stoichiometry from only the SC-XRD data is challenging. The presented composition is an educated estimate, based on SC-XRD refinement and experimental observations, but exact determination would necessitate obtaining a pure phase of the compound.

The original sulfide exhibits disordered occupation of several sulfide positions, which are replaced with a more ordered, but still partially occupied polyselenide chain in the selenide analog. The polyselenide/sulfide regions of the monoanion variations are selectively replaced with polytelluride chains in the structure of $Ba_9Fe_4Te_{3.5}S_{12.5+\delta}$. A comparative illustration between the three related structures is shown in Figure 19. The main structural differences are most prevalently observed at the center of each figure.
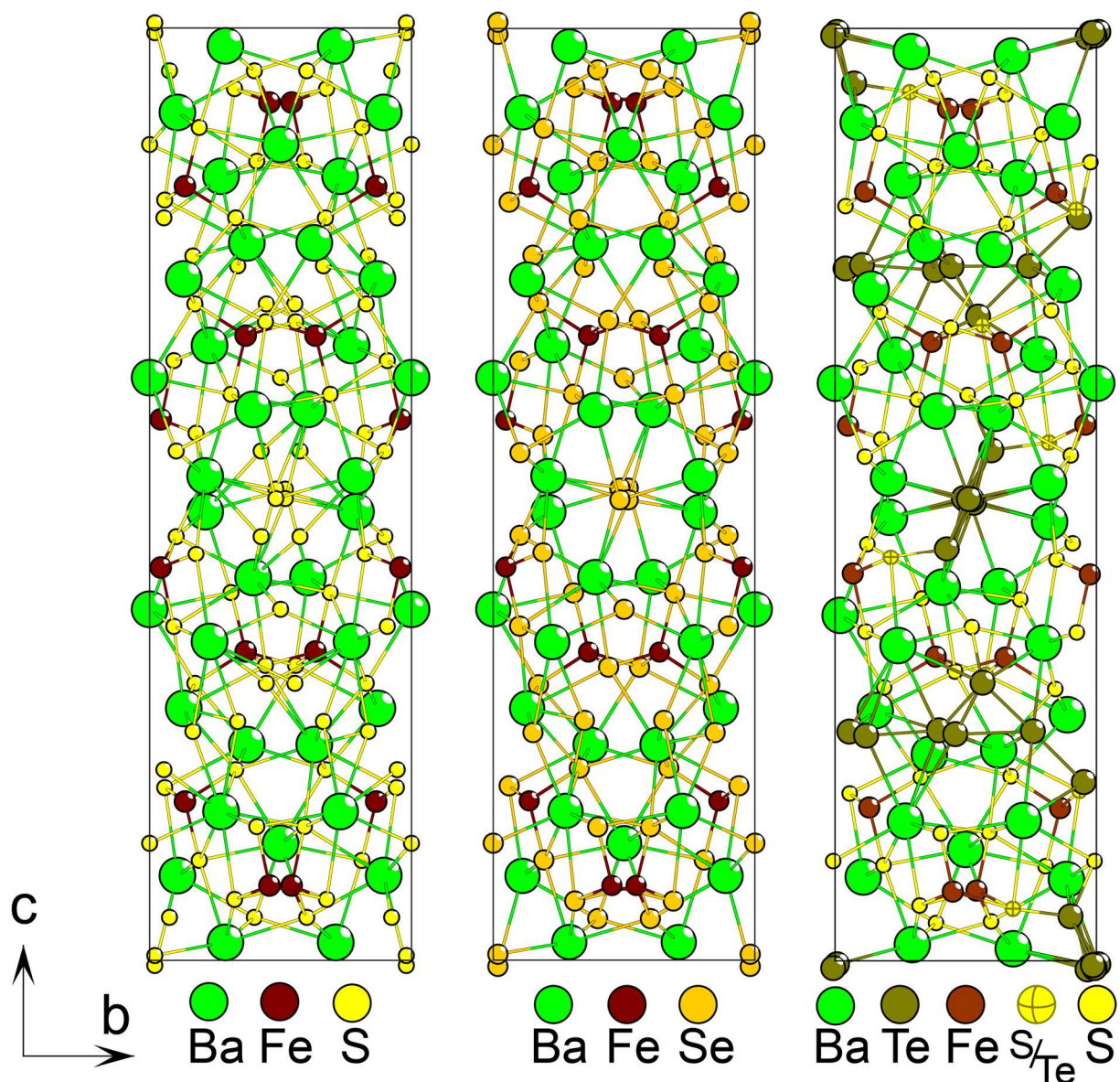
Figure 19: A comparative illustration between the crystal structures of the similar $Ba_9Fe_4S_{16.63}$, $Ba_9Fe_4Se_{16}$ and $Ba_9Fe_4Te_{3.5}S_{12.5+\delta}$ phases.

Directly comparing the three structures, one may observe that the sulfide-telluride assumes the same crystal structure as the monoanions, but a distinct form of disorder, intermediate between the sulfide and selenide forms. The selenide exhibits only a centered chain, while the sulfide additionally exhibits four adjacent sulfide positions. The telluride exhibits a similar central chain, with additionally two adjacent telluride positions. Additionally, while the arrangement of Te in the central chain are similar to the Se analog, the Te positions exhibit further splitting along the *a*-axis.

The Te – Te interatomic distances are sufficiently short to indicate there is a significant degree of interaction between them. Considering the structural disorder there are likely several polytelluride species present in the structure. The presence of pertelluride is likely, but the species beyond this cannot be said with any certainty. There are several Te – Te distances that are too short to be realistic, and as such it possible the Te-chain is incommensurate with the remainder of the crystal structure, or multiple different motifs are represented in a smaller unit cell, resulting in an apparent disorder.

A notable feature of the sulfide-telluride is the fact that, as far as the structure is presently resolved, is the apparent coordination of polytelluride species with sulfide positions, which might imply one of the following: a mixed-species polychalchogenide, the associated tellurium being nearly charge neutral, or a tellurium-polytelluride coordination, any of which would be unusual.

The partial replacement of the anions had the obvious effect of lowering the symmetry somewhat; the original structure type exhibits the space group $I4_1/a$, while the sulfide-telluride loses the body-centric symmetry and glide plane, assuming the $P4_1$ symmetry.

In terms of outlook for this compound, potential structural analogs for $Ba_9Fe_4Te_{3.5}S_{12.5+\delta}$ are somewhat uncertain, as the oxidation states are ambiguous due to the polytelluride species present. More broadly, structural motifs of monoanion chalcogenides which exhibit linear polychalcogenide structures may be substituted as sulfide-tellurides. A direct example of a potential compound that may exist from these considerations is $Ba_9V_3Te_6S_9$, from the $Ba_9V_3Se_{15}$ structure type,[196] potentially exhibiting parallel polytelluride chains.

Substituting polytelluride with polyiodide is also a possibility, although either partial valency or a mixed substitute of the Fe positions would be necessary.

4.5.2. Ba₃VTeS₄

The Ba_3VTeS_4 phase was discovered after an attempt at the previously suggested $Ba_9V_3Te_6S_9$ phase.[194] It assumes a known crystal structure described by the *Cmcm* (No. 63) space group with lattice parameters a = 6.7533(3) Å, b = 16.1831(7) Å and c = 9.6458(4) Å (Figure 20). The detailed crystal structure, along with the refinement data, are supplied in appendix 9.1.2. The crystal structure was originally observed in the Ba_3GaS_4I phase,[197] and later for Ba_3GeTeS_4.[190] It is a specular black compound which readily forms large crystals, suitable for

SC-XRD. The crystal used for the structure determination was prepared as an impure phase by heating a nominal composition of $Ba_9V_3Te_6S_9$ to 800 °C for 48 hours.

The crystal structure exhibits V^{4+} in a tetrahedral, homoleptic coordination with sulfide. The barium positions exhibit two different heteroleptic 2+6 coordinations, with the telluride positions arranged in *fac*/*trans*-coordinations in both cases, but the central Ba positions are coordinated as either square prismatic or square antiprismatic.

While two analogs of this structure type are already known, this phase is the first magnetically active variant, exhibiting V^{4+} with a d^1 electron configuration. Preliminary theoretical investigation by DFT+U is inconclusive in determining the magnetic behavior of the compound, suggesting FM at lower values of U_{eff}, transitioning to AFM at higher U_{eff}. The coupling energy is comparatively small, as could be expected of a dilute system of d^1 magnetic ions.
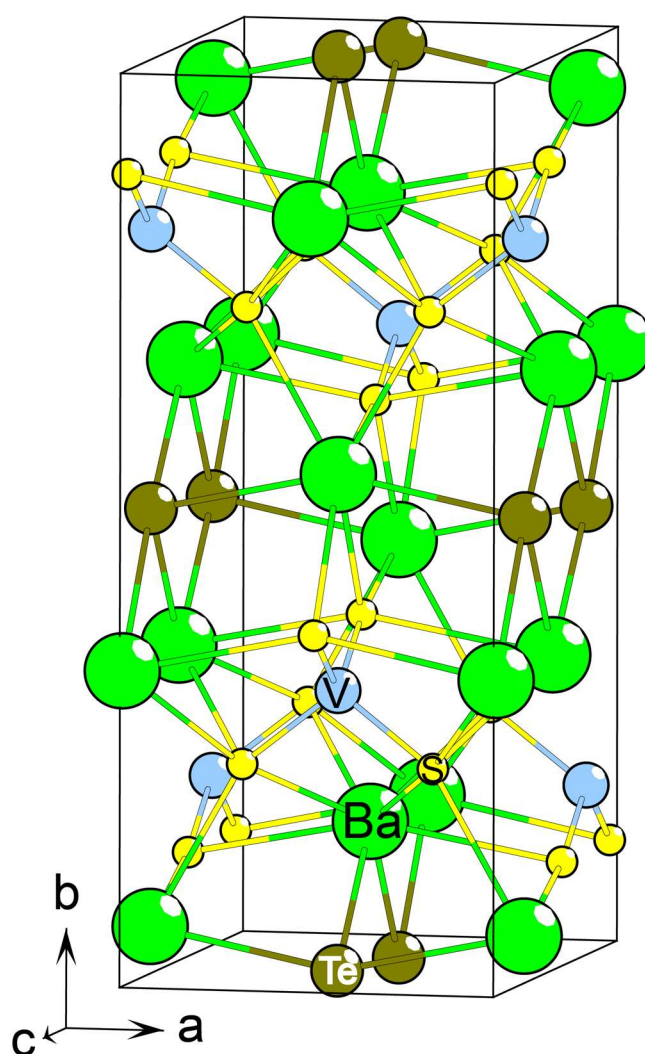
Figure 20: Crystal structure of Ba_4VTeS_4.

4.5.3. $Ba_2Mn_3Te_2S_3$

The $Ba_2Mn_3Te_2S_3$ phase was discovered as a secondary phase during attempts to synthesize a pure product of BaMnTeS, formed after heating a stoichiometric mixture of the latter composition to 900 °C for 72 hours.[194] The crystal structure and composition were determined by SC-XRD (Figure 21). The compound assumes an orthorhombic crystal structure described by the *Pbam* (No. 55) space group, with lattice parameters $a = 11.8025(4)$ Å, $b = 9.0163(3)$ Å and $c = 4.8592(2)$ Å. The crystal structure and the refinement data are supplied in appendix 9.1.3.

$Ba_2Mn_3Te_2S_3$ is a structural analog to the known $Sr_2Fe_3S_2O_3$ structure type,[193] with one crucial difference: While the $Sr_2Fe_3S_2O_3$ structure is fully ordered, $Ba_2Mn_3S_3Te_2$ appears to exhibit structural disorder in the Mn positions. The implication is obvious; the size of the ions present in the structure are not of a suitable ratio for the ordered crystal structure to form properly, thus the stress is released by shifting the position of a few ions. In the shown structure, only the Mn position is distorted, but an adjacent sulfide position situated between two such Mn positions exhibits distinctly elongated thermal parameters, indicating that the adjacent local structure reorganizes sufficiently to be detectable.

Preliminary investigations of the crystal structure by DFT affirm the general idea that the fully ordered $Sr_2Fe_3S_2O_3$ structure type is unstable, and that the structure would indeed assume at least some degree of structural disorder, within the unit cell representation derived from SC-XRD.

Between structural considerations and preliminary DFT analysis, the origin of the disorder could be suggested to be the size of the sulfide ions being too large to accommodate the Mn positions in a fully square lattice, resulting in distorted arrangements. Alternatively, one might consider the Mn ion too small to properly coordinate with the telluride, causing the Ba-Te lattice to collapse in, and the sulfide square lattice to distort.

Nominally, disregarding the distortion in the crystal structure, the Mn positions in the crystal structure exhibit two different heteroleptic coordinations: A 2+4 *trans*-octahedral configuration, as well as an unusual 3+3 *mer*-idional octahedral arrangement. All barium in the structure is arranged in a single symmetric position, exhibiting a 4+5 *c-fac*-square antiprismatic coordination.

Synthesis of a pure phase of this compound was, as with the other Mn-based phase in this work, complicated by uncontrolled loss of reagents to sublimation and decomposition at the necessary synthesis temperature.

In terms of outlook, possible analogs of this crystal structure depend on what part of the crystal structure is causing the distorting strain. We may consider the typical substitution of Mn^{2+}, Fe^{2+}, as well as Co^{2+}, which is known from the oxysulfide analog. Cobalt is, as previously mentioned, not known to form sulfide-tellurides, making the Fe analog the only one likely to exist. If it does exist, it is also the most likely analog to be easily prepared as a pure phase under simple synthesis conditions. Another potential substitution is replacing Ba with Sr, but this seems unlikely to succeed, as the reduced size of the spacer would further reduce the available space in the already strained square lattice. If one assumes the distortion is due to the Mn ion being too small for the sulfide lattice, a larger alternative such as Pb^{2+} could be a possibility.
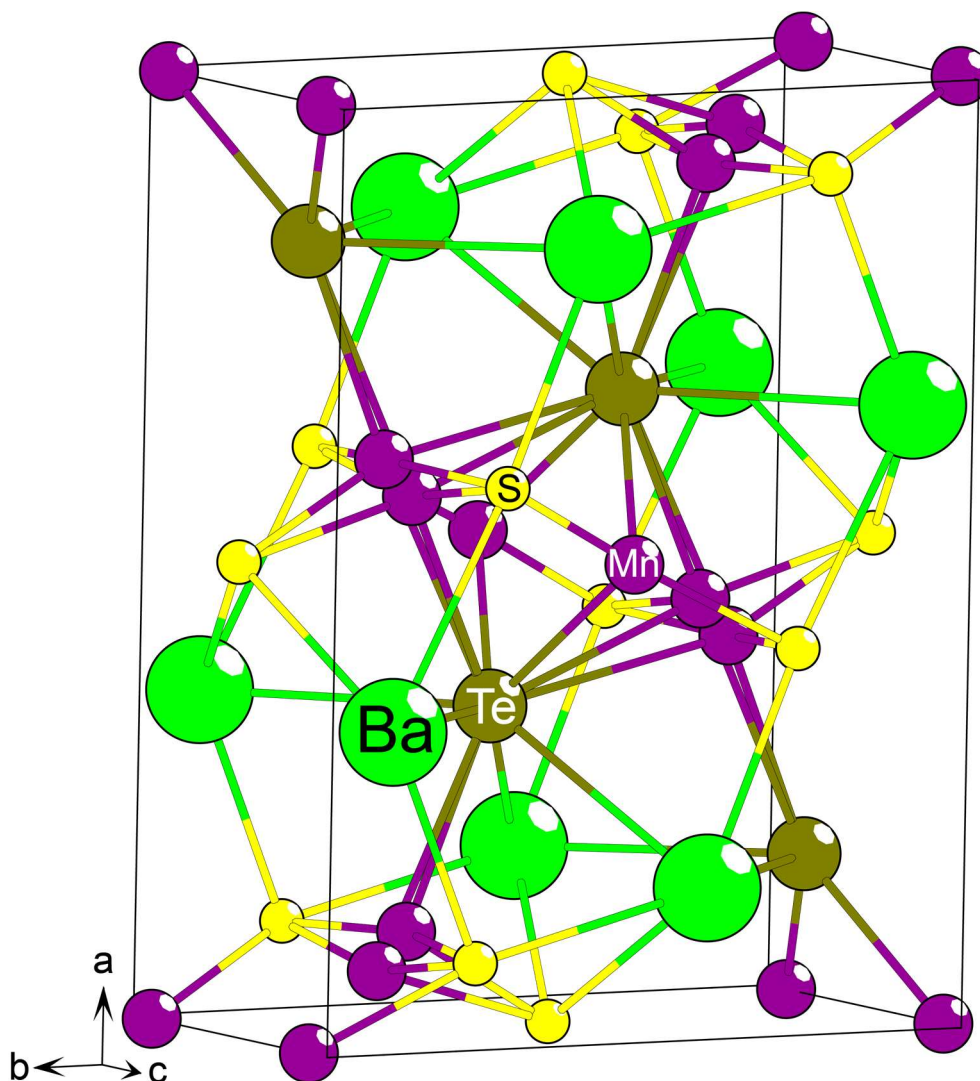
Figure 21: The crystal structure of $Ba_2Mn_3Te_2S_3$.

4.5.4. $La_{10}Te_{14+x}S_{1-x}$ and La_2TeS_2

These two compounds, $La_{10}Te_{14+x}S_{1-x}$ and La_2S_2Te are direct analogs of their well-known oxysulfide equivalents.[194] The latter is also a lanthanum substitution of the known Nd_2S_2Te phase. The crystal structures and refinement data are given in appendix 9.1.4 and 9.1.5.

The preparation of pure phases of these compounds was primarily hindered by the tendency of lanthanum to form the oxysulfide analog, reacting with the corundum crucibles to form $La_{10}S_{14+x}O_{1-x}$ impurities, as well as the ease of forming $La_{10}Te_{14+x}S_{1-x}$ while targeting La_2S_2Te.

Rather simple analogs, they have not been characterized to any degree beyond determining the crystal structure. Comparing the sulfide-tellurides with their respective oxysulfides from the literature the lattice parameters of the former are all significantly greater, as would be expected from the substitution with larger anions.

As simple lanthanide-based compounds, structural analogs of all trivalent lanthanides are likely to exist, and doping with optically active lanthanides is likely easily achieved.

4.6. A Discussion of the Bichalcogenides in General

4.6.1. Characteristics and Notes of Synthesis

A common characteristic observed for bichalcogenide synthesis in general is that the resulting compounds are typically good crystal formers. The syntheses require no mineralizer, nor extrinsic melt, to produce crystals of significant size. Even if the initial composition was very different from the resulting phase, the components of the initial mixture would often segregate to form useful crystals. Every compound discovered in this work has formed crystals of sufficient size and quality to be characterized by SC-XRD. This includes the phases that necessitated a low-temperature synthesis, so it is not simply a consequence of high synthesis temperature relative to the respective melting points of the compounds involved. Many of the phases did show a tendency for intergrowth, forming multi-crystals and/or twins. Characterization of the crystal-forming behavior of the bichalcogenides is a full project in itself, and beyond the scope of this text, but SEM analysis of both mixed and pure phase compositions offer certain indications. In particular, a series of observations during the attempts to produce a pure phase of LFCSO are of interest: In the mixed phases, a consistent observation was that crystals with clear habitus were distinctly growing out of other, more amorphous-looking crystal structures. This feature was no longer observed in the final pure phase, suggesting a

complex growth behavior of various elements. Other observations, such as notable lack of habitus in pure crystals also supports this perspective.

From observing the characteristics of the synthesis products, the majority of bichalcogenide syntheses appear to melt incongruently, resulting in a solid-liquid phase mixture, or remaining solid-state throughout, as opposed to forming a single melt. This melting behavior is broadly as expected, and may be attributed to the wide range of melting temperatures for the different precursors and intermediates. For instance, for $BaGe_{0.5}TeS$, the melting points of the binaries is 2508 K for BaS,[198] and 998 K for GeTe.[199] A relatively simple behavior was observed for BaZnTeS, which only formed upon crystallizing a congruent melt.

There were also observations of systems where non-stoichiometric bichalcogenide compositions appeared to assist with formation of certain phases. One particularly clear example was observed with attempted BaMnTeS syntheses: PXRD analysis of the product obtained from heating a stoichiometric composition exhibited no traces of BaMnTeS formation. However, a synthesis of with the nominal composition $Ba_2Mn_3Te_2S_3$, under identical heating conditions, would distinctly exhibit the BaMnTeS phase among the products.

In general, the constituent elements of the syntheses did not exhibit particularly unusual diffusion rates through the synthesis; long synthesis times and multiple rounds of regrinding were typically a necessity to obtain pure phases. The necessity for low-temperature synthesis for less stable phases exacerbated this in some cases, but the optimized syntheses aiming for pure phases typically proceeded in a fairly unremarkable manner for solid-state syntheses.

4.6.2. Considerations for Investigation of Bichalcogenide Systems

When explicitly searching for novel crystal structures in bichalcogenide systems, there are few reference points on how to proceed. There is very little information available on phase diagrams and stability of multianion systems in the literature, and the compositions of entirely novel crystal structures are difficult to predict. Finding nominal compositions which produce novel phases in sufficient quantity to identify the crystal structure can be very challenging.

Through this project, this difficulty was mostly avoided by utilizing the favorable crystal forming characteristics of many bichalcogenides. Due to the bichalcogenide phases having a tendency to separate out as single crystals, a rather simple approach could be adapted for discovering entirely novel phases: The initial stage of the search was to simply start from a

rough initial composition, close to the center of the common phase diagram. The resulting product was then analyzed, both by PXRD, and by manually testing crystals by SC-XRD. Upon the discovery of a novel phase, the potential avenues for finding more compounds in the same phase diagrams was considered, although the specifics depended on the particular phase. The main two approaches were testing alternate points within the same phase diagram as where the initial compound was found and substitution of elements.

For the lanthanum oxysulfide phases, the full scope of a five-element phase diagram was simply too large to extensively investigate under the constraints of the relatively short time frame available. After the initial discovery of LFCSO, the chosen approach was to attempt to make use of the favorable crystallization properties again to obtain single crystal samples. The lanthanum, sulfur and oxygen compositions were kept fixed at a roughly centered position in the phase diagram, while the transition metal elements were varied: both the ratio between them, as well as the elements included in the composition. The decision to keep the La-O-S elements static was rooted in two factors, beyond simply limiting the scope of the search: Firstly, it was a composition known from the literature to be capable of forming a range of structural arrangements as a matrix component, and secondly, as the three elements would always form the phases La_2O_2S and $La_{10}S_{14+x}O_{1-x}$ in the absence of other reactions, both of which are very stable.[61,62] The latter factor, as both oxygen- and sulfur-rich phases were available, meant that the La-O-S component of a trial synthesis could spontaneously adapt for a wide range of shifts in the stoichiometry from the transition elements reacting to form a stable phase. Simultaneously, the number of secondary phases was kept to a minimum, consisting of mostly easily identifiable compounds, thus making novel species easily spotted in PXRD. The initial tests focused on variation of the Fe:Cu ratio, followed by substitution of Fe with other first-row transition elements. Syntheses targeting the LFCSO composition with other first row transition elements was also attempted. The substitution of Fe, rather than Cu, was chosen on the basis that the crystal structure of LFCSO appears more closely related to the known La-Cu-S-O phases. This sweep led to the discovery of the LICSO and LCCSO phases.

For the barium sulfide-telluride phases, the search for compounds followed a similar approach, except the synthesis temperature was found to be more critical. With the four-element compositions of the sulfide-tellurides, varying the full composition during the search for different phases was more viable. Additionally, searching for a range of sulfide-telluride analogs of simple oxysulfide structures proved viable.

Ultimately, this project was only allotted so much time, and the degree to which any of the phase diagrams under consideration in this thesis have been investigated remains sporadic. At this point, the feasibility of the formation of stable compounds in a series of compositions has been established. A full systematic investigation of every phase diagram where a compound was discovered through the course of this project remains as tasks for further work.

Predicting whether a particular combination of elements is suitable for forming a stable bianion compound is a very complex matter, and the difficulty escalates as the number of elements increases. It is possible to make a rough guess on the viability of a given system, as well as the complexity of the necessary synthesis, utilizing the physical phase transition temperatures of both the precursors and the likely intermediates. If these are roughly similar, it may be considered a positive indication for the viability of a multianion phase forming. If they are too different, obtaining a multianion compound is complicated even if a nominally stable phase does exist, perhaps necessitating alternative synthesis routes such as chemical vapor transport. If the necessary reaction temperature is above the decomposition temperature of the multianion phase, forming this compound may be unattainable without more involved synthesis procedures. It is possible to avoid this issue to some extent by explicitly avoiding thermodynamic minima in a synthesis composition. If the ratio of anions to cations does not match that of particularly stable undesired species, it is plausible to push the synthesis towards the desired multianions.

Even for compatible groups of elements, the thermodynamics may be very complex, as shown by the phase stability behavior of the Ba-Fe-Te-S phases. There are also instances where the bianion compound is the more stable state, but one of the precursors or intermediates will decompose or sublimate away at the synthesis temperature, which was observed with BaMnTeS in particular. Complete phase diagrams for quaternary multianion systems are scarce, but some do exist, a bichalcogenide example being the $Tl_2S - Sb_2Te_3$ diagram.[200] This system only forms solid solution structures of the monoanionic species, but the phase behavior is already very complex.

A crude approach to simplify the search for compatible elements for a particular bianion pair, is to search for elements that form at least one quaternary compound with this pairing (the existence of a ternary phase is not a useful indicator). For instance, all three of the *TME* subdivisions of the lanthanum oxysulfide phases discovered in this work, La-Fe-S-O, La-Cr-S-O and La-Cu-S-O, are all individually known to form at least one compound each.[78,175,201] Conversely, certain cations may be inherently difficult to incorporate with a given bianion pair,

indicated by a complete absence of known compounds. A previously noted case is the incorporation of cobalt in sulfide-tellurides, probably due to stable Co-based binaries.

Among the unsuccessful attempts in synthesizing bichalcogenides over the course of this project, the cation-anion pairing simply being incompatible and producing a mixture of monoanion compounds is by far the most commonly observed mode of failure. Another difficulty with bichalcogenide synthesis is that certain combinations of ions (this may be either just between anions, or cations with anions) are incompatible from a redox perspective. While attempting the synthesis of barium oxysulfides, the extremely stable barium sulfate (barite) was typically found to have formed instead. Barium oxysulfides do exist,[188] so it is possible to stabilize them, but the conditions where the possibility exists are comparatively limited.

A major complicating factor in the investigation of bichalcogenide systems, especially involving selenide or telluride ions, is the possibility of polychalcogenide formation. These species are known to exhibit a wide range of structures and oxidation states from single-anion chemistry, but the existing literature on their behavior in multianion chemistry is lacking. Predicting the coordination behavior of a particular polychalcogenide species is doable, observed examples mostly follow the HSAB principle. However, anticipating if and/or what polychalcogenide will form under given multianion conditions, is not likely to be reliable without further data.

Ultimately, the library of known bichalcogenides compounds is still limited. As such, a synthesis aiming for novel compounds is still very likely to yield unexpected results; these results add to the knowledge, such that a comprehensive understanding of multianion structures and properties may eventually be attained. General methodologies for targeting specific structural characteristics in multianion crystal structures are described in the next section (4.6.3).

DFT could also be used as an assisting measure in the search for multianion compounds. Once a crystal structure has been discovered, it is possible to calculate the enthalpy of formation of this crystal structure with different elements. This may provide theoretical insight into what compositions are potentially viable, and narrow down the scope of the work necessary for experimental analysis.

4.6.3. Design of Synthesis: Targeting Specific Properties

Here, we expand the scope slightly. The principles described in this section apply to bichalcogenides, but they are sufficiently general that they may be considered a viable perspective to bi- or even multi-anion syntheses in general.

Within the field of monoanionic compounds, a very large library of stable phases has been established over the years. Through analysis of this data set, a number of rules and general expectations have been established. These inform what crystal structure types could result from a particular composition, what elemental substitutions are likely to be viable, and what properties this compound is likely to have.

With the introduction of a second anion with a significantly different radius, completely new strategies and systems need to be established. There are, as has been previously noted, cases where the direct substitution of a second anion into a monoanionic crystal structure results in an isostructural arrangement with anionic superstructure, but this is still rare. Typically, the resulting compound will assume a completely different crystal structure. As such, if one wishes to target a specific crystal structure, the only somewhat reliable approach is to target the composition of a previously known multianionic composition, which exhibits the desired crystal structure.

For multianion synthesis targeting specific properties, the number of known multianion compounds, and the degree of characterization for these compounds, is still too low. The introduction of a second anion significantly complicates the prediction for what crystal structures are likely to occur, so accurate predictions require a wide range of precedents to extrapolate from. However, while detailed predictions for compounds remain very imprecise at present, it is possible to design a synthesis such as to improve the likelihood of particular characteristics or properties occurring in the product compound.

One of the desired aspects, when tuning multianionic compounds, is the coordination of the cation of interest (henceforth referred to as the functional element/cation through this section (4.6.3)). At the most basic level, the likelihood of homo- vs. heteroleptic coordination of any particular species, is primarily decided by the HSAB principles, as well as the composition of the synthesis. As has been previously noted, the harder anions (hardness increasing with smaller radius and greater charge) in the bichalcogenide systems will preferentially coordinate with the harder cations. As such, you may induce particular cationic species to a certain coordinations by judicious selection of elements around the target cation and its oxidation state.

Considering the case of preparing a trial synthesis, aiming for a novel bianion compound with particular characteristics: If, for a given functional cation, one aims for a homoleptic coordination by the softer anion, the factors which would promote this are: increasing the proportion of soft anions, including one or more harder cations in the composition (for instance in the selection of spacer cation(s)), and a proportion of harder cations large enough to fully coordinate all of the harder anions (a 1:1 ratio is the minimum). Promoting the formation of a homoleptic coordination of the harder anions would entail the opposite considerations.

Targeting a heteroleptic coordination is more involved, as there are multiple strategies that may be utilized to promote the desired outcome. The first option is to choose the elements involved such that one anion preferentially coordinates with the functional element (again, as per HSAB), and limiting the quantity of this preferentially coordinated anion. If the supply of this anion is too low, such that it cannot fully occupy all coordinations of the functional element, this will promote a heteroleptic coordination. This approach may also be utilized to target structural features in the resulting crystal structures: If the preferentially coordinated anion is in short supply, the functional cations are more likely to coordinate around these limited anions, forming structural elements such as chains, planes or networks as necessary to maximize the more favorable coordinations. By controlling the proportion of anions, one may theoretically tailor specific structural elements. By extension, the prevalence of specific heteroleptic coordinations may also be manipulated.

The second option for targeting heteroleptic coordinations, is to utilize spacer elements with similar hardness to the functional element. For example, the hardness of alkaline earth elements is quite similar to that of divalent first-row transition metal elements. In this case, there is limited thermodynamic preference for coordination of particular cation-anion pairs, limiting the influence of HSAB on the coordinations. In this case, the crystal structures are more likely to assume crystal structures closer in line with the principle of closest-packing crystal structures. Consequently, among bichalcogenides (or isovalent multianion compounds in general), these compounds are the most likely to allow higher-symmetry structures, with compositions involving similar proportions of elements. If one is aiming for lower-symmetry structures, this may be achieved by shifting the anion ratio further towards one species or the other.

In addition to the previous considerations, the synthesis temperature may be critical, as multianion systems may well exhibit low-temperature phases, with completely different compositions and crystal structures. Depending on the elements involved, and what cations are the target for a particular coordination, the requirements for the synthesis temperature change.

For elements with multiple possible oxidation states, the choice of temperature may determine oxidation state, which could completely change the viable crystal structures (even if another ion changed oxidation state to compensate) as per the HSAB rules. This is especially complicated with the potential for formation of polychalcogenides.

While predicting precise outcomes for novel synthesis remains difficult at present, the above principles may be employed to target desired qualities. An example where tailoring of particular heteroleptic coordinations could be of significant, is in development of phosphors. The emission wavelengths of fluorescent ions are significantly dependent on the crystal field splitting. Thus, the ability to tailor-make host materials with specific heteroleptic coordinations would allow for a novel approach to the preparation of phosphors with unique properties. The potential of heteroleptically coordinated lanthanides has already been demonstrated with the applications of for instance Gd_2O_2S,[202] but another possibility is the substitution of Er^{2+} into barium- or strontium-based compounds for the same purposes.

The effect of the crystal field splitting may also be considered as what was previously introduced (section 2.1.2.2.1) as the forced Jahn-Teller effect. For heteroleptic coordinations of transition elements (or open-shell f-elements) with the appropriate electron configurations, this may result in strong single ion anisotropy and single-ion molecular magnets.

4.6.4. Cross-Compound Structural Considerations

With regards to the La-O structures observed in LFCSO, LTCSO and related compounds, there is an interesting observation to be made: the structures constitute an anti-structure of common arrangements for tetrahedral metal coordinations. The similarity of the $[La_4O]$ units are trivial, but $[LaO]$ planes, for instance, are matched one-to-one by FeAs in the $LaFeAsO$[203] structure, and the hourglass-shaped units observed in LTCSO are observed in a configuration of infinite chains in $Ba_9(Fe_2S_4)_8$.[204] This is of interest, as the many potential coordinations of the *TME*s is a field where a lot of work has been previously carried out.[205] Further efforts in the field of $[LaO]$ unit construction may thus build off this in the search for yet further rare-earth coordinations.

An interesting parallel one may observe in the lanthanum oxysulfide phases discovered in this work, is that they both exhibit some form of disorder or partial occupancy. LFCSO is the worst offender, but the partial occupancy and disordered sulfide positions of LTCSO falls under the same case. This behavior extends beyond the two structural motifs here and may be traced to

the La-*TME*-O-S phase systems in general. Of the known compounds in this system, several exhibit at least some degree of disorder: $La_5Cu_6O_4S_7$,[175] $La_8Ti_{10}S_{24}O_4$,[206] and $La_4Ti_3S_4O_8$[207] all exhibit this trait.

The prevalence of apparent disordered compounds observed in this work emphasizes a particular difficulty with proper characterization of the structure of multianion phases in SC-XRD: There are often major structural elements, which may consist of all the heaviest elements in the compound (due to the HSAB preferences for anion-cation pairing), repeating through the structure with a comparatively small unit cell. Other elements, often the small, lighter species, are arranged in a lattice with order that requires a several times larger unit cell to describe. However, as the major structural units dominate the reflections in XRD-based techniques, the subtle superstructure indicating the longer lattice of the smaller species' ordering is lost in the background signal.

One can imagine this is less of a frequent issue in monoanionic compounds; with only a single anionic species, there is no thermodynamic incentive for a specific species of atoms to preferentially group together in units with a smaller dimensionality than the rest of the structure, reducing the incidence of cases where a smaller sub-periodicity overshadows the full cell.

Over the course of this project, three phases in the Ba-Fe-Te-S system were discovered: BaFeTeS, $Ba_6Fe_2Te_3S_7$, and $Ba_9Fe_4Te_{3.5}S_{12.5+\delta}$ phases, constituting the low-, intermediate- and high-temperature phases respectively. It may be noted that their characteristics follow a temperature trend: Only the low-temperature phase exhibits heteroleptic coordination of the iron positions. It is also the only phase which exhibits divalent Fe. The mid-temperature phase exclusively coordinates trivalent Fe with sulfur, and while the oxidation states in the high-temperature phase are somewhat uncertain, they should still be closer to trivalent. The high-temperature phase also predominantly coordinates Fe with S, although the partial occupancies render matters somewhat unclear. This preference may be explained from a thermodynamics perspective, as the iron-sulfide coordination is comparatively more stable. Further, only the mid- and high-temperature phases exhibit polytellurides. It may also be noted that the polytellurides increase in length from oligomer to polymer with temperature, but assuming this to be a trend from just two examples is excessive. In both cases, the polytellurides appear to consist at least partially of telluride triplets, similar to $[Te_3]^{4-}$, despite the different arrangements of the polytellurides themselves, which is interesting. This four-valent triplet may be preferable in the multianion environment. Additionally, similar disordered polytelluride chains to those found in $Ba_9Fe_4Te_{3.5}S_{12.5+\delta}$ were observed in other novel crystal structures discovered through

this work as well. The crystal structures of these compounds were only partly resolved, and the compositions remain uncertain, thus they are not further remarked upon.

Expanding beyond the purview of the bichalcogenides, the existence of the BaM_xTeS (x = 0.5, 1) (M = Fe, Mn, Zn, Ge), $Ba_2Mn_3Te_2S_3$ and $La_{10}Te_{14+x}S_{1-x}$ phases as analogs of the equivalent oxysulfides, opens for the possibility that other multianionic species may be scaled equivalently, while obtaining the same crystal structures. Following periodicity, one may make a prediction that structural analogs of fluoride-chlorides may exist among the chloride-iodides, or similarly for other anionic groups. As an extension, this may also apply to multianion pairings with anions from two different groups: Oxychlorides may have analogs in the sulfide-iodide system, etc.

A quick literature search showed that there are in fact cases of sulfide-iodides assuming oxychloride structural motifs. An example is the $La_3(SiS_4)_2I$ and $La_3(SiO_4)_2Cl$ compositions assuming the same structure.[208,209] This, again, couples back to the sulfide-tellurides: As observed with Ba_3VTeS_4 being an analog of a sulfide-iodide structure, iodide may substitute for telluride positions in crystal structures. This makes sense, as their ionic radii are very similar. There are several implications to this possibility. Firstly, every sulfide-iodide structure is a potential motif for sulfide-tellurides, and *vice versa*, if a second species is appropriately substituted to balance the charge difference. As an example, the BaMTeS structure could be substituted for a BaMSI motif, with a monovalent species M, for instance Cu or Li. Alternatively, a partial substitution of Te by I in sulfide-tellurides could allow for doping of an active element, such as achieving a subvalent state of Fe in BaFeTeS, which would be of interest for the compound as a potential iron superconductor. Whether this potential for substitution extends to polyiodides is unknown, a literature search found no examples of known isostructural polytellurides and polyiodides. Further, examples of multianion compounds of polyanion components are scarce, leaving few structural examples to consider. There are cases which indicate similar behaviors between polytellurides and polyiodides in multianion conditions, such as the $K_{10}(Nb_2O_2F_9)_3(I_{0.5}(I_3)_{0.5})$ compound of the $K_{10}(Nb_2O_2F_9)_3Br$ structure type[210] exhibiting remarkable similarity to the case of telluride substitution observed with $Ba_9Fe_4Te_{3.5}S_{12.5+\delta}$, but due to this lack of documented examples, the potential for substitution of (poly)telluride with (poly)iodide and *vice versa* is simply too uncertain to say much about.

4.6.5. Final Remarks

Between the fully characterized phases in this work, a wide range of qualitative properties were observed: From cluster glass to singlet-state magnetism, to compounds which unexpectedly fail to assume an ordered spin state. Disordered crystal structures with variable-range charge-carrier hopping and narrow band gap semiconductors with anomalous temperature dependence and Mössbauer spectra.

While covering a wide range of properties and characteristics, there is one notable absence in this list: There is not a single example of a compound behaving in a manner fully described in simple terms, without some complicating factor. Every phase proved to require extensive investigation and consideration to properly describe, if a full description was even possible with the available data. Some characteristics required extensive trailing of the literature to understand; others could not be found elsewhere at all.

While this observation may be from a small selection of novel compounds, the complexity and uniqueness of the compounds' characteristics is rather telling: At this point, we know quite little about the bichalcogenides. Whether their possible crystal structures, properties and practical applications, most aspects remain largely unknown. There is a vastness of challenges remaining ahead; so, here, we have taken a few more steps.

5. Summary, Conclusion and Outlook

Through this work, a number of novel bichalcogenide compounds have been discovered and characterized.

$La_{18}Fe_5Cu_4S_{24}O_8$ was found to exhibit a novel crystal structure with a very unusual guest-in-host motif, with a substantial degree of structural disorder in the guest-part of the structure. This disorder was resolved to suggest an ordered local motif, but with the separate guest regions being out of phase with each other to produce the experimentally observed disorder. The compound was determined to be a magnetic cluster glass at lower temperatures, a property assigned to freezing of spin dynamics.

A pair of chemically similar compounds to $La_{18}Fe_5Cu_4S_{24}O_8$, $La_{14}TME_6CuS_{24}O_4$ (*TME* = Fe, Cr), were found to exhibit certain structural similarities, in the form of preferential Lanthanum – Oxygen coordination, and a degree of structural disorder. The compounds assume a novel crystal structure, exhibiting multivalent chains of *TME* positions. While the compound is suspected to form large magnetic domains, the exact nature of the magnetic properties of these compounds remain unknown, as evidence suggests contradictory properties.

$Ba_6Fe_2Te_3S_7$ exhibits a novel crystal structure, exhibiting an unusual dimeric coordination of Fe^{3+}, as well as a very rare polytelluride species, $[Te_3]^{4-}$. The compound was found to assume a singlet spin-state, with the Fe in each dimer only coupling locally.

The Ba*M*TeS (*M* = Fe, Mn, Zn, Ge) phases were found to be structural analogs of the previously known Ba*M*SO (*M* = Co, Zn) phases, exhibiting anisotropic magnetic coupling along different axes. The BaFeTeS analog was found to behave very differently from BaCoSO, not assuming magnetic ordering, nor a paramagnetic state across the 2-300 K range. The Fe analog also exhibited a Mössbauer anomaly which could not be easily explained. A dynamic charge density wave model was proposed to explain the observations.

Finally, several other sulfide-telluride phases were discovered, but not characterized beyond the crystal structure: Ba_3VTeS_4, $Ba_9Fe_4Te_{3.5}S_{12.5+\delta}$, $Ba_2Mn_3Te_2S_3$, $La_{10}Te_{14+x}S_{1-x}$ and La_2TeS_2 all exhibit crystal structures analogous with previously known compounds.

The aim of this project was the discovery, synthesis, and characterization of novel bichalcogenide compounds. We have described and discussed the observations and notes pertaining to the experimental synthesis of bichalcogenides, and the approaches utilized to increase efficiency in discovery of novel phases. Over the course of the work, thirteen novel

phases, with nine different crystal structures, have been discovered. Of these, five were prepared as sufficiently pure samples for detailed characterization, while the remaining eight had their crystal structures and compositions determined.

The common structural motifs in the crystal structures of the compounds discovered through this project, and the trends in how these form, have been discussed. Further, how these considerations couple into the wider field of bichalcogenides and multianion compounds in general, has been considered.

Much further work is needed; novel phases were discovered at such a rate that efforts to optimize syntheses for sufficiently pure phases could not keep up. There are a wealth of as-yet undiscovered bichalcogenide compounds, and many do not require more than simple solid-state synthesis conditions to form. The exploration of the sulfide-tellurides, in particular, is underdeveloped. As demonstrated with several of the new phases discovered in this project, structural motifs accessible for the oxysulfides are also viable for the sulfide-tellurides. Thus, the larger library of known oxysulfide phases represents potential motifs in the sulfide-telluride phase diagrams, and grounds for further work on the topic.

6. On the Optimization of Colloidal Zn$_3$N$_2$ Nanoparticle Synthesis

6.1. Introduction and Inspiration

Interest in semiconductor nanoparticles as functional materials has drastically increases in recent decades, reaching a milestone in 2023, with the Nobel Prize in chemistry being awarded for the discovery of quantum dots and its synthesis.[211] The size-tunable properties of these materials make them highly adaptable, which now sees them used in a wide range of applications, including displays and LEDs,[212,213] solar panels,[214] biomedical applications[215,216] and many more.[217–221]

Unfortunately, current day technology employs nanoparticles based on environmentally harmful elements such as cadmium, as well as expensive and technology critical elements such as indium.[220–222] The latter example, indium, is commercially utilized as InP in Samsung QD-LED screens.[223] As such there is an interest in finding replacements for the current technology using environmentally friendly, cheap and abundant elements.

A prime candidate for such a replacement is Zn$_3$N$_2$. This compound has, for instance, previously been identified as a viable nontoxic alternative for QD LED displays.[224] Zn$_3$N$_2$ is a direct, small-gap semiconductor. The width of the bulk band gap is somewhat uncertain, with a range of values ranging from $1-3.2$ eV being reported in the literature.[225–227] It is worth noting that the upper boundary of this range coincides closely with the bulk band gap of ZnO of 3.37 eV.[228] Zn$_3$N$_2$ is relatively difficult to work with, as it is prone to oxidation on any contact with oxygen in air or water.[229] Critically, this oxidation is not self-limiting and results in complete oxidation if exposure continues for too long.[230]

In 2014, Taylor et al. published a paper detailing a new approach to synthesis of zinc nitride nanoparticles with tunable particle size (D = 2.1-7.1 nm) and optical properties in the visible range (λ = 585-1073 nm), by injection of diethylzinc into a mixture of 1-octadecene and oleylamine under ammonia gas flow.[231] On inspecting their results, a number of points for improvements were identified.

The primary point of note was the colloidal hot-injection methodology Taylor et al. employed to tune the size of the product nanoparticles. This was achieved by repeated swift injections of diethylzinc into the emulsion and progressively grow the nanoparticles larger, until the desired nanoparticle size fraction was obtained. In the reported results, the photoluminescence emission spectra exhibit comparatively very wide full-width half maximum (FWHM) values of 117 nm,

163 nm and 282 nm for peak emission wavelengths corresponding roughly to yellow (585 nm), deep red – to infrared (752 nm) and infrared (1073 nm), respectively. Along with the TEM images provided, the results suggest a significant degree of polydispersity in the obtained nanoparticles. Similar broad FWHM are also observed in a later study by Ahumada et al. (with Taylor among the authors) on the fundamental optical properties of Zn_3N_2 nanoparticles, using the same methodology.[226] We identified the repeated injections as a likely cause of the polydispersity, as this would cause multiple nucleation events.

As such, we aimed to reduce the polydispersity of the Zn_3N_2 nanoparticles by using only a single injection for the synthesis, and rather tune the nanoparticle size by adjusting the reaction temperature of the synthesis. In this approach, only a singular instance of nucleation conditions occurs during the synthesis, which give more control on the nucleation step relative to the growth period for all the nanoparticles, and thus reduce the polydispersity. Further, by using dilute diethylzinc, rather than pure, the heat evolution from the reaction of diethylzinc with ammonia, as well as premature reaction of diethylzinc with ammonia prior to dispersion in the solvent mixture would be braked down, improving control of the reaction.

6.2. Methodology

6.2.1. Chemicals

1-octadecene (Synthesis Grade, Sigma-Aldrich), oleylamine (70% Technical grade, Sigma-Aldrich), diethylzinc ($\geq$ 52 wt.% Zn basis, Sigma-Aldrich), hexane (95% HPLC Plus, Sigma-Aldrich) and isobutyronitrile (99%, Sigma-Aldrich) were obtained from Merck. Due to the oxygen sensitivity of both the precursor and the product, all solvents were degassed by the freeze-pump-thaw (FPT) method, carrying out as many FPT cycles as necessary for bubbling during the thawing process to stop. The prepared solvents were then stored in an MBraun glove box operated in Ar (O_2 < 0.1 ppm; H_2O < 0.1 ppm). Ar ($\geq$ 99.999%) and ammonia (NH_3) ($\geq$ 99.999%, Water Free) were obtained from Nippon Gases and used as received.

6.2.2. Synthesis Procedure – Equipment and Preparation

Prior to the start of a synthesis, all glassware and other equipment that would be exposed to the reactant or solvents, except needles, were dried at 150°C in a heating cabinet, before being

moved into the MBraun glove box. The equipment was then left in the glove box overnight to allow any remnant humidity to desorb.

The diethylzinc solution is prepared inside the glove box by first inserting 1 mL of 1-octadecene into a 50 mL round bottom flask with a magnetic stir bar (Figure 22i). Then, 0.5 mL of diethylzinc is drawn out by syringe from the bulk storage and inserted into the same round bottom flask. An unpenetrated silicone septum is used to seal the round bottom flask. The diethylzinc solution was kept in the glove box until directly prior to injection. (Certain earlier syntheses were carried out with a 1:4 ratio between diethylzinc and 1-octadecene.)
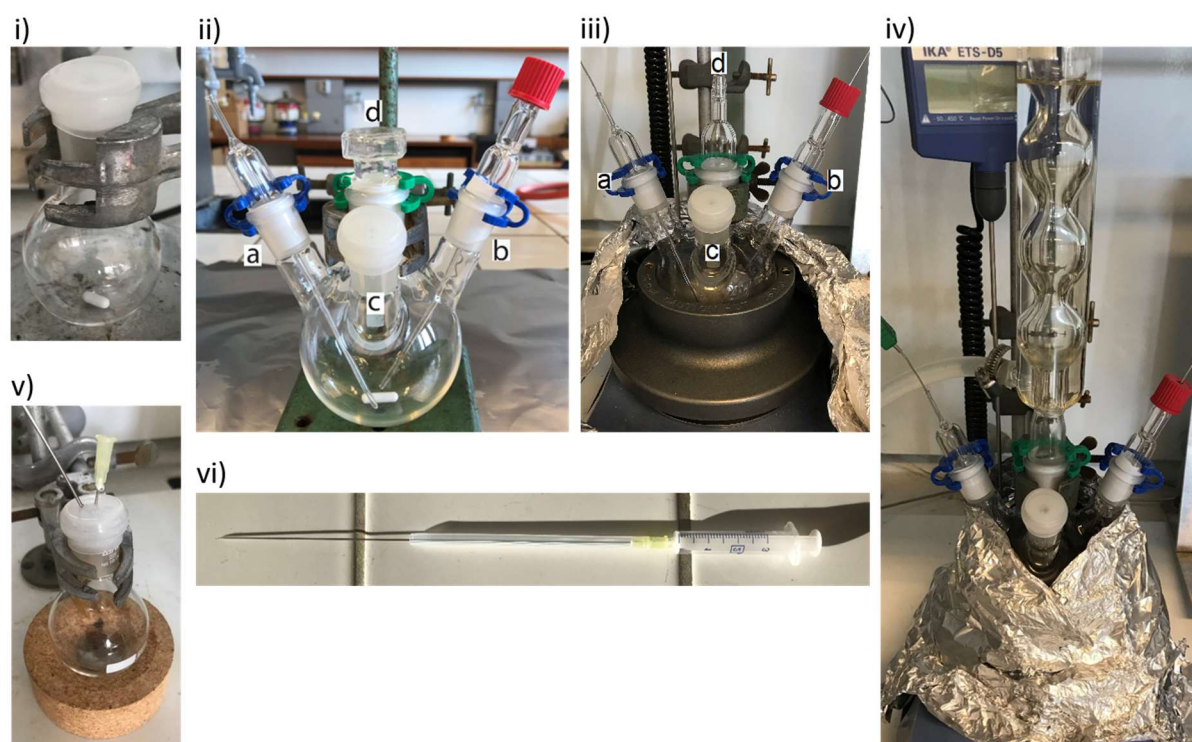
Figure 22: i) Round flask for diethylzinc; ii) four-neck synthesis flask as arranged when removed from the MBraun glove box operated in Ar, sans the solvent mixture; iii) four-neck synthesis flask prepared for removal of water; iv) synthesis setup equipped with the 400 mm water cooled condenser and wrapped in an aluminum foil; v) Ar- flushing round flask. The left needle is for in-flow and the right needle is for out-flow, vi) injection needle with a cut sleeve to act as a spacer.

The main synthesis setup, sans the condenser column, was assembled in the glove box to ensure no air pockets within the system. A magnetic stir bar, 30 mL of 1-octadecene and 1 mL of oleylamine was added to a four-necked 250 mL round-bottom flask (Figure 22ii). Each neck of this round-bottom flask was connected to, respectively: a glass liner for the thermocouple (glass thickness of 1 mm) (a, Figure 22ii), a glass tube for bubbling gas into the solvent mixture (b,

Figure 22ii), a silicone septum (c, Figure 22ii), and a regular glass stopper in the neck for the condenser column (d, Figure 22ii). Each glass joint was lined with Teflon tape. The gas bubbler tube (b, Figure 22ii) was sealed with a screw cap, with a penetrable septum.

Once sealed, the four-neck flask was removed from the glove box and placed in a heating block mounted on an IKA® RCT basic hotplate in a fume hood located in the main laboratory. A needle connected to the (Ar and NH_3) gas supply was penetrated through the gas bubbler septum (neck b, Figure 22ii) to maintain an Ar overpressure within the synthesis environment. A second needle was inserted through the silicone septum (neck c, Figure 22ii) to release excessive overpressure during this step. A K-type thermocouple was inserted into the designated glass sleeve (neck a, Figure 22ii), and connected to a FLUKE 54 II B digital thermometer.

Under a high Ar flow, the glass stopper (neck d, Figure 22ii) was removed, and a narrow-necked hose adapter plug was set in place and left open (Figure 22iii). This plug was needed for water removal in the synthesis, prior to the attachment of the 400 mm water cooled condenser column. The purpose of the adapter plug is to narrow down the opening where Ar flows out. This increases the rate of flow of Ar through the opening, preventing inflow of air, without necessitating an increased volume of exchanged gas. With the hose adaptor plug in place, the needles for equilibrating pressure were removed (neck c, Figure 22iii).

Separately, a syringe for Zn-precursor injection was prepared by repeatedly flushing it with Ar, and then leaving it with the needle inserted into an Ar flushing bottle; see Figure 22v. The Ar flushing bottle has a constant Ar flow, with the in-flow of gas at a sufficient rate to keep an overpressure in the flask relative to atmospheric conditions, ensuring no oxygen or humidity passes into the syringes until they were needed.

6.2.3. Synthesis Procedure – Synthesis

The synthesis procedure is based on the standard hot-injection approach. Maintaining a high flow of Ar, the stir bar was turned on, with a speed of 400 revolutions per minute (rpm). The solvent mixture is heated to 150°C and left at this temperature for 30 minutes to remove any potential remnants of water. Then the gas flow is increased, while the narrow tube adapter is removed (neck a, Figure 22iii), and the condenser column is put in place (neck a, Figure 22iv). The upper end of the condenser column is attached to a gas bubbler to maintain a slight overpressure in the synthesis system, and for visual inspection of the gas flow. With the column in place on the four-neck round bottom flask, the system is flushed with high flow of Ar for

another 15 minutes to clear out air and moisture from the condenser column. The water cooling of the condenser column is then turned on, the Ar flow is turned off, and a 5 standard cubic centimeters per minute (sccm) flow of NH_3 gas is bubbled through the solvent mixture. The four-neck round bottom flask was subsequently covered in aluminum foil to insulate the system (Figure 22iv), and finally the temperature was increased and stabilized at the target temperature for the synthesis.

Once the targeted synthesis temperature was attained, the diethylzinc solution was retrieved from the glove box to prepare for injection. It was placed on a magnetic stirring plate under constant stirring at an arbitrary rpm. The previously prepared syringe to be used was first filled with about 2 mL Ar from the Ar flushing bottle (Figure 22v). Then, while the needle was directly above the diethylzinc round flask (Figure 22i), about half of that volume was continuously expelled, while inserting the needle through the septum. Then, the remaining 1 mL Ar was expelled inside the round flask to create a small overpressure of Ar. In the next step, 0.5 mL of the diluted diethylzinc was drawn into the syringe, followed by a small quantity of Ar to fill the needle itself and form an inert buffer between the air and the diluted diethylzinc.

The diethylzinc was then injected into the four-neck reaction flask (Figure 22iv) in one rapid go. A cut needle sleeve was used as a spacer (Figure 22vi) to ensure the needle was at a constant position between different syntheses. The reaction was kept at the pre-fixed reaction temperature for 20 minutes after the injection before the hotplate was turned off, the aluminum insulation was removed, and the NH_3 gas flow was stopped and replaced with 15 sccm of Ar. In this configuration, the reaction mixture was allowed to cool to room temperature.

Once cooled, the condenser column is removed, and the four-neck round-bottom flask is stoppered under high Ar flow (with a needle to equilibrate overpressure) and moved into the MBraun glove box. Needles through the septum were used to equilibrate the pressure inside the round-bottom flask during flushing of the antechamber.

The suspensions were then bottled for long-term storage inside the MBraun glove box. The product was found to be stable in an inert atmosphere, remaining visually unchanged for more than half a year.

6.2.4. Washing Procedure

During the washing procedure, all handling of solvents and the unsealed sample took place within the MBraun glove box. The sample was sealed and moved outside the glove box for each centrifugation run, but never exposed to ambient conditions.

The washing procedure took place in four steps. First, the raw reaction mixture was centrifuged in a (VWR® 15 ml, 12500g, Conical-bottom, PP) centrifuge tube at 9500 rpm for 10 minutes to expel larger impurities. Second, 1 mL of the reaction mixture was added to an identical centrifuge tube with an inserted glass liner, and mixed with 1 mL of isobutyronitrile, before centrifuging at 9500 rpm for 5 minutes. Third, the resulting sediment was re-dispersed in 1 mL of hexane, before adding 1 mL of isobutyronitrile, and centrifuging at 9500 rpm for 5 minutes. The fourth step is a repeat of the third.

It is important to note that isobutyronitrile, and especially a mixture of hexane and isobutyronitrile, will swiftly leach material from plastic equipment. Glass, or glass lined equipment is a necessity to avoid contamination of the suspension.

The washing solvents need to be extensively dried using molecular sieves. If they are not completely dry, the nanoparticles will be severely damaged during the washing procedure.

6.2.5. Characterization

There were four different approaches utilized in the attempt to characterize the nanoparticles: UV-fluorescence spectroscopy, X-ray diffraction (XRD), scanning electron microscopy (SEM) in transmission imaging mode, and scanning transmission electron microscopy (STEM).

The initial characterization attempts were made with XRD. Two different XRD instruments and several approaches were attempted to obtain XRD data on the particles. Initially, a Bruker D8-A25 instrument with a Ge(111) Johanssen monochromator for selection of Cu$K\alpha_1$ X-rays and a Lynxeye detector was utilized for capillary XRD measurements. As the sensitivity of the particles were a known variable, it was initially attempted to carry out XRD directly on the product suspension, stored in a capillary which was sealed against the atmosphere with putty. This failed, as the concentration of the nanoparticles was too low to obtain any significant signal, even with the largest capillaries available (2 mm diameter). Subsequent attempts tried to improve the same approach by increasing the concentration of nanoparticles by a single

flocculation with ethanol, and redispersing the particles with a minimal quantity of hexane, but this too failed, resulting in practically zero signal.

For other attempts, a Bruker D8 Discover instrument with a Bragg-Brentano geometry and a Ge(111) Johanssen monochromator, Cu$K\alpha_1$ X-rays, and Lynxeye detector was employed. Samples were prepared within the MBraun glove box by the washing procedure described above, with the final hexane dispersion being deposited on a zero-background-oriented silicon XRD sample plate, and left to dry. This process was repeated until a suitable quantity of nanoparticles were deposited on the plate. The sample was then covered with Kapton® tape to protect it from exposure to ambient conditions before being moved from the glove box to the instrument. This approach failed, as any potential signal from the nanoparticles failed to stand out from the background. A third approach, employing transmission XRD through a sample held in place by two layers of Kapton® tape again failed with no discernable signal.

Characterization by SEM imaging was carried out with a Hitachi SU8230 field emission scanning electron microscope in transmission imaging mode with an acceleration voltage of 25 kV, utilizing TEM grids of holey carbon film supported on copper 300 square mesh. Washed nanoparticles were prepared by applying a single drop of the hexane suspension to a TEM grid, which was subsequently left to dry in the MBraun glove box. The dry TEM grid was mounted on a holder and placed in a plastic box with a lid to maintain inert atmosphere for transport to the SEM. Outside the glove box, the sample holder was directly moved from the box to the SEM instrument.

UV-fluorescence spectroscopy was carried out using a 385 nm UV-source, and a FLAME-S-XR1 spectrometer. Shorter wavelengths were attempted on certain samples, but this failed to yield more useful data. The incident UV-source and the detector were arranged at a 90° angle to each other. The measurements were carried out directly on the product of the synthesis suspensions, except that the larger impurities had been removed by the initial step of the washing procedure. A suitable quantity of the suspension was transferred to a dried glass sample holder and sealed with an air-tight cap, before the sample was removed from the glove box.

STEM characterization was carried out using a FEI Titan G2 60-300 kV equipped with a CEOS DCOR probe-corrector and Super-X-EDS detectors. The FEG electron source was operating at an acceleration voltage of 300 kV. The images were obtained using a high-angle annular dark field (HAADF), bright-field (BF) and dark-field (DF4) detectors. To ensure inert conditions during transport of the sample between the argon glove box and the STEM instrument, a Gatan

Double Tilt Vacuum Transfer Holder (Model 648) was used. The samples were otherwise prepared in the same manner as for the SEM.

6.3. Results

The goal of the current study was to develop the Tayler et al.[231] colloidal synthesis route for Zn_3N_2 nanoparticle synthesis. We aimed to document that a narrower nanoparticle size distribution could be obtained by tuning the nanoparticle size with manipulation of the reaction temperature and concentration of the reactants rather than number of diethylzinc injections. The work was unfortunately halted during the experimental period due to unviability of the key reactant, diethylzinc. A replacement could not be obtained as the waiting time from ordering turned out to be more than a full year due to repeated delays from supplier. Based on this, solely the initial experiments were completed. These are listed in Table 1 along with the resulting product characteristics.

Table 4: Overview of the colloidal Zn_3N_2 nanoparticle syntheses carried out, with associated ID, synthesis conditions, purpose of the experiment, photo luminescence (PL) color and other notes. For syntheses ID 1-8, 29 mL 1-octadecene and 1 mL oleylamine was used. Syntheses ID 9 and later used 30 mL 1-octadecene and 1 mL oleylamine. The NH_3 flow for all syntheses was 5 sccm. Undiluted NH_3 was used, there was no flow of Ar during the injection step.

ID	Concentration (Per Volume) (diethylzinc:1-octadecene)	Injection Volume (mL)	Reaction Temperature	Purpose	PL Color	Notes
	Initial tests for optimizing the experimental procedure					
1	1:4	0.5	229°C	Concentration Test	Blue-Green	
2	1:2	0.5	225°C	Concentration Test + Temperature Test	Yellow	Photo in Figure 23
						SEM imaging
3	1:2	0.5	240°C	Temperature Test	Orange	Photo in Figure 23
						Sample preparation testing (XRD/SEM)
						SEM imaging

4	1:2	0.5	210°C	Temperature Test	Indistinguishable from the UV source	Photo in Figure 23
5	1:2	0.5	250°C	Temperature Test	Orange	Sample preparation testing
6	1:2	0.5	200°C	Temperature Test	Indistinguishable from the UV source	
7	1:2	0.3	225°C	Injection Quantity Test	Indistinguishable from the UV source	
8	1:1	0.4	225°C	Concentration Test	Darker Orange	Very vigorous reaction
Optimized synthesis conditions (according to description in Experimental)						
9	1:2	0.6	225°C	Injection Quantity Test	Orange	UV-VIS
10	1:2	0.6	225°C	Replicate	Orange	UV-VIS Outlier: Exceptionally narrow FWHM
11	1:2	0.6	225°C	Replicate	Yellow	Failed Injection; Faulty Needle
Completely Reproducible Synthesis						
12	1:2	0.6	225°C	Replicate	Orange	UV-VIS
13	1:2	0.6	225°C	Replicate	Orange	UV-VIS

The initial eight syntheses (ID 1-8) were carried out to establish best practices and approaches for the synthesis procedure, as well as initial observations on the effect of varying the synthesis parameters. Syntheses IDs 2-6 were focused on determining the effect of varying the reaction temperature, and establishing the limits of how far the temperature could be varied, while still producing useful products. Syntheses IDs 1, 2 and 8 were intended to investigate the effects of varying the concentration of diethylzinc, while ID 7 and ID 9 were intended to investigate the effects of varying the injection quantity. Synthesis ID 3 and ID 5 were also the batches used to test washing procedures, SEM imaging and XRD approaches.

Starting from synthesis ID 9, the synthesis setup was fully established, and the goal shifted to targeting highly reproducible syntheses. Starting from synthesis ID 12, this objective was

achieved. Sans the failed synthesis ID 11, the products of these four syntheses were all characterized by fluorescence spectroscopy, which is further discussed later. From the few experiments carried out, we still can extract some initial key findings useful for further work. In the following we will elaborate on the key findings.

1. Role of tuning the reaction temperature, keeping all other synthesis parameters fixed.

The experiments show that controlling the nanoparticle size by adjusting the reaction temperature, while keeping all other factors constant, is indeed possible. The nanoparticle size increases with increasing reaction temperature, and vice versa. This is seen in the change in the fluorescent color of the product nanoparticles (Figure 23). The redder color corresponds to a longer wavelength of light emitted, which directly correlates with the nanoparticles being larger, as this effect is a consequence of quantum confinement: The diameter of the physical particle confines the wave function, such that the smaller the particle, the greater the energy gap responsible for the emitted color becomes, which directly correlates with a shift towards colors with shorter wavelengths. By the observed trend, one would expect the smallest particles corresponding to the blue colors at temperatures below 225°C.
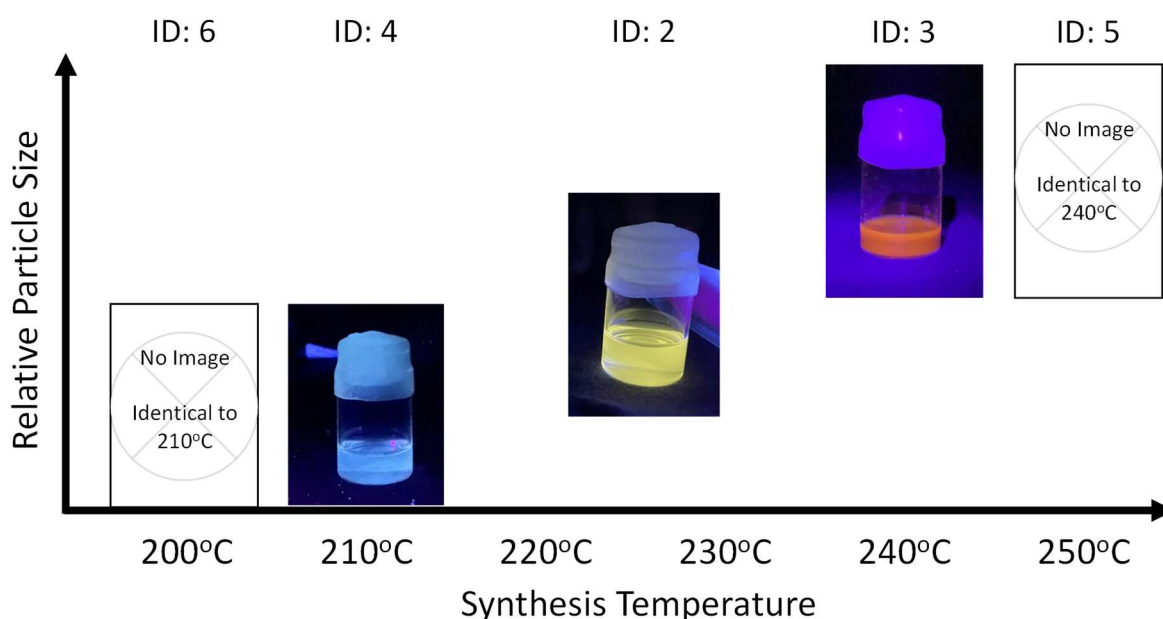

Figure 23: Variation in visible fluorescence of Zn_3N_2 nanoparticles when varying the reaction temperature in the range from 200 to 250°C whereof all other parameters were constant (see Table 1). The synthesis at 210°C does not fluoresce properly, but rather scatters and broadens incident UV light. The synthesis at 250°C was visually identical to the 240°C product.

However, the temperature-variation approach has certain limitations: Reducing the reaction temperature to obtain smaller nanoparticles has a hard limit for how far you can go. The exact temperature limit is not determined in this study, but at 210°C and below, the nitride nanoparticles do not form, or at least, do not fluoresce properly. This is visually observed as the product of the synthesis exhibiting a pale yellow color under regular light. Under UV light, the reaction mixture does not exhibit a single color characteristic color like the nitride nanoparticles, but rather varies with the UV source. Measured under fluorescence spectroscopy, one observes that the product of these low-temperature syntheses (200°C and 210°C) rather scatters and broadens incident UV light, as opposed to emitting a characteristic color. Shorter wavelengths of UV was attempted with these samples, in case the wavelength used for other measurements was insufficient, but this yielded the same outcome. Synthesis at 240°C and 250°C give products with visually indistinguishable fluorescent color, showing a practical ceiling to the available temperature range for tuning the synthesis. It should be noted that these upper and lower limits have only been studied for the 1:2 precursor:solvent concentration. How the change in the precursor concentration affects these limits is a matter for further work.

2. Role of tuning the quantity of injected precursor.

Another variable that was tested, was the volume of injected precursor. With reference to synthesis IDs 2, 7 and 9, we noticed the greater the volume of precursor for a given diethylzinc-concentration, the larger the nanoparticles. Equivalent with the temperature variation, a larger injection volume resulted in a product which emitted at longer wavelengths. Injection volume also showed a lower limit for synthesis, where nanoparticles failed to form, resulting in the same UV-scattering product as insufficient temperature produced. A failure to form nanoparticles due to insufficient injection volume was observed in synthesis 7, despite the molar quantity of diethylzinc being greater than synthesis 1, which succeeded.

3. Evaluation on the reproducibility of the synthesis when the procedure was optimized.

Pertaining to the syntheses which are categorized as controlled (ID 9-13), it is emphasized that the synthesis produces highly reproducible results. The fluorescence emission spectra of the four final syntheses (except the failed ID 11) are shown in Figure 24, which show excellent homogeneity in the products, sans the one outlier with a notably narrower FWHM. The peak emission wavelengths, as well as the FWHM of these four syntheses, are given in Table 5. It should be noted that the results show the same shoulder at longer wavelengths as Taylor et al.[231] Whether this is a sign of rod formation or if it is of a different cause, has not been investigated.
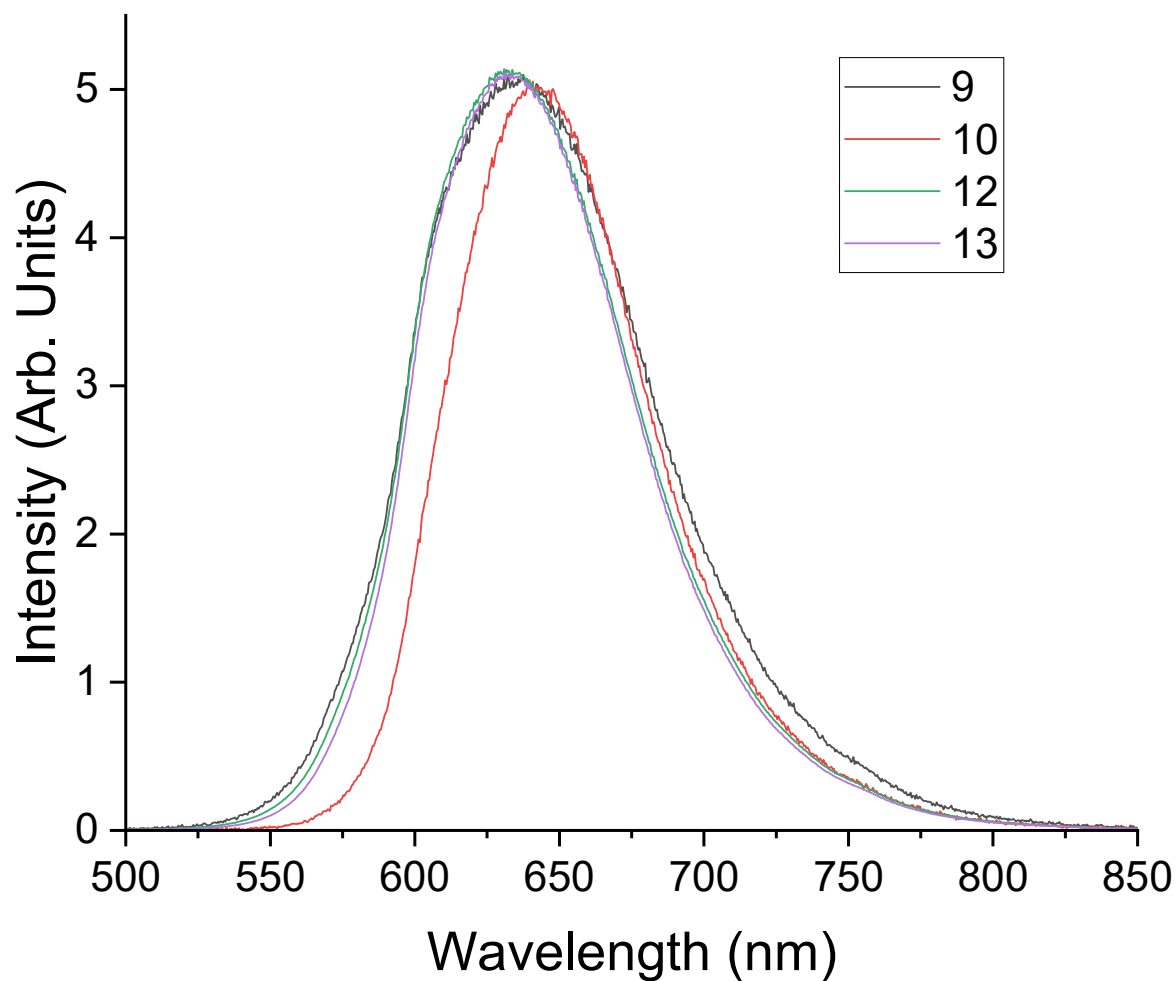
Figure 24: Fluorescence spectroscopy of the four final syntheses (IDs 9, 10, 12 and 13). The legend gives the synthesis ID.

Table 5: Peak Emission Wavelength and FWHM values of the product under optimized synthesis conditions.

Synthesis ID	Peak Emission Wavelength (nm)	FWHM (nm)
9	635.4	94.5
10	642.4	79.5
12	632.1	87.6
13	632.5	85.1

The fluorescence emission wavelength of a given nanoparticle is predominantly decided by its size. As such, the FWHM of the emission may be interpreted as a direct indicator of the size dispersity of the produced nanoparticles; the narrower the FWHM, the less the dispersity.

The quality of the produced nanoparticles, as judged by the FWHM of the fluorescence, are a major improvement over the original procedure of Taylor et al.[231] Comparatively, Taylor et al. reports FWHM values of 117 nm and 163 nm for peak emissions at 585 nm and 752 nm, respectively, while this alternate synthesis approach results in a FWHM of 86 nm for peak emission at 632 nm for the final two syntheses. All four final syntheses give an average FWHM of 87 nm. Interpolating the FWHM of Taylor et al. to the peak emission at 632 nm, this is a reduction of the FWHM by roughly 30%. The outlier, synthesis 10, produced a FWHM of 79.5 nm, a nearly 40% decrease from Taylor, showing that further improvement is possible.

While the particles were damaged by an incomplete washing procedure, TEM images, (Figure 25) along with EDS elemental spectroscopy, were taken of some selected particles of synthesis ID 12. The results showed that, while there were remnants of nitrogen in the particles, the washing procedure had substantially damaged the product. Furthermore, the damaged particles exhibited a tendency to flocculate into larger clusters. These clusters made determining the size of the individual nanoparticles very challenging, with a large degree of uncertainty. We did succeed in obtaining atomic resolution on the images, ascertaining that the particles were indeed crystalline (Figure 25). While the quality of the damaged nanoparticles was insufficient for a detailed analysis of the size distribution, it was still sufficient to make out the general magnitude of the particle sizes. This range was found to be around 3-8 nm, in rough agreement with the particle diameters reported by Taylor et al.[231]
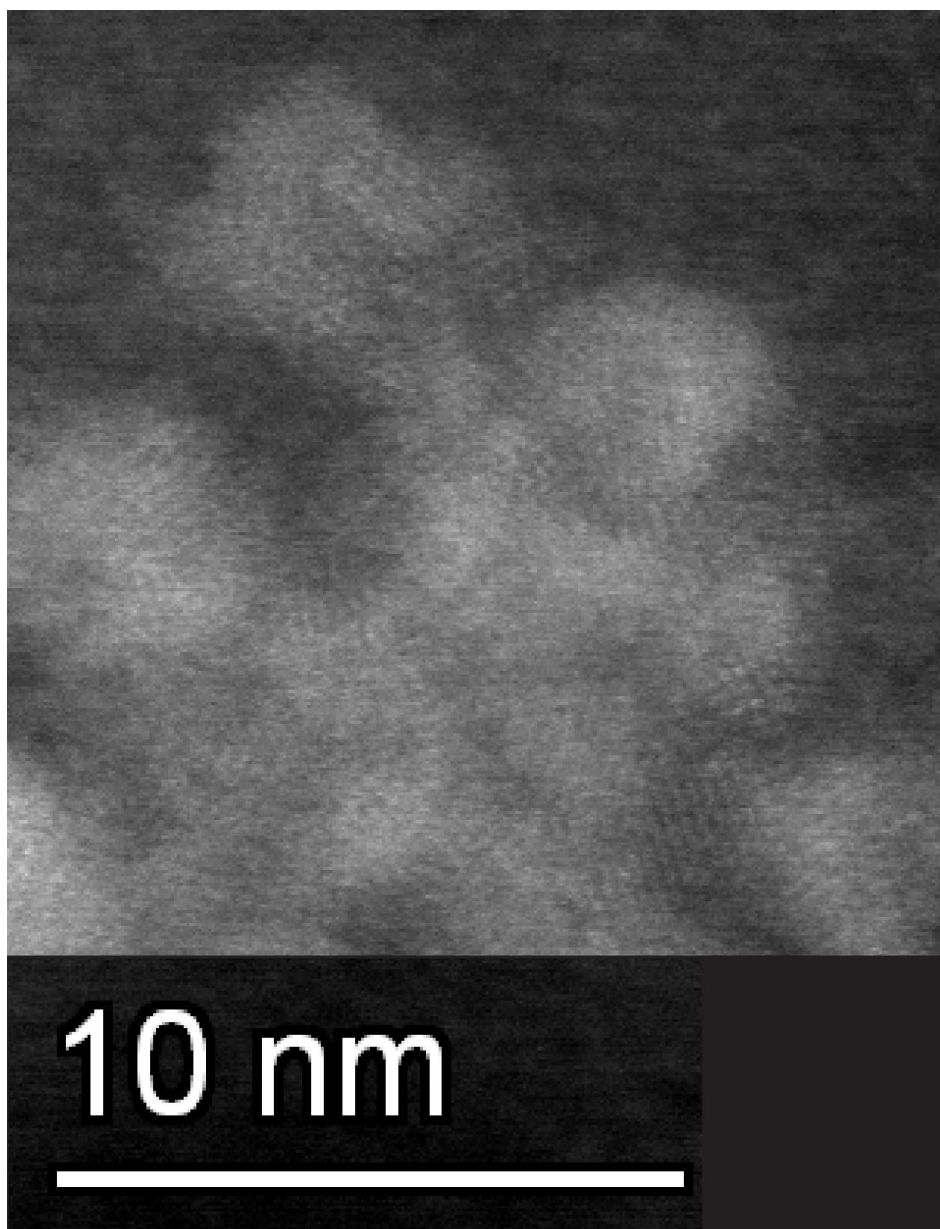
Figure 25: STEM image of a cluster of damaged Zn_3N_2 nanoparticles, showing atomic resolution.

4. Role of lack of inertness in the synthesis apparatus and stability of product in air

In the earlier parts of the work, we did have one instance where the synthesis setup was insufficiently inert (not included in the list of syntheses). The resulting product had a wrong color compared with what we were expecting, along with a murky color and lack transparency that did not occur with the proper syntheses. The most prominent color also corresponded to a

shorter wavelength than expected for the nitride, as one would expect from oxidation damage which is known to increase the band gap, or smaller particle size.

We also carried out a couple of tests on the product to see how it reacted with ambient air and direct water exposure. Adding water to the reaction mixture resulted in immediate destruction of the Zn_3N_2 nanoparticles, converting it into colorless ZnO. Leaving the sample exposed to air resulted in approximately the same outcome, only slower. Over the course of 15 minutes, the originally rust-brown drop of the product suspension gradually turned clear starting from the edges (Figure 26). Notably, the nanoparticles don't change color, their color simply fades in intensity until nothing.
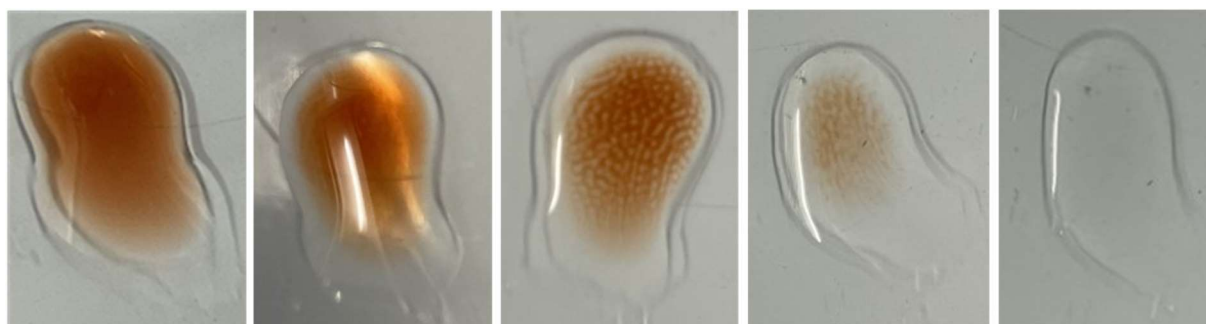

Figure 26: Effect of air exposure on a drop of the product from a synthesis. The destruction of the zinc nitride occurred over the course of about 15 minutes.

6.4. Discussion and Challenges in the Work

The key finding in this project is that the FWHM of the PL peak emission at 632 nm of the Zn_3N_2 nanoparticle product may be significantly reduced by utilizing a single-injection approach rather than multi-injection during the colloidal hot-injection synthesis route. As the FWHM directly correlates with the size distribution of the nanoparticles, the resulting product may be inferred to exhibit significantly more monodisperse particles compared with those of Taylor et al.[231] As an alternative to repeated injections, we tested the effect of altering the reaction temperature of the synthesis to tune the nanoparticle size. Initial results show that this approach is indeed a viable approach, with an increased reaction temperature resulting in larger nanoparticles.

Observing larger nanoparticles when increasing the reaction temperature is opposite of what one would expect from the kinetics of nanoparticle nucleation/growth. We suggest that the reaction is limited by the solubility of ammonia in the 1-octadecene – oleylamine mixture. With increased temperature, the concentration of dissolved ammonia in the solvent decreases, while

simultaneously increasing the rate both at which the reaction proceeds, and the zinc precursor decomposes to nitride monomers. The reaction kinetics for the formation of the product also increases. In effect, the nucleation step proceeds with limited monomers available, resulting in fewer nuclei to form, which grow larger as the ammonia is replenished at a relatively slow rate. The observation also fits the general LaMer explanation, when the supersaturation is decreasing when NH_3 concentration is reduced implying nucleation is suppressed. The formation of fewer nuclei will allow increased particle growth in the next step as the reminding monomers is distributed between fewer nuclei. This view agrees with the work of Taylor et al., who observed that the particle size of the product increased when they decreased the flow of ammonia at constant temperature, and vice versa.

Further, we observed an upper limit to the effect of increasing the temperature. It is possible that once the temperature exceeds a certain threshold, the limiting factor is no longer the solubility of ammonia in the solution. A similar feature was observed in Taylor et al.'s paper,[231] where the upper size limit of the nanoparticles appeared to plateau according to the amount of diethylzinc per injection, independent of the number of injections.

If one wished to construct a synthesis matrix for tuning the size of the zinc nitride nanoparticles, we have four variables to consider: Temperature, NH_3 flow rate, molar quantity of precursor, and precursor concentration. The first three have all been established to control the nanoparticle size; the first and third show a direct correlation with the nanoparticle size while the second has an inverse relation. With three established variables to alter to tune a single characteristic of the product, there is a fair degree of freedom for optimizing the product, while keeping the particle size constant. The effects of the fourth variable, precursor concentration, was not fully established, but reducing the concentration (reducing the ratio of diethylzinc to 1-octadecene) did significantly reduce the vigor of the reaction. This may help to improve the quality of the products, but this has not been properly established.

The one-injection approach is an excellent choice for obtaining monodisperse Zn_3N_2 nanoparticles with highly reproducible results. Further, with several options for tuning the size of the nanoparticles, judicious choice of parameters may allow for a wide range of particle sizes, even while constrained to a single injection of precursor.

The primary challenge throughout this work was ensuring that the synthesis setup was always fully inert at all times. Even trace contaminations (O_2, H_2O) in the steps prior to the diethylzinc

injection step could greatly affect the outcome of the synthesis. As such, every step of the process required extra considerations, to extract all points of failure from the equation.

The same applied for the steps connected to the handling of the produced nanoparticles as they were highly sensitive to both oxygen and water, causing rapid reaction to form colorless ZnO particles. As previously described, even protected by the reaction mixture, the damage was discernable to an observer after a few minutes of exposure.

The final challenge for this project ended up the washing procedure, in attempts to prepare the nanoparticles for TEM imaging, with the purpose to document nanoparticle size, the size distribution within one synthesis batch as well as correct stoichiometry ($Zn:N = 3:2$). Initial attempts tried using ethanol as the washing agent, and hexane as redispersing agent, however it was found that regardless of drying procedure, the zinc nitride nanoparticles would be destroyed by the washing procedure. Ultimately, it was concluded that the ethanol itself had to be reacting with the nanoparticles.

As protic solvents were not suited for the task, the next choice was isobutyronitrile. Unfortunately, the mixture of isobutyronitrile and hexane proved to rapidly dissolve small quantities of plastic from the centrifuge tubes and micropipette tips, contaminating the samples with a non-volatile solution of dissolved plastics. Use of glass pipettes and glass-lined centrifuge tubes eventually solved this issue.

The final issue that prevented TEM imaging is believed to simply be the presence of water in the isobutyronitrile, which would require a drying procedure prior to being used for washing, by for instance molecular sieves.

Throughout this work, the sensitivity of the zinc nitride nanoparticles to oxygen and water, and even protic solvents like ethanol, has thus been the central concern for the synthesis procedure. However, there have been two recent reports of zinc nitride synthesis being carried out in aqueous conditions (from mostly the same authors).[232,233] From our observations through the course of this work, we note that these claims do not agree with our experience on the matter.

6.5. Beyond Zn$_3$N$_2$ – A Wider Point of View

6.5.1. The Zn$_3$N$_2$ Synthesis Procedure in Perspective

When the development of controlled (non-oxide) nanoparticle synthesis started in the 1980's, there were a series of realizations on three critical conditions which could drastically affect the quality of the product: Crystallinity, inert conditions, and particle capping.[234,235]

The challenges of ensuring inert conditions has been extensively discussed previously in the text, and applying the crystallinity condition is simple: improving the crystallinity of the nanoparticles could be attained simply by increasing the synthesis temperature.

The concept of capping the particles is more involved. Nanoparticles, as directly synthesized, often have highly reactive surfaces, which is simultaneously both a useful and problematic characteristic. Increased reactivity is useful while you seek to modify the surface of the particle, but it is deleterious to the stability of the nanoparticle after the conclusion of the synthesis. This reactivity may be quenched by forming a shell structure around the nanoparticle. This may be achieved by growing a layer of a less reactive compound around the core particle, or simply modifying the core surface with a less reactive. Beyond chemical stability, shell structures also allow for tuning the particle properties, reduces surface defects of the core, and numerous other possibilities.[236] In practice, capping for the purpose of passivating the particle surfaces, is utilized in all commercially applied nanoparticles. More complex nanoparticles, again, often intended for commercial applications, may have multiple layers of capping with different compounds, intended to optimize particular properties. An example is the multilayer structure of InP/ZnSe/ZnS nanoparticles utilized in Samsung QLED screens.[223]

The synthesis procedure we employed, utilized the first two principles: Extensive effort was placed into ensuring inert conditions, and the synthesis occurred at a relatively high temperature, promoting higher crystallinity. We did not have the opportunity to attempt different alternatives for capping the nitride nanoparticles, although this could potentially have resulted in a substantial increase in the resilience of the product against oxygenating conditions. If the width of the FWHM we observed for our products was substantially caused by surface defect effects, rather than particle size distribution, proper application of capping could also have reduced the FWHM. Possibilities for capping of the Zn$_3$N$_2$ nanoparticles is discussed in more detail shortly.

To attain further improvement of the basic Zn$_3$N$_2$ nanoparticles with the current fundamental approach, would mainly come down to optimization of parameters. Both general optimizations,

and specific tuning depending on the target particle size is potentially possible, with the number of variable parameters available in this system: Total solvent volume, solvent-to-surfactant ratio, precursor injection volume, ammonia flow rate and synthesis temperature are all potential variables that may potentially be tuned. Carrying out the synthesis within a fully inert environment, rather than moving equipment through ambient conditions could also improve the results.

More sophisticated methods of controlling the growth of colloidal nanoparticles beyond the simple, rapid, hot-injection methodology have been devised through the years. One such example is particle size tuning by constant, slow addition of precursors to a solution at synthesis temperature.[237] The synthesis approach we have utilized could potentially be refined by applying this approach, but this would necessitate the introduction of more complex equipment.

6.5.2. Nanoparticles of Other Nitrides

Nitride nanoparticles at large is not an obscure topic in the literature. Several nitride compounds have received significant attention from the scientific community. However, there is a major imbalance in what compounds receive attention: Nanoparticles of the more stable nitride compounds, such as TiN, Si_3N_4, BN, and especially graphitic carbon nitride, constitute major parts of the total literature by number of associated articles, according to Web of Science. The transition metal nitride nanoparticles specifically have received attention for potential applications in heterogeneous catalysts,[238] biomedical use,[239,240] battery applications[241,242] and more.

Many of the nitrides under typical consideration do not appear to be as heavily constrained by the need for completely inert conditions even after synthesis. The nitrides that receive the greater attention in the literature are, as mentioned previously, also more generally stable. This allows, for instance, synthesis procedures involving precursors such as metal oxide[243] or hydroxide-based compounds,[244] or even direct synthesis of nitride nanoparticles in air.[245] A majority of reported syntheses do occur under inert, reactive nitrogen or ammonia atmospheres, so the presence of oxygen can and often will be problematic during synthesis, but it doesn't seem to be a specifically marked issue in most instances. Do note that this is likely at least in part due to the tendency in scientific literature to only report the final success, with limited mentions of what difficulties were encountered.

6.5.3. Fluorescent Nanoparticles – Comparison of Properties

The final syntheses of this project produced nanoparticles with peak photoluminescent emission at a wavelength of 632 nm, with a FWHM of 86 nm. As previously discussed, these results are a significant improvement over Taylor et al.[231] However, compared with currently commercially utilized nanoparticles, there is a significant difference. The best non-toxic systems available around the same wavelengths, namely InP/ZnSe/ZnS quantum dots, exhibit emission FWHM of about 35 nanometers.[223] The results obtained in this our work is thus still far from the commercial standard, although this is to be expected; the experimental synthesis procedure is still rough, relatively speaking. And again, these InP nanoparticles are developed, and utilized by Samsung,[223] meaning the resources available for development greatly exceeds ours.

The main advantage of this work is rather the materials involved. Current commercial quantum dots rely in large part on toxic elements, cadmium in particular has remained a part of the cutting edge for decades, as well as scarce elements such as indium.[221] If these could be exchanged for the cheap, abundant, non-toxic and environmentally friendly combination of zinc and nitrogen, it would reduce the harmful impacts of growing utilization of quantum dot technologies. The possibility of tuning the particles for the full human visual range is also very useful, as the nitrides could potentially be used for any light-emission application for human purposes.

6.5.4. The Path Forwards – Core-Shell Structures and Multianion Nanoparticles

An obvious path forwards for the zinc nitride nanoparticles, when aiming for functional properties, would be the addition of one or more layers of other compounds around the main Zn_3N_2 nanoparticle. This is, as implied in the previous section, a common approach to the optimization of nanoparticle properties. This principle could be applied for the improvement of the properties of the Zn_3N_2 nanoparticles as well. Beyond optimization of the basic properties, the shell would serve a critical purpose in protecting the zinc nitride core from reacting with ambient conditions, making them more reasonably applicable in commercial products.

The possible choices for the shell immediately adjacent to the zinc nitride are likely quite limited. Oxides are unusable, as the synthesis process would undoubtedly destroy the nitride. The nitride being generally unstable, most anions in reactive synthesis conditions would also likely replace the nitrogen. As such, it is difficult to suggest any compounds apart from other nitrides as potentially suitable candidates. Unfortunately, many of these have unsuitable

properties for synthesis in similar conditions to the zinc nitride; devising a synthesis procedure which allows the formation of a nitride shell layer without damaging the zinc nitride core would likely be challenging. The air-stable, wide band gap nitrides which could serve as a protective outer layer for an optically active core, Si_3N_4, BN and GaN, often require synthesis temperatures of 1000 °C or higher by conventional approaches, which is unattainable in this case.[246–248] There are, however, reports of both Si_3N_4 and GaN being formed at much lower temperatures, including the range available to the Zn_3N_2 synthesis setup.[249,250] As such, it is possible that devising a suitable approach for capping Zn_3N_2 with one of these highly stable nitrides is achievable.

For active shell structures, intended to interact with the core and modify its properties rather than just shield it, there are a couple of options that may have potential. Synthesis of one of the iron nitrides, for example, has been reported with annealing at the relatively low temperature of 300 °C.[251] As such, this compound may potentially form within similar synthesis conditions to what we have utilized in this project, which could allow for direct of a core-shell structure in one synthesis. The practical viability would also hinge on whether there exists a suitable precursor, which is both sufficiently reactive, and won't harm the Zn_3N_2 with side products.

One of the initial goals for this nanoparticle synthesis project was to establish a synthesis procedure for nanoparticles of the multianion Zn_2NF phases. This was the original link between the two thematically isolated aspects of this Ph.D. work; the synthesis of the nitride was intended as an initial step for testing, verifying and improving the inert synthesis conditions prior to the introduction of fluoride anions into the synthesis.

The possibilities of multianion chemistry have gained attention in recent years, and as the field gained traction, increased efforts were devoted to the branching possibilities of multianion materials, beyond the properties of simple bulk materials. These efforts have seen nanoparticle development in the more actively investigated multianion phases such as certain oxysulfides,[252] but for the less developed multianion fields such as the nitride-fluorides, work remains entirely within the range of bulk materials.

A major advantage of the hypothetical Zn_2NF nanoparticles over the pure nitride would have been expected to be an increase in stability of the compound. Zn_3N_2, as extensively observed through this work, is highly sensitive to air and water in ambient conditions. It is thus difficult to work with, complicating production and limiting the potential applications. Zn_2NF, as indicated by previous reports, is significantly more stable, and does not appear to react swiftly

with water. Combined with a favorable alignment of the energy gap edges relative to water, it has been tested as a photocatalytic agent for water splitting.[253]

Zn_2NF is an aliovalent substitution of the ZnO composition, which also forms a range of compositions of the form $ZnO_{1-x-y}N_xF_y$ ($0 \leq x, y \leq 0.5$). If the proportion of oxygen is about 0.2 or greater substituted from fluorine, the compound assumes the hexagonal crystal structure of ZnO.[253] Below this oxygen content, the compound may assume two forms, α- or β-, corresponding to the low- and high-temperature structures, respectively. These forms are orthorhombic ($P2_12_12_1$ No. 19) and tetragonal ($P4_12_12$ No. 92), again respectively. Interestingly, both forms assume enantiomorphic crystal structures, exhibiting anionic superstructures. Based on an enantiomorphic crystal structure, Zn_2NF nanoparticles could potentially exhibit properties such as nonlinear optics, or different biological activity between each handed form, but this is purely hypothetical at the current stage. A range of zinc nitride-halides have been reported to exist; these compounds could also potentially be considered for multianion nanoparticle synthesis by an approach similar to what we have employed here.[254]

An anticipated difficulty with nanoparticles in the $Zn - N - F$ system, is the number of different potential phases that may form. There are three different compounds in the system which are currently known, with two of them having at least two possible crystal structures. In addition to the nanoparticle size, the synthesis procedure would also require tuning to minimize the quantity of secondary phases forming, which could potentially prove to be a greatly complicating factor, beyond the initial challenge of forming nitride-fluorides in the first place.

6.6. Conclusion and Outlook

We have synthesized zinc nitride nanoparticles by a hot-injection methodology utilizing a single injection of the diethylzinc precursor, rather than the multiple previously employed. The obtained nanoparticles were found to fluoresce with a substantially reduced FWHM compared with the multi-injection approach, and the resulting nanoparticle product were found to be highly reproducible. A cursory investigation into the effects of precursor quantity and temperature indicated that the particle size could be adjusted with either parameter, but the project was interrupted before a proper range of syntheses and replicates could be carried out.

There are a lot of potential avenues to explore off the initial findings in this work. In addition to completing the work which was interrupted in this study, the full synthesis matrix requires further investigation to identify the optimal synthesis conditions. As the outlier synthesis (ID10)

showed, there is still room for major improvement of the synthesis conditions. Potential further work, beyond the parameters of just nitride synthesis, could include the introduction of other reactive gasses in addition to ammonia, to attempt to form multianion nanoparticles, or multi-step syntheses, to form a protective shell around the reactive zinc nitride nanoparticles with a more inert substance. These directions would have been the natural next steps in this project, if we had not encountered so many challenges.

7. References

(1) Yadav, G.; Ahmaruzzaman, Md. Multi Anion-Based Materials: Synthesis and Catalytic Applications. *Mater. Res. Bull.* **2022**, *152*, 111836. https://doi.org/10.1016/j.materresbull.2022.111836.

(2) Zhao, C.-X.; Wang, H.-F.; Li, B.-Q.; Zhang, Q. Multianion Transition Metal Compounds: Synthesis, Regulation, and Electrocatalytic Applications. *Acc. Mater. Res.* **2021**, *2* (11), 1082–1092. https://doi.org/10.1021/accountsmr.1c00136.

(3) Zulkiflee, A.; Khan, M. M.; Harunsani, M. H. Bismuth Oxyhalides: Recent Progress and Its Applications in Photocatalysis, Hydrogen Production, Antibacterial Studies, and Sensors. *Mater. Sci. Semicond. Process.* **2023**, *163*, 107547. https://doi.org/10.1016/j.mssp.2023.107547.

(4) Wu, G.; Xie, Y. L.; Chen, H.; Zhong, M.; Liu, R. H.; Shi, B. C.; Li, Q. J.; Wang, X. F.; Wu, T.; Yan, Y. J.; Ying, J. J.; Chen, X. H. Superconductivity at 56 K in Samarium-Doped SrFeAsF. *J. Phys. Condens. Matter* **2009**, *21* (14), 142203. https://doi.org/10.1088/0953-8984/21/14/142203.

(5) Pérez-Vicente, C.; Alcántara, R. New Perspectives on the Multianion Approach to Adapt Electrode Materials for Lithium and Post-Lithium Batteries. *Phys Chem Chem Phys* **2023**, *25* (23), 15600–15623. https://doi.org/10.1039/D2CP06044B.

(6) Wang, Q.; Sarkar, A.; Wang, D.; Velasco, L.; Azmi, R.; Bhattacharya, S. S.; Bergfeldt, T.; Düvel, A.; Heitjans, P.; Brezesinski, T.; Hahn, H.; Breitung, B. Multi-Anionic and -Cationic Compounds: New High Entropy Materials for Advanced Li-Ion Batteries. *Energy Env. Sci* **2019**, *12* (8), 2433–2442. https://doi.org/10.1039/C9EE00368A.

(7) Hirai, T.; Orikoshi, T. Preparation of Yttrium Oxysulfide Phosphor Nanoparticles with Infrared-to-Green and -Blue Upconversion Emission Using an Emulsion Liquid Membrane System. *J. Colloid Interface Sci.* **2004**, *273* (2), 470–477. https://doi.org/10.1016/j.jcis.2003.12.013.

(8) Popovici, E.-J.; Muresan, L.; Hristea-Simoc, A.; Indrea, E.; Vasilescu, M.; Nazarov, M.; Jeon, D. Y. Synthesis and Characterisation of Rare Earth Oxysulphide Phosphors. I. Studies on the Preparation of Gd_2O_2S:Tb Phosphor by the Flux Method. *Opt. Mater.* **2004**, *27* (3), 559–565. https://doi.org/10.1016/j.optmat.2004.07.006.

(9) Lo, C.-L.; Duh, J.-G.; Chiou, B.-S.; Peng, C.-C.; Ozawa, L. Synthesis of Eu^{3+}-Activated Yttrium Oxysulfide Red Phosphor by Flux Fusion Method. *Mater. Chem. Phys.* **2001**, *71* (2), 179–189. https://doi.org/10.1016/S0254-0584(01)00279-6.

(10) Lei, B.; Liu, Y.; Tang, G.; Ye, Z.; Shi, C. Spectra and Long-Lasting Properties of Sm^{3+}-Doped Yttrium Oxysulfide Phosphor. *Mater. Chem. Phys.* **2004**, *87* (1), 227–232. https://doi.org/10.1016/j.matchemphys.2004.06.002.

(11) Chen, X.; Ok, K. M. Metal Oxyhalides: An Emerging Family of Nonlinear Optical Materials. *Chem Sci* **2022**, *13* (14), 3942–3956. https://doi.org/10.1039/D1SC07121A.

(12) Kageyama, H.; Hayashi, K.; Maeda, K.; Attfield, J. P.; Hiroi, Z.; Rondinelli, J. M.; Poeppelmeier, K. R. Expanding Frontiers in Materials Chemistry and Physics with Multiple Anions. *Nat. Commun.* **2018**, *9* (1), 772. https://doi.org/10.1038/s41467-018-02838-4.

(13) Barbier, J. Refinement of the Eulytide-Type $Pb_4(PO_4)_2SO_4$ Structure. *Eur. J. Solid State Inorg. Chem.* **1994**, *31*, 163–171.

(14) Chen, H.; Hautier, G.; Ceder, G. Synthesis, Computed Stability, and Crystal Structure of a New Family of Inorganic Compounds: Carbonophosphates. *J. Am. Chem. Soc.* **2012**, *134* (48), 19619–19627. https://doi.org/10.1021/ja3040834.

(15) Graf, C.; Assoud, A.; Mayasree, O.; Kleinke, H. Solid State Polyselenides and Polytellurides: A Large Variety of Se–Se and Te–Te Interactions. *Molecules* **2009**, *14* (9), 3115–3131. https://doi.org/10.3390/molecules14093115.

(16)   Herz, W. Über Wismutoxychlorid Und -Bromid. *Z. Für Anorg. Chem.* **1903**, *36* (1), 346–348. https://doi.org/10.1002/zaac.19030360147.

(17)   Bragg, W. H.; Bragg, W. L. The Reflection of X-Rays by Crystals. *Proc. R. Soc. Lond. Ser. Contain. Pap. Math. Phys. Character* **1997**, *88* (605), 428–438. https://doi.org/10.1098/rspa.1913.0040.

(18)   Alsén, N. Röntgenographische Untersuchung Der Kristallstrukturen von Magnetkies, Breithauptit, Pentlandit, Millerit Und Verwandten Verbindungen. *Geol. Fören. Stockh. Förh.* **1925**, *47* (1), 19–72. https://doi.org/10.1080/11035892509443177.

(19)   Ramsdell, L. S. The Crystal Structure of Some Metallic Sulfides*. *Am. Mineral.* **1925**, *10* (9), 281–304.

(20)   Bannister, F. A. The Crystal-Structure and Optical Properties of Matlockite (PbFCl). *Mineral. Mag. J. Mineral. Soc.* **1934**, *23* (146), 587–597. https://doi.org/10.1180/minmag.1934.023.146.02.

(21)   Kuribayashi, T.; Nagase, T.; Nozaki, T.; Ishibashi, J.; Shimada, K.; Shimizu, M.; Momma, K. Hitachiite, $Pb_5Bi_2Te_2S_6$, a New Mineral from the Hitachi Mine, Ibaraki Prefecture, Japan. *Mineral. Mag.* **2019**, *83* (5), 733–739. https://doi.org/10.1180/mgm.2019.45.

(22)   Zachariasen, W. H. Crystal Chemical Studies of the 5*f*-Series of Elements. I. New Structure Types. *Acta Crystallogr.* **1948**, *1* (5), 265–268. https://doi.org/10.1107/S0365110X48000703.

(23)   Zachariasen, W. H. Crystal Chemical Studies of the 5*f*-series of Elements. VII. The Crystal Structure of Ce_2O_2S, La_2O_2S and Pu_2O_2S. *Acta Crystallogr.* **1949**, *2*, 60–62.

(24)   Zachariasen, W. H. Crystal Chemical Studies of the 5*f*-Series of Elements. X. Sulfides and Oxysulfides. *Acta Crystallogr.* **1949**, *2*, 291–296.

(25)   Nieuwenkamp, W.; Bijvoet, J. M. Die Kristallstruktur von Bleifluochlorid PbFCl. *Z. Für Krist. - Cryst. Mater.* **1932**, *81*, 469–474.

(26)   Zachariase, W. H. CRYSTAL CHEMICAL STUDIES OF THE 5*f*-SERIES OF ELEMENTS. XIV. OXYFLUORIDES, XOF. *Acta Cryst* **1951**, *Vol:* https://doi.org/10.1107/S0365110X51000787.

(27)   Zachariasen, W. H. Crystal Chemical Studies of the 5*f*-Series of Elements. XII. New Compounds Representing Known Structure Types. *Acta Crystallogr.* **1949**, *2* (6), 388–390. https://doi.org/10.1107/S0365110X49001016.

(28)   SOVERS, O.; YOSHIOKA, T. FLUORESCENCE OF TRIVALENT-EUROPIUM-DOPED YTTRIUM OXYSULFIDE. *J. Chem. Phys.* **1968**, *49* (11), 4945-. https://doi.org/10.1063/1.1669982.

(29)   Wu, M. K.; Ashburn, J. R.; Torng, C. J.; Hor, P. H.; Meng, R. L.; Gao, L.; Huang, Z. J.; Wang, Y. Q.; Chu, C. W. Superconductivity at 93 K in a New Mixed-Phase Y-Ba-Cu-O Compound System at Ambient Pressure. *Phys Rev Lett* **1987**, *58* (9), 908–910. https://doi.org/10.1103/PhysRevLett.58.908.

(30)   Valldor, M. Anion Ordering in Bichalcogenides. *Inorganics* **2016**, *4* (3), 23. https://doi.org/10.3390/inorganics4030023.

(31)   Headspith, D. A.; Sullivan, E.; Greaves, C.; Francesconi, M. G. Synthesis and Characterisation of the Quaternary Nitride-Fluoride $Ce_2MnN_3F_{2-\delta}$. *Dalton Trans* **2009**, No. 42, 9273–9279. https://doi.org/10.1039/B908591B.

(32)   Horky, K.; Schnick, W. $LiCa_4Si_4N_8F$ and $LiSr_4Si_4N_8F$: Nitridosilicate Fluorides with a BCT-Zeolite-Type Network Structure. *Eur. J. Inorg. Chem.* **2017**, *2017* (7), 1107–1112. https://doi.org/10.1002/ejic.201601386.

(33)   Durach, D.; Schnick, W. Non-Condensed (Oxo)Nitridosilicates: La_3-$[SiN_4]F$ and the Polymorph o-La_3-$[SiN_3O]O$. *Eur. J. Inorg. Chem.* **2015**, *2015* (24), 4095–4100. https://doi.org/10.1002/ejic.201500644.

(34) Pust, P.; Schnick, W. LiSr$_2$[TaN$_3$]F – a Single Chain Nitridotantalate. *Z. Für Anorg. Allg. Chem.* **2011**, *637* (11), 1486–1489. https://doi.org/10.1002/zaac.201100207.

(35) Rohrer, F. E.; Nesper, R. M$_2$BN$_2$X(M=Ca, Sr; X=F, Cl): New Halogenide Compounds with Isolated BN$^{3-}_2$ Units. *J. Solid State Chem.* **1998**, *135* (2), 194–200. https://doi.org/10.1006/jssc.1997.7624.

(36) Rohrer, F. E.; Nesper, R. Ba$_8$(BN$_2$)$_5$F: A Barium Fluoride Compound with Isolated BN$^{3-}_2$Units. *J. Solid State Chem.* **1999**, *142* (1), 192–198. https://doi.org/10.1006/jssc.1998.8027.

(37) Yamanaka, S.; Kawaji, H.; Hotehama, K.; Ohashi, M. A New Layer-Structured Nitride Superconductor. Lithium-Intercalated β-Zirconium Nitride Chloride, Li$_x$ZrNCl. *Adv. Mater.* **1996**, *8* (9), 771–774. https://doi.org/10.1002/adma.19960080917.

(38) Shamoto, S.; Kato, T.; Ono, Y.; Miyazaki, Y.; Ohoyama, K.; Ohashi, M.; Yamaguchi, Y.; Kajitani, T. Structures of β-ZrNCl and Superconducting Li$_{0.16}$ZrNCl: Double Honeycomb Lattice Superconductor. *Phys. C Supercond.* **1998**, *306* (1), 7–14. https://doi.org/10.1016/S0921-4534(98)00357-8.

(39) Yamanaka, S.; Hotehama, K.; Kawaji, H. Superconductivity at 25.5 K in Electron-Doped Layered Hafnium Nitride. *Nature* **1998**, *392* (6676), 580–582. https://doi.org/10.1038/33362.

(40) Peng, J.; Zhang, S. Synthesis and Superconductivity of Layered Compounds with Orthogonal [Zr$_2$N$_2$] Network. *J. Supercond. Nov. Magn.* **2017**, *30* (9), 2457–2463. https://doi.org/10.1007/s10948-017-4089-2.

(41) Armytage, D.; Fender, B. E. F. Anion Ordering in TaON: A Powder Neutron-Diffraction Investigation. *Acta Crystallogr. Sect. B* **1974**, *30* (3), 809–812. https://doi.org/10.1107/S0567740874003761.

(42) Masubuchi, Y.; Ohtaki, S.; Fujii, K.; Yashima, M.; Higuchi, M.; Kikkawa, S. Preparation and Thermal Stability of Oxynitride Perovskite Solid Solution Sr$_{1-x}$La$_x$Ta$_{1-x}$Ti$_x$O$_2$N. *10th Int. Symp. Nitrides* **2020**, *40* (16), 6288–6292. https://doi.org/10.1016/j.jeurceramsoc.2019.10.004.

(43) Fujii, K.; Shimada, K.; Yashima, M. Crystal-Structure and Electron-Density Analyses of the Perovskite-Type Oxynitrides BaNbO$_2$N and SrNbO$_2$N through Synchrotron X-Ray Powder Diffraction. *J. Ceram. Soc. Jpn.* **2017**, *125* (11), 808–810. https://doi.org/10.2109/jcersj2.17177.

(44) Oró-Solé, J.; Fina, I.; Frontera, C.; Gàzquez, J.; Ritter, C.; Cunquero, M.; Loza-Alvarez, P.; Conejeros, S.; Alemany, P.; Canadell, E.; Fontcuberta, J.; Fuertes, A. Engineering Polar Oxynitrides: Hexagonal Perovskite BaWON$_2$. *Angew. Chem. Int. Ed.* **2020**, *59* (42), 18395–18399. https://doi.org/10.1002/anie.202006519.

(45) Fuertes, A. Chemistry and Applications of Oxynitride Perovskites. *J Mater Chem* **2012**, *22* (8), 3293–3299. https://doi.org/10.1039/C2JM13182J.

(46) Kamihara, Y.; Hiramatsu, H.; Hirano, M.; Kawamura, R.; Yanagi, H.; Kamiya, T.; Hosono, H. Iron-Based Layered Superconductor: LaOFeP. *J. Am. Chem. Soc.* **2006**, *128* (31), 10012–10013. https://doi.org/10.1021/ja063355c.

(47) McQueen, T. M.; Regulacio, M.; Williams, A. J.; Huang, Q.; Lynn, J. W.; Hor, Y. S.; West, D. V.; Green, M. A.; Cava, R. J. Intrinsic Properties of Stoichiometric LaFePO. *Phys Rev B* **2008**, *78* (2), 024521. https://doi.org/10.1103/PhysRevB.78.024521.

(48) Kamihara, Y.; Watanabe, T.; Hirano, M.; Hosono, H. Iron-Based Layered Superconductor La[O$_{1-x}$F$_x$]FeAs (x = 0.05−0.12) with T$_c$ = 26 K. *J. Am. Chem. Soc.* **2008**, *130* (11), 3296–3297. https://doi.org/10.1021/ja800073m.

(49) Chen, X. H.; Wu, T.; Wu, G.; Liu, R. H.; Chen, H.; Fang, D. F. Superconductivity at 43 K in SmFeAsO$_{1-x}$F$_x$. *Nature* **2008**, *453* (7196), 761–762. https://doi.org/10.1038/nature07045.

(50) Ren, Z.-A.; Yang, J.; Lu, W.; Yi, W.; Shen, X.-L.; Li, Z.-C.; Che, G.-C.; Dong, X.-L.; Sun, L.-L.; Zhou, F.; Zhao, Z.-X. Superconductivity in the Iron-Based F-Doped Layered Quaternary Compound Nd[$O_{1-x}F_x$]FeAs. *Europhys. Lett.* **2008**, *82* (5), 57002. https://doi.org/10.1209/0295-5075/82/57002.

(51) Ren, Z. A.; Yang, J.; Lu, W.; Yi, W.; Che, G. C.; Dong, X. L.; Sun, L. L.; Zhao, Z. X. Superconductivity at 52 K in Iron Based F Doped Layered Quaternary Compound Pr[$O_{1-x}F_x$]FeAs. *Mater. Res. Innov.* **2008**, *12* (3), 105–106. https://doi.org/10.1179/143307508X333686.

(52) Cheng, P.; Fang, L.; Yang, H.; Zhu, X.; Mu, G.; Luo, H.; Wang, Z.; Wen, H. Superconductivity at 36 K in Gadolinium-Arsenide Oxides $GdO_{1-x}F_xFeAs$. *Sci. China Ser. G Phys. Mech. Astron.* **2008**, *51* (6), 719–722. https://doi.org/10.1007/s11433-008-0075-9.

(53) Chen, G. F.; Li, Z.; Wu, D.; Li, G.; Hu, W. Z.; Dong, J.; Zheng, P.; Luo, J. L.; Wang, N. L. Superconductivity at 41 K and Its Competition with Spin-Density-Wave Instability in Layered $CeO_{1-x}F_xFeAs$. *Phys Rev Lett* **2008**, *100* (24), 247002. https://doi.org/10.1103/PhysRevLett.100.247002.

(54) Shirage, P. M.; Miyazawa, K.; Kito, H.; Eisaki, H.; Iyo, A. Superconductivity at 43 K at Ambient Pressure in the Iron-Based Layered Compound $La_{1-x}Y_xFeAsO_y$. *Phys Rev B* **2008**, *78* (17), 172503. https://doi.org/10.1103/PhysRevB.78.172503.

(55) Biswal, G.; Mohanta, K. L. A Recent Review on Iron-Based Superconductor. *Int. Conf. Nanomater. Energy Environ. Sustain. ICNEES-2019* **2021**, *35*, 207–215. https://doi.org/10.1016/j.matpr.2020.04.503.

(56) Si, Q.; Yu, R.; Abrahams, E. High-Temperature Superconductivity in Iron Pnictides and Chalcogenides. *Nat. Rev. Mater.* **2016**, *1* (4), 16017. https://doi.org/10.1038/natrevmats.2016.17.

(57) Bardeen, J.; Cooper, L. N.; Schrieffer, J. R. Microscopic Theory of Superconductivity. *Phys Rev* **1957**, *106* (1), 162–164. https://doi.org/10.1103/PhysRev.106.162.

(58) Boeri, L.; Dolgov, O. V.; Golubov, A. A. Is $LaFeAsO_{1-x}F_x$ an Electron-Phonon Superconductor? *Phys Rev Lett* **2008**, *101* (2), 026403. https://doi.org/10.1103/PhysRevLett.101.026403.

(59) Shannon, R. D. Revised Effective Ionic Radii and Systematic Studies of Interatomic Distances in Halides and Chalcogenides. *Acta Crystallogr. Sect. A* **1976**, *32* (5), 751–767. https://doi.org/10.1107/S0567739476001551.

(60) Koehler, W. C.; Wollan, E. O. Neutron-Diffraction Study of the Structure of the It A-Form of the Rare Earth Sesquioxides. *Acta Crystallogr.* **1953**, *6* (8–9), 741–742. https://doi.org/10.1107/S0365110X53002076.

(61) Morosin, B. La_2O_2S Structure Refinement and Crystal Field. *Acta Crystallogr. Sect. B* **1973**, *29* (11), 2647–2648. https://doi.org/10.1107/S0567740873007284.

(62) Besançon, P.; Carré, D.; Laruelle, P. Mécanisme de La Solution Solide Des Oxysulfures de Terres Rares It $La_{10}S_{15-x}O_x$. *Acta Crystallogr. Sect. B* **1973**, *29* (5), 1064–1066. https://doi.org/10.1107/S0567740873003869.

(63) Zhou, W.; Yao, W.-D.; Tang, R.-L.; Xue, H.; Guo, S.-P. Second-Order Nonlinear Optical and Photoelectric Properties of Zn4B6O12S. *J. Alloys Compd.* **2021**, *867*, 158879. https://doi.org/10.1016/j.jallcom.2021.158879.

(64) Meignen, V.; Deudon, C.; Lafond, A.; Boyer-Candalen, C.; Meerschaut, A. Single Crystal Structure and Magnetic Properties of a New Quaternary Samarium-Titanium Oxyselenide: $Sm_3Ti_3Se_2O_8$. *Solid State Sci.* **2001**, *3* (1), 189–194. https://doi.org/10.1016/S1293-2558(00)01130-4.

(65) Brennan, T. D.; Aleandri, L. E.; Ibers, J. A. Synthesis and Structure of $Ln_2Ta_3Se_2O_8$ (Ln = La, Ce, Pr, Nd). *J. Solid State Chem.* **1991**, *91* (2), 312–322. https://doi.org/10.1016/0022-4596(91)90086-W.

(66)   Free, D. G.; Herkelrath, S. J. C.; Clarke, S. J. $Sr_2Mn_2O_4Se$: A New Oxychalcogenide with Antiferromagnetic Chains. *Z. Für Anorg. Allg. Chem.* **2012**, *638* (15), 2532–2537. https://doi.org/10.1002/zaac.201200254.

(67)   Céolin, R.; Rodier, N. Structure Cristalline de l'oxysulfure de Cérium et de Bismuth $CeBiOS2$. *Acta Crystallogr. Sect. B* **1976**, *32* (5), 1476–1479. https://doi.org/10.1107/S0567740876005591.

(68)   Jaulmes, S.; Godlewski, E.; Palazzi, M.; Etienne, J. Deux Structures Isotypes à Sites Anioniques et Cationiques Lacunaires: $(CeO)_4Ga_2S_5$ et $(LaO)_4As_2S_5$. *Acta Crystallogr. Sect. B* **1982**, *38* (6), 1707–1710. https://doi.org/10.1107/S0567740882007006.

(69)   Gamon, J.; Perez, A. J.; Jones, L. A. H.; Zanella, M.; Daniels, L. M.; Morris, R. E.; Tang, C. C.; Veal, T. D.; Hardwick, L. J.; Dyer, M. S.; Claridge, J. B.; Rosseinsky, M. J. $Na_2Fe_2OS_2$, a New Earth Abundant Oxysulphide Cathode Material for Na-Ion Batteries. *J Mater Chem A* **2020**, *8* (39), 20553–20569. https://doi.org/10.1039/D0TA07966A.

(70)   Valldor, M.; Merz, P.; Prots, Y.; Schnelle, W. Bad-Metal-Layered Sulfide Oxide CsV_2S_2O. *Eur. J. Inorg. Chem.* **2016**, *2016* (1), 23–27. https://doi.org/10.1002/ejic.201501154.

(71)   Raw, A. D.; Ibers, J. A. Synthesis and Structural Characterization of the New Compound $UEr_2O_2S_3$ and the Evidence for the Old Compound $U_2ErO_2S_3$. *J. Solid State Chem.* **2012**, *187*, 282–285. https://doi.org/10.1016/j.jssc.2011.12.040.

(72)   Mayer, J. M.; Schneemeyer, L. F.; Siegrist, T.; Waszczak, J. V.; Van Dover, B. New Layered Iron-Lanthanum-Oxide-Sulfide and -Selenide Phases: $Fe_2La_2O_3E_2$ (E = S,Se). *Angew. Chem. Int. Ed. Engl.* **1992**, *31* (12), 1645–1647. https://doi.org/10.1002/anie.199216451.

(73)   Pearson, R. G. Hard and Soft Acids and Bases—the Evolution of a Chemical Concept. *Coord. Chem. Rev.* **1990**, *100*, 403–425. https://doi.org/10.1016/0010-8545(90)85016-L.

(74)   Ijjaali, I.; Deng, B.; Ibers, J. A. Seven New Rare-Earth Transition-Metal Oxychalcogenides: Syntheses and Characterization of Ln_4MnOSe_6 (Ln=La, Ce, Nd), Ln_4FeOSe_6 (Ln=La, Ce, Sm), and La_4MnOS_6. *J. Solid State Chem.* **2005**, *178* (5), 1503–1507. https://doi.org/10.1016/j.jssc.2005.02.022.

(75)   Ijjaali, I.; Haynes, C. L.; McFarland, A. D.; Van Duyne, R. P.; Ibers, J. A. Synthesis, Structure, and Optical Properties of the New Lanthanum Copper Oxysulfide $La_3CuO_2S_3$. *J. Solid State Chem.* **2003**, *172* (2), 257–260. https://doi.org/10.1016/S0022-4596(03)00058-6.

(76)   Palazzi, M.; Jaulmes, S. Structure Du Conducteur Ionique $(LaO)AgS$. *Acta Crystallogr. Sect. B* **1981**, *37* (7), 1337–1339. https://doi.org/10.1107/S0567740881005876.

(77)   Bryhan, D. N.; Rakers, R.; Klimaszewski, K.; Patel, N.; Bohac, J. J.; Kremer, R. K.; Mattausch, H.; Zheng, C. $La_3TWS_3O_6$ (T = Cr, Mn, Fe, Co, Ni): Quinary Rare Earth Transition-Metal Compounds Showing a Nonmagnetic/Magnetic Transition (T = Co) – Synthesis, Structure and Physical Properties. *Z. Für Anorg. Allg. Chem.* **2010**, *636* (1), 74–78. https://doi.org/10.1002/zaac.200900501.

(78)   Dugué, J.; Voyan, T.; Villers, J. Etude Structurale Des Oxysulfures de Chrome(III) et de Terres Rares. I. Structure de l'oxysulfure $LaCrOS_2$. *Acta Crystallogr. Sect. B* **1980**, *36* (6), 1291–1294. https://doi.org/10.1107/S0567740880005948.

(79)   Wintenberger, M.; Dugue, J.; Guittard, M.; Dung, N. H.; Van Tien, V. Ferro- and Antiferromagnetism in Oxychalcogenides $LnCrOX_2$ (Ln = La or Nd and X = S or Se). *J. Solid State Chem.* **1987**, *70* (2), 295–302. https://doi.org/10.1016/0022-4596(87)90068-5.

(80)   Mazurier, A.; Maneglier-Lacordaire, S.; Ghémard, G.; Jaulmes, S. Structure Cristalline Du Sulfotellurure de Gallium Ga_2S_2Te. *Acta Crystallogr. Sect. B* **1979**, *35* (5), 1046–1049. https://doi.org/10.1107/S0567740879005549.

(81)   Jaulmes, S.; Laruelle, P. Structure Cristalline Du Sulfure d'erbium-Gallium, Er$_3$GaS$_6$. *Acta Crystallogr. Sect. B* **1973**, *29* (2), 352–354. https://doi.org/10.1107/S0567740873002463.

(82)   Sappl, J.; Jung, F.; Hoch, C. Facile One-Step Syntheses of Several Complex Ionic Lithium Gallates from LiGa as Intermetallic Precursors. *Chem. Mater.* **2020**, *32* (2), 866–873. https://doi.org/10.1021/acs.chemmater.9b04540.

(83)   Romers, C.; Blaisse, B. A.; IJdo, D. J. W. Complex Sulphur Compounds. I. The Crystal Structure of MgGa$_2$S$_4$. *Acta Crystallogr.* **1967**, *23* (4), 634–640. https://doi.org/10.1107/S0365110X67003317.

(84)   Klepov, V. V.; Berseneva, A. A.; Pace, K. A.; Kocevski, V.; Sun, M.; Qiu, P.; Wang, H.; Chen, F.; Besmann, T. M.; zur Loye, H.-C. NaGaS$_2$: An Elusive Layered Compound with Dynamic Water Absorption and Wide-Ranging Ion-Exchange Properties. *Angew. Chem. Int. Ed.* **2020**, *59* (27), 10836–10841. https://doi.org/10.1002/anie.202001203.

(85)   Shi, Z.-H.; Chi, Y.; Sun, Z.-D.; Liu, W.; Guo, S.-P. Sn$_2$Ga$_2$S$_5$: A Type of IR Nonlinear-Optical Material. *Inorg. Chem.* **2019**, *58* (18), 12002–12006. https://doi.org/10.1021/acs.inorgchem.9b02021.

(86)   Klee, W. E.; Schaefer, H. Zur Darstellung Und Kristallstruktur von CaAl$_6$Te$_{10}$ Und CaGa$_6$Te$_{10}$. *Z. Fuer Naturforschung Teil B Anorg. Chem. Org. Chem.* **1979**, No. 34, 657–661.

(87)   Atuchin, V. V.; Liang, F.; Grazhdannikov, S.; Isaenko, L. I.; Krinitsin, P. G.; Molokeev, M. S.; Prosvirin, I. P.; Jiang, X.; Lin, Z. Negative Thermal Expansion and Electronic Structure Variation of Chalcopyrite Type LiGaTe$_2$. *RSC Adv* **2018**, *8* (18), 9946–9955. https://doi.org/10.1039/C8RA01079J.

(88)   Eisenmann, B.; Jakowski, M.; Schaefer, H. Neue Ternaere Varianten Der Tl Se-Struktur: Zur Kenntnis von BaAl$_2$Te$_4$(II), SrGa$_2$Te$_4$, SrIn$_2$Te$_4$ Und BaIn$_2$Te$_4$. *Rev. Chim. Miner.* **1982**, *19*, 263–273.

(89)   Agostinellt, E.; Gastaldi, L.; Viticoli, S. Crystal Growth and X-Ray Structural Investigatton of Two Forms of HgGa$_2$Te$_4$. *Mater. Chem. Phys.* **1985**, *12* (4), 303–312. https://doi.org/10.1016/0254-0584(85)90101-4.

(90)   Wu, E. J.; Pell, M. A.; Fuelberth, T. M.; Ibers, J. A. Crystal Structure of Caesium Gallium Ditelluride, CsGaTe$_2$. *Z. Für Krist. - New Cryst. Struct.* **1997**, *212* (1), 91–91. https://doi.org/doi:10.1524/ncrs.1997.212.1.91.

(91)   Huang, F. Q.; Ibers, J. A. Syntheses, Structures, and Theoretical Study of LaCuSTe and SmCuSTe. *Inorg. Chem.* **1999**, *38* (26), 5978–5983. https://doi.org/10.1021/ic990835e.

(92)   Kohatsu, I.; Wuensch, B. J. The Crystal Structure of Gladite, PbCuBi$_5$S$_9$, a Superstructure Intermediate in the Series Bi$_2$S$_3$–PbCuBiS$_3$ (Bismuthinite–Aikinite). *Acta Crystallogr. Sect. B* **1976**, *32* (8), 2401–2409. https://doi.org/10.1107/S0567740876007851.

(93)   Jaulmes, S.; Rivet, J.; Laruelle, P. Cuivre–Étain–Soufre Cu$_4$SnS$_4$. *Acta Crystallogr. Sect. B* **1977**, *33* (2), 540–542. https://doi.org/10.1107/S0567740877004002.

(94)   Chapuis, G.; Niggli, A. The Crystal Structure of the `normal Tetrahedral' Compound Cu$_2$CdSiS$_4$. *Acta Crystallogr. Sect. B* **1972**, *28* (5), 1626–1628. https://doi.org/10.1107/S0567740872004704.

(95)   Garin, J.; Parthé, E. The Crystal Structure of Cu$_3$PSe$_4$ and Other Ternary Normal Tetrahedral Structure Compounds with Composition 13564. *Acta Crystallogr. Sect. B* **1972**, *28* (12), 3672–3674. https://doi.org/10.1107/S0567740872008568.

(96)   Ohmasa, M.; Nowacki, W. A Redetermination of the Crystal Structure of Aikinite [BiS$_2$/S/Cu^{IV}Pb^{VII}]. *Z. Für Krist. - Cryst. Mater.* **1970**, *132* (1–6), 71–86. https://doi.org/doi:10.1524/zkri.1970.132.16.71.

(97) Gladisch, F. C.; van Leusen, J.; Passia, M. T.; Kögerler, P.; Steinberg, S. $Rb_3Er_4Cu_5Te_{10}$: Exploring the Frontier between Polar Intermetallics and Zintl-Phases via Experimental and Quantumchemical Approaches. *Eur. J. Inorg. Chem.* **2021**, *2021* (47), 4946–4953. https://doi.org/10.1002/ejic.202100795.

(98) Klepp, K. O. Darstellung Und Kristallstruktur von $NaCu_3Te_2$ / Preparation and Crystal Structure of $NaCu_3Te_2$. *Z. Für Naturforschung B* **1987**, *42* (2), 130–134. https://doi.org/doi:10.1515/znb-1987-0202.

(99) Wang, Y. C.; DiSalvo, F. J. Structure and Physical Properties of $BaCu_2Te_2$. *J. Solid State Chem.* **2001**, *156* (1), 44–50. https://doi.org/10.1006/jssc.2000.8956.

(100) Laing, C. C.; Weiss, B. E.; Pal, K.; Quintero, M. A.; Xie, H.; Zhou, X.; Shen, J.; Chung, D. Y.; Wolverton, C.; Kanatzidis, M. G. $ACuZrQ_3$ (A = Rb, Cs; Q = S, Se, Te): Direct Bandgap Semiconductors and Metals with Ultralow Thermal Conductivity. *Chem. Mater.* **2022**, *34* (18), 8389–8402. https://doi.org/10.1021/acs.chemmater.2c02104.

(101) Eickmeier, K.; Poschkamp, R.; Dronskowski, R.; Steinberg, S. Exploring the Impact of Lone Pairs on the Structural Features of Alkaline-Earth (A) Transition-Metal (M,M') Chalcogenides (Q) AMM'Q3. *Eur. J. Inorg. Chem.* **2022**, *2022* (28), e202200360. https://doi.org/10.1002/ejic.202200360.

(102) Hodges, J. M.; Xia, Y.; Malliakas, C. D.; Slade, T. J.; Wolverton, C.; Kanatzidis, M. G. Mixed-Valent Copper Chalcogenides: Tuning Structures and Electronic Properties Using Multiple Anions. *Chem. Mater.* **2020**, *32* (23), 10146–10154. https://doi.org/10.1021/acs.chemmater.0c03620.

(103) Huang, F. Q.; Ibers, J. A. Syntheses and Structures of the Quaternary Copper Tellurides $K_3Ln_4Cu_5Te_{10}$ (Ln=Sm, Gd, Er), $Rb_3Ln_4Cu_5Te_{10}$ (Ln=Nd, Gd), and $Cs_3Gd_4Cu_5Te_{10}$. *J. Solid State Chem.* **2001**, *160* (2), 409–414. https://doi.org/10.1006/jssc.2001.9256.

(104) Savelsberg, G.; Schäfer, H. Zur Kenntnis von $Na_2Cu_4S_3$ Und KCu_3Te_2. *Mater. Res. Bull.* **1981**, *16* (10), 1291–1297. https://doi.org/10.1016/0025-5408(81)90100-8.

(105) Gladisch, F. C.; Pippinger, T.; Meyer, J.; Pries, J.; Richter, J.; Steinberg, S. Examination of a Structural Preference in Quaternary Alkali-Metal (A) Rare-Earth (R) Copper Tellurides by Combining Experimental and Quantum-Chemical Means. *Inorg. Chem.* **2022**, *61* (24), 9269–9282. https://doi.org/10.1021/acs.inorgchem.2c01002.

(106) Kolb, A.; Klepp, K. O. $K_4Ti_3Te_9$ – A New Pseudo One-Dimensional Polyanionic Alkali Chalcogenometallate(IV). **2003**, *58* (7), 633–638. https://doi.org/10.1515/znb-2003-0705.

(107) Patschke, R.; Brazis, P.; Kannewurf, C. R.; Kanatzidis, M. $K_2Ag_3CeTe_4$: A Semiconducting Tunnel Framework Made from the Covalent "Link-Up" of $[Ag_2CeTe_4]^{3-}$ Layers with Ag. *Inorg. Chem.* **1998**, *37* (26), 6562–6563. https://doi.org/10.1021/ic981177l.

(108) Palazzi, M.; Jaulmes, S.; Laruelle, P. Structure Cristalline de K_3AsS_4. *Acta Crystallogr. Sect. B* **1974**, *30* (10), 2378–2381. https://doi.org/10.1107/S0567740874007151.

(109) Burschka, C. Zur Kristallstruktur Der Thiocuprate $K_3Cu_8S_6$ Und $Rb_3Cu_8S_6$. *Z. Fuer Naturforschung Teil B Anorg. Chem. Org. Chem.* **1979**, No. 34, 675–677.

(110) Li, Y.; Song, X.; Liu, Y.; Guo, Y.; Sun, Y.; Ji, M.; You, Z.; An, Y. Syntheses, Structures, and Photocatalytic Properties of Open-Framework Ag–Sn–S Compounds. *Dalton Trans* **2020**, *49* (33), 11708–11714. https://doi.org/10.1039/D0DT02513E.

(111) Li, Z.; Jiang, X.; Yi, C.; Zhou, M.; Guo, Y.; Luo, X.; Lin, Z.; Wu, Y.; Shi, Y.; Yao, J. K2MnGe3S8: A New Multifunctional Semiconductor Featuring $[MnGe_3S_8]^{2-}$ Layers and Demonstrating Interesting Nonlinear Optical Response and Antiferromagnetic Properties. *J Mater Chem C* **2018**, *6* (37), 10042–10049. https://doi.org/10.1039/C8TC03694B.

(112) Tan, D.-M.; Lin, C.-S.; Luo, Z.-Z.; Zhang, H.; Zhang, W.-L.; He, Z.-Z.; Cheng, W.-D. Synthesis and Characterization of a New Mid-Infrared Transparent Compound: Acentric

$Ba_5In_4Te_4S_7$. *Dalton Trans* **2015**, *44* (16), 7673–7678. https://doi.org/10.1039/C5DT00228A.

(113) Grey, I. E. The Structure of $Ba_5Fe_9S_{18}$. *Acta Crystallogr. Sect. B* **1975**, *31* (1), 45–48. https://doi.org/10.1107/S0567740875002087.

(114) Wu, X.; Gu, X.; Pan, H.; Hu, Y.; Wu, K. Synthesis, Crystal Structures, Optical Properties and Theoretical Calculations of Two Metal Chalcogenides Ba_2AlSbS_5 and $Ba_2GaBiSe_5$. *Crystals* **2018**, *8* (4). https://doi.org/10.3390/cryst8040165.

(115) Abudurusuli, A.; Wu, K.; Tudi, A.; Yang, Z.; Pan, S. $ABaSbQ_3$ (A = Li, Na; Q = S, Se): Diverse Arrangement Modes of Isolated SbQ_3 Ligands Regulating the Magnitudes of Birefringences. *Chem Commun* **2019**, *55* (35), 5143–5146. https://doi.org/10.1039/C9CC00560A.

(116) Teske, Chr. L. Darstellung Und Kristallstruktur von Barium-Cadmium-Thiostannat (Iv) $BaCdSnS_4$. *Z. Für Anorg. Allg. Chem.* **1980**, *460* (1), 163–168. https://doi.org/10.1002/zaac.19804600115.

(117) Abudurusuli, A.; Wu, K.; Li, J.; Yalikun, A.; Yang, Z.; Pan, S. $LiBa_2M^{III}Q_4$ (M^{III} = Al, Ga, In; Q = S, Se): A Series of Metal Chalcogenides with a Structural Transition. *Inorg. Chem.* **2019**, *58* (19), 12859–12866. https://doi.org/10.1021/acs.inorgchem.9b01810.

(118) Ishtiyak, M.; Jana, S.; Narayanswamy, S.; Nishad, A. K.; Panigrahi, G.; Bhattacharjee, P. P.; Prakash, J. Intrinsic Extremely Low Thermal Conductivity in $BaIn_2Te_4$: Synthesis, Crystal Structure, Raman Spectroscopy, Optical, and Thermoelectric Properties. *J. Alloys Compd.* **2019**, *802*, 385–393. https://doi.org/10.1016/j.jallcom.2019.06.036.

(119) Yadav, S.; Jana, S.; Panigrahi, G.; Malladi, S. K.; Niranjan, M. K.; Prakash, J. Five Coordinated Mn in $Ba_4Mn_2Si_2Te_9$: Synthesis, Crystal Structure, Physical Properties, and Electronic Structure. *Dalton Trans* **2022**, *51* (24), 9265–9277. https://doi.org/10.1039/D2DT01167K.

(120) Brinkmann, C.; Eisenmann, B.; Schäfer, H. Darstellung Und Struktur Der Verbindungen Ba_2SiTe_4 Und Ba_2SiSe_4. *Z. Für Anorg. Allg. Chem.* **1985**, *524* (5), 83–89. https://doi.org/10.1002/zaac.19855240511.

(121) Brinkmann, C.; Eisenmann, B.; Schäfer, H. $Ba_2Ge_2Te_5$, Ein Neues Kettentelluridogermanat(III). *Z. Für Anorg. Allg. Chem.* **1984**, *517* (10), 143–148. https://doi.org/10.1002/zaac.19845171013.

(122) Lissner, F.; Meyer, S. P.; Schleid, T. $CsTb_3STe_4$ Und $CsTb_5S_2Te_6$: Zwei Pseudo-Ternäre Caesium-Terbium-Chalkogenide Mit Geordneten S^{2-}- Und Te^{2-}-Anionen. *Z. Für Naturforschung B* **2019**, *74* (1), 99–107. https://doi.org/doi:10.1515/znb-2018-0174.

(123) Laing, C. C.; Shen, J.; Quintero, M. A.; Weiss, B. E.; Xia, Y.; Li, Z.; He, J.; Wolverton, C.; Kanatzidis, M. G. Homologous Alkali Metal Copper Rare-Earth Chalcogenides $A_2Cu_{2n}Ln_4Q_{7+n}$ (n = 1, 2, 3). *Chem. Mater.* **2022**, *34* (7), 3409–3422. https://doi.org/10.1021/acs.chemmater.2c00223.

(124) Bronger, W.; Brüggemann, W.; von der Ahe, M.; Schmitz, D. Zur Synthese Und Struktur Ternärer Chalcogenide Der Seltenen Erden $AlnX_2$ Mit A ≙ Alkalimetall Und X ≙ Schwefel, Selen Oder Tellur. *J. Alloys Compd.* **1993**, *200* (1), 205–210. https://doi.org/10.1016/0925-8388(93)90495-9.

(125) Yao, J.; Deng, B.; Ellis, D. E.; Ibers, J. A. Syntheses, Structures, Physical Properties, and Electronic Structures of KLn_2CuS_4 (Ln=Y, Nd, Sm, Tb, Ho) and $K_2Ln_4Cu_4S_9$ (Ln=Dy, Ho). *J. Solid State Chem.* **2003**, *176* (1), 5–12. https://doi.org/10.1016/S0022-4596(03)00233-0.

(126) Yue, Q.-G.; Zhou, S.-H.; Li, B.; Wu, X.-T.; Lin, H.; Zhu, Q.-L. Quaternary Noncentrosymmetric Rare-Earth Sulfides $Ba_4RE_2Cd_3S_{10}$ (RE = Sm, Gd, or Tb): A Joint Experimental and Theoretical Investigation. *Inorg. Chem.* **2022**, *61* (3), 1797–1804. https://doi.org/10.1021/acs.inorgchem.1c03820.

(127) Klepov, V. V.; Pace, K. A.; Breton, L. S.; Kocevski, V.; Besmann, T. M.; zur Loye, H.-C. Nearly Identical but Not Isotypic: Influence of Lanthanide Contraction on $Cs_2NaLn(PS_4)_2$ (Ln = La–Nd, Sm, and Gd–Ho). *Inorg. Chem.* **2020**, *59* (3), 1905–1916. https://doi.org/10.1021/acs.inorgchem.9b03200.

(128) Eickmeier, K.; Steinberg, S. Exploring the Frontier between Polar Intermetallics and Zintl Phases for the Examples of the Prolific $ALnTnTe_3$-Type Alkali Metal (A) Lanthanide (Ln) Late Transition Metal (Tn) Tellurides. **2021**, *76* (10–12), 635–642. https://doi.org/10.1515/znb-2021-0100.

(129) Marchuk, O. V.; Daszkiewicz, M.; Gulay, L. D.; Olekseyuk, I. D.; Pietraszko, A. Investigation of the R_2Te_3–M_2Te–PbTe (R=Tb, Dy; M=Cu, Ag) Systems at 770K. *J. Alloys Compd.* **2008**, *455* (1), 186–190. https://doi.org/10.1016/j.jallcom.2007.01.065.

(130) Tougait, O.; Noël, H.; Ibers, J. A. Serendipitous Syntheses of the Series $Cs_3Ln_7Te_{12}$ (Ln = Sm, Gd, Tb): Compounds with Large Tunnels. *Solid State Sci.* **2001**, *3* (4), 513–518. https://doi.org/10.1016/S1293-2558(01)01162-1.

(131) Prakash, J.; Mesbah, A.; Beard, J. C.; Ibers, J. A. Syntheses and Crystal Structures of $BaAgTbS_3$, $BaCuGdTe_3$, $BaCuTbTe_3$, $BaAgTbTe_3$, and $CsAgUTe_3$. *Z. Für Anorg. Allg. Chem.* **2015**, *641* (7), 1253–1257. https://doi.org/10.1002/zaac.201500027.

(132) Jiang, S.; Liu, J.; Bai, L.; Li, X.; Li, Y.; He, S.; Yan, S.; Liang, D. Anomalous Compression Behaviour in Nd_2O_3 Studied by X-Ray Diffraction and Raman Spectroscopy. *AIP Adv.* **2018**, *8* (2), 025019. https://doi.org/10.1063/1.5018020.

(133) Schleid, T.; Lissner, F. Einkristalle von A-Nd_2S_3, U-Ho_2S_3, D-Er_2S_3 Und E-Lu_2S_3 Durch Oxidation Reduzierter Chloride Der Lanthanide Mit Schwefel. *Z. Für Anorg. Allg. Chem.* **1992**, *615* (9), 19–26. https://doi.org/10.1002/zaac.19926150905.

(134) Bertaut, E.-F.; Ballestracci, R. Étude Cristallographique de Nouveaux Séléniures de Terres Rares et de Sodium. *Bull. Minéralogie* **1965**, *88* (1), 136–138. https://doi.org/10.3406/bulmi.1965.5816.

(135) Raccah, P. M.; Longo, J. M.; Eick, H. A. The Crystal Structure of Neodymium Monotellurooxide-Nd_2O_2Te. *Inorg. Chem.* **1967**, *6* (8), 1471–1473. https://doi.org/10.1021/ic50054a008.

(136) Schleid, T.; Klein, E. K. Nd_2S2Te: Neodymium(III) Sulfide Telluride with Ce_2O_2S-Type Crystal Structure. *Z. Für Anorg. Allg. Chem.* **2001**, *627* (5), 807–808. https://doi.org/10.1002/1521-3749(200105)627:5<807::AID-ZAAC807>3.0.CO;2-R.

(137) Khurana, R.; Gupta, S.; Ali, Md. E. First-Principles Investigations of Magnetic Anisotropy and Spin-Crossover Behavior of Fe(III)–TBP Complexes. *J. Phys. Chem. A* **2021**, *125* (10), 2197–2207. https://doi.org/10.1021/acs.jpca.1c00022.

(138) Sharma, D. K.; Shukla, S.; Sharma, K. K.; Kumar, V. A Review on ZnO: Fundamental Properties and Applications. *Natl. Conf. Funct. Mater. Emerg. Technol. Appl. Mater. Sci.* **2022**, *49*, 3028–3035. https://doi.org/10.1016/j.matpr.2020.10.238.

(139) Sabine, T. M.; Hogg, S. The Wurtzite It Z Parameter for Beryllium Oxide and Zinc Oxide. *Acta Crystallogr. Sect. B* **1969**, *25* (11), 2254–2256. https://doi.org/10.1107/S0567740869005528.

(140) Sambrook, T.; Smura, C. F.; Clarke, S. J.; Ok, K. M.; Halasyamani, P. S. Structure and Physical Properties of the Polar Oxysulfide CaZnOS. *Inorg. Chem.* **2007**, *46* (7), 2571–2574. https://doi.org/10.1021/ic062120z.

(141) Tsujimoto, Y.; Juillerat, C. A.; Zhang, W.; Fujii, K.; Yashima, M.; Halasyamani, P. Shiv.; zur Loye, H.-C. Function of Tetrahedral ZnS_3O Building Blocks in the Formation of $SrZn_2S_2O$: A Phase Matchable Polar Oxysulfide with a Large Second Harmonic Generation Response. *Chem. Mater.* **2018**, *30* (18), 6486–6493. https://doi.org/10.1021/acs.chemmater.8b02967.

(142)   Ninomiya, S.; Adachi, S. Optical Properties of Cubic and Hexagonal CdSe. *J. Appl. Phys.* **1995**, *78* (7), 4681–4689. https://doi.org/10.1063/1.359815.

(143)   Li, Q.; Li, X.; Yu, J. Chapter 10 - Surface and Interface Modification Strategies of CdS-Based Photocatalysts. In *Interface Science and Technology*; Yu, J., Jaroniec, M., Jiang, C., Eds.; Elsevier, 2020; Vol. 31, pp 313–348. https://doi.org/10.1016/B978-0-08-102890-2.00010-5.

(144)   Pan, A.; Yang, H.; Liu, R.; Yu, R.; Zou, B.; Wang, Z. Color-Tunable Photoluminescence of Alloyed CdS_xSe_{1-x} Nanobelts. *J. Am. Chem. Soc.* **2005**, *127* (45), 15692–15693. https://doi.org/10.1021/ja056116i.

(145)   Kanamori, J. Superexchange Interaction and Symmetry Properties of Electron Orbitals. *J. Phys. Chem. Solids* **1959**, *10* (2–3), 87–98. https://doi.org/10.1016/0022-3697(59)90061-7.

(146)   Goodenough, J. B. Theory of the Role of Covalence in the Perovskite-Type Manganites $[La,M(II)]MnO_3$. *Phys. Rev.* **1955**, *100* (2), 564–573. https://doi.org/10.1103/PhysRev.100.564.

(147)   Valldor, M.; Rößler, U. K.; Prots, Y.; Kuo, C.-Y.; Chiang, J.-C.; Hu, Z.; Pi, T.-W.; Kniep, R.; Tjeng, L. H. Synthesis and Characterization of Ba[CoSO]: Magnetic Complexity in the Presence of Chalcogen Ordering. *Chem. – Eur. J.* **2015**, *21* (30), 10821–10828. https://doi.org/10.1002/chem.201501024.

(148)   Hardy, A. E. The Performance Characteristics of Yttrium Oxysulfide—A New Red Phosphor for Color Television. *IEEE Trans. Electron Devices* **1968**, *15* (11), 868–872. https://doi.org/10.1109/T-ED.1968.16530.

(149)   Rajamohan Reddy, K.; Annapurna, K.; Sooraj Hussain, N.; Buddhudu, S. Fluorescence Spectra of Tb^{3+}: Ln_2O_2S Powder Phosphors. *Spectrosc. Lett.* **1997**, *30* (5), 819–824. https://doi.org/10.1080/00387019708001630.

(150)   Bang, J.; Abboudi, M.; Abrams, B.; Holloway, P. H. Combustion Synthesis of Eu-, Tb- and Tm- Doped Ln_2O_2S (Ln=Y, La, Gd) Phosphors. *J. Lumin.* **2004**, *106* (3), 177–185. https://doi.org/10.1016/j.jlumin.2003.09.005.

(151)   Hakmeh, N.; Chlique, C.; Merdrignac-Conanec, O.; Fan, B.; Cheviré, F.; Zhang, X.; Fan, X.; Qiao, X. Combustion Synthesis and Up-Conversion Luminescence of $La_2O_2S:Er^{3+},Yb^{3+}$ Nanophosphors. *J. Solid State Chem.* **2015**, *226*, 255–261. https://doi.org/10.1016/j.jssc.2015.02.015.

(152)   Kuo, T.-W.; Liu, W.-R.; Chen, T.-M. High Color Rendering White Light-Emitting-Diode Illuminator Using the Red-Emitting Eu^{2+}-Activated CaZnOS Phosphors Excited by Blue LED. *Opt Express* **2010**, *18* (8), 8187–8192. https://doi.org/10.1364/OE.18.008187.

(153)   Gál, Z. A.; Rutt, O. J.; Smura, C. F.; Overton, T. P.; Barrier, N.; Clarke, S. J.; Hadermann, J. Structural Chemistry and Metamagnetism of an Homologous Series of Layered Manganese Oxysulfides. *J. Am. Chem. Soc.* **2006**, *128* (26), 8530–8540. https://doi.org/10.1021/ja060892o.

(154)   Zhu, W. J.; Hor, P. H. Unusual Layered Transition-Metal Oxysulfides: $Sr_2Cu_2MO_2S_2$(M=Mn, Zn). *J. Solid State Chem.* **1997**, *130* (2), 319–321. https://doi.org/10.1006/jssc.1997.7299.

(155)   Okada, S.; Terasaki, I.; Ooyama, H.; Matoba, M. Dielectric Responses of the Layered Cobalt Oxysulfide $Sr_2Cu_2CoO_2S_2$ with CoO_2 Square Planes. *J. Appl. Phys.* **2004**, *95* (11), 6816–6818. https://doi.org/10.1063/1.1689772.

(156)   Giacovazzo, C.; Monaco, H. L.; Viterbo, D.; Scordari, F.; Gilli, G.; Zanotti, G.; Catti, M. *Fundamentals of Crystallography*; IUCr Texts on Crystallography; 1992.

(157)   Petříček, V.; Dušek, M.; Palatinus, L. Crystallographic Computing System JANA2006: General Features. *Z. Für Krist. - Cryst. Mater.* **2014**, *229* (5), 345–352. https://doi.org/10.1515/zkri-2014-1737.

(158) Petříček, V.; Palatinus, L.; Plášil, J.; Dušek, M. Jana2020 – a New Version of the Crystallographic Computing System Jana. **2023**, *238* (7–8), 271–282. https://doi.org/10.1515/zkri-2023-0005.

(159) Debye, P. Zur Theorie Der Spezifischen Wärmen. *Ann. Phys.* **1912**, *344* (14), 789–839. https://doi.org/10.1002/andp.19123441404.

(160) Atkins, P.; Ronald, F. *Molecular Quantum Dynamics*, Fifth.; Oxford University Press: Oxford, New York.

(161) Anisimov, V. I.; Zaanen, J.; Andersen, O. K. Band Theory and Mott Insulators: Hubbard U Instead of Stoner I. *Phys Rev B* **1991**, *44* (3), 943–954. https://doi.org/10.1103/PhysRevB.44.943.

(162) Dudarev, S. L.; Botton, G. A.; Savrasov, S. Y.; Humphreys, C. J.; Sutton, A. P. Electron-Energy-Loss Spectra and the Structural Stability of Nickel Oxide: An LSDA+U Study. *Phys. Rev. B* **1998**, *57* (3), 1505–1509. https://doi.org/10.1103/PhysRevB.57.1505.

(163) Kresse, G.; Furthmüller, J. Efficiency of Ab-Initio Total Energy Calculations for Metals and Semiconductors Using a Plane-Wave Basis Set. *Comput. Mater. Sci.* **1996**, *6* (1), 15–50. https://doi.org/10.1016/0927-0256(96)00008-0.

(164) Kresse, G.; Furthmüller, J. Efficient Iterative Schemes for *Ab Initio* Total-Energy Calculations Using a Plane-Wave Basis Set. *Phys. Rev. B* **1996**, *54* (16), 11169–11186. https://doi.org/10.1103/PhysRevB.54.11169.

(165) Perdew, J. P.; Burke, K.; Ernzerhof, M. Generalized Gradient Approximation Made Simple. *Phys. Rev. Lett.* **1996**, *77* (18), 3865–3868. https://doi.org/10.1103/PhysRevLett.77.3865.

(166) Sun, J.; Ruzsinszky, A.; Perdew, J. P. Strongly Constrained and Appropriately Normed Semilocal Density Functional. *Phys Rev Lett* **2015**, *115* (3), 036402. https://doi.org/10.1103/PhysRevLett.115.036402.

(167) Adamo, C.; Barone, V. Toward Reliable Density Functional Methods without Adjustable Parameters: The PBE0 Model. *J. Chem. Phys.* **1999**, *110* (13), 6158–6170. https://doi.org/10.1063/1.478522.

(168) Krukau, A. V.; Vydrov, O. A.; Izmaylov, A. F.; Scuseria, G. E. Influence of the Exchange Screening Parameter on the Performance of Screened Hybrid Functionals. *J. Chem. Phys.* **2006**, *125* (22), 224106. https://doi.org/10.1063/1.2404663.

(169) Kresse, G.; Joubert, D. From Ultrasoft Pseudopotentials to the Projector Augmented-Wave Method. *Phys. Rev. B* **1999**, *59* (3), 1758–1775. https://doi.org/10.1103/PhysRevB.59.1758.

(170) Valldor, M. Manuscript in Production.

(171) Wichelhaus, W. The Rare-Earth Oxide Disulfides $La_2O_2S_2$, $Pr_2O_2S_2$, and $Nd_2O_2S_2$. *Naturwissenschaften* **1978**, *65* (11), 593–594. https://doi.org/10.1007/BF00364913.

(172) Julien-Pouzol, M.; Jaulmes, S.; Mazurier, A.; Guittard, M. Structure Du Disulfure de Lanthane et de Cuivre. *Acta Crystallogr. Sect. B* **1981**, *37* (10), 1901–1903. https://doi.org/10.1107/S0567740881007516.

(173) Johnson, V.; Jeitschko, W. ZrCuSiAs: A "Filled" PbFCl Type. *J. Solid State Chem.* **1974**, *11* (2), 161–166. https://doi.org/10.1016/0022-4596(74)90111-X.

(174) Ito, H.; Miura, A.; Goto, Y.; Mizuguchi, Y.; Moriyoshi, C.; Kuroiwa, Y.; Azuma, M.; Liu, J.; Wen, X.-D.; Nishioka, S.; Maeda, K.; Masubuchi, Y.; Rosero-Navarro, N. C.; Tadanaga, K. An Electronic Structure Governed by the Displacement of the Indium Site in In–S6 Octahedra: $LnOInS_2$ (Ln = La, Ce, and Pr). *Dalton Trans* **2019**, *48* (32), 12272–12278. https://doi.org/10.1039/C9DT01562K.

(175) Huang, F. Q.; Brazis, P.; Kannewurf, C. R.; Ibers, J. A. Synthesis, Structure, Electrical Conductivity, and Band Structure of the Rare-Earth Copper Oxychalcogenide $La_5Cu_6O_4S_7$. *J. Solid State Chem.* **2000**, *155* (2), 366–371. https://doi.org/10.1006/jssc.2000.8926.

(176) Palazzi, M.; Jaulmes, S. Structure d'un Oxysulfure à Deux Cations d'un Type Nouveau: $La_4O_3(AsS_3)_2$. *Acta Crystallogr. Sect. B* **1981**, *37* (7), 1340–1342. https://doi.org/10.1107/S0567740881005888.

(177) Kabbour, H.; Cario, L.; Moëlo, Y.; Meerschaut, A. Synthesis, X-Ray and Optical Characterizations of Two New Oxysulfides: $LaInS_2O$ and $La_5In_3S_9O_3$. *J. Solid State Chem.* **2004**, *177* (4), 1053–1059. https://doi.org/10.1016/j.jssc.2003.10.012.

(178) Jaulmes, S.; Mazurier, A.; Guittard, M. Structure de l'oxypentasulfure de Gallium et de Trilanthane, $GaLa_3OS_5$. *Acta Crystallogr. Sect. C* **1983**, *39* (12), 1594–1597. https://doi.org/10.1107/S0108270183009397.

(179) Freelon, B.; Yamani, Z.; Swainson, I.; Flacau, R.; Karki, B.; Liu, Y. H.; Craco, L.; Laad, M. S.; Wang, M.; Chen, J.; Birgeneau, R. J.; Fang, M. Magnetic and Structural Properties of the Iron Oxychalcogenides $La_2O_2Fe_2OM$ (M=S, Se). *Phys Rev B* **2019**, *99* (2), 024109. https://doi.org/10.1103/PhysRevB.99.024109.

(180) Cohen, S.; Rendon-Diazmiron, L. E.; Steinfink, H. Phases in the $Ba_3Fe_{1+x}S_5$ Series: The Structure of β-$Ba_9Fe_4S_{15}$ and Its Low-Temperature α Polymorph. *J. Solid State Chem.* **1978**, *25* (2), 179–187. https://doi.org/10.1016/0022-4596(78)90101-9.

(181) Mosymow, E.; Glaum, R.; Kremer, R. K. Searching for "$LiCr^{II}PO_4$." *J. Solid State Chem.* **2014**, *218*, 131–140. https://doi.org/10.1016/j.jssc.2014.06.020.

(182) LITTERSCHEID, C.; GLAUM, R. MIXED CHROMIUM (II) TITANIUM (III) PHOSPHATES: CRYSTAL GROWTH, STRUCTURES AND ELECTRONIC ABSORPTION SPECTRA. *Phosphorus Res. Bull.* **2005**, *19*, 54–59. https://doi.org/10.3363/prb1992.19.0_54.

(183) Ciampolini, M.; Nardi, N. Trigonal Bipyramidal Complexes of Bivalent Manganese, Iron, and Zinc with Tris (2-Dimethylaminoethyl)Amine. *Inorg. Chem.* **1966**, *5* (7), 1150–1154. https://doi.org/10.1021/ic50041a016.

(184) Wojciechowski, W. The Metal-Metal Interaction in Coordination Compounds. Magnetic Properties. I. The Dn Dn Electron Systems with Negative Exchange Integral. *Inorganica Chim. Acta* **1967**, *1*, 319–323. https://doi.org/10.1016/S0020-1693(00)93195-5.

(185) Frisch, G.; Röhr, C. Fehlende Glieder Bekannter Reihen: Die Oxoferrate(III) $Rb_8[Fe_2O_7]$, $Rb_6[Fe_2O_6]$ Und $K_4[Fe_2O_5]$ / Missing Links in Known Series: The Oxoferrates(III) $Rb_8[Fe_2O_7]$, $Rb_6[Fe_2O_6]$, and $K_4[Fe_2O_5]$. **2005**, *60* (7), 732–740. https://doi.org/10.1515/znb-2005-0706.

(186) Frisch, G.; Roehr, C. $A_5[Fe_3O_6]$ (A: Rb, Cs), $Cs[FeO_2]$ and $Cs_8[Fe_2O_7]$: New Oxoferrates of the Heavy Alkaline Metals. *ChemInform* **2004**, *35* (40). https://doi.org/10.1002/chin.200440003.

(187) Jana, S.; Yadav, S.; Bishnoi, S.; Niranjan, M. K.; Prakash, J. $Ba_{14}Si_4Sb_8Te_{32}(Te_3)$: Hypervalent Te in a New Structure Type with Low Thermal Conductivity. *Dalton Trans.* **2023**. https://doi.org/10.1039/D3DT01532G.

(188) Broadley, S.; Gál, Z. A.; Corà, F.; Smura, C. F.; Clarke, S. J. Vertex-Linked ZnO_2S_2 Tetrahedra in the Oxysulfide BaZnOS: A New Coordination Environment for Zinc in a Condensed Solid. *Inorg. Chem.* **2005**, *44* (24), 9092–9096. https://doi.org/10.1021/ic051240o.

(189) Salter, E. J. T.; Blandy, J. N.; Clarke, S. J. Crystal and Magnetic Structures of the Oxide Sulfides CaCoSO and BaCoSO. *Inorg. Chem.* **2016**, *55* (4), 1697–1701. https://doi.org/10.1021/acs.inorgchem.5b02615.

(190) Yadav, S.; Panigrahi, G.; Niranjan, M. K.; Prakash, J. Ba_3GeTeS_4: A New Quaternary Heteroanionic Chalcogenide Semiconductor. *J. Solid State Chem.* **2023**, *323*, 124028. https://doi.org/10.1016/j.jssc.2023.124028.

(191) Qin, S.; Li, Y.; Zhang, Q.; Le, C.; Hu, J. Theoretical Studies of Superconductivity in Doped BaCoSO. *Front. Phys.* **2018**, *13* (3), 137502. https://doi.org/10.1007/s11467-018-0745-7.

(192) Klos, S.; Beck, J. The Gallate Pnictides $Ba_9[GaO_4]_3Pn$ (Pn=Sb, Bi) and a Partially Oxidized Zintl Anion in $Ba_2[GaO_2As]$. *Z. Für Anorg. Allg. Chem.* **2022**, *648* (10), e202100363. https://doi.org/10.1002/zaac.202100363.

(193) Lai, K. T.; Adler, P.; Prots, Y.; Hu, Z.; Kuo, C.-Y.; Pi, T.-W.; Valldor, M. Successive Phase Transitions in Fe^{2+} Ladder Compounds $Sr_2Fe_3Ch_2O_3$ (Ch = S, Se). *Inorg. Chem.* **2017**, *56* (20), 12606–12614. https://doi.org/10.1021/acs.inorgchem.7b02042.

(194) Frøen, E. H. Manuscript in Production.

(195) Berthebaud, D.; Preethi Meher, K. R. S.; Pelloquin, D.; Maignan, A. Synthesis, Crystal Structure and Electronic Properties of the New Iron Selenide $Ba_9Fe_4Se_{16}$. *J. Solid State Chem.* **2014**, *211*, 184–190. https://doi.org/10.1016/j.jssc.2013.12.024.

(196) Zhang, J.; Liu, M.; Wang, X.; Zhao, K.; Duan, L.; Li, W.; Zhao, J.; Cao, L.; Dai, G.; Deng, Z.; Feng, S.; Zhang, S.; Liu, Q.; Yang, Y.; Jin, C. Ba9V3Se15: A Novel Compound with Spin Chains. *J. Phys. Condens. Matter* **2018**, *30* (21), 214001. https://doi.org/10.1088/1361-648X/aabdff.

(197) Li, M.-Y.; Zhang, Y.-X.; Lin, H.; Ma, Z.; Wu, X.-T.; Zhu, Q.-L. Combined Experimental and Theoretical Investigations of Ba_3GaS_4I: Interesting Structural Transformation Originated from Halogen Substitution. *Dalton Trans* **2019**, *48* (47), 17588–17593. https://doi.org/10.1039/C9DT04033A.

(198) Stinn, C.; Nose, K.; Okabe, T.; Allanore, A. Experimentally Determined Phase Diagram for the Barium Sulfide-Copper(I) Sulfide System Above 873 K (600 °C). *Metall. Mater. Trans. B* **2017**, *48* (6), 2922–2929. https://doi.org/10.1007/s11663-017-1107-5.

(199) Schlieper, A.; Feutelais, Y.; Fries, S. G.; Legendre, B.; Blachnik, R. Thermodynamic Evaluation of the Germanium — Tellurium System. *Calphad* **1999**, *23* (1), 1–18. https://doi.org/10.1016/S0364-5916(99)00012-7.

(200) Jafarov, Y. I.; Babanly, M. B.; Amiraslanov, I. R.; Gasimov, V. A.; Shevelkov, A. V.; Aliev, Z. S. Study of the $3Tl_2S+Sb_2Te_3\leftrightarrow3Tl_2Te+Sb_2S_3$ Reciprocal System. *J. Alloys Compd.* **2014**, *582*, 659–669. https://doi.org/10.1016/j.jallcom.2013.07.141.

(201) Oogarah, R. K.; Suard, E.; McCabe, E. E. Magnetic Order and Phase Transition in the Iron Oxysulfide $La_2O_2Fe_2OS_2$. *J. Magn. Magn. Mater.* **2018**, *446*, 101–107. https://doi.org/10.1016/j.jmmm.2017.09.024.

(202) Greskovich, C.; Duclos, S. CERAMIC SCINTILLATORS. *Annu. Rev. Mater. Sci.* **1997**, *27* (1), 69–88. https://doi.org/10.1146/annurev.matsci.27.1.69.

(203) Frankovsky, R.; Marchuk, A.; Pobel, R.; Johrendt, D. Synthesis of $LaO_{1-x}F_xFeAs$ (X=0–0.15) via Solid State Metathesis Reaction. *Spec. Issue Iron-Based Supercond.* **2012**, *152* (8), 632–634. https://doi.org/10.1016/j.ssc.2011.11.028.

(204) Hoggins, J. T.; Steinfink, H. Compounds in the Infinitely Adaptive Series $Ba_p(Fe_2S_4)_q$:$Ba_9(Fe_2S_4)_8$. *Acta Crystallogr. Sect. B* **1977**, *33* (3), 673–678. https://doi.org/10.1107/S0567740877004440.

(205) You, J. F.; Snyder, B. S.; Papaefthymiou, G. C.; Holm, R. H. On the Molecular Solid-State Boundary. A Cyclic Iron-Sulfur Cluster of Nuclearity Eighteen: Synthesis, Structure, and Properties. *J. Am. Chem. Soc.* **1990**, *112* (3), 1067–1076. https://doi.org/10.1021/ja00159a028.

(206) Cario, L.; Deudon, C.; Meerschaut, A.; Rouxel, J. Synthesis and Structure Determination of $La_8Ti_{10}S_{24}O_4$. *J. Solid State Chem.* **1998**, *136* (1), 46–50. https://doi.org/10.1006/jssc.1997.7649.

(207) Cody, J. A.; Ibers, J. A. Synthesis and Characterization of the New Rare-Earth/Transition-Metal Oxysulfides $La_6Ti_2S_8O_5$ and $La_4Ti_3S_4O_8$. *J. Solid State Chem.* **1995**, *114* (2), 406–412. https://doi.org/10.1006/jssc.1995.1062.

(208) Hatscher, S. T.; Urland, W. Lanthanum Iodide Thio\-Silicate, $La_3I[SiS_4]_2$. *Acta Crystallogr. Sect. E* **2002**, *58* (11), i100–i102. https://doi.org/10.1107/S1600536802019256.

(209) Hatscher, S. T.; Urland, W. Synthesis and Structures of Chloride Thiosilicates with Lanthanides $Ln_3Cl[SiS_4]_2$ (Ln = La, Ce, Pr). *Mater. Res. Bull.* **2002**, *37* (7), 1239–1247. https://doi.org/10.1016/S0025-5408(02)00770-5.

(210) Holland, M.; Donakowski, M. D.; Pozzi, E. A.; Rasmussen, A. M.; Tran, T. T.; Pease-Dodson, S. E.; Halasyamani, P. S.; Seideman, T.; Van Duyne, R. P.; Poeppelmeier, K. R. Polar Alignment of Λ-Shaped Basic Building Units within Transition Metal Oxide Fluoride Materials. *Inorg. Chem.* **2014**, *53* (1), 221–228. https://doi.org/10.1021/ic402177j.

(211) Press Release. Nobel Prize Outreach AB 2023. November 13, 2023. https://www.nobelprize.org/prizes/chemistry/2023/press-release.

(212) Zhu, R.; Luo, Z.; Chen, H.; Dong, Y.; Wu, S.-T. Realizing Rec. 2020 Color Gamut with Quantum Dot Displays. *Opt Express* **2015**, *23* (18), 23680–23693. https://doi.org/10.1364/OE.23.023680.

(213) Shen, H.; Gao, Q.; Zhang, Y.; Lin, Y.; Lin, Q.; Li, Z.; Chen, L.; Zeng, Z.; Li, X.; Jia, Y.; Wang, S.; Du, Z.; Li, L. S.; Zhang, Z. Visible Quantum Dot Light-Emitting Diodes with Simultaneous High Brightness and Efficiency. *Nat. Photonics* **2019**, *13* (3), 192–197. https://doi.org/10.1038/s41566-019-0364-z.

(214) Shen, X.; Jia, J.; Lin, Y.; Zhou, X. Enhanced Performance of CdTe Quantum Dot Sensitized Solar Cell via Anion Exchanges. *J. Power Sources* **2015**, *277*, 215–221. https://doi.org/10.1016/j.jpowsour.2014.12.022.

(215) Harish, V.; Tewari, D.; Gaur, M.; Yadav, A. B.; Swaroop, S.; Bechelany, M.; Barhoum, A. Review on Nanoparticles and Nanostructured Materials: Bioimaging, Biosensing, Drug Delivery, Tissue Engineering, Antimicrobial, and Agro-Food Applications. *Nanomater. Basel Switz.* **2022**, *12* (3). https://doi.org/10.3390/nano12030457.

(216) Mitchell, M. J.; Billingsley, M. M.; Haley, R. M.; Wechsler, M. E.; Peppas, N. A.; Langer, R. Engineering Precision Nanoparticles for Drug Delivery. *Nat. Rev. Drug Discov.* **2021**, *20* (2), 101–124. https://doi.org/10.1038/s41573-020-0090-8.

(217) Farzin, M. A.; Abdoos, H. A Critical Review on Quantum Dots: From Synthesis toward Applications in Electrochemical Biosensors for Determination of Disease-Related Biomolecules. *Talanta* **2021**, *224*, 121828. https://doi.org/10.1016/j.talanta.2020.121828.

(218) García de Arquer, F. P.; Talapin, D. V.; Klimov, V. I.; Arakawa, Y.; Bayer, M.; Sargent, E. H. Semiconductor Quantum Dots: Technological Progress and Future Challenges. *Science 373* (6555), eaaz8541. https://doi.org/10.1126/science.aaz8541.

(219) Khan, I.; Saeed, K.; Khan, I. Nanoparticles: Properties, Applications and Toxicities. *Arab. J. Chem.* **2019**, *12* (7), 908–931. https://doi.org/10.1016/j.arabjc.2017.05.011.

(220) Dabhane, H.; Ghotekar, S.; Tambade, P.; Pansambal, S.; Murthy, H. C. A.; Oza, R.; Medhane, V. A Review on Environmentally Benevolent Synthesis of CdS Nanoparticle and Their Applications. *Environ. Chem. Ecotoxicol.* **2021**, *3*, 209–219. https://doi.org/10.1016/j.enceco.2021.06.002.

(221) Jang, E.; Jang, H. Review: Quantum Dot Light-Emitting Diodes. *Chem. Rev.* **2023**, *123* (8), 4663–4692. https://doi.org/10.1021/acs.chemrev.2c00695.

(222) Jalali, H. B.; Sadeghi, S.; Dogru Yuksel, I. B.; Onal, A.; Nizamoglu, S. Past, Present and Future of Indium Phosphide Quantum Dots. *Nano Res.* **2022**, *15* (5), 4468–4489. https://doi.org/10.1007/s12274-021-4038-z.

(223)   Won, Y.-H.; Cho, O.; Kim, T.; Chung, D.-Y.; Kim, T.; Chung, H.; Jang, H.; Lee, J.; Kim, D.; Jang, E. Highly Efficient and Stable InP/ZnSe/ZnS Quantum Dot Light-Emitting Diodes. *Nature* **2019**, *575* (7784), 634–638. https://doi.org/10.1038/s41586-019-1771-5.

(224)   Cotta, M. A. Quantum Dots and Their Applications: What Lies Ahead? *ACS Appl. Nano Mater.* **2020**, *3* (6), 4920–4924. https://doi.org/10.1021/acsanm.0c01386.

(225)   Trapalis, A.; Farrer, I.; Kennedy, K.; Kean, A.; Sharman, J.; Heffernan, J. Temperature Dependence of the Band Gap of Zinc Nitride Observed in Photoluminescence Measurements. *Appl. Phys. Lett.* **2017**, *111* (12), 122105. https://doi.org/10.1063/1.4997153.

(226)   Ahumada-Lazo, R.; Fairclough, S. M.; Hardman, S. J. O.; Taylor, P. N.; Green, M.; Haigh, S. J.; Saran, R.; Curry, R. J.; Binks, D. J. Confinement Effects and Charge Dynamics in Zn3N2 Colloidal Quantum Dots: Implications for QD-LED Displays. *ACS Appl. Nano Mater.* **2019**, *2* (11), 7214–7219. https://doi.org/10.1021/acsanm.9b01714.

(227)   Yoo, S.-H.; Walsh, A.; Scanlon, D. O.; Soon, A. Electronic Structure and Band Alignment of Zinc Nitride, Zn3N2. *RSC Adv* **2014**, *4* (7), 3306–3311. https://doi.org/10.1039/C3RA46558F.

(228)   Kołodziejczak-Radzimska, A.; Jesionowski, T. Zinc Oxide—From Synthesis to Application: A Review. **2014**. https://doi.org/10.3390/ma7042833.

(229)   Yang, T.; Zhang, Z.; Li, Y.; Lv, M.; Song, S.; Wu, Z.; Yan, J.; Han, S. Structural and Optical Properties of Zinc Nitride Films Prepared by Rf Magnetron Sputtering. *Appl. Surf. Sci.* **2009**, *255* (6), 3544–3547. https://doi.org/10.1016/j.apsusc.2008.07.210.

(230)   Trapalis, A.; Farrer, I.; Kennedy, K.; Kean, A.; Sharman, J.; Heffernan, J. Improved Ambient Stability of Thermally Annealed Zinc Nitride Thin Films. *AIP Adv.* **2020**, *10* (3), 035018. https://doi.org/10.1063/1.5144054.

(231)   Taylor, P. N.; Schreuder, M. A.; Smeeton, T. M.; Grundy, A. J. D.; Dimmock, J. A. R.; Hooper, S. E.; Heffernan, J.; Kauer, M. Synthesis of Widely Tunable and Highly Luminescent Zinc Nitride Nanocrystals. *J. Mater. Chem. C* **2014**, *2* (22), 4379–4382. https://doi.org/10.1039/C4TC00403E.

(232)   Prabha, S.; Durgalakshmi, D.; Subramani, K.; Aruna, P.; Ganesan, S. Enhanced Emission of Zinc Nitride Colloidal Nanoparticles with Organic Dyes for Optical Sensors and Imaging Application. *ACS Appl. Mater. Interfaces* **2020**, *12* (17), 19245–19257. https://doi.org/10.1021/acsami.9b21585.

(233)   Soundharraj, P.; Dhinasekaran, D.; Rajendran, A. R. Fluorescence Sensing of NADH Using Silica-Zinc Nitride Nanocomposite for Monitoring Diabetes. *Surf. Interfaces* **2023**, *41*, 103207. https://doi.org/10.1016/j.surfin.2023.103207.

(234)   Efros, A. L.; Brus, L. E. Nanocrystal Quantum Dots: From Discovery to Modern Development. *ACS Nano* **2021**, *15* (4), 6192–6210. https://doi.org/10.1021/acsnano.1c01399.

(235)   Montanarella, F.; Kovalenko, M. V. Three Millennia of Nanocrystals. *ACS Nano* **2022**, *16* (4), 5085–5102. https://doi.org/10.1021/acsnano.1c11159.

(236)   Ghosh Chaudhuri, R.; Paria, S. Core/Shell Nanoparticles: Classes, Properties, Synthesis Mechanisms, Characterization, and Applications. *Chem. Rev.* **2012**, *112* (4), 2373–2433. https://doi.org/10.1021/cr100449n.

(237)   Vreeland, E. C.; Watt, J.; Schober, G. B.; Hance, B. G.; Austin, M. J.; Price, A. D.; Fellows, B. D.; Monson, T. C.; Hudak, N. S.; Maldonado-Camargo, L.; Bohorquez, A. C.; Rinaldi, C.; Huber, D. L. Enhanced Nanoparticle Size Control by Extending LaMer's Mechanism. *Chem. Mater.* **2015**, *27* (17), 6059–6066. https://doi.org/10.1021/acs.chemmater.5b02510.

(238) Dongil, A. B. Recent Progress on Transition Metal Nitrides Nanoparticles as Heterogeneous Catalysts. *Nanomaterials* **2019**, *9* (8). https://doi.org/10.3390/nano9081111.

(239) Shibata, M.; Kanetaka, H.; Furuya, M.; Yokota, K.; Ogawa, T.; Kawashita, M. Cytotoxicity Evaluation of Iron Nitride Nanoparticles for Biomedical Applications. *J. Biomed. Mater. Res. A* **2021**, *109* (10), 1784–1791. https://doi.org/10.1002/jbm.a.37171.

(240) Ifijen, I. H.; Maliki, M. A Comprehensive Review on the Synthesis and Photothermal Cancer Therapy of Titanium Nitride Nanostructures. *Inorg. Nano-Met. Chem.* **2023**, *53* (4), 366–387. https://doi.org/10.1080/24701556.2022.2068596.

(241) Chen Ruwen, T. X., Chen Dezhi. Transition Metal Nitrides for Lithium-Ion Batteries. *Prog. Chem.* **2015**, *27* (4), 416–423.

(242) Zhou, P.; Yao, D.; Liang, H.; Xia, Y.; Zeng, Y.-P. Core-Shell Titanium Nitride/Silicon Nitride Modified Separators as Polysulfide Shuttling Barriers for Lithium-Sulfur Batteries via a Facile and Recyclable Molten-Salt Route. *Ceram. Int.* **2023**, *49* (1), 1381–1389. https://doi.org/10.1016/j.ceramint.2022.09.119.

(243) Chen, Y.; Maniruzzaman, M.; Kim, J. Soft-Chemistry Based Fabrication of Gallium Nitride Nanoparticles. *Int. J. Precis. Eng. Manuf.* **2011**, *12* (3), 573–576. https://doi.org/10.1007/s12541-011-0073-0.

(244) Khashan, K. S.; Abbas, S. F. Indium Nitride Nanoparticles Prepared by Laser Ablation in Liquid. *Int. J. Nanosci.* **2019**, *18* (02), 1850021. https://doi.org/10.1142/S0219581X18500217.

(245) Chen, Q.; Li, X.; Cheng, Y.; Zhou, W. Rapid Synthesis of Mo_2N and Mo_2C Nanoparticles Using Non-Toxic Nitrogen Sources in Air Atmosphere. *Adv. Powder Technol.* **2022**, *33* (1), 103375. https://doi.org/10.1016/j.apt.2021.11.027.

(246) Şen, Ö.; Emanet, M.; Çulha, M. One-Step Synthesis of Hexagonal Boron Nitrides, Their Crystallinity and Biodegradation. *Front. Bioeng. Biotechnol.* **2018**, *6*. https://doi.org/10.3389/fbioe.2018.00083.

(247) Riley, F. L. Silicon Nitride and Related Materials. *J. Am. Ceram. Soc.* **2000**, *83* (2), 245–265. https://doi.org/10.1111/j.1151-2916.2000.tb01182.x.

(248) Riedel, R.; Chen, I.-W. *Ceramics Science and Technology, Volume 2: Materials and Properties*; Wiley, 2015; Vol. 2.

(249) Li, F.; Fu, L.; Ma, X.; Sun, C.; Wang, L.; Guo, C.; Qian, Y.; Qian, Y. Additive-Assisted Nitridation to Synthesize Si_3N_4 Nanomaterials at a Low Temperature. *J. Am. Ceram. Soc.* **2009**, *92* (2), 517–519. https://doi.org/10.1111/j.1551-2916.2008.02845.x.

(250) Qaeed, M. A.; Ibrahim, K.; Saron, K. M. A.; Salhin, A. Cubic and Hexagonal GaN Nanoparticles Synthesized at Low Temperature. *Superlattices Microstruct.* **2013**, *64*, 70–77. https://doi.org/10.1016/j.spmi.2013.08.015.

(251) Zieschang, A.-M.; Bocarsly, J. D.; Dürrschnabel, M.; Molina-Luna, L.; Kleebe, H.-J.; Seshadri, R.; Albert, B. Nanoscale Iron Nitride, ε-Fe_3N: Preparation from Liquid Ammonia and Magnetic Properties. *Chem. Mater.* **2017**, *29* (2), 621–628. https://doi.org/10.1021/acs.chemmater.6b04088.

(252) Larquet, C.; Carenco, S. Metal Oxysulfides: From Bulk Compounds to Nanomaterials. *Front. Chem.* **2020**, *8*.

(253) Lingampalli, S. R.; Manjunath, K.; Shenoy, S.; Waghmare, U. V.; Rao, C. N. R. Zn_2NF and Related Analogues of ZnO. *J. Am. Chem. Soc.* **2016**, *138* (26), 8228–8234. https://doi.org/10.1021/jacs.6b04198.

(254) Liu, X.; Wessel, C.; Pan, F.; Dronskowski, R. Synthesis and Single-Crystal Structure Determination of the Zinc Nitride Halides Zn_2NX (X=Cl, Br, I). *J. Solid State Chem.* **2013**, *203*, 31–36. https://doi.org/10.1016/j.jssc.2013.03.046.

(255)   *CRC Handbook of Chemistry and Physics*, 97th ed.; Haynes, W. M., Lide, D. R., Bruno, T. J., Eds.; CRC Press, 2016. https://doi.org/10.1201/9781315380476.

(256)   Лидин, Р. А.; Андреева, Л. Л.; Молочко, В. А. *Константы неорганич веществ Справочник*; 2006.

(257)   Valluri, S. K.; Schoenitz, M.; Dreizin, E. Preparation and Characterization of Silicon-Metal Fluoride Reactive Composites. *Nanomaterials* **2020**, *10* (12). https://doi.org/10.3390/nano10122367.

(258)   Kasi, S. R.; Liehr, M.; Cohen, S. Chemistry of Fluorine in the Oxidation of Silicon. *Appl. Phys. Lett.* **1991**, *58* (25), 2975–2977. https://doi.org/10.1063/1.104686.

8. Appendix – Other Work

This section covers work that was carried out in association with this Ph. D. project, but ultimately did not yield results suitable for inclusion in the main text of the thesis, whether because no usable results were obtained, or because the subject was not found to fall within the main topic. The elements herein discussed are intended as a record of the difficulties encountered, and the results obtained.

8.1. $FeI_2 \cdot 4H_2O$ – A Case Study in Deceptive Crystal Twinning

During a cursory search for novel multianion compounds in a synthesis with nominal composition Fe_2SIO, a high quality, colorless single crystal was obtained.

Refining the structure after measuring SC-XRD data for the compound, a structure described by the *Cmcm* space group was obtained, with a predicted composition SIO_2 (Figure 27). The lattice parameters were $a = 4.605(4)$ Å, $b = 12.291(10)$ Å and $c = 7.404(6)$ Å. The refinement parameters and atomic positions are given in appendix 9.1.6. While the compound proved air sensitive and decomposed during the measurement, the refinement parameters of the structure looked excellent. PXRD suggested a considerable amount of the compound had formed, and so attempts to synthesize this compound pure commenced.
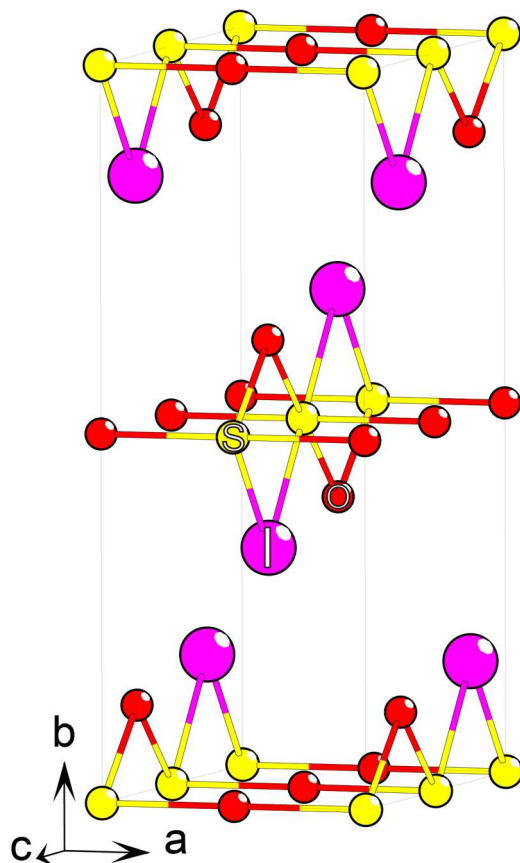
Figure 27: Apparent crystal structure of the twinned SIO_2 structure.

Reliably synthesizing the compound proved impossible; the conditions where the compound appeared to form appeared to be random. SEM/EDX analysis gave wildly varying results and failed to identify the composition with any reliability. The compounds presence was not observed again in the PXRD. New single crystals were intermittently obtained and measured, but the resulting crystal structure, and corresponding composition, was always the same.

In retrospect, knowing what the compound was, the deciding factor for its formation was atmospheric humidity. The hydrate only appears to form under rather specific humidity: To low, and the formation is slow to nonexistent. Single crystals do not appear to form either, only poorly diffracting powder. If the humidity is too high, the iron iodide either does not form usable hydrate single crystals, or deliquesces to lose all structure, and cannot be measured.

The true composition of the SIO_2 compound was in fact $FeI_2 \cdot 4H_2O$, which exhibits the same structure type as the chloride and bromide analogs: A monoclinic structure with the $P2_1/c$ space group. The actual lattice parameters, again determined by SC-XRD data, are $a = 6.5577$ Å, $b = 7.3954$ Å, $c = 9.1963$ Å, and $\beta = 110.3814°$. The crystal structure is shown in Figure 28, and

the refinement details are given in appendix 9.1.6. As one would expect from the ionic radii, all lattice parameters are increased compared with the Cl and Br analogs. The lattice angle, however, consistently decreases as the anion radius increases.
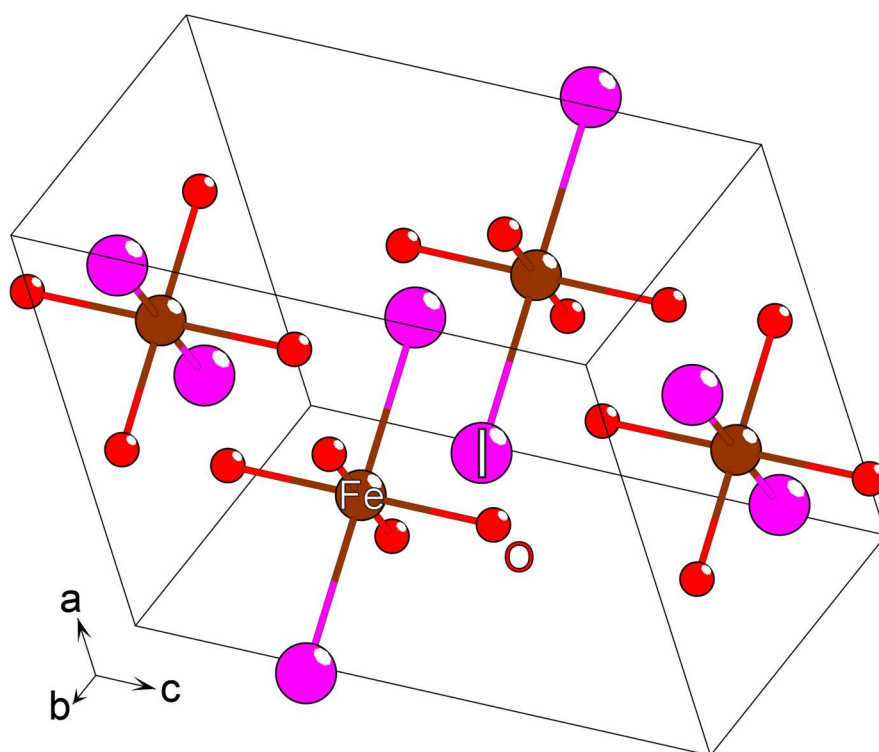

Figure 28: The real crystal structure of the "SIO$_2$" phase, with composition FeI$_2$•4H$_2$O. The hydrogen ions are not depicted.

FeI$_2$•4H$_2$O is a poorly characterized compound, with information scattered and poorly referenced. This is likely due to the sensitivity of FeI$_2$ to atmospheric water, and possibly the purported existence of di-, tetra-, hexa- and nona-hydrates (unsourced Wikipedia claim, no online source could be found for any hydrate except the tetra coordination, although this may be language barriers) complicating and conflating matters.

The tetrahydrate is reported to be either black,[255] or green,[256] although the latter may be a spelling error for white, as the Russian source uses abbreviated words for the compound color, so white and green only differ by one letter (бел vs. зел). We observed the individual crystals to be colorless, which would yield a white powder. The crystals did gradually change color during measurement, slowly turning black, but this was accompanied by a gradual loss in diffraction intensity. The fully converted black crystals gave no discernable diffraction spots, indicating low to nonexistent crystallinity in this converted species. It should be noted that the single crystal reflections did not distort or change as the black phase formed, only weakened,

so there does not appear to be a different crystalline phase formed during the decomposition of the tetrahydrate.

The cause behind the confusion of the crystal structure and its composition, is partly the propensity of $FeI_2 \cdot 4H_2O$ to form crystal twins, and partly a coincidental relation between the nominal composition of the synthesis and the atomic numbers of the constituent atoms.

The twin law describing the crystallographic twins of $FeI_2 \cdot 4H_2O$ is a *c*-mirror law, one of the most common variations of crystal twinning for monoclinic systems. It is an example of a non-merohedral twinning arrangement, where certain positions within the resulting unit cell are doubly occupied, while others overlap. In this particular case, the iodine- and oxygen-positions overlap with themselves, which makes no difference, while the Fe-positions end up with an apparent halved occupancy. However, a Fe^{2+} ion has 24 electrons associated with it. With a 0.5 occupancy, this is indistinguishable from S^{4+}, or S^{5+} as the composition SIO_2 would theoretically have, for XRD-based methods.

Now, while working backwards to find the twinning arrangement from the correct structure is trivial with modern computer tools, which will directly solve the problem at the press of a button, determining the correct crystal structure when all measurements give a completely different unit cell is a significantly more complicated matter. The author is not aware of any simple computer tool which can solve this particular case.

Due to the apparent randomness of the "SIO_2" synthesis conditions, and the sensitivity of the compound to atmospheric conditions, obtaining a usable sample for EDX analysis was difficult. When a usable sample was finally obtained, the indication that the compound consisted at least in part of iron and iodine was the first indication that the crystal structure was derived from a twin. Reexamining the crystal structure of "SIO_2" with this perspective, and starting from the apparent *Cmcm* crystal structure that results from the measurement, the process to realize the correct structure went as follows:

1. Assume the *Cmcm* structure is the product of a twin crystal, with half-occupied Fe-positions.
2. Double the *a*- and *b*-axes, while filling in with the atomic positions with unit cells, as this is the minimum cell to resolve for an ordered arrangement from the 0.5 occupancy of Fe.
3. Selectively remove Fe-positions to obtain an ordered crystal structure that could theoretically be stable, without immediately rearranging.

4. Search the resulting structure for a smaller unit cell, which turned out to be monoclinic.
5. Use the new monoclinic cell as a starting point and constraint for redetermination of the unit cell from the raw SC-XRD data.
6. Refine the structure from the new unit cell, including the appropriate twin law.

Once the correct crystal structure was known, it was swiftly identified as an analog of the $FeX_2 \cdot 4H_2O$ (X = Cl, Br) compounds, which made the identity of the compound obvious.

Another factor that served to deceive as to the correct nature of this compound, was the PXRD, gathered on the same sample from which "SIO_2" was originally discovered. The twinned *Cmcm* and correct $P2_1/c$ crystal structures would theoretically have very similar PXRD signals, but the monoclinic structure should exhibit different peak intensities, certain split peaks, and some additional peaks. The PXRD, however, showed none of the features that would indicate the final monoclinic structure, and rather matched better with the expected diffraction from the twinned *Cmcm* structure.

8.2. Oxy- and Nitride-Fluorides

The initial plan for the nitride-fluorides and oxyfluorides, was to employ the same methodology as for the bichalcogenides, utilizing a corundum crucible with a silica ampoule. This ran into an immediate stumbling block, as fluorides are volatile, and highly reactive at elevated temperatures. It was found that the fluorides would sublimate off, either as fluorides or as transient oxyfluorides, react with the SiO_2 in the ampoule, and transport the SiO_2 back into the initial reaction mixture to form silicate impurities. Depending on the atomic species involved in a given reaction, and the duration of the synthesis, the quantity of silicates could become the majority constituent of the product. It was evident that this was a gas diffusion-based side reaction from the fact that certain syntheses would be halfway converted; only the half closer to the opening of the crucible would have formed silicates.

As many fluorides would also readily react with Al_2O_3, even at comparatively low temperatures, the corundum crucibles were also found to be unsuitable for the task. In an attempt to remedy these issues, crucibles of a Monel alloy (composed primarily of Nickel and Copper with smaller quantities of iron and other metals), which could be crimped shut, were attempted. These worked well for pure fluorides, but mixtures of oxides and fluorides remained problematic, due to what is assumed to be multiple reasons. Firstly, the fluorides exhibited a trend to sublimate at temperatures needed for the oxides to react at any appreciable rate.

Secondly, the combination of oxides and fluorides appears to form transient, volatile species with excellent gas transport properties.

This same issue affected the attempts at nitride-fluoride syntheses as well. The commercial nitrides utilized were rarely completely free of oxygen contamination. The small initial proportion of oxygen started the oxyfluoride transport mechanism, which proceeded to bring in more oxygen from the ampoule walls, leading to a feedback loop that continuously sped up the introduction of more oxygen. The eventual consequence was usually a complete loss of the nitride species by conversion to oxides or oxy-nitrides depending on the cations involved.

An interesting observation made over the course of these experiments, was that a mixture of certain oxides and fluorides, if heated to 750-800 °C in the presence of a Monel alloy, would cause gas transport of SiO_2 from the amorphous silica ampoule to the Monel alloy surface, forming a fibrous material, soft to the touch, of crystalline quartz. The transport is believed to be caused by the formation of silicon oxyfluorides, which are highly volatile.[257,258]

Two examples of compositions which would cause this effect was ZnF_2 + ZnO in a 1:1 molar ratio at 800 °C, and CoF_3 + CoO + Co in a 5:4:1 molar ratio at 750 °C. The result from these syntheses are illustrated in Figure 29. SEM imaging of the latter is shown in Figure 30.

Figure 29: Monel crucibles covered in fibrous quartz after attempted oxyfluoride synthesis. The left and right crucibles correspond to "ZnOF" and "$Co_{10}O_4F_{15}$" syntheses, respectively.
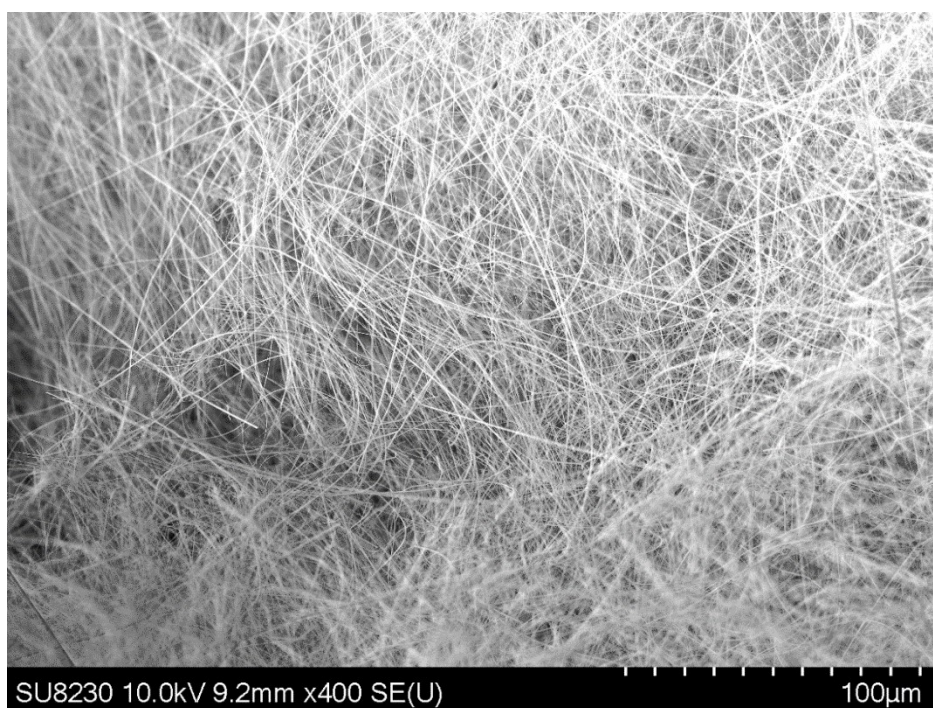
Figure 30: SEM image of fibrous quartz structures observed to form on Monel alloy crucibles during certain attempts at oxyfluoride syntheses.

The fibers mostly range in thickness from around 100 nm in diameter up to a couple hundred, with some outliers exhibiting a diameter of about 1.5-2 μm. They are highly electrically insulating and attempting to image them close up results in severe distortion of the image from build-up of charge.

It should be noted that we have no data on how large a proportion of the fibrous structure is crystalline; it is possible that only certain parts of the fibrous structures are crystalline, while the remainder consists of fibrous glass, but this would lack a thermodynamic incentive for the silica to selectively transfer off the glass walls.

A potential usage case for such quartz fibers would be as a potential alternative to asbestos, similar to the usage of glass fiber. This would, of course, depend on whether these fibers are less harmful to humans than asbestos. Another usage case would be as an inert matrix for deposition of an active coating.

9. Appendix – Additional Data

9.1. Appendix – Crystal Structure Refinement Data

This section provides further details on the refinement statistics for the compounds not discussed in full articles. Further, the ionic positions of the crystal structures are provided in full.

9.1.1. Appendix – Refinement Data and Crystal Structure of $Ba_9Fe_4Te_{3.5}S_{12.5+\delta}$

Table 6: Structure and refinement data of $Ba_9Fe_4Te_{3.5}S_{12.5+\delta}$.

Formula	$Ba_9Fe_4Te_{3.5}S_{12.622}$
Radiation	Mo $K\alpha$ ($\lambda = 0.71073$ Å)
Instrument	BRUKER D8 Venture
Physical Appearance	Black
Crystal System	Orthorombic
Space Group	$P4_1$ (No. 76)
Formula Weight/g mol^{-1}	2310.71
Temperature/K	293
a/Å	9.7818(3)
c/Å	34.851(2)
V/Å^3	3334.7(2)
Z	4
ρ_{calc}/g cm^{-3}	4.6025
Independent Reflections	9304
No. of variables	306
GOF (obs) on F^2	1.82
GOF (all) on F^2	1.79
R1 (obs)/%	3.23
R1 (all)/%	3.58
wR2 (obs)/%	9.57
wR2 (all)/%	9.67

Table 7: Atomic sites, occupancies and isotropic thermal parameters for the refinement of $Ba_9Fe_4Te_{3.5}S_{12.5+\delta}$.

Atom	Site	x	y	z	Occupancy	U_{iso} (Å^2)
Ba1	4a	0.23033(5)	0.75160(5)	0.51902(3)	1	0.0120(2)
Ba2	4a	0.36084(6)	0.56736(6)	0.41271(3)	1	0.0185(2)
Ba3	4a	0.83927(6)	0.98127(7)	0.54918(3)	1	0.0243(2)
Ba4	4a	0.09607(6)	0.95442(5)	0.41730(2)	1	0.0182(2)
Ba5	4a	0.62338(6)	0.95787(6)	0.37499(3)	1	0.0194(2)
Ba6	4a	0.88865(6)	0.57192(5)	0.37031(2)	1	0.0179(2)

Ba7	4a	0.00917(7)	0.36466(6)	0.48683(2)	1	0.0238(2)
Ba8	4a	0.62033(6)	0.52860(7)	0.54987(3)	1	0.0284(2)
Ba9	4a	0.45151(7)	0.14136(6)	0.48936(3)	1	0.0288(2)
Te1	4a	0.8528(5)	0.2425(3)	0.39609(9)	0.81(2)	0.0296(7)
Te2	4a	0.1310(5)	0.2831(2)	0.3905(2)	0.79(2)	0.0298(7)
Te3	4a	0.4928(1)	0.26250(8)	0.39502(3)	0.810(2)	0.0300(2)
Te4	4a	0.0364(2)	0.3140(2)	0.58147(4)	0.224(3)	0.0288(5)
Te5	4a	0.6727(2)	0.5686(2)	0.45551(5)	0.153(3)	0.0296(6)
Te6	4a	0.6842(3)	0.3486(3)	0.44717(7)	0.243(2)	0.0231(8)
Te7	4a	0.787(6)	0.2570(9)	0.3924(2)	0.16(2)	0.053(7)
Te8	4a	0.193(4)	0.2712(8)	0.3949(2)	0.15(2)	0.039(4)
Te9	4a	0.8232(4)	0.2984(4)	0.5907(2)	0.16(4)	0.024(2)
Fe1	4a	0.5973(2)	0.7999(2)	0.47381(4)	1	0.0124(3)
Fe2	4a	0.8654(2)	0.7076(2)	0.47482(4)	1	0.0125(3)
Fe3	4a	0.1821(2)	0.1191(2)	0.56372(4)	1	0.0131(3)
Fe4	4a	0.2750(2)	0.3884(2)	0.56292(4)	1	0.0124(3)
S1	4a	0.0364(2)	0.3140(2)	0.58147(4)	0.776(3)	0.0288(5)
S2	4a	0.6727(2)	0.5686(2)	0.45551(5)	0.847(3)	0.0296(6)
S3	4a	0.1261(2)	0.9223(2)	0.59589(6)	1	0.0130(5)
S4	4a	0.3403(2)	0.5775(2)	0.59713(6)	1	0.0141(6)
S5	4a	0.9187(2)	0.6599(2)	0.53708(6)	1	0.0155(6)
S6	4a	0.5407(2)	0.8457(2)	0.53602(7)	1	0.0183(6)
S7	4a	0.4019(2)	0.1935(2)	0.57882(6)	1	0.0159(6)
S8	4a	0.7910(2)	0.9269(2)	0.45903(6)	1	0.0154(6)
S9	4a	0.3243(2)	0.4437(2)	0.50083(6)	1	0.0152(6)
S10	4a	0.0619(2)	0.6521(2)	0.44186(6)	1	0.0139(6)
S11	4a	0.4067(2)	0.8644(2)	0.44028(6)	1	0.0152(6)
S12	4a	0.1341(2)	0.0646(2)	0.50183(7)	1	0.0170(6)
S13	4a	0.7272(3)	0.2574(3)	0.50643(1)	1	0.044(1)

9.1.2. Appendix – Refinement Data and Crystal Structure of Ba_3VTeS_4

Table 8: Structure and refinement data of Ba_3VTeS_4

Formula	Ba_3VTeS_4
Radiation	Mo $K\alpha$ ($\lambda = 0.71073$ Å)
Instrument	BRUKER D8 Venture
Physical Appearance	Black
Crystal System	Orthorombic
Space Group	$Cmcm$ (No. 63)
Formula Weight/g mol^{-1}	718.8
Temperature/K	293
a/Å	6.7533(3)
b/Å	16.1831(7)
c/Å	9.6458(4)
V/Å^3	1054.18(8)

Z	4
ρ_{calc}/g cm^{-3}	4.5290
Independent Reflections	1182
No. of variables	31
GOF (obs) on F^2	1.71
GOF (all) on F^2	1.67
R1 (obs)/%	1.66
R1 (all)/%	1.95
wR2 (obs)/%	4.55
wR2 (all)/%	4.62

Table 9: Atomic positions and isotropic thermal parameters for the refinement of Ba$_3$VTeS$_4$

Atom	Site	x	y	z	U_{iso} (Å^2)
Ba1	8f	0	0.34498(1)	0.47912(2)	0.01405(6)
Ba2	4c	½	0.55131(2)	¼	0.01149(7)
V1	4c	½	0.31441(4)	¼	0.0099(2)
Te1	4c	0	0.50845(2)	¼	0.01314(7)
S1	8g	0.2436(2)	0.23140(5)	¼	0.0150(2)
S2	8f	½	0.38652(5)	0.44374(8)	0.0162(2)

9.1.3. Appendix – Refinement Data and Crystal Structure of Ba$_2$Mn$_3$Te$_2$S$_3$

Table 10: Structure and refinement data of Ba$_2$Mn$_3$Te$_2$S$_3$.

Formula	Ba$_2$Mn$_3$Te$_2$S$_3$
Radiation	Mo $K\alpha$ ($\lambda = 0.71073$ Å)
Instrument	BRUKER D8 Venture
Crystal System	Orthorombic
Space Group	$Pbam$ (No. 55)
Formula Weight/g mol^{-1}	790.87
Temperature/K	293
a/Å	11.8025(4)
b/Å	9.0163(3)
c/Å	4.8592(2)
V/Å^3	517.09(3)
Z	2
ρ_{calc}/g cm^{-3}	5.0795
Independent Reflections	2685
No. of variables	36

GOF (obs) on F^2	1.98
GOF (all) on F^2	1.72
R1 (obs)/%	3.67
R1 (all)/%	7.69
wR2 (obs)/%	6.77
wR2 (all)/%	8.19

Table 11: Atomic sites, occupancies and isotropic thermal parameters for the refinement of $Ba_2Mn_3Te_2S_3$.

Atom	Site	x	y	z	Occupancy	U_{iso} ($Å^2$)
Ba1	4g	0.33999(2)	0.90514(2)	0	1	0.01194(4)
Te1	4h	0.33579(2)	0.60023(2)	½	1	0.01555(5)
Mn1	4e	½	½	0.9064(4)	0.5	0.0466(6)
Mn2	4h	0.6015(2)	0.7743(2)	½	0.5	0.0233(3)
Mn3	4h	0.5613(2)	0.7292(2)	½	0.5	0.0233(3)
S1	2d	½	0	½	1	0.0136(3)
S2	4g	0.59176(6)	0.73102(8)	0	1	0.0114(2)

9.1.4. Appendix – Refinement Data and Crystal Structure of La_2TeS_2

Table 12: Structure and refinement data of La_2TeS_2

Formula	La_2TeS_2
Radiation	Mo $K\alpha$ (λ = 0.71073 Å)
Instrument	BRUKER D8 Venture
Crystal System	Trigonal
Space Group	$P\bar{3}m1$ (No. 164)
Formula Weight/g mol^{-1}	469.53
Temperature/K	293
a/Å	4.7127(1)
c/Å	7.8044(3)
V/Å^3	150.110(7)
Z	1
ρ_{calc}/g cm^{-3}	5.1940
Independent Reflections	607
No. of variables	9
GOF (obs) on F^2	1.83
GOF (all) on F^2	1.71
R1 (obs)/%	3.84
R1 (all)/%	5.78
wR2 (obs)/%	7.31
wR2 (all)/%	7.68

Table 13: Atomic positions and isotropic thermal parameters for the refinement of La_2TeS_2

Atom	Site	x	y	z	U_{iso} ($Å^2$)
La1	2d	0.33333	0.66667	0.26536(4)	0.01005(9)
Te1	1a	0	0	0	0.01058(2)
S1	2d	0.66667	0.33333	0.36388	0.0111(3)

9.1.5. Appendix - Refinement Data and Crystal Structure of $La_{10}Te_{14+x}S_{1-x}$

Table 14: Structure and refinement data of $La_{10}Te_{14+x}S_{1-x}$.

Formula	$La_{10}Te_{14.077}S_{0.923}$
Radiation	Mo $K\alpha$ ($\lambda = 0.71073$ Å)
Instrument	BRUKER D8 Venture
Crystal System	Tetrahedral
Space Group	$I4_1/acd$ (No. 142)
Formula Weight/g mol^{-1}	3214.86
Temperature/K	293
a/Å	16.930(3)
c/Å	22.485(3)
V/Å^3	6445(2)
Z	8
ρ_{calc}/g cm^{-3}	6.6268
Independent Reflections	1150
No. of variables	58
GOF (obs) on F^2	1.98
GOF (all) on F^2	1.69
R1 (obs)/%	6.63
R1 (all)/%	14.96
wR2 (obs)/%	14.17
wR2 (all)/%	15.89

Table 15: Atomic positions and isotropic thermal parameters for the refinement of $La_{10}Te_{14+x}S_{1-x}$

Atom	Site	x	y	z	Occupancy	U_{iso} ($Å^2$)
La1	16f	0.3633(2)	0.1367(2)	0	1	0.0145(8)
La2	32g	0.1381(2)	0.0101(2)	0.07004(9)	1	0.0194(8)
La3	32g	0.6301(2)	0.2238(2)	0.07766(9)	1	0.0241(9)
Te1	32g	0.8422(2)	0.1763(2)	0.0329(1)	1	0.0193(9)

Te2	32g	0.6768(2)	0.0382(2)	0.0452(1)	1	0.0186(9)
Te3	32g	0.4769(2)	0.1323(2)	0.1196(2)	1	0.0262(9)
Te4	16e	¼	0.1487(2)	0.125	1	0.040(2)
Te5	8a	0	0	0	0.08(2)	0.037(7)
S1	8a	0	0	0	0.92(2)	0.037(7)

9.1.6. Appendix – Refinement Data and Crystal Structures of FeI$_2$•4H$_2$O and the Twinned "SIO$_2$"

Table 16: Structure and refinement data of FeI$_2$•4H$_2$O. The effect of hydrogen is neglected.

Formula	FeI$_2$•4H$_2$O
Radiation	Mo $K\alpha$ (λ = 0.71073 Å)
Instrument	BRUKER D8 Venture
Physical Appearance	Colorless
Crystal System	Monoclinic
Space Group	$P2_1/c$ (No. 14)
Formula Weight/g mol^{-1}	373.65
Temperature/K	293
a/Å	6.5578(8)
b/Å	7.3956(8)
c/Å	9.197(2)
β/Å	110.380(4)
V/Å^3	418.1024(8)
Z	2
ρ_{calc}/g cm^{-3}	2.9680
Independent Reflections	1151
No. of variables	35
GOF (obs) on F^2	1.73
GOF (all) on F^2	1.58
R1 (obs)/%	3.80
R1 (all)/%	6.86
wR2 (obs)/%	7.98
wR2 (all)/%	8.75

Table 17: Atomic positions and isotropic thermal parameters for the refinement of FeI$_2$•4H$_2$O

Atom	Site	x	y	z	U_{iso} (Å^2)
Fe1	2a	½	0	½	0.0250(5)
I1	4e	0.17538(7)	0.27928(9)	0.4201(2)	0.0322(2)
O1	4e	0.498(2)	0.9982(8)	0.2680(5)	0.050(3)

144

O2	4e	0.7369(8)	0.2005(7)	0.558(1)	0.043(2)

Table 18: Structure and refinement data of the twinned structure "SIO$_2$".

Formula	SIO$_2$
Radiation	Mo $K\alpha$ ($\lambda = 0.71073$ Å)
Instrument	BRUKER D8 Venture
Physical Appearance	Colorless
Crystal System	Orthorombic
Space Group	*Cmcm* (No. 63)
Formula Weight/g mol^{-1}	230.81
Temperature/K	293
a/Å	4.605(4)
b/Å	12.29(1)
c/Å	7.404(6)
V/Å^3	419.0(6)
Z	4
ρ_{calc}/g cm^{-3}	3.6586
Independent Reflections	231
No. of variables	17
GOF (obs) on F^2	1.94
GOF (all) on F^2	1.63
R1 (obs)/%	3.93
R1 (all)/%	8.17
wR2 (obs)/%	7.64
wR2 (all)/%	8.48

Table 19: Atomic positions and isotropic thermal parameters for the refinement of twinned structure "SIO$_2$".

Atom	Site	x	y	z	U_{iso} (Å^2)
S1	4a	0	0.1625(2)	¼	0.0535(6)
I1	4c	0	0	0	0.040(2)
O1	4b	½	0	0	0.060(6)
O2	4c	0	0.119(2)	¾	0.099(9)

9.2. Appendix – Failed Syntheses

This appendix is intended as a record of the phase diagrams that were probed for novel phases over the course of this work, but which failed to yield any products aside from previously

reported phases. These are here briefly listed so that next-coming researcher in this field does not have to repeat the same failures.

Table 20: A record of phase diagrams which were probed for new phases, but failed to yield anything of note, beyond previously reported compounds.

System	Synthesis Temperature (°C)
$CaO + CoF_3$	750 – 1000
$SrO + CoF_3$	750
$MnO + CoF_3$	750 – 850
$Al_2O_3 + CoF_3$	750
$CoO + CoF_3 + Co$	750 – 950
$ZnO + ZnF_2$	500 – 950
$MnO + ZnF_2$	750
$ZnF_2 + MnF_2 + Fe_2O_3$	750
$La_2O_3 + CoF_3$	750
$La_2O_3 + MgF_2$	750
$La_2O_3 + ZnF_2$	750
$La_2O_3 + CaF_2$	750
$La_2O_3 + MnF_2$	750
$La_2O_3 + LiF$	750
$La_2O_3 + TiF_3$	750
$La_2O_3 + NaH$	500
$La_2O_3 + CaH_2$	500
$Li_3N + MgF_2$	500
$Li_3N + ZnF_2$	500
$Li_3N + CaF_2$	500
$Li_3N + MnF_2$	500
$Li_3N + LiF$	500
$Li_3N + TiF_3$	500
$Zn_3N_2 + CaF_2$	500
$Zn_3N_2 + MgF_2$	500
$Zn_3N_2 + MnF_2$	500
$Zn_3N_2 + LiF$	500
$Zn_3N_2 + TiF_3$	500
$Ca_3N_2 + CoF_3$	500
$Ca_3N_2 + MgF_2$	500
$Ca_3N_2 + ZnF_2$	500 - 750
$Ca_3N_2 + MnF_2$	750
$Ca_3N_2 + Zn_3N_2 + MnF_2 + ZnF_2$	500
$Li_2O + ZnO + TiF_3$	1000
$Ca_3N_2 + TiF_3$	1000
$Mg_3N_2 + CoF_3$	750
$Mg_3N_2 + MnF_2$	750
$Mg_3N_2 + ZnF_2$	750
$Mg_3N_2 + CaF_2$	750
$Mg_3N_2 + MnF_2$	750
$Mg_3N_2 + LiF$	750

$Mg_3N_2 + TiF_3$	750 – 1000
$CaO + CaF_2$	1000 - 1100
$Al_2O_3 + TiF_3$	450 - 800
$Al_2O_3 + ZnF_2$	500
$LiF + Cr_2O_3 + SrO$	500
$LiF + Cr_2O_3 + Al_2O_3$	750
$Cr_2O_3 + MnF_2$	750
$Cr_2O_3 + MnF_2 + SrO$	750
$SrO + TiF_3$	500
$SrO + TiH_2$	500 – 1000
$TiO + TiH_2$	800 – 900
$SrF_2 + TiH_2$	800 – 1100
$Ti + TiH_2 + TiF_3$	450 – 800
$La_2O_3 + TiO_2 + Ti + TiF_3$	800
$TiO_2 + TiH_2$	600 – 800
$Ni + TiH_2 + TiF_3$	800
$LaN + TiF_3$	500
$LaN + Co + CoF_3$	500
$LaN + TiF_3 + Ti$	500
$LaN + MnF_3$	500
$LaN + CoF_3$	500
$LaN + CoF_3 + Co$	500
$LaN + MnF_2 + Mn$	500
$LaN + MgF_2$	500 – 1000
$LaN + ZnF_2$	500
$LaN + CaF_2$	500 – 1000
$LaN + LiF$	500
$LaN + SrF_2$	500
$LaN + BaF_2$	500
$LaN + CoF_3 + Ni$	500
$NbN + CoF_3$	500
$NbN + CoF_3 + Co$	500
$NbN + MgF_2$	500
$NbN + ZnF_2$	500
$LaN + MgF_2 + Mg$	500
$NbN + CaF_2$	500
$NbN + MnF_3$	500
$NbN + LiF$	500
$LaN + SrO$	1000
$LaN + Si_3N_4 + SrF_2$	1000
$LaN + AgF_2$	400
$LaN + La + I$	700
$Si_3N_4 + AgF_2$	400
$Si_3N_4 + CaF_2$	1000
$Si_3N_4 + BaF_2$	1000
$Si_3N_4 + LaN + La + MnF_3$	900
$LaN + BaF_2 + AgF_2$	400
$ZnF_2 + SeO_2$	300

$ZnF_2 + TeO_2$	700
$BaF_2 + SrO + Ni + Cu + S$	800
$Si_3N_4 + TiN + TiF_2$	800
$La + Li + Te + S$	900
$La + Cr2O3 + Cr + S$	1000
$Ti + Te + TiH_2$	300
$CaH_2 + Te$	500
$La + ZnO + S$	1000 – 1100
$La + Fe + ZnO + S$	1000 – 1100
$La + Fe + CaO + S$	1000 – 1100
$La + Fe + CaO + Se$	1000 – 1100
$La + La_2O_3 + Al_2O_3 + Fe + S$	1000 – 1100
$La + La_2O_3 + Ni + S$	1000 – 1100
$La + La_2O_3 + Fe + Ti + S$	1000 – 1100
$La + La_2O_3 + Fe + V + S$	1000 – 1100
$La + La_2O_3 + Al + Cr + S$	1000 – 1100
$La + La_2O_3 + Al + Mn + S$	1000 – 1100
$La + La_2O_3 + Al + Ni + S$	1000 – 1100
$La + La_2O_3 + Al + Zn + S$	1000 – 1100
$La + La_2O_3 + Al + Ti + S$	1000 – 1100
$La + La_2O_3 + Al + V + S$	1000
$La + La_2O_3 + CdS + Al + S$	900
$La + La_2O_3 + CdS + Fe + S$	900
$La + CuO + Al + S$	1000
$La + Ga + Fe + La_2O_3 + S$	1000
$La + MnO + S$	1000
$La + MnO + Fe + S$	1000
$La + La_2O_3 + Fe + Cr + S$	1000
$La + La_2O_3 + Fe + Co + S$	1000
$La + La_2O_3 + Fe + Ni + S$	1000
$La + La_2O_3 + CdS + Ga + S$	900
$Ga + Te + S$	850
$La + TiO_2 + S$	1000
$Na_2S + V_2O_5 + V + S$	700
$La + La_2O_3 + Cr + S$	1000
$La + La_2O_3 + Ti + S$	1000
$La + La_2O_3 + V + S$	1000
$La + La_2O_3 + Co + S$	1000
$La + La_2O_3 + Cu + S$	1000
$Cs_2O + V_2O_5 + V + Se$	700
$CsCl + Fe + S + Te$	750
$Ni + S + Te + I$	600
$SrS + Fe + Fe_2O_3 + S$	1000
$CsCl + La_2O_3 + Cu + S$	800
$Li + Ni + S + I$	700
$Ni + In_2O_3 + S$	1000
$La + Fe + Te + S$	750
$CuO + Ge + CdS + S$	800

148

SrS + Cu + Te	700
HgO + Cu + I	400
La$_2$O$_3$ + HgO + Cu + I	400
CaF$_2$ + Fe + B	1000
SrF$_2$ + SrO + CuO	900
CdS + HgO	600
CdS + HgO + I	450 - 500
SrS + Fe + Te	700 - 1000
BaS + CdS + Fe + Te	900
La$_2$O$_3$ + CdS + Cu + S	900
SrS + SrO + Fe + S	1000
TeO$_2$ + I	1000
SeO$_2$ + I	1000
BaS + CdS + NiS + Ge + Te	800
La + HgO + I	700
HgCl$_2$ + Fe + As	700
La$_2$O$_3$ + In$_2$S$_3$ + CdS + CuO	800
BaS + Ti + Te	800 – 1000
BaS + Co + Te	800 – 1100
BaS + Ni + Te	1000
La + Fe + As + Te	800
La$_2$O$_3$ + Cu + Mn + S	800
La$_2$O$_3$ + Cu + V + S	800
La$_2$O$_3$ + Cu + Co + S	800
La$_2$O$_3$ + Cu + Ni + S	800
BaS + Sc + Te	700 – 900
Ca + Fe + Te + S	750 – 900
La + HgO + Te	600
La$_2$O$_3$ + Ti + Cu + S	1000
La$_2$O$_3$ + V + Cu + S	1000
La$_2$O$_3$ + Mn + Cu + S	1000
La$_2$O$_3$ + Co + Cu + S	1000
La$_2$O$_3$ + Ni + Cu + S	1000
La$_2$O$_3$ + Zn + Cu + S	1000
La$_2$O$_3$ + Ni + Ti + S	1000
La$_2$O$_3$ + Ni + Cr + S	1000
Tl + Fe + Te + S	800
HgO + Ti + S	550
HgO + V + S	550
HgO + Co + S	550
HgO + Fe + S	550
HgO + Ni + S	550
HgO + Cu + S	550
HgO + Zn + S	550
Tl + Ti + S + Te	600 – 700
BaS + Fe + Ge + Te	650 – 700
La$_2$O$_3$ + Sc + Cu + S	1000

10. Appendix – Associated Papers 1–4

I

Article

Synthesis and Properties of $Ba_6Fe_2Te_3S_7$, with an Fe Dimer in a Magnetic Singlet State

Emil H. Frøen, Peter Adler, and Martin Valldor*

Read Online

ACCESS | Metrics & More | Article Recommendations

ABSTRACT: A new quaternary sulfide telluride, $Ba_6Fe_2Te_3S_7$, was synthesized by a solid-state reaction, and its crystal structure is novel. X-ray diffraction data on powder and single crystals reveal an orthorhombic lattice with a = 9.7543(3) Å, b = 18.2766(6) Å, and c = 12.0549(4) Å, and the noncentrosymmetric space group $Cmc2_1$ (No. 36). The properties of the compound were studied by magnetic susceptibility investigations, specific heat measurements, Mössbauer spectroscopy, and density functional theory calculations. Assuming Ba^{2+} and, as verified by the Mössbauer spectra, Fe^{3+}, the charge balance requires the presence of a polytelluride, suggested to be a straight-chain $[Te_3^{4-}]$ polyanion. Further, the crystal structure contains $[Fe_2S_7]^{8-}$ dimers of two vertex-sharing tetrahedra, with a nearly linear Fe–S–Fe atom arrangement. The dimer exhibits antiferromagnetic coupling, with a coupling constant J = −10.5 meV (H = −$2JS_1S_2$) and S = 5/2, resulting in a spin singlet ground state. The interdimer magnetic interaction is so weak that the magnetic dimers can be treated as individuals.
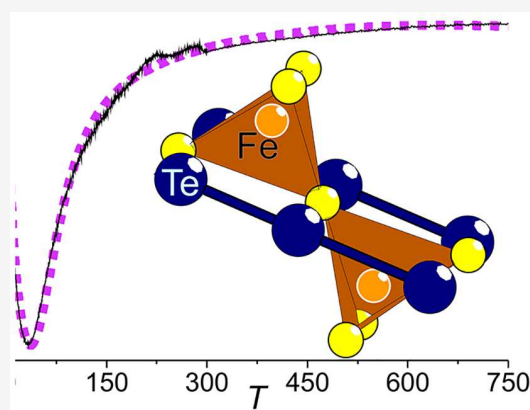
INTRODUCTION

Iron is the fourth most abundant element in the Earth's crust,[1] and it is environmentally friendly and cheap. As such, the discovery that the element could form high-temperature superconductors was a matter of significant interest to the scientific community. Iron can, in fact, form superconducting compounds with heavier chalcogenides. FeSe is probably the most widely known example,[2] but FeTe has also been shown to assume a superconducting state under strained conditions.[2,3] Sulfur-based compounds are not known to superconduct under ambient conditions, but $BaFe_2S_3$ has been reported to undergo a superconducting transition under high pressure.[4] Iron is the essential component in other superconductors as well, such as $LiFeAs$[5] and $NaFeAs$,[6] underlining its importance to fundamental science. Iron telluride also exhibits spin density waves along with several other spin arrangements, depending on the exact composition.[7,8]

As such, there is an incentive to search for novel compounds in iron chalcogenide systems. A relatively new approach, to this end, is the search for ordered multianionic compounds.[9,10] According to Hume-Rothery, two distinct anionic species cannot form solid solutions if the ionic radii differ by more than approximately 15%. Beyond this limit, the two ions will assume distinct atomic sites.[11] As the radius of Te is more than 15% larger than that of sulfur, telluride sulfides should contain ordering among the chalcogenide ions. Tellurides are also prone to forming polyanions of greatly varying lengths, ranging from simple pertelluride ions in $FeTe_2$ to 15-chain

polytellurides or infinite arrangements, making them a structural component with great potential for forming novel crystal structures.[12−14] This makes iron bichalcogenide systems very interesting to investigate.

Here, we introduce a novel quaternary telluride sulfide, $Ba_6Fe_2Te_3S_7$, and report its synthesis, crystal structure, charge configuration, heat capacity, magnetic properties, and calculated properties, as obtained by density functional theory (DFT).

EXPERIMENTAL SECTION

Sample Preparation. All of the handling of the sample during the synthesis took place inside an argon-filled glovebox (H_2O and O_2 < 1 ppm). A stoichiometric mixture of about 0.5 g of BaS (Alfa Aesar, 99.7%), Fe (Alfa Aesar, 99%), and Te (Thermo Scientific, 99.99%) powders was homogenized in an agate mortar and pressed into a 13 mm diameter pellet with 3 tons of pressure. The resulting pellets were broken, and the fragments were placed in a corundum crucible. The crucible was sealed inside an evacuated silica ampule using an oxygen−hydrogen torch. Subsequently, the sample was placed in a muffle oven and heated to 700 °C at a 5 °C min⁻¹ heating
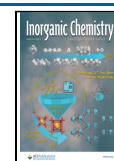
rate. The synthesis progressed at this temperature for 48 h before the furnace was turned off. The cooled sample was put back into the glovebox. All steps, including grinding, pelletization, sealing in a silica tube, and heating at 700 °C with subsequent cooling, were performed four times for a total of 192 h at 700 °C before the final sample was obtained. The single crystals, used for structure determination, were obtained from a similar synthesis with 46 h of heating but with a different target stoichiometry, $Ba_9Fe_4Te_4S_{12}$, while attempting a different synthesis.

The powder sample and single crystals of the title compound were specular black and appeared to be stable under ambient conditions. A minor Te (0.16 vol % from Rietveld refinement) impurity was observed in the powder X-ray diffraction (pXRD) pattern, but no other secondary phase was observed.

X-ray Structure Determination. The pXRD data were obtained using a Bruker D8 Discover instrument with a Bragg−Brentano geometry and a Ge(111) Johanssen monochromator, CuKα$_1$ X-rays, and a Lynxeye detector. A zero-background-oriented silicon crystal XRD plate, covered with silicone grease, was used as the sample holder. An energy filter in the detector suppressed the fluorescence from Fe. The single-crystal data were collected at room temperature using a Bruker D8 Venture single-crystal diffractometer equipped with a MoKα InCoatec microfocus X-ray source and a Photon 100 detector. The atomic structure was determined and refined using the JANA2006 software.[15]

Physical Property Measurement System (PPMS). The electric, magnetic, and heat capacity properties were determined using a Quantum Design PPMS. For the heat capacity measurements between 2 and 300 K, sintered polycrystalline pellets were used in the non-adiabatic thermal relaxation approach, and the sample was equilibrated at each temperature (15 min of extra waiting) before starting measurements. Apiezon N grease was used to attach the sample to the holder. Two sequential measurements were carried out at each temperature point, and the sample coupling never fell below 97% throughout the investigation. The magnetic measurements were performed on a powdered sample from a ground pellet in a polypropylene sample holder. To subtract a proper background signal, the empty holder was measured with the same parameters as those used for the sample measurement. For DC magnetization measurements, field-cooled (FC) protocols were carried out between 2 and 300 K with applied magnetic fields of 1, 3, and 6 T. A magnetization measurement was carried out at 300 K to determine the effect of ferromagnetic impurities, with applied fields from −7 to 7 T (data not shown). The electric conductivity of the sample was measured at room temperature, but the compound was found to be completely insulating within instrument measurement capacity (>2 MΩ).

For magnetic measurements above 300 K, a Lake Shore Cryotronics 7400-S Series VSM was utilized with an applied magnetic field of 1 T. The sample holder was made of BN, and the sample was held under a protective argon atmosphere during measurement.

Scanning Electron Microscope (SEM) Imaging and Energy Dispersive X-ray (EDX) Analysis. SEM imaging and EDX analysis were carried out using a Hitachi SU 8230 Field Emission Gun Scanning Electron Microscope with an XFlash 6l10 EDX detector. A 15 keV acceleration voltage was used for both SEM and EDX. EDX analyses were carried out by determining the elemental composition of 13 separate crystallites and averaging the obtained values. The heaviest element, barium, was used as a reference point for the composition.

Mössbauer Spectroscopy. [57]Fe Mössbauer spectra were collected at temperatures between 5 K and room temperature (295 K) using a standard WissEl spectrometer in the constant acceleration mode ([57]Co/Rh source) and a Janis SHI 850−5 closed-cycle refrigerator. About 30 mg of $Ba_6Fe_2Te_3S_7$ powder was mixed with BN and distributed in an acrylic glass sample container with an inner diameter of 13 mm. All isomer shifts are given relative to α-iron. The data were evaluated with the MossWinn program[16] using the thin absorber approximation.

Computational Details. The theoretical calculations were carried out using the Vienna Ab initio Simulation Package (VASP)[17,18]

utilizing the generalized gradient approximation (GGA) approach for the exchange-correlation energy, as formulated by Perdew-Burk-Ernzerhof (PBE).[19] The calculations employed projected augmented wave (PAW) pseudopotentials[20] with a plane wave energy cutoff of 400 eV and self-consistent field energy convergence criteria of 10^{-6} eV. To describe the strong correlation of the Fe-3d orbital electrons, a Hubbard U_{eff} repulsion term is added under the rotationally invariant Dudarev approach.[21] A range of U_{eff} values from 0 to 6 eV were employed to observe how the parameter affected the description of the compound. Integrations over the Brillouin zone were carried out with a 4 × 2 × 3 gamma-centered sampling grid using the tetrahedron method with Blöchl corrections. Density of states (DOS) calculations were carried out with a doubled grid for integration of the Brillouin zone (8 × 4 × 6). The band structure path was determined with the Materials Cloud SeeK-path tool.[22,23]

An initial, noncollinear calculation incorporating spin−orbit coupling was carried out on a static structure relaxed nonmagnetically at $U_{eff} = 0$ eV to determine the alignment of the iron spin states relative to the structure and to investigate whether the ground state involves a noncollinear spin arrangement. These calculations utilized the same sampling grid used for the Brillouin zone. The use of symmetry was disabled for these calculations. As the ground state was found to be spin-collinear, all other calculations utilized a spin-collinear configuration. With one exception, the structures of all magnetic alignments were allowed to fully relax with respect to both unit cell and ionic positions until all forces were less than 10^{-2} eV Å^{-1}. The calculation of magnetic couplings utilized static unit cells, which were structurally relaxed with the ground-state magnetic alignment.

Using the PBE0[24] and HSE06[25] functionals, hybrid functional calculations were carried out to determine the magnetic couplings, using only the gamma point for sampling the Brillouin zone and Gaussian smearing with a width of 0.02 eV. Otherwise, the parameters were the same as for the GGA calculations.

■ RESULTS

Crystal Structure. The analysis of the single-crystal XRD data of $Ba_6Fe_2Te_3S_7$ at room temperature reveals a unique crystal structure, described in the $Cmc2_1$ (No. 36) space group symmetry, with lattice constants $a = 9.7522(5)$ Å, $b = 18.093(1)$ Å, $c = 12.0036(7)$ Å, $V = 2117.9(2)$ Å^3, and $Z = 4$ (Figure 1). The complete unit cell is given in Figure 1, and the refinement and structural parameters are given in Table 1 and Table 2, respectively.

Each of the four distinct Ba^{2+} ions in the structure exhibits an individual coordination to sulfur and tellurium, with two, three, or four telluride neighbors (Figure 2). Ba2 and Ba3 assume a similar distorted-square, antiprismatic arrangement with four and two telluride coordinations, respectively. The even number of telluride ions allows the coordination to assume a symmetric arrangement of the anions. For Ba2, the position is bonded to four anionic species arranged separately on two perpendicular planes, similar to a *mer*-idional coordination, exhibiting an $mm2$ symmetry. The Ba3 arrangement is similar except that two tellurides are replaced by sulfur; the two remaining tellurides are situated adjacently. Ba1 is coordinated by three telluride ions and assumes a *fac* bicapped trigonal prismatic arrangement, with the telluride ions arranged on one side. Finally, Ba4 coordinates 3 Te and 5 S, but the spatial separation of Te by S can be represented as a 1+5+2 coordination, with the telluride ions occupying opposite sides of the barium ion and a five-coordinate belt of sulfur ions separating the unequally distributed telluride ions.

Three Te ions are arranged along an essentially straight vector parallel with the *bc*-plane, with a Te1−Te2−Te3 angle of 179.8(1)° (Figure 1). There are two different vectors the telluride chains follow within a single *bc*-plane, which differ by
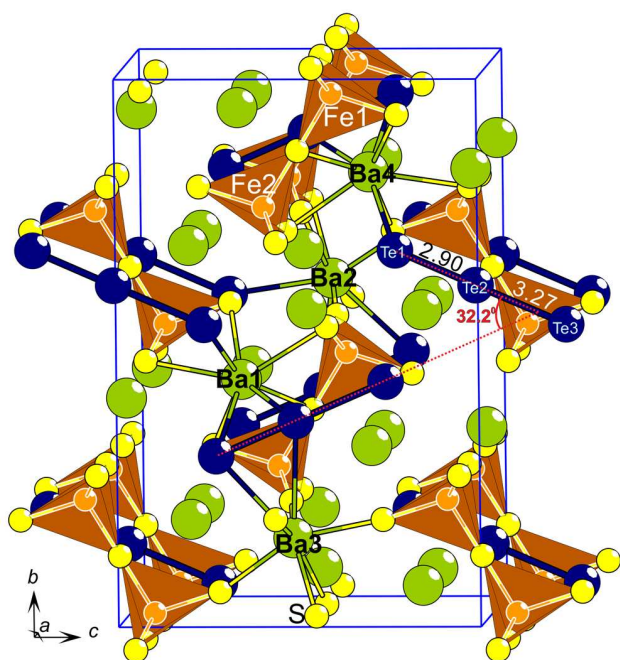
Figure 1. Extended unit cell content of the $Ba_6Fe_2Te_3S_7$ crystal structure. The dashed red lines represent the vector along which the telluride triplets are arranged, and the angle between these vectors is given. The Te–Te distances are given in Å.

Table 1. Single-Crystal Data Refinement Parameters for $Ba_6Fe_2Te_3S_7$

formula	$Ba_6Fe_2Te_3S_7$
radiation	Mo $K\alpha$ ($\lambda = 0.71073$ Å)
instrument	Bruker D8 Venture
physical appearance	specular black
crystal system	orthorhombic
space group	$Cmc2_1$ (No. 36)
formula weight	1542.95
temperature (K)	293
a (Å)	9.7522(5)
b (Å)	18.093(1)
c (Å)	12.0036(7)
V (Å^3)	2117.9(2)
Z	4
ρ_{calc} (g cm^{-3})	4.8389
no. of independent reflections	1827
no. of variables	97
GOF (all) on F^2	1.67
$R1$ (obs) (%)	3.04
$R1$ (all) (%)	3.50
$wR2$ (obs) (%)	6.95
$wR2$ (all) (%)	7.09
CSD No.	2264569

a 32.2° angle (Figure 1). The three tellurides have slightly different spacing among them, with Te1 and Te2 being 2.90 Å apart and Te2 and Te3 being 3.27 Å apart, indicating the presence of a pertelluride. The Te1–Te2 bond length is slightly longer than that of a pertelluride ion coordinated with barium (2.77 Å in $BaTe_2$[26]) but about equal with the bonding in $FeTe_2$ (2.90 Å[12]). Alternatively, the Te trimer row in the title compound may be a $[Te_3^{4-}]$ polytelluride ion. In 2009, a

Table 2. Ionic Positions of $Ba_6Fe_2Te_3S_7$, as Determined by Single-Crystal X-ray Diffraction

| atom	site	x	y	z	U (Å^2)
Ba1	8b	0.2809(1)	0.4360(1)	0.3252(1)	0.0166(3)
Ba2	4a	0	0.4185(1)	0.0275(1)	0.0162(4)
Ba3	4a	0	0.1632(1)	0.4844(1)	0.0115(3)
Ba4	8b	0.2495(1)	0.1829(1)	0.1868(1)	0.0181(3)
Fe1	4a	1/2	0.4723(2)	0.5965(3)	0.021(1)
Fe2	4a	1/2	0.2701(2)	0.4116(2)	0.021(1)
S1	4a	1/2	0.3045(3)	0.2326(5)	0.015(2)
S2	8b	0.3042(4)	0.2153(2)	0.4588(3)	0.022(2)
S3	8b	0.3066(4)	0.5311(2)	0.5587(3)	0.018(2)
S4	4a	1/2	0.3725(5)	0.5031(7)	0.031(2)
S5	4a	1/2	0.4342(4)	0.7755(5)	0.021(2)
Te1	4a	0	0.3120(1)	0.2728(2)	0.0193(5)
Te2	4a	0	0.3763(2)	0.4941(2)	0.0193(4)
Te3	4a	1/2	0.0518(1)	0.2437(2)	0.0215(5)
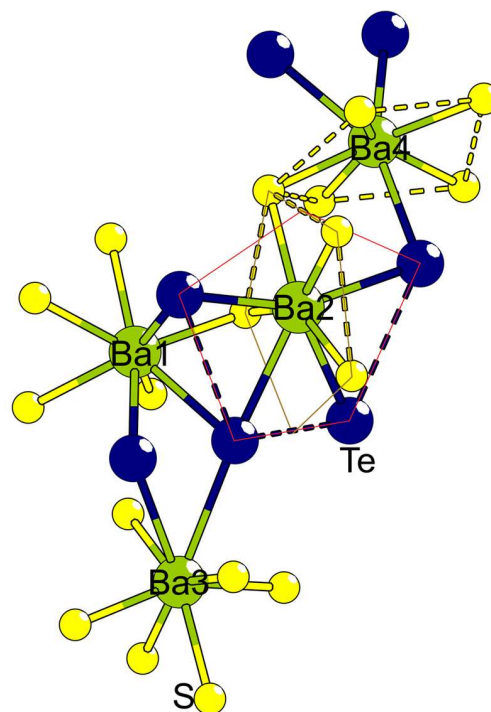
Figure 2. Barium ion coordinations. The Te–Te and S–S connections are to clarify coordination rather than bonding. The two polygons of thin lines represent the two mirror planes that penetrate the Ba2 site.

review stated that no isolated, linear example of this species has ever been reported.[13] The same review also remarked that species isoelectronic with $[Te_3^{4-}]$, such as linear $[I_3^-]$, may exhibit deviation from the ideal centrosymmetric distribution, which matches the observations for $Ba_6Fe_2Te_3S_7$. However, very recently, a centrosymmetric variation of the $[Te_3^{4-}]$ ion was suggested in $Ba_{14}Si_4Sb_8Te_{32}(Te_3)$,[27] having the same total length of the ion, which could indicate that it is a polytelluride ion. Alternatively, the $[Te_2^{2-}][Te^{2-}]$ straight chain is a coincident atomic arrangement. Beyond the trimer, the smallest Te–Te interatomic distance is at least 4.4 Å, so the chains would not behave as an extended polytelluride. The low

electrical conductivity at room temperature corroborates this perspective.

The two distinct iron positions assume a vertex-sharing dimeric arrangement tetrahedrally coordinated with sulfur, forming an Fe−S−Fe angle of 178.8(5)°. The tetrahedra are arranged in a staggered configuration (Figure 3). It should be
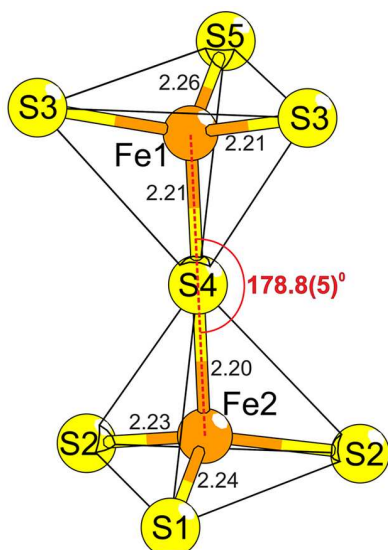

Figure 3. Dimeric structure of iron in $Ba_6Fe_2Te_3S_7$. Interatomic distances are given in Å.

noted that other single-crystal measurements were refined to give an Fe−S−Fe angle even closer to 180°, including 179.6(6)° and 180.0(6)°. The central sulfide ion seems to be almost at an inversion symmetric point for the dimer, although this is not a symmetry in the suggested space group, and the Fe−S distances are slightly different between the two tetrahedra. The uneven spacing of the ions in the Te triplet also contributes to a different chemical environment between the two iron positions. The Fe−S−Fe dimers occupy the same bc-planes as the telluride chains, stacked alternatingly along the a-axis (Figure 1).

Edge-sharing Fe dimers, such as K_3FeSe_3,[28] $Rb_6Fe_2S_6$,[29] and others,[29] are known and characterized. For vertex-sharing arrangements, there are selected organic salts which exhibit transition metal elements in similar structures when bonded with transition metal (oxy-) halide anions such as $[Fe_2OBr_6]^{2-}$, $[Fe_2OCl_6]^{2-}$, and $[Hg_2I_7]^{2-}$.[30−32] The dimeric arrangements of Fe^{3+} consistently exhibit a singlet spin state.

Powder XRD. A refinement from pXRD yields more accurate lattice parameters compared to those from single-crystal measurements. Rietveld refinement (Figure 4) of the lattice parameters from the pXRD data yields a = 9.7543(3) Å, b = 18.2766(6) Å, and c = 12.0549(4) Å. Overall, the measured and calculated diffraction patterns match excellently.

SEM and EDX Analysis. Viewed in SEM, $Ba_6Fe_2Te_3S_7$ exhibits roughly rectangular prism crystal shapes, consistent with the expected mode of growth from the unit cell (Figure 5). EDX analysis gives the composition $Ba_{6.00(8)}Fe_{2.06(9)}Te_{3.06(4)}S_{7.1(2)}$, in excellent agreement with the determined crystal structure. Further, using the composition of $Ba_6Fe_2Te_3S_7$ in a synthesis resulted in an X-ray pure sample.
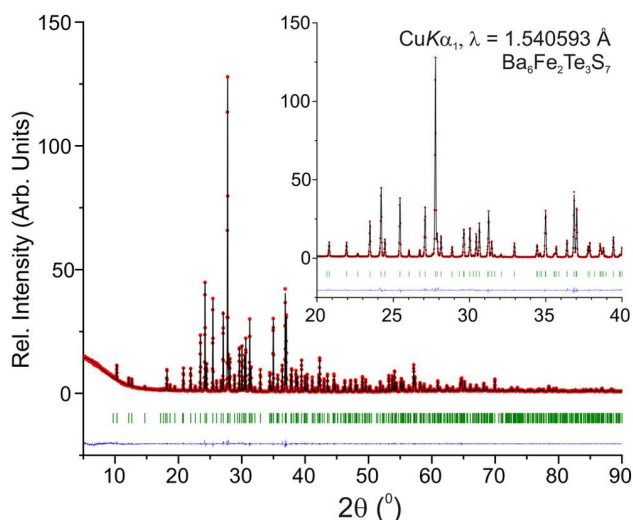

Figure 4. Rietveld refinement of $Ba_6Fe_2Te_3S_7$ pXRD data. The vertical lines (green) indicate the Bragg positions. Differences between the observed data (red) and the calculated data (black) are given in blue. The inset shows the fitting of the most prevalent peaks in more detail.
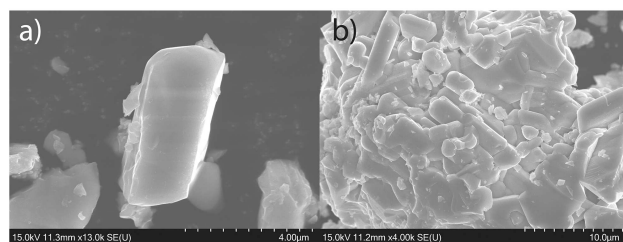
Figure 5. SEM images of (a) a single crystal of $Ba_6Fe_2Te_3S_7$ and (b) a larger cluster of crystallites. The scaling bars correspond to 4 and 10 μm, in (a) and (b), respectively.

Mössbauer Spectroscopy. The room-temperature Mössbauer spectrum of $Ba_6Fe_2Te_3S_7$ consists of a single quadrupole doublet with an isomer shift (IS) = 0.174(1) mm s^{-1} and a quadrupole splitting (QS) = 1.086(3) mm s^{-1} (Figure 6). The crystal structure actually exhibits two distinct lattice sites for
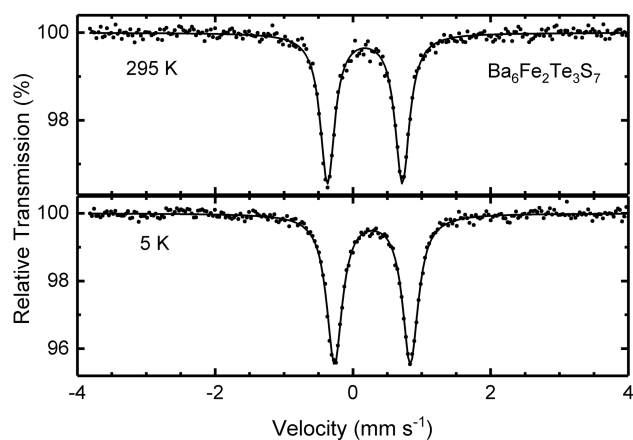

Figure 6. Mössbauer spectra of $Ba_6Fe_2Te_3S_7$ at room temperature and 5 K. Dots and solid lines correspond to the experimental and calculated spectra, respectively.

Fe; however, the difference in their local coordination geometries is too small to be resolved in the Mössbauer spectra. The quadrupole doublet persists despite cooling, and down to 5 K there are no signs of magnetic ordering or freezing. The Mössbauer parameters at 5 K are IS = 0.283(1) mm s^{-1} and QS = 1.101(2) mm s^{-1}. The small isomer shift values are typical for Fe^{3+} in a tetrahedral environment;[33] for example, IS = 0.16 mm s^{-1} at 300 K for KFeS$_2$, and IS = 0.155 mm s^{-1} for Rb$_6$[Fe$_2$O$_6$], an oxoferrate(III) with edge-sharing Fe dimers.[29] Remarkably, the QS is quite large for Fe^{3+} where, for the half-filled $e^2 t_2^3$ configuration, only a lattice but no valence contribution to the electric field gradient occurs. As expected for Fe^{3+} and in contrast to Fe^{2+}, the QS is nearly independent of temperature. The large QS can be attributed to the asymmetric local environment of Fe^{3+}, which is due to the formation of dimers in the crystal structure.[29] Thus, the compound can be formulated as either Ba$_6^{2+}$Fe$_2^{3+}$Te$_3^{4-}$S$_7^{2-}$ or Ba$_6^{2+}$Fe$_2^{3+}$Te$_2^{2-}$Te^{2-}S$_7^{2-}$, in agreement with the crystal structure analysis indicating the presence of per- or polytellurides. Finally, it is noted that within the error limits of about 2%, there are no signs of Fe-containing impurities.

Magnetic Properties. The magnetic susceptibility of Ba$_6$Fe$_2$Te$_3$S$_7$ corresponds to neither a typical (anti)-ferromagnetic behavior nor a paramagnetic behavior (Figure 7). The majority of the 2−750 K temperature range is
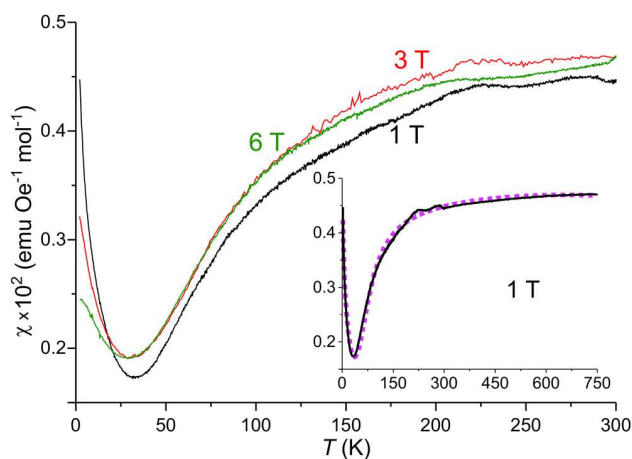
Figure 7. Field-cooled (FC) DC magnetic susceptibility of Ba$_6$Fe$_2$Te$_3$S$_7$ with temperatures in the range 2−300 K, for applied fields of 1, 3, and 6 T. The values shown in the figure are corrected for the contribution of ferromagnetic impurities, instrumental background from the sample holder, and the standard diamagnetic contribution of the atomic species present.[38] The inset shows an extended curve, synthesized from two different measurements, ranging from 2−300 and 300−750 K, respectively, with an applied field of 1 T. The absolute value of the higher-temperature measurement has been shifted by simple addition to match the transition temperature with the lower-temperature measurement. The purple dashed curve in the inset is the Van Vleck fitting.

dominated by an apparent asymptotic increase in susceptibility with increasing temperature, although it should be noted that the reliability of the absolute values for the susceptibility measured in the 300−750 K region is lower than that of the measurements in the low-temperature region. The high-temperature values in the Figure 7 inset have been shifted by simple addition to ensure continuous overlap with the low-temperature measurements. The increase in susceptibility at

the lowest temperatures is probably due to paramagnetic iron impurities.

There are a number of irregularities in the curves, but the origin of these cannot be specified. Due to the small absolute scale of the susceptibility, even marginal effects from impurities would appear as major contributions, making the assignment of any meaning to these anomalies uncertain. At least some of the irregularities, particularly in the 200−300 K range, are due to instrumental errors.

Considering the structural motif of iron dimers and the results from Mössbauer spectroscopy, it can be assumed that the shape of the magnetic susceptibility curve of Ba$_6$Fe$_2$Te$_3$S$_7$ reflects antiferromagnetic coupling of the S = 5/2 (Fe^{3+}) centers within the dimers via the bridging S^{2-} ions, which leads to a diamagnetic singlet ground state (S' = 0).

The magnetic properties of the dimeric magnetic species are typically described by the isotropic spin-exchange Hamiltonian $H = -2J S_1 \cdot S_2$. Using the Van Vleck formula (eq 1) with $S_1 = S_2$ = 5/2 affords[28,32,34–37]

$$\chi_M = \frac{2 N_A g^2 \mu_B^2}{k_B T}\left[\frac{e^{2x} + 5e^{6x} + 14e^{12x} + 30e^{20x} + 55e^{30x}}{1 + 3e^{2x} + 5e^{6x} + 7e^{12x} + 9e^{20x} + 11e^{30x}}\right](1-p)$$
$$+ \frac{35 N_A \mu_B^2}{3 k_B (T-\theta)} p + \text{TIM} \tag{1}$$

where $x = \frac{J}{k_B T}$, N_A is the Avogadro constant, g is a g-factor (fixed to 2 in our fitting to avoid overparameterization), μ_B is the Bohr magneton, k_B is the Boltzmann factor, T is the temperature in Kelvin, p is the fraction of magnetic Fe^{3+} impurities, and J is the magnetic coupling constant. TIM is a temperature independent of paramagnetic contribution. Exponential parts of the equation correspond to the thermal population of the excited spin states of the dimer with S' = 1, 2, 3, 4, and 5, respectively.

The Van Vleck equation provides an adequate fit to the measured data (inset of Figure 7) over the entire temperature range, although there is a consistent mismatch for the location of the susceptibility minimum between the fit and the measurement, with the fitted minimum always located at a slightly higher temperature. The obtained value for the coupling constant J is −10.5(2) meV or −85(2) cm^{-1}, averaged between three measurements at 1, 3, and 6 T. This value is comparable to the coupling constants of −14.2 and −10.4 meV reported for the edge-sharing dimers in the compounds Na$_3$FeS$_3$ and Cs$_3$FeS$_3$, respectively.[37] The overall shape and magnitude of the curves reported in the same paper correspond well with those observed here. The fitted θ and p values are field-dependent due to saturation of the para-magnetic contribution. The obtained p values range from about 0.8% to 1.9%, increasing with the applied magnetic field.

Heat Capacity. The heat capacity of Ba$_6$Fe$_2$Te$_3$S$_7$ exhibits no distinct features beyond discontinuities that we assign to minor measurement errors (Figure 8). There is no indication that the compound undergoes a common long-range magnetic or structural transition.

Density Functional Theory (DFT). The initial consideration that the magnetic structure might be noncollinear at 0 K was extracted from the alignment of the iron positions. Comparison of collinear and noncollinear arrangements with spin−orbit coupling effects indicated that the collinear, antiferromagnetic arrangement of spins is the more stable
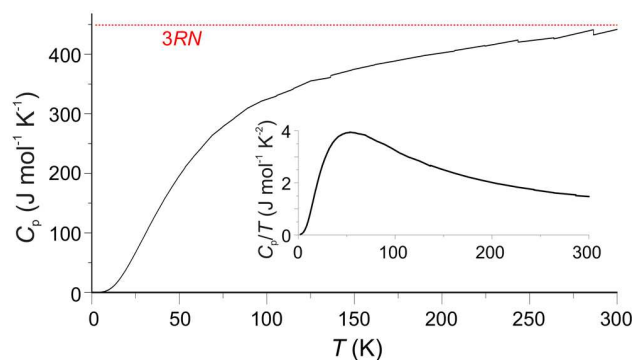
Figure 8. Specific heat measurements of $Ba_6Fe_2Te_3S_7$, with the Dulong-Petit limit inserted in red. The inset depicts the specific heat divided by the temperature vs temperature.

configuration. The difference in energy between the collinear and noncollinear arrangements was 3.4 meV per dimer.

The overall agreement of the relaxed unit cells with the pXRD refinement lattice parameters is exceptional (Figure 9a).
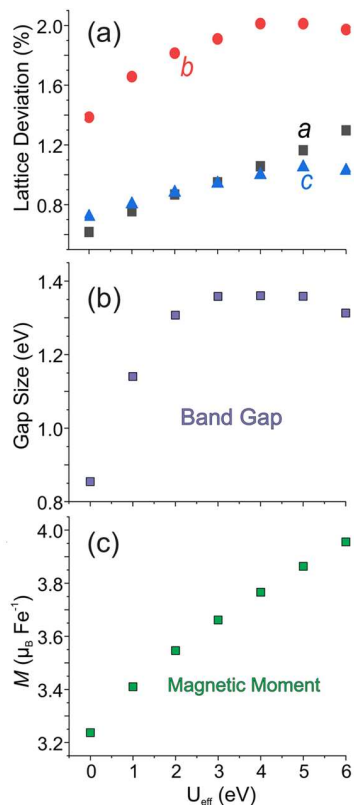
Figure 9. (a) The difference between the calculated and experimental lattice parameters with a varying Hubbards parameter, expressed in terms of percentage deviation. (b) The band gap of $Ba_6Fe_2Te_3S_7$ with variation in U_{eff}. (c) The local magnetic moment on the Fe ion with variation in U_{eff}.

With U_{eff} = 0 eV, only the b-parameter differs from the experimental values by more than 1%, although the calculated values consistently overestimate the lattice parameters. Applying the +U correction caused the a-parameter to increase nearly linearly across the full U_{eff} range, while the b- and c-parameters plateau at U_{eff} values of 4−5 eV.

Bader charge analysis of the telluride ions shows that the number of electrons associated with each position in the triplet chains is not an even distribution or a distinct pertelluride−telluride pairing. Rather, the terminal telluride positions are associated with similar electron charges, while the central position is associated with significantly fewer electron charges. Utilizing the Bader charge distribution of BaTe and $BaTe_2$ as references for tellurides and pertellurides, respectively, one finds that the central telluride position is associated with approximately the equivalent charge of a pertelluride species. The terminal telluride positions are associated with an intermediate amount of charge between telluride and pertelluride characters. With a linear interpolation between the pure telluride and pertelluride extremes, the terminal telluride positions exhibit roughly equal character of both. Interpreting the character as valency and summing between the tellurides in each triplet, this equals the associated charge that one would expect from a total valency of −4, which is the value one should expect. The comparatively similar charges of the terminal positions strongly suggest a three-chain polytelluride. If the chains were formed from a discrete pertelluride−telluride pair, $[Te_2^{2-}][Te^{2-}]$, the terminal positions should exhibit a substantial difference in character. The difference in the calculated valence is roughly 11%, with the more isolated ion being associated with a greater charge. This behavior is largely independent of the U_{eff} parameter and occurs with both hybrid functionals. As such, the Bader analysis may be considered to provide substantial support toward the view of the $[Te_3^{4-}]$ polytelluride description.

$Ba_6Fe_2Te_3S_7$ is found to be a semiconductor, although the nature of the band gap varies with the U_{eff} parameter. As the U_{eff} value exceeds 2 eV, the band gap changes character and becomes comparatively independent of U_{eff} (Figure 9b). The obtained band gaps range from 0.85 to 1.36 eV for the GGA +U approach.

The local magnetic moment of the Fe ions ranges from 3.2 to 4.0 μ_B, increasing nearly linearly with the U_{eff} parameter (Figure 9c). This high value agrees with the high-spin state of Fe^{3+}. The values displayed in the figure are averages, as the two iron ions in the dimer are not exactly equal due to the lack of symmetry to enforce an identical environment. The calculated magnetic moments for the Fe ions in one dimer differ by 0.030 to 0.017 μ_B as U_{eff} varies from 0 to 6 eV, respectively.

The change in the bandwidth of U_{eff} is accompanied by a change in the nature of the gap transition. When U_{eff} is between 0 and 2 eV, the transition is of mixed character between a Mott insulator and a charge transfer insulator. The valence band (VB) maximum is composed of Fe-3d orbitals along with S-3p orbitals with roughly equal contributions, while the conduction band (CB) minimum is predominantly of Fe-3d character (Figure 10a).

At U_{eff} values exceeding 2 eV, the composition of the edges of the band gap changes and the influence on the valence-band-maximum (VBM) by the Fe-3d orbitals is greatly diminished. Instead, the transition approaches a pure charge transfer-like character, with equal contributions from S-3p and Te-5p orbitals. Further increase in the U_{eff} parameter shifts the VBM character further toward a Te-5p composition (Figure 10b).

A feature of the band structure that occurs for all tested values of U_{eff} is that the electronic states are spin-dependent (Figure 11). For U_{eff} = 0 eV, this results in the lowest energy transitions involving spin reversal. The lowest energy
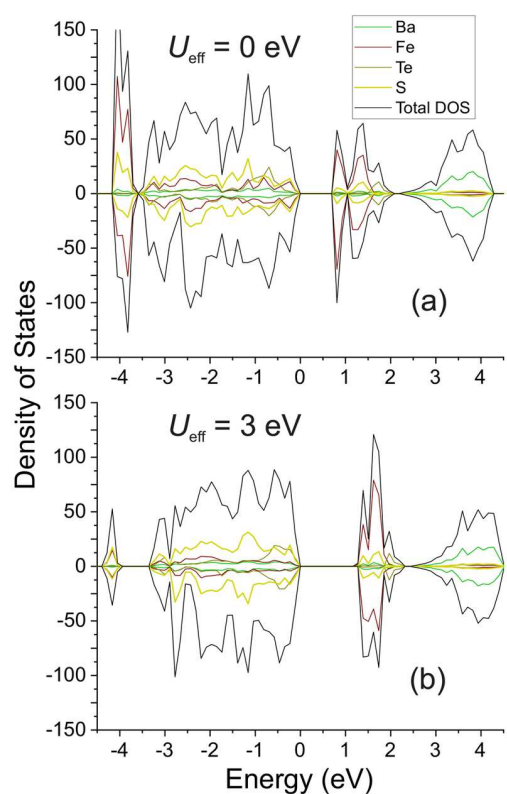
Figure 10. DOS of $Ba_6Fe_2Te_3S_7$, calculated with (a) $U_{eff} = 0$ eV and (b) $U_{eff} = 3$ eV.
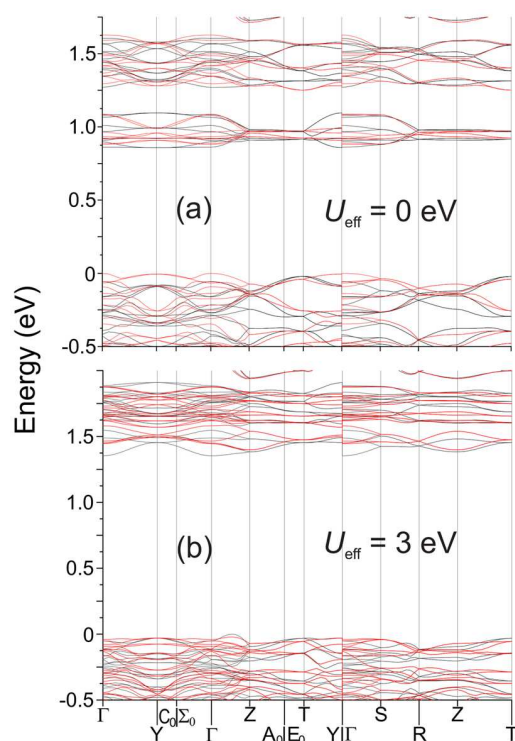
Figure 11. Band structure of $Ba_6Fe_2Te_3S_7$, calculated with (a) $U_{eff} = 0$ eV or (b) $U_{eff} = 3$ eV. The black bands represent spin-up states, and the red bands represent spin-down states. The energy scale is relative to the Fermi energy.

transitions are the $\Gamma-Y$ and $\Gamma-\Gamma$ transitions, which have nearly equal energy. For transitions without spin reversal, the indirect $T-Y$ transition is the smallest, with a gap of 0.88 eV.

At $U_{eff} = 3$ eV, the lowest energy transition occurs from an off-symmetry position in the VBs, between Γ and Z, to an Γ position in the CB. Notably, the entirety of the lowest energy CB states, as well as the VB maximum, are composed of electronic states with a single spin.

The most favorable magnetic interaction remains constant throughout the range of U_{eff} values. Singlet-arranged dimers are where the paired Fe ions exhibit spins in opposite directions. Energy contributions from interdimeric magnetic interactions are marginal and can be disregarded. A diamagnetic, low-spin configuration is enormously unfavorable, with energy levels that are about 2−4 eV per dimer higher compared to the high-spin configuration (depending on the U_{eff} employed), further suggesting that the system is not in a low-spin Fe^{2+} configuration. The most favorable long-range collinear antiferromagnetic configuration with iron in alternating bc-planes exhibits opposite spins, and the ferromagnetic spin arrangements are 0.48 and 0.54 eV per dimer, respectively, above the lowest energy state, with $U_{eff} = 0$ eV. These values are notably quite similar, suggesting that the interdimeric coupling is much weaker than the intradimer coupling.

The typical approach for determining the coupling constant J of dimeric species in DFT is the broken symmetry approach. Based on the same spin-exchange Hamiltonian $H = -2JS_1 \cdot S_2$, as defined in the experimental description, the coupling constant, per dimeric pair, may be determined from the difference in energy between singlet and triplet states[39]

$$J = \frac{E_{singlet} - E_{triplet}}{4S_1S_2} \qquad (2)$$

The coupling constant obtained from this equation is dependent on the accuracy of the exchange-correlation functional employed. For S, either the ideal value or the DFT calculated value may be employed. For high-spin Fe^{3+} with $S = 5/2$, eq 2 becomes

$$J = \frac{E_{singlet} - E_{triplet}}{25} \qquad (3)$$

Using the ideal spin value (5/2) for Fe^{3+}, the coupling constant comes out in the range of −24.9 to −8.9 meV, decreasing with a higher $+U_{eff}$ parameter. The hybrid calculations give coupling constants of −14.3 and −14.4 meV for PBE0 and HSE06, respectively. The closest approximation to the hybrid calculations is obtained with $+U_{eff} = 3$ eV, giving a coupling constant of 14.2 meV. The hybrid results exhibit decent agreement with the experimental fittings but overestimate the magnitude by about 36−37%. DFT is known to substantially overestimate the magnitude of magnetic coupling energies, with the scope of error potentially up to two- to four-fold the experimental value,[40−42] although literature on calculations with dimeric sulfur-based compounds is scarce. Studies suggest hybrid functionals provide significantly more accurate coupling constants, with HSE and PBEh providing coupling constants with a mean absolute percentage error of about 10% for organic compounds with Fe dimers.[39]

In general, the model corroborates the experimental expectation of a singlet state. Analysis of the spin density of the singlet system shows that the system exhibits super-

exchange mediated via a p orbital on the shared-vertex sulfide ion.

DISCUSSION

The different analyses of $Ba_6Fe_2Te_3S_7$ give a coherent picture of the origin of its unusual susceptibility data. Mössbauer spectroscopy data and DFT calculations both agree that Fe in $Ba_6Fe_2Te_3S_7$ is in a trivalent high-spin state, with antiferromagnetic coupling rendering the total spin state of each dimer a singlet at low temperatures. In effect, the bulk material exhibits a very low magnetic susceptibility, despite exhibiting strong electronic correlations. The lack of magnetic coupling between the spin dimers, as suggested by DFT calculations, agrees with the Mössbauer spectroscopy and heat capacity, indicating the absence of magnetic long-range ordering down to 2 K. The temperature dependence of the magnetic susceptibility can be described reasonably well over the whole measured temperature range of 2−750 K, if isotropic exchange between the $S = 5/2$ Fe^{3+} centers within the dimer is assumed and the corresponding Van Vleck equation is used. The pronounced antiferromagnetic coupling with an exchange constant of -10.5 meV $(85$ cm$^{-1})$ is a consequence of superexchange through the central sulfide ion, as per the Goodenough-Kanamori rule,[43,44] and combined with the high magnetic isolation of the diamagnetic matrix, each dimer essentially behaves like a binuclear entity.

The exact nature of the telluride triplets in the structure is difficult to assign accurately from experimental data due to the *sliding-scale* nature of polytellurides. Among the charge balancing, the trivalent Fe ions, and the interatomic distances, the shorter telluride−telluride distance may be confidently established as a feature of a pertelluride. Whether the third telluride in the chain is part of a $[Te_3^{4-}]$ unit is likely true because of the recently observed centrosymmetric $[Te_3^{4-}]$ unit. Bader charge analysis provides a case toward the $[Te_3^{4-}]$ description, with a similar charge assignment on the terminal positions. While the distortion from a centrosymmetric chain likely gives the tellurides a mixed nature between $[Te_2^{2-}]$-$[Te^{2-}]$ and $[Te_3^{4-}]$, the latter is deemed to be a better description for the smaller difference in charge character between the terminal positions. Thus, the most reliable representation of the compound charge distribution is $(Ba^{2+})_6(Fe^{3+})_2(Te_3)^{4-}(S^{2-})_7$.

CONCLUSION

Powder and single crystals of $Ba_6Fe_2Te_3S_7$ were prepared by solid-state synthesis, heating a mixture of BaS, Fe, S, and Te. Characterization of the compound by structural determination, magnetic and heat capacity measurements, Mössbauer spectroscopy, and DFT analysis suggests the presence of trivalent iron arranged in dimers with a spin-singlet ground state. The telluride component of the compound was determined to constitute a straight-chain $[Te_3^{4-}]$ polyanion. The compound was measured to be an electric insulator at room temperature, which was confirmed by DFT analysis of the band structure.

ASSOCIATED CONTENT

Accession Codes

CCDC 2264569 contains the supplementary crystallographic data for this paper. These data can be obtained free of charge via www.ccdc.cam.ac.uk/data_request/cif, by emailing data_request@ccdc.cam.ac.uk, or by contacting The Cambridge Crystallographic Data Centre, 12 Union Road, Cambridge CB2 1EZ, UK; fax: +44 1223 336033.

AUTHOR INFORMATION

Corresponding Author

Martin Valldor − *Centre for Materials Science and Nanotechnology (SMN), Department of Chemistry, University of Oslo, NO-0371 Oslo, Norway;* orcid.org/0000-0001-7061-3492; Email: b.m.valldor@kjemi.uio.no

Authors

Emil H. Frøen − *Centre for Materials Science and Nanotechnology (SMN), Department of Chemistry, University of Oslo, NO-0371 Oslo, Norway;* orcid.org/0000-0001-5599-6982

Peter Adler − *Max-Planck-Institute for Chemical Physics of Solids, DE-01187 Dresden, Germany*

Complete contact information is available at:
https://pubs.acs.org/10.1021/acs.inorgchem.3c01775

Author Contributions

The manuscript was written through contributions of all authors.

Notes

The authors declare no competing financial interest.

REFERENCES

(1) *CRC Handbook of Chemistry and Physics*, 97th ed.; Haynes, W. M., Lide, D. R., Bruno, T. J., Eds.; CRC Press, Boca Raton, FL, 2016. DOI: 10.1201/9781315380476.

(2) Ge, J.-F.; Liu, Z.-L.; Liu, C.; Gao, C.-L.; Qian, D.; Xue, Q.-K.; Liu, Y.; Jia, J.-F. Superconductivity above 100 K in Single-Layer FeSe Films on Doped SrTiO$_3$. *Nat. Mater.* **2015**, *14* (3), 285−289.

(3) Han, Y.; Li, W. Y.; Cao, L. X.; Wang, X. Y.; Xu, B.; Zhao, B. R.; Guo, Y. Q.; Yang, J. L. Superconductivity in Iron Telluride Thin Films under Tensile Stress. *Phys. Rev. Lett.* **2010**, *104* (1), 017003.

(4) Takahashi, H.; Sugimoto, A.; Nambu, Y.; Yamauchi, T.; Hirata, Y.; Kawakami, T.; Avdeev, M.; Matsubayashi, K.; Du, F.; Kawashima, C.; Soeda, H.; Nakano, S.; Uwatoko, Y.; Ueda, Y.; Sato, T. J.; Ohgushi, K. Pressure-Induced Superconductivity in the Iron-Based Ladder. *Material BaFe2S3. Nat. Mater.* **2015**, *14* (10), 1008−1012.

(5) Morozov, I.; Boltalin, A.; Volkova, O.; Vasiliev, A.; Kataeva, O.; Stockert, U.; Abdel-Hafiez, M.; Bombor, D.; Bachmann, A.; Harnagea, L.; Fuchs, M.; Grafe, H.-J.; Behr, G.; Klingeler, R.; Borisenko, S.; Hess, C.; Wurmehl, S.; Büchner, B. Single Crystal Growth and Characterization of Superconducting LiFeAs. *Cryst. Growth Des.* **2010**, *10*, 4428−4432.

(6) Parker, D. R.; Pitcher, M. J.; Baker, P. J.; Franke, I.; Lancaster, T.; Blundell, S. J.; Clarke, S. J. Structure, Antiferromagnetism and Superconductivity of the Layered Iron Arsenide NaFeAs. *Chem. Commun.* **2009**, 2189−2191.

(7) Subedi, A.; Zhang, L.; Singh, D. J.; Du, M. H. Density Functional Study of FeS, FeSe, and FeTe: Electronic Structure, Magnetism, Phonons, and Superconductivity. *Phys. Rev. B* **2008**, *78* (13), 134514.

(8) Stock, C.; Rodriguez, E. E.; Bourges, P.; Ewings, R. A.; Cao, H.; Chi, S.; Rodriguez-Rivera, J. A.; Green, M. A. Competing Spin Density Wave, Collinear, and Helical Magnetism in Fe$_{1+x}$Te. *Phys. Rev. B* **2017**, *95* (14), 144407.

(9) Clarke, S. J.; Adamson, P.; Herkelrath, S. J. C.; Rutt, O. J.; Parker, D. R.; Pitcher, M. J.; Smura, C. F. Structures, Physical

Properties, and Chemistry of Layered Oxychalcogenides and Oxypnictides. *Inorg. Chem.* **2008**, *47* (19), 8473−8486.

(10) Valldor, M. Anion Ordering in Bichalcogenides. *Inorganics* **2016**, *4* (3), 23.

(11) Hume-Rothery, W.; Powell, H. M. On the Theory of Super-Lattice Structures in Alloys. *Z. Für Krist. - Cryst. Mater.* **1935**, *91* (1−6), 23−47.

(12) Rahman, A.; Zhang, D.; Rehman, M. U.; Zhang, M.; Wang, X.; Dai, R.; Wang, Z.; Tao, X.; Zhang, Z. Multiple Magnetic Phase Transitions, Electrical and Optical Properties of FeTe$_2$ Single Crystals. *J. Phys.: Condens. Matter* **2020**, *32* (3), 035808.

(13) Graf, C.; Assoud, A.; Mayasree, O.; Kleinke, H. Solid State Polyselenides and Polytellurides: A Large Variety of Se−Se and Te−Te Interactions. *Molecules* **2009**, *14* (9), 3115−3131.

(14) Kysliak, O.; Marcus, M.; Bredow, T.; Beck, J. Polytellurides of Mn, Fe, and Zn from Mild Solvothermal Reactions in Liquid Ammonia. *Inorg. Chem.* **2013**, *52* (15), 8327−8333.

(15) Petříček, V.; Dušek, M.; Palatinus, L. Crystallographic Computing System JANA2006: General Features. *Z. Für Krist. - Cryst. Mater.* **2014**, *229* (5), 345−352.

(16) Klencsár, Z.; Kuzmann, E.; Vértes, A. User-Friendly Software for Mössbauer Spectrum Analysis. *J. Radioanal. Nucl. Chem. Artic.* **1996**, *210* (1), 105−118.

(17) Kresse, G.; Furthmüller, J. Efficiency of Ab-Initio Total Energy Calculations for Metals and Semiconductors Using a Plane-Wave Basis Set. *Comput. Mater. Sci.* **1996**, *6* (1), 15−50.

(18) Kresse, G.; Furthmüller, J. Efficient Iterative Schemes for *Ab Initio* Total-Energy Calculations Using a Plane-Wave Basis Set. *Phys. Rev. B* **1996**, *54* (16), 11169−11186.

(19) Perdew, J. P.; Burke, K.; Ernzerhof, M. Generalized Gradient Approximation Made Simple. *Phys. Rev. Lett.* **1996**, *77* (18), 3865−3868.

(20) Kresse, G.; Joubert, D. From Ultrasoft Pseudopotentials to the Projector Augmented-Wave Method. *Phys. Rev. B* **1999**, *59* (3), 1758−1775.

(21) Dudarev, S. L.; Botton, G. A.; Savrasov, S. Y.; Humphreys, C. J.; Sutton, A. P. Electron-Energy-Loss Spectra and the Structural Stability of Nickel Oxide: An LSDA+U Study. *Phys. Rev. B* **1998**, *57* (3), 1505−1509.

(22) Hinuma, Y.; Pizzi, G.; Kumagai, Y.; Oba, F.; Tanaka, I. Band Structure Diagram Paths Based on Crystallography. *Comput. Mater. Sci.* **2017**, *128*, 140−184.

(23) Togo, A.; Tanaka, I. *Spglib: A Software Library for Crystal Symmetry Search*. 2018, 1−11. DOI: 10.48550/ARXIV.1808.01590.

(24) Adamo, C.; Barone, V. Toward Reliable Density Functional Methods without Adjustable Parameters: The PBE0Model. *J. Chem. Phys.* **1999**, *110* (13), 6158−6170.

(25) Krukau, A. V.; Vydrov, O. A.; Izmaylov, A. F.; Scuseria, G. E. Influence of the Exchange Screening Parameter on the Performance of Screened Hybrid Functionals. *J. Chem. Phys.* **2006**, *125* (22), 224106.

(26) Li, J.; Guo, H.-Y.; Proserpio, D. M.; Sironi, A. Exploring Tellurides: Synthesis and Characterization of New Binary, Ternary, and Quaternary Compounds. *J. Solid State Chem.* **1995**, *117* (2), 247−255.

(27) Jana, S.; Yadav, S.; Bishnoi, S.; Niranjan, M. K.; Prakash, J. Ba14Si4Sb8Te32(Te3): Hypervalent Te in a New Structure Type with Low Thermal Conductivity. *Dalton Trans* **2023**, DOI: 10.1039/D3DT01532G.

(28) Bronger, W.; Genin, H. S.; Müller, P. K$_3$FeSe$_3$ und K$_3$Fe$_2$Se$_4$, zwei neue Verbindungen im System K/Fe/Se. *Z. Für Anorg. Allg. Chem.* **1999**, *625* (2), 274−278.

(29) Schwarz, M.; Stüble, P.; Röhr, C. Rubidium Chalcogenido Diferrates(III) Containing Dimers [Fe$_2$Q$_6$]$^{6-}$ of Edge-Sharing Tetrahedra (Q = O, S, Se). *Z. Für Naturforschung B* **2017**, *72* (8), 529−547.

(30) Maithufi, N.; Otto, S. The Bis(Acetonitrile-κ *N*)Bis[*N*, *N*-Bis(Diphenylphosphanyl)Ethanamine-κ ^{2} *P*, *P* ′]Iron(II) Tetrabromidoferrate(II) and μ-Oxido-Bis[Tribromidoferrate(III)] Complex Salts. *Acta Crystallogr. C* **2011**, *67* (8), m279−m283.

(31) Hu, N.-H.; Liu, Y.-S.; Aoki, K. Interactions of Thiamine with Anions: (Hthiamine)(Thiamine) Heptaiododimercurate Dihydrate and Its Dimethanol Monohydrate. *Acta Crystallogr. C* **1999**, *55* (3), 304−308.

(32) Haselhorst, G.; Wieghardt, K.; Keller, S.; Schrader, B. The (.Mu.-Oxo)Bis[Trichloroferrate(III)] Dianion Revisited. *Inorg. Chem.* **1993**, *32* (5), 520−525.

(33) Reiff, W. M.; Grey, I. E.; Fan, A.; Eliezer, Z.; Steinfink, H. The Oxidation State of Iron in Some Ba—Fe—S Phases: A Mössbauer and Electrical Resistivity Investigation of Ba$_2$FeS$_3$, Ba$_7$Fe$_6$S$_{14}$, Ba$_6$Fe$_8$S$_{15}$, BaFe$_2$S$_3$, and Ba$_9$Fe$_{16}$S$_{32}$. *J. Solid State Chem.* **1975**, *13* (1−2), 32−40.

(34) Chang, J.-C.; Ho, W.-Y.; Sun, I.-W.; Chou, Y.-K.; Hsieh, H.-H.; Wu, T.-Y.; Liang, S.-S. Synthesis and Properties of New (μ-Oxo)Bis[Trichloroferrate(III)] Dianion Salts Incorporated with Dicationic Moiety. *Polyhedron* **2010**, *29* (15), 2976−2984.

(35) Lledós, A.; Moreno-Mañas, M.; Sodupe, M.; Vallribera, A.; Mata, I.; Martínez, B.; Molins, E. Bent and Linear Forms of the (M-Oxo)Bis[Trichloroferrate(III)] Dianion: An Intermolecular Effect − Structural, Electronic and Magnetic Properties. *Eur. J. Inorg. Chem.* **2003**, *2003* (23), 4187−4194.

(36) Murray, K. S. Binuclear Oxo-Bridged Iron(Iii) Complexes. *Coord. Chem. Rev.* **1974**, *12* (1), 1−35.

(37) Bronger, W.; Ruschewitz, U.; Muller, P. Zur Struktur und zum Verhalten der Zweikernverbindungen Cs$_3$FeS$_3$, Na$_3$FeS$_3$, und Na$_3$FeSe$_3$. *J. Alloys Compd.* **1992**, *187* (1), 95−103, DOI: 10.1016/0925-8388(92)90525-E.

(38) Bain, G. A.; Berry, J. F. Diamagnetic Corrections and Pascal's Constants. *J. Chem. Educ.* **2008**, *85* (4), 532.

(39) Joshi, R. P.; Phillips, J. J.; Mitchell, K. J.; Christou, G.; Jackson, K. A.; Peralta, J. E. Accuracy of Density Functional Theory Methods for the Calculation of Magnetic Exchange Couplings in Binuclear Iron(III) Complexes. *Polyhedron* **2020**, *176*, 114194.

(40) Sharma, P.; Truhlar, D. G.; Gagliardi, L. Magnetic Coupling in a Tris-Hydroxo-Bridged Chromium Dimer Occurs through Ligand Mediated Superexchange in Conjunction with Through-Space Coupling. *J. Am. Chem. Soc.* **2020**, *142* (39), 16644−16650.

(41) Singh, G.; Gamboa, S.; Orio, M.; Pantazis, D. A.; Roemelt, M. Magnetic Exchange Coupling in Cu Dimers Studied with Modern Multireference Methods and Broken-Symmetry Coupled Cluster Theory. *Theor. Chem. Acc.* **2021**, *140* (10), 139.

(42) Logsdail, A. J.; Downing, C. A.; Catlow, C. R. A.; Sokol, A. A. Magnetic Coupling Constants for MnO as Calculated Using Hybrid Density Functional Theory. *Chem. Phys. Lett.* **2017**, *690*, 47−53.

(43) Kanamori, J. Superexchange Interaction and Symmetry Properties of Electron Orbitals. *J. Phys. Chem. Solids* **1959**, *10* (2−3), 87−98.

(44) Goodenough, J. B. Theory of the Role of Covalence in the Perovskite-Type Manganites [La,M(II)]MnO$_3$. *Phys. Rev.* **1955**, *100* (2), 564−573.

II

III

IV